# Platinum-free electrocatalysts for the oxygen reduction reaction in fuel cells

**Kathrin Preuss**

**Submitted in partial fulfilment of the requirements of the Degree of Doctor of Philosophy**


**School of Engineering and Materials Science,
Queen Mary University of London
London, United Kingdom**

## Statement of originality

I, Kathrin Preuss, confirm that the research included within this thesis is my own work or that where it has been carried out in collaboration with, or supported by others, that this is duly acknowledged below and my contribution indicated. Previously published material is also acknowledged below.

I attest that I have exercised reasonable care to ensure that the work is original, and does not to the best of my knowledge break any UK law, infringe any third party's copyright or other Intellectual Property Right, or contain any confidential material.

I accept that the College has the right to use plagiarism detection software to check the electronic version of the thesis.

I confirm that this thesis has not been previously submitted for the award of a degree by this or any other university.



Kathrin Preuss
Date: 11th September 2018

Details of publications:

- Preuss, K., Qiao, M. and Titirici, M.-M. (2018) Vol. 2 - Chapter 3. Hydrothermal Carbon Materials for the Oxygen Reduction Reaction in *Carbon-Based Metal-Free Catalysts: Design and Applications*. Wiley VCH, pp.369-401.
- Preuss, K., Tănase, L.C., Teodorescu, C.M., Abrahams, I., and Titirici, M.-M. (2017) Sustainable metal-free carbogels as oxygen reduction electrocatalysts. *J. Mater. Chem. A*, **5** (31), 16336–16343.

The following characterisation techniques were carried out by collaborators:

- XPS analysis (National Institute of Materials Physics in Bucharest, Romania)
- XRD analysis (National Research and Development Institute for Chemistry and Petrochemistry in Bucharest, Romania)
- ICP analysis and in situ TEM (King Abdullah University of Science and Technology in Saudi Arabia)

**Dedicated to my parents**

## Acknowledgements

Firstly, I would like to thank my supervisor Professor Magdalena Titirici for giving me the opportunity to carry out my PhD research in her group. She has been the most amazing mentor and role model I could have ever asked for, her support and advice have been invaluable to my personal and academic development. I particularly would like to thank her for the unconditional support and understanding she showed while I was going through some challenging times. I greatly appreciate everything she has done for me.

To Dr Isaac Abrahams, my second supervisor, I would like to say a sincere thank you for the support and discussions.

A big thank you has to go to all those who have helped me gather results and analysed samples for me because of limited access to the respective characterisation techniques. I am extremely grateful to Liviu and Cristina for helping with XPS measurements and never ever complaining about the many samples I sent. Thank you to Amira and Nitin for helping with ICP and in situ TEM measurements. Thanks to Ovidiu for carrying out XRD measurements. Thank you to Dr Andrei Sapelkin for offering advice and support with the proposal and subsequent beamtime at the Diamond Synchrotron. Thank you to Russell and Nadia for always helping out and giving advice during SEM and TEM sessions. And lastly thank you to my final year students, Alexander, Sushila and Adaeze who have helped in making samples and have taught me how to share knowledge.

A special thank you also has to go to Dr Lorenzo Botto, a good friend and wonderful person, who enabled me to start this PhD, without his support and believe in me I wouldn't have come this far. Similarly, if it wasn't for Dr Shelly Singh, who made London feel like a second home with all her love and friendship, I might have never come back to start my PhD. Though far away now, she will always be close at heart. Also thank you to my friend Dr Keeran Ward for his support, love and unconditional hospitality.

Thank you to Adam and Finos, who have greatly helped me and given me advice when I was lost at the beginning of my PhD. Mo, who started this journey with me and was always up for sharing experience and having a discussion about our results. Thank you to Servann and Philipp for being amazing colleagues and making home feel closer by making sure I am not forgetting my German. To Maria, who always offered moral uplift over a cup of tea. Jingyu, who always made work fun and was a great support with all things related to electrochemistry. Sabina, a wonderful person who I wish I could have spent more time with, but she has been a great help nevertheless. Thank you to all my other colleagues from the Titirici group, both old

and new, and those I spent time in the lab with, for the help, support and laughter, which made work feel like meeting friends.

To those who made this PhD special by sharing the joy and sorrow and becoming close friends. Thank you to Marta for being there for me every day and always looking after me. Thank you to Servann for his serenity and ability to always put things back in perspective. To Anuroopa, whose endless strength and determination have inspired me and taught me to never give up, her unconditional love has given me more than I can ever thank her for. To Sheetal, who made every day at work easier thanks to her wonderful sense of humour. Thank you to Awais for his cheerful presence and friendship. Also thank you to all the others who became close friends throughout the last years and have raised my spirits every day.

To those friends I left behind to embark on this journey, Bine, Dina, Jenny, Sarah, Axel and Jonas. Thank you for being my emotional support and for always making me feel at home regardless of my whereabouts.

Thank you to my parents, who made me the person I am today. They have been the greatest support throughout all my life with their unconditional love and trust. They have always supported me in all of my pursuits and encouraged me to follow my dreams. Without them I could not have done any of this, and I am infinitely grateful for all they have done for me.

Lastly, I would like to thank my wonderful husband Asad for giving me strength and his endless support and encouragement. His unconditional love and patience kept me going and I am so grateful for always having him by my side.

## Abstract

While climate change remains a persistent threat, long lasting alternatives must be developed to avoid greenhouse gas emissions. One solution could be the shift to a hydrogen based energy economy, where hydrogen could be won from renewable energy resources and used in fuel cells, where hydrogen and air are converted into electricity, heat and water. For this, a catalyst is needed both at the anode and cathode side of the fuel cell, which is typically platinum supported on carbon. As platinum is a scarce and noble metal with limited resources, it not only drastically increases a fuel cells cost, but also makes them unsustainable. Furthermore, shortcomings such as sluggish oxygen reduction reaction kinetics and low durability, create a high need for alternative materials.

The aim of this research was the development of platinum-free electrocatalysts for the oxygen reduction reaction based on carbon materials doped with non-noble metals and/or metal-free heteroatom dopants.

For this, an environmentally friendly and low cost approach for producing heteroatom doped materials was used, called hydrothermal carbonisation, where biomass or biomass precursors can be converted into different multifunctional nanoporous carbon materials with a high specific surface area and large pore volume. Materials were synthesised from glucose and ovalbumin, a protein that can be won from chicken egg white, yielding nitrogen doped cryogels. The influence of oxygen activation during the high temperature pyrolysis was investigated on the resulting carbogels and was found to aid higher surface area at the cost of yield loss and less incorporated nitrogen. Additional doping with metal-free heteroatoms sulphur and boron decreased the surface area, while sulphur did not interfere with the structure formation of the cryogel, the presence of a boron precursor caused an altered morphology and higher nitrogen content due to boric acid acting as structure directing agent and ovalbumin being fully utilised as nitrogen source. The sample containing nitrogen and additional boron was found to exhibit the most favourable electrocatalytic activity towards the oxygen reduction reaction due to a higher active sites density.

The influence of iron on the glucose-ovalbumin system was further investigated, where the addition of low amounts of ferric iron salt was found to be beneficial for the structure formation during the hydrothermal carbonisation as well as during the high temperature pyrolysis resulting in a higher surface area and better graphitisation, thus drastically improving the oxygen reduction reaction activity. The addition of other heteroatoms, sulphur and boron, to the iron/nitrogen material was further studied and caused a reduction in surface area. Similar to the metal-free versions, sulphur did not interfere with the structure formation, while the

boron precursor competed with the iron and ovalbumin to direct the structure resulting in an inhomogeneous morphology. The pure nitrogen/iron doped version exhibited the best catalytic activity in alkaline and acidic media, closely followed by the sample containing additional boron.

Due to controllability issues with surface area and dopant amount during the cryo- and carbogel synthesis, another set of materials was synthesised using a hard templating approach. This was carried out to get a better understanding of how different parameters like surface area, dopants and amount of dopant can influence the catalytic activity towards the oxygen reduction reaction. Different silica templates were used to yield varying surface area and pore volume, where a higher surface area only resulted in a better oxygen reduction reaction performance for the undoped control version, while doped carbons did not show any improvement. Different heteroatom dopant precursors were tested for their ability to dope the respective heteroatom into the carbon material. Urea was found to yield the highest nitrogen doping, boric acid was used as boron, allyl disulphide as sulphur and phosphoric acid as phosphorus source. Sulphur doping posed a challenge and resulted in very low dopant amounts, the large atomic size of sulphur was assumed to cause an issue during incorporation. While doping with different concentrations as well as co doping different heteroatoms, it was observed that only nitrogen species, namely pyridinic and graphitic nitrogen, seemed to act as active sites, e.g. a higher dopant amount resulted in a better catalytic activity. Whereas the other heteroatom dopants, boron, sulphur and phosphorus were assumed not to act as actual active sites but rather create defects within the carbon framework which enhanced the oxygen reduction reaction performance. Additional iron doping caused a slight improvement for all heteroatom dopants, though only iron and nitrogen were found to drastically boost the catalytic activity by forming the presumed $FeN_x$ active sites.

# Table of Contents

# List of Abbreviations

| | |
|---|---|
| Ag/AgCl | Silver-silver chloride reference electrode |
| BET | Brunauer-Emmett-Teller |
| CV | Cyclic voltammetry |
| DFT | Density functional theory |
| EA | Elemental analysis |
| EDX | Energy-dispersive x-ray spectroscopy |
| ETN | Electron transfer number |
| EXAFS | Extended x-ray absorption fine structure |
| FC | Fuel cell |
| FT-IR | Fourier transform infrared spectroscopy |
| HER | Hydrogen evolution reaction |
| HMF | Hydroxymethylfurfural |
| HOR | Hydrogen oxidation reaction |
| HTC | Hydrothermal carbonisation |
| ICP | Inductively coupled plasma spectroscopy |
| LSV | Linear sweep voltammetry |
| OER | Oxygen evolution reaction |
| ORR | Oxygen reduction reaction |
| PEMFC | Polymer electrolyte membrane fuel cell |
| RDE | Rotating disk electrode |
| RHE | Reversible hydrogen electrode |
| RRDE | Rotating ring disk electrode |
| SEM | Scanning electron microscope |
| STEM | Scanning transmission electron microscope |
| TCA | 2-Thiophenecarboxaldehyde |
| TEM | Transmission electron microscope |
| TGA | Thermogravimetric analysis |
| XAFS | X-ray absorption fine structure |
| XANES | X-ray absorption near edge structure |
| XPS | X-ray photoelectron spectroscopy |
| XRD | X-ray diffraction spectroscopy |

# List of Figures

# List of Tables

# Chapter 1 | Introduction

Increasing population and wealth are causing an ever rising need for energy in nowadays society, causing an energy crisis with serious consequences for our earth. Climate change is now on the brink of causing irreversible damage unless greenhouse gas emissions are drastically reduced.[1] At the Paris climate agreement in 2015, world leaders committed to take action against greenhouse gas emissions in order to keep the total increase of global warming below 2 ºC. Considering this ambitious goal, a fast shift from a fossil fuel based society to a sustainable and renewable energy society is required. Many countries have announced bans for fossil based vehicles, becoming effective as early as 2025 for some. All this does not only entail a rise in renewable energy generation through wind, solar or water power, but also with fuel cells and bioenergy. To balance out demand and supply as well as for future electric car technologies, efficient energy storage such as batteries and supercapacitors are also needed.

With these drastic changes towards renewable energy technologies, sustainability must be kept in mind. A well known definition of sustainability was defined in 1987 by the Brundtland Commission as "… development that meets the needs of the present without compromising the ability of future generations to meet their own needs".[2] Many of the renewable energy technologies rely heavily on scarce and noble metals, such as lithium and cobalt for batteries, gallium and germanium for solar cells, or platinum group metals for fuel cells.[3] Figure 1.1 shows the periodic table with endangered elements highlighted, classed in limited availability, rising threat and serious threat. Considering these predictions, alternative materials and/or better and more efficient ways of element recovery must be found in order to ensure availability of all elements for future generations, making nowadays element utilisation sustainable. Apart from sustainability, with most noble metal resources being limited to very few regions of the globe, for example more than 75 % of platinum are mined in South Africa,[4] dependence on market fluctuation and thus price variations are a serious concern when planning a future with renewable energy solutions.

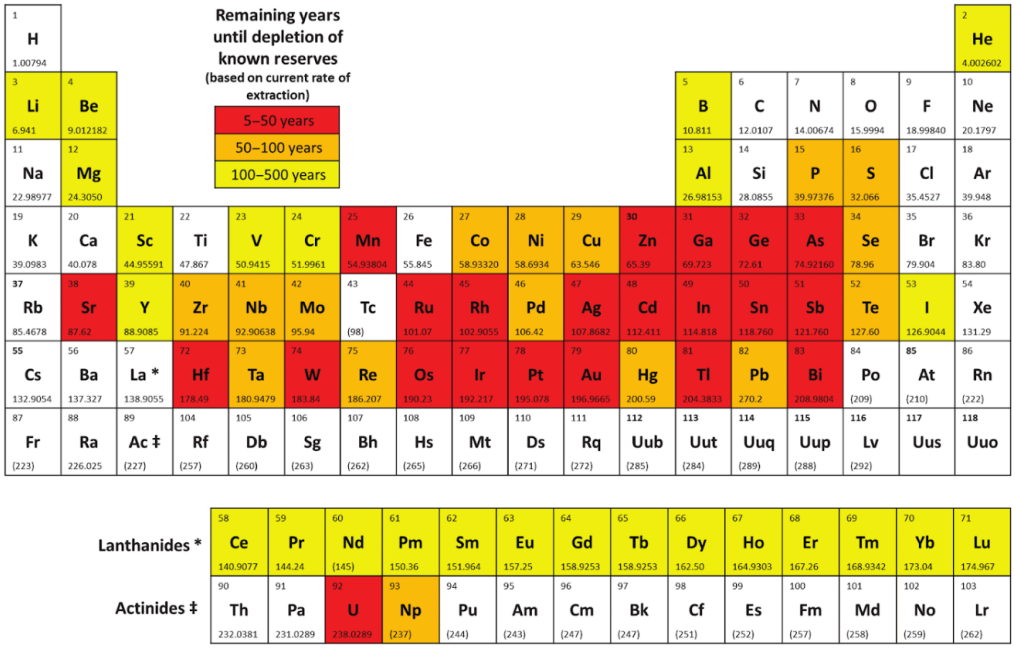


*Figure 1.1 Periodic table of endangered elements, showing elements under serious threat (red), rising threat (orange) and with limited availability (yellow). Reproduced from Hunt et al.,[3] Copyright 2013 Royal Society of Chemistry.*

Many of these technologies already use carbon materials as catalyst support or electrodes and much research is carried out in order to fully replace scarce and noble elements with carbon based alternatives. Carbon is one of the most abundant elements in universe and one of the main building blocks of organic life. It exists in different allotropes with the most common occurring as diamond and graphite. Up to date, two Nobel Prizes have been awarded for carbon allotropes, fullerenes in 1996 and graphene in 2010.[5] New synthesis techniques have generated a multitude of novel nanostructures such as carbon onions, carbon aerogels, carbon fibres or multiwalled CNTs. While carbon can be won from fossil fuel based precursors, there are also ways to utilise biomass and -waste as starting materials for sustainable carbons via hydrothermal carbonisation. Here, in a matter of hours, any kind of biomass can be converted into carbon materials with water as a solvent under moderate temperatures and self generated pressure.[6] This process is based on coal formation on the earth over millions of years, allowing the synthesis of cheap, environmental friendly and easily tuneable carbon materials.

As mentioned earlier, there are a number of renewable energy technologies for energy generation, one of them being fuel cells. There are different types of fuel cells, ranging from low to high temperature, with the former mostly being used in stationary applications and the latter in stationary, portable or automotive/transport applications. Generally, fuel cells are a promising alternative for energy generation due to their high

fuel efficiency and possibility to use different fuels,[7] which contributes to the steady increase in market growth (Figure 1.2). Predictions for future fuel cell usage estimate a compound annual growth rate (CAGR) of 20.9 % until 2025.[8]

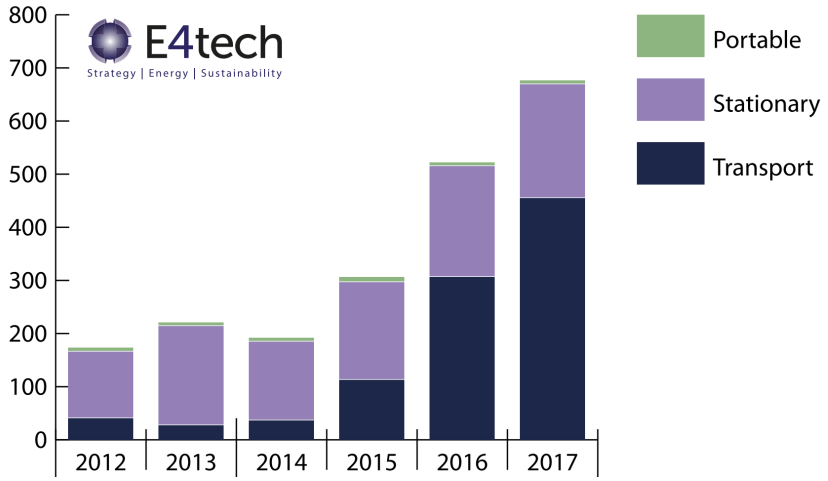


*Figure 1.2 Megawatts shipped of power generated by fuel cells, separated in their different applications (portable, stationary and transport/automotive) for the years 2012 – 2017. Reproduced from E4tech,[9] Copyright 2017 E4tech.*

One of the most commonly used fuel cell type are polymer electrolyte membrane fuel cells (PEMFC), as can be seen in Figure 1.3, operating at low temperatures, using hydrogen and air/oxygen as fuels.

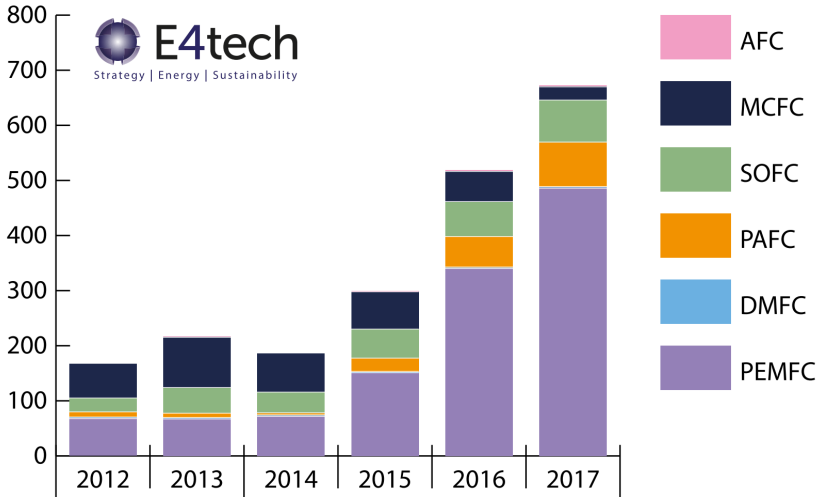


*Figure 1.3 Megawatts shipped of power generated by different types of fuel cells for the years 2012 – 2017. AFC – alkaline fuel cell, MCFC – molten carbonate fuel cell, SOFC – solid oxide fuel cell, PAFC – phosphoric acid fuel cell, DMFC – direct methanol fuel cell, PEMFC – polymer electrolyte membrane fuel cell. Reproduced from E4tech,[9] Copyright 2017 E4tech.*

Though most commonly used, there are still critical drawbacks limiting extensive commercialisation of PEMFCs, one being, as discussed earlier, the usage of the scarce

and noble metal platinum as catalyst, both at the anode and cathode side. Moreover, the use of hydrogen as a fuel also poses a challenge regarding sustainability, as most hydrogen produced still originates from fossil based resources like natural gas or coal with carbon dioxide as a by product.[10] Though less popular, but on the ascending branch is hydrogen production by thermochemical conversion of biomass or more ideally, as completely $CO_2$ neutral, via water splitting (biophotolysis, electrolysis, photovoltaic electrolysis).[11]

Ideally, water splitting could be coupled with the fuel cell technology to generate $CO_2$ neutral electricity, for this a series of electrochemical reactions is employed. During electrolysis, the hydrogen evolution reaction (HER) and the oxygen evolution reaction (OER) take place at the cathode and anode, respectively. While in a fuel cell, the hydrogen oxidation reaction (HOR) occurs at the anode and the oxygen reduction reaction (ORR) at the cathode. The correlated polarisation curves and respective reactions can be seen in Figure 1.4.

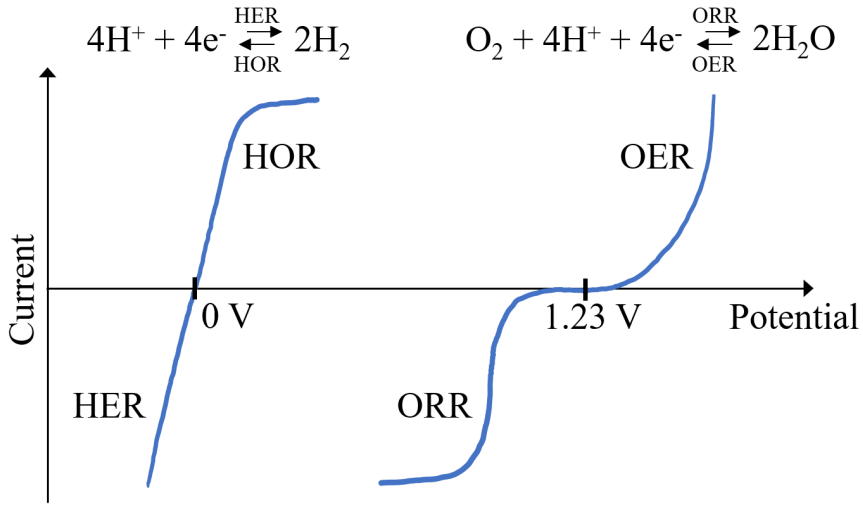


*Figure 1.4 Schematic polarisation curves for corresponding electrochemical reactions for hydrogen and oxygen with equilibrium potentials (vs RHE). Axes are not drawn to scale.*

As can be seen, the electrochemical reactions involving oxygen can cause significant overpotentials which lead to an efficiency loss of the fuel cell. Thus electrocatalysts, such as platinum for the ORR have to be used in high amounts, making it a popular research topic in electrocatalysis.

This thesis is based on the development of platinum-free electrocatalysts for the oxygen reduction reaction in fuel cells. For this, carbon based materials were produced via different methods, hydrothermal carbonisation and direct pyrolysis, starting from the biomass precursor glucose.

The main objectives of this research project were:

- To synthesise metal-free and non-noble metal electrocatalyst from sustainable biomass precursors and investigate the influence of different heteroatom and metal precursor on the material properties by physiochemically characterisation and test these catalysts electrochemically for the oxygen reduction reaction
- To synthesise model metal-free and non-noble metal electrocatalysts to get a better understanding of how different dopants and surface area can influence the catalytic activity towards the oxygen reduction reaction

This thesis consists of seven chapters. Chapter 1 gives a brief introduction into the necessity for renewable energy applications such as fuel cells and the objectives of this research project.

Chapter 2 gives some theoretical background on fuel cells, their working principle and different electrocatalysts for the oxygen reduction reaction. It also gives an introduction into the history and mechanism of hydrothermal carbonisation, and carbon aerogels in particular.

Chapter 3 and 4 focus on the development and characterisation of carbogels as oxygen reduction reaction electrocatalysts via hydrothermal carbonisation. Here, chapter 3 is dedicated to metal-free catalysts doped with different heteroatoms such as nitrogen, sulphur and boron, while chapter 4 is based on a further advancement of these metal-free catalysts by combining them with the non-noble metal iron to improve their physical and catalytic properties.

Chapter 5 is introducing hard templated model carbon catalysts to investigate the influence of different metal-free heteroatom dopants, also in combination with iron, and surface area on the oxygen reduction reaction activity.

Chapter 6 offers a summary on the findings presented in chapters 3, 4 and 5, and concludes this thesis with suggestions on future work based on this research project.

Chapter 7 presents synthesis methods and characterisation techniques used in this thesis.

# Chapter 2 | State of the Art

In the following chapter a general understanding of fuel cells and their working principle is presented, with a focus on different electrocatalysts for the oxygen reduction reaction. Moreover, the history and mechanism of hydrothermal carbonisation is discussed with the special example of carbon aerogels.

## 2.1 Fuel cells

A fuel cell (FC) is an electrochemical galvanic cell that can convert chemical energy into electrical energy. For this, a fuel is usually oxidised at the anode side (hydrogen oxidation reaction - HOR) while an oxidant is reduced at the cathode (oxygen reduction reaction - ORR) with the most common fuel and oxidant being hydrogen and oxygen/air, respectively. Different types of FCs exist which are mainly categorised by their electrolyte. These different types of FCs can be separated into high temperature and low temperature FCs, an overview of different FCs can be found in Table 2.1. Though high temperature FCs (SOFC, MCFC) usually have a higher electric efficiency, their use is mostly limited to large stationary power plants due to operating temperatures above 500 ºC as well as their sensitivity to non-continuous (start/stop) operation.[12] The most common low temperature FC type is the polymer electrolyte membrane or proton exchange membrane, short PEM, fuel cell. Implementations for this type of FC can be found in various automotive, stationary and portable power applications.

*Table 2.1 Different types of fuel cells and their key features.*[12–15]

| **Type of fuel cell** | **Electrolyte** | **Temperature** | **Half-cell reactions** |
|---|---|---|---|
| Polymer electrolyte membrane (PEMFC) | Polymer membrane | 40 – 80 ºC | A: $H_2 \longrightarrow 2H^+ + 2e^-$<br>C: $½\ O_2 + 2H^+ + 2e^- \longrightarrow H_2O$ |
| Direct methanol (DMFC) | Polymer membrane | 30 – 80 ºC | A: $CH_3OH + H_2O \longrightarrow CO_2 + 6H^+ + 6e^-$<br>C: $^3/_2\ O_2 + 6H^+ + 6e^- \longrightarrow 3H_2O$ |
| Alkaline (AFC) | KOH | 65 – 250 ºC | A: $H_2 + 2OH^- \longrightarrow 2H_2O + 2e^-$<br>C: $½\ O_2 + H_2O + 2e^- \longrightarrow 2OH^-$ |
| Phosphoric acid (PAFC) | $H_3PO_4$ | 150 – 250 ºC | A: $H_2 \longrightarrow 2H^+ + 2e^-$<br>C: $½\ O_2 + 2H^+ + 2e^- \longrightarrow H_2O$ |
| Molten carbonate (MCFC) | $(Na,K)_2CO_3$ | 500 – 700 ºC | A: $H_2 + CO_3^{2-} \longrightarrow H_2O + CO_2 + 2e^-$<br>C: $½\ O_2 + CO_2 + 2e^- \longrightarrow CO_3^{2-}$ |
| Solid oxide (SOFC) | $(Zr,Y)O_{2-\delta}$ | 600 – 1000 ºC | A: $H_2 + O^{2-} \longrightarrow H_2O + 2e^-$<br>C: $½\ O_2 + 2e^- \longrightarrow O^{2-}$ |

The very first PEMFC was developed in the 1960`s for the Gemini Space Program and has been constantly improved since then.[15] The main component of a PEMFC is the membrane electrode assembly (MEA), which consists of a proton conductive polymer membrane, a cathode and an anode, as shown in Figure 2.1. The most commonly used membrane nowadays is made up of perfluorosulfonylfluorideethylpropylvinylether, also called Nafion® (Dupont).

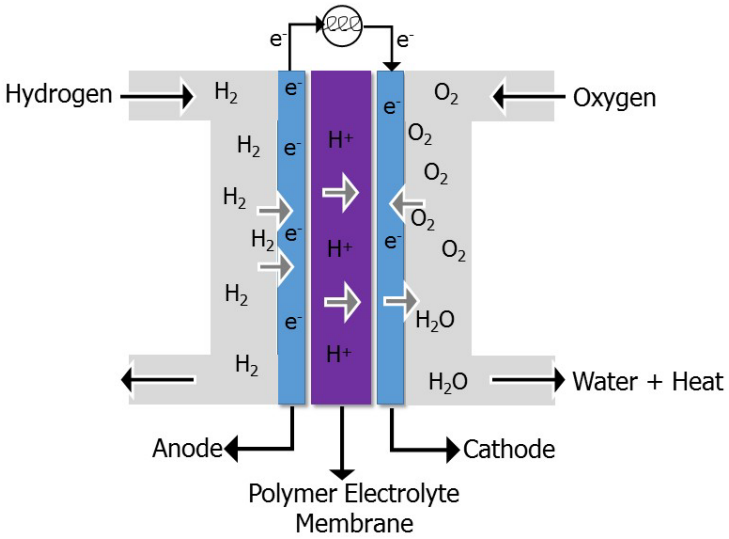


*Figure 2.1 Schematic model of a polymer electrolyte membrane fuel cell (PEMFC).*

A fuel, usually hydrogen, is fed into the anode section, which is then split into protons and electrons. The protons are able to travel through the polymer electrolyte membrane, the electrons are collected, where they can be used as direct source of electricity and can also be re-entered to the other side of the membrane. At the cathode side oxygen is injected, which reacts together with the hydrogen protons and electrons to water in an exothermic reaction.

Each single PEMFC can generate up to 1V,[15] depending on the desired application, a higher output voltage may be needed, which can be achieved by connecting multiple fuel cells in series, which is called a fuel cell stack.

Due to the lower operating temperature in PEMFCs, DMFCs, AFCs and PAFCs the catalyst commonly used both at the anode and cathode side is platinum, while high temperature FCs (MCFC and SOFC) can operate without noble metal catalysts due to more favourable kinetics at such high temperatures.

### 2.1.1 Thermodynamic fundamentals

When reactants are converted to products in an electrochemical cell, the maximum work available is equal to the Gibbs free energy, $\Delta G$.

$$\Delta G = \Delta H - T\Delta S, \qquad \textit{Equation 1}$$

where $\Delta H$ is the enthalpy difference, $T$ is the temperature and $\Delta S$ is the difference in entropy.[15] Electrochemical work, $W_e$, can be expressed as:

$$W_e = nFE, \qquad \textit{Equation 2}$$

with $n$ being the number of electrons transferred and $F$ being the Faraday constant (charge carrier by a mole of electrons).[15] In the case of reversibility, all Gibbs free energy can be converted to electrochemical work/energy and the cell potential, $E$, can be related according to the following equation:

$$\Delta G = -nFE. \qquad \textit{Equation 3}$$

At equilibrium conditions, Gibbs free energy can be expressed via the following equation:

$$\Delta G = \Delta G^0 + RTlnQ = \Delta G^0 + RTln\left(\frac{P}{P_0}\right), \qquad \textit{Equation 4}$$

where $R$ is the gas constant, $P$ is the pressure and $P_0$ is the standard pressure.[16] Based on the above presented equations, a relationship between the cell potential, $E$, and the reaction quotient, $Q$, can be established, which is called the Nernst equation:[16]

$$E = E^0 - \frac{RT}{nF} lnQ. \qquad \textit{Equation 5}$$

In a hydrogen/air fuel cell at room temperature, if all Gibbs free energy can be utilised, the ideal cell potential corresponds to 1.23 V.

A fuel cells efficiency $\eta$ can be calculated by the ratio of energy output (energy produced), $\Delta G$, to energy input (enthalpy of hydrogen), $\Delta H$.[17] The theoretical efficiency of a fuel cell is 83 %, far higher than the maximum theoretical Carnot efficiency (applicable for heat engines), especially at low temperatures, which makes fuel cells highly attractive.[7]

### 2.1.2 Electrochemical fundamentals

Electrochemical reactions are defined by an activation energy barrier between electrolyte and solid electrode that must be overcome by charge.[15] The rate at which the electrons are released/consumed is defined as the electrical current. Current density, $i$, is the current normalised with the electrode surface area. The exchange current density, $i_0$, is a rate constant at which the forward and backward reactions proceed at an eqilibrium.[15] Ideally, the exchange current density should be large, which helps obtain a high current at low overpotentials. A relationship between the current and potential is expressed by the Butler-Volmer equation:

$$i = i_0 \left[exp\left(\frac{n\alpha F\eta}{RT}\right) - exp\left(\frac{n[1-\alpha]F\eta}{RT}\right)\right], \qquad \textit{Equation 6}$$

where $\alpha$ is the charge transfer coefficient and $\eta$ is the activation overpotential (electrode potential minus equilibrium potential), which is the potential difference required to generate current.[16] If the overpotential becomes large, the backward (anode polarisation) can be neglected and the Butler-Volmer equation can be adjusted to:[17]

$$i_c = i_0 \left[ exp\left(\frac{n\alpha F \eta_c}{RT}\right)\right]. \qquad \textit{Equation 7}$$

From this the so called Tafel equation can be derived, which is:

$$\Delta V = a + b\ log(i), \qquad \textit{Equation 8}$$

where $b$ is called the Tafel slope and $a$ is the intercept if the potential is plotted against the logarithmic current density.[15] The exchange current density can be obtained where the line subtends the x axis, as can be seen in Figure 2.2

$$a = 2.3\frac{RT}{\alpha F}\log(i_0) \qquad b = 2.3\ \frac{RT}{\alpha F}. \qquad \textit{Equation 9 and 10}$$

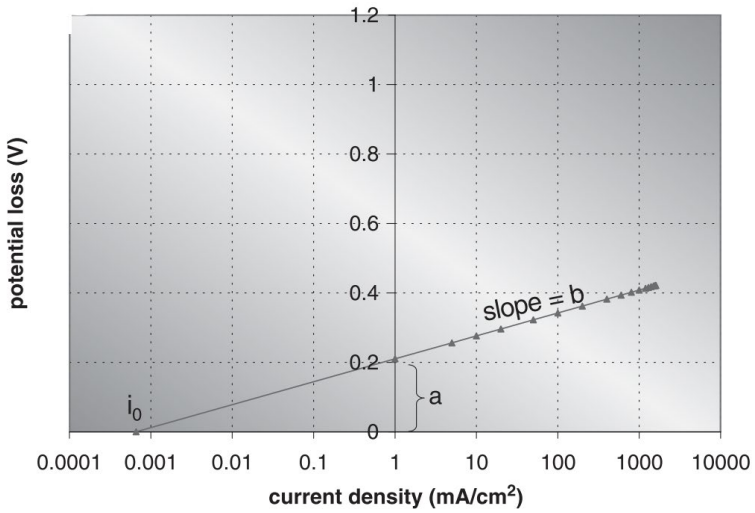


*Figure 2.2 Theoretical Tafel plot showing potential vs current density. Reproduced from Barbir,[15] Copyright 2013 Elsevier Inc.*

If the electrical circuit of a fuel cell is open, no current is generated and the so called open circuit potential is obtained.[15] Theoretically this potential should be close to the ideal cell potential of 1.23 V, though in reality it is lower due to a number of voltage losses as can be seen in Figure 2.3. Activation polarisation occurs at low current densities due to sluggish reaction kinetics of the oxygen reduction reaction, followed by ohmic polarisation at intermediate current densities caused by resistance in flow of ions (electrolyte) and electrons (electrode).[15] At high current densities concentration polarisation dominates due to mass transport effects as reactants are consumed rapidly while products accumulate and transport limitations occur.[17]

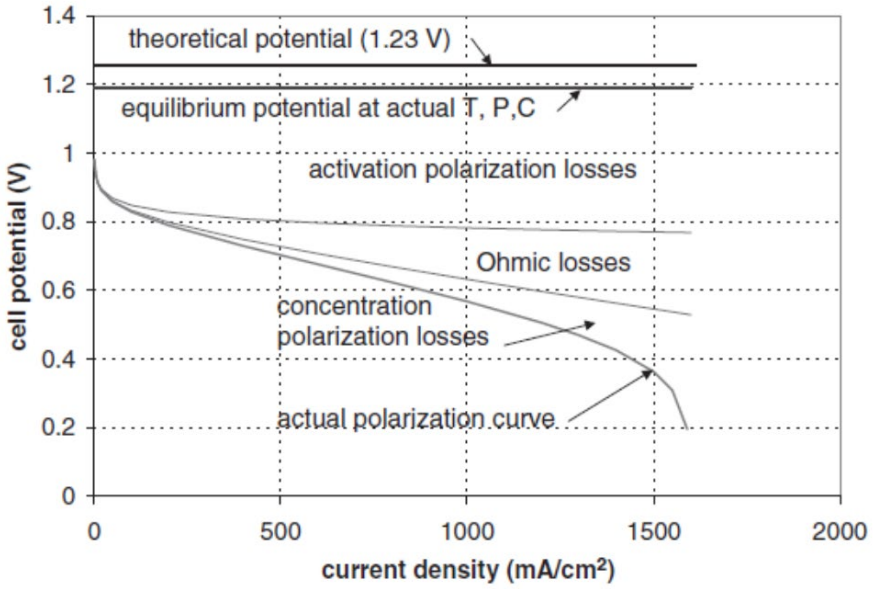


*Figure 2.3 Theoretical polarisation curves depicting the different voltage losses in a fuel cell. Reproduced from Barbir,[15] Copyright 2013 Elsevier Inc.*

### 2.1.3 Electrocatalysts for the oxygen reduction reaction

The most likely reason why low temperature FCs have not been greatly commercialised up to this point, may be the tremendous costs caused during the production of the electrodes. This part can make up to 52 % of the overall cost when producing a PEMFC due to the common use of platinum as an electrocatalyst.[18] To overcome this drawback and many more disadvantages caused by a platinum-based electrocatalyst, alternative materials with excellent electrocatalytic activity need to be developed. While platinum is used both at the anode and at the cathode side, research focuses on alternative cathode materials, due to the considerably higher use of Pt (around 80-90 % of total Pt content) compared to the anode side, owing to slower reaction kinetics for the ORR than for the HOR.[19] Different approaches try to reduce the platinum loading or preferably replace the platinum with other noble metals, like palladium, as well as with non-noble metals, like iron, whereas other research is trying to produce completely metal-free electrocatalysts for the ORR, sometimes even via a sustainable synthesis route. Despite the difference in composition, all these catalytic materials should, in general, have the same reaction pathway in common.

The ORR in acidic and alkaline aqueous electrolyte can follow two different pathways, the 4- and 2-electron pathway, as shown in Table 2.2.

*Table 2.2 Possible 4- and 2-electron pathway for the oxygen reduction reaction in acidic and alkaline aqueous electrolyte with relative reduction potentials.*[20–22]

| **Acidic aqueous electrolyte** | | **Alkaline aqueous electrolyte** | |
|---|---|---|---|
| $O_2 + 4H^+ + 4e^- \rightarrow 2H_2O$ | 1.23 V | $O_2 + 2H_2O + 4e^- \rightarrow 4OH^-$ | 0.40 V |
| $O_2 + 2H^+ + 2e^- \rightarrow H_2O_2$ | 0.68 V | $O_2 + H_2O + 2e^- \rightarrow HO_2^- + OH^-$ | -0.43 V |
| $H_2O_2 + 2H^+ + 2e^- \rightarrow 2H_2O$ | 1.77 V | $HO_2^- + H_2O + 2e^- \rightarrow 3OH^-$ | 0.94 V |

In FCs the 4-electron pathway, also called full reduction, is always the favoured option in order to increase the fuel cell`s efficiency and to prevent for example PEMFC components from corroding due to hydrogen peroxide being formed during the 2-electron pathway, also called partial reduction.[23] A schematic depicting the full and partial reduction of oxygen forming either water or hydrogen peroxide, respectively, can be seen in Figure 2.4

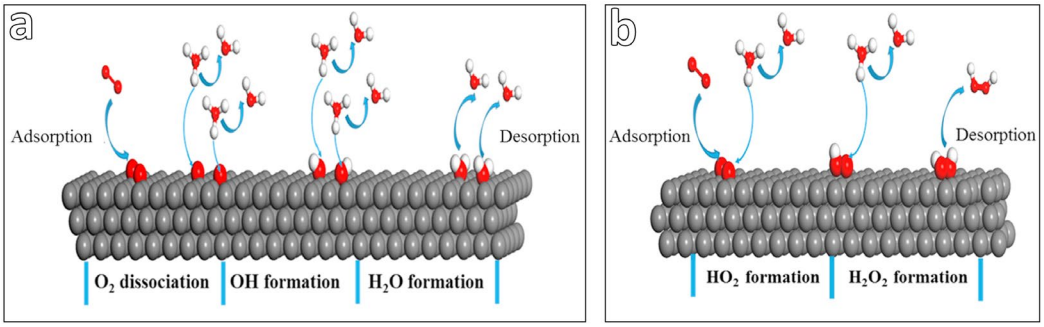


*Figure 2.4 Schematics showing the full (a) and partial(b) reduction of oxygen forming water or hydrogen peroxide, respectively. Reproduced from Stacy et al.,*[24] *Copyright 2016 Elsevier Ltd.*

ORR catalysts always proceed via a mix of the 2- and 4-electron pathway, with even platinum forming low amounts of $H_2O_2$ during the reaction. Recently, Muthukrishnan et al. reported a possible overestimation of the direct 4-electron pathway, especially at high catalyst loadings, due to the inclusion of a quasi-4-electron pathway, a two site reduction process where $H_2O_2$ adsorbed on the surface and matrix is further reduced to $H_2O$ without any free peroxide species being released.[25,26]

When discussing electron transfer reactions, disruption due to the interface between the electrode (solid) and the electrolyte solution should not be neglected. Interactions between the ions in the electrolyte and the electrode surface will be different as compared to those in solution only, while the additional charge at the electrode due to potentiostatic control can also influence the transfer.[27] Due to this, an electrical double layer is formed at the interface, which can be described by different models. In 1853, Helmholtz first described the phenomena of two layers with opposite charge at the boundary between electrode and electrolyte, similar to an electrical capacitor with two plates of charge

separated by a distance.[28] To balance the electrode charge, the attracted ions collect at the electrode surface, where the distance is assumed to be limited by the ion radius as well as a single sphere of solvation around each ion.[27] This results in a double layer and a potential drop which is limited to this specific region, also called outer Helmholtz plane (OHP),[29] as can be seen in a simplified schematic in Figure 2.5. Since then, newer models have emerged accounting, for example, for the possibility of absorption on the surface, as well as diffusion and mixing in solution, which are the diffuse-layer model by Gouy and Chapman, the compact diffuse-layer model by Stern, the triple-layer model by Esin and Markov, Grahame and Devanathan, and the water-dipole model by Bockris, Devanathan and Muller.[27]

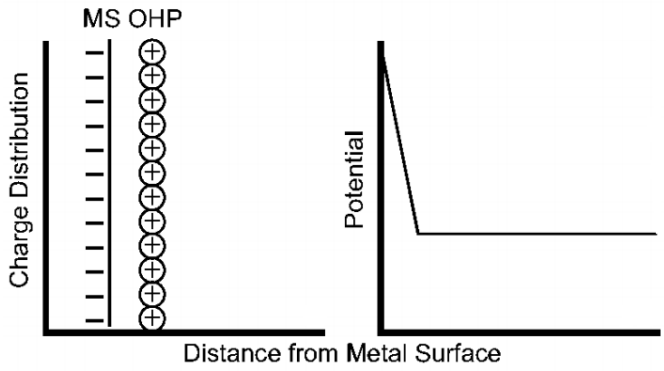


*Figure 2.5 Schematic of the electrical double layer at the electrode/electrolyte interface as described by Helmholtz. Reproduced from Srinivasan,[27] Copyright 2006 Springer.*

There have been many efforts to increase the activity of electrocatalysts for the oxygen reduction reaction and while platinum remains the most commonly used catalyst, research interest has also spread towards other noble and non-noble metals. A typical way to compare different catalysts towards their ability for an electrochemical reaction is the volcano plot, as can be seen in Figure 2.6 for the oxygen reduction reaction. Here, the activity is plotted against the binding energies for different metals with a single oxygen atom, where on the left branch oxygen binding is considered too strong, while on the right branch it is too weak. Platinum is the metal closest to the theoretical activity peak, though even platinum's binding energy is around 0.2 eV too strong.[30] Alloying metals as well as combining them with heteroatoms, for example iron and nitrogen, can change the binding energies and make them more suitable candidates for the ORR.

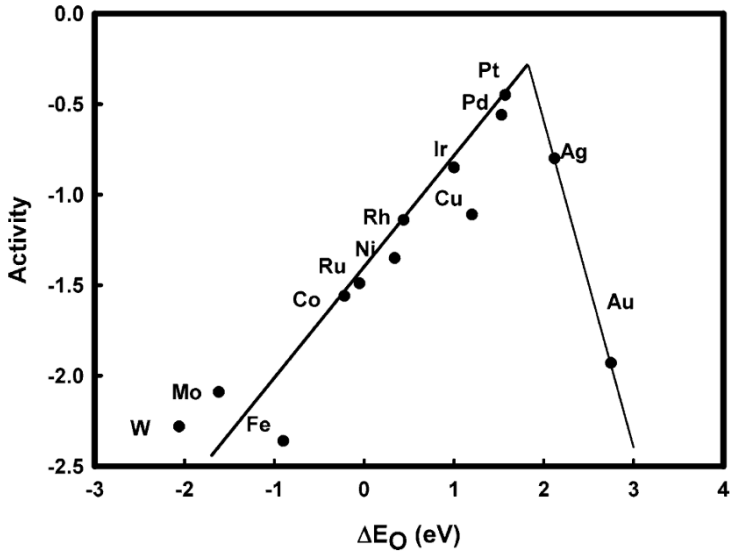


*Figure 2.6 Oxygen reduction activity vs the oxygen binding energy of different metals. Reproduced from Nørskov et al.,[30] Copyright 2004 American Chemical Society.*

In the following subchapters the three different classes of ORR electrocatalysts, noble metal, non-noble metal and metal-free, will be discussed.

### *2.1.3.1 Noble metal catalysts*

As already mentioned, the most common electrocatalyst used in low temperature FCs is platinum supported on carbon. Apart from the fact that platinum is a scarce and expensive material with resources limited to very few regions of the globe, it also shows relatively slow ORR kinetics, due to the formation of –OH(ads) species,[21,31] low durability/stability in terms of long time usage and low tolerance for methanol or CO poisoning.[23] The ORR mechanism on platinum is thought to be largely understood and proceeds via two different mechanisms depending on the current density range, as can be seen in Table 2.3.[30] While the dissociative mechanism is a detailed version of the 4-electron pathway, with no $H_2O_2$ formation, the associative mechanism is a proposed alternative without $O_2$ dissociation before its hydrogenation. Instead of water being formed at the third step during the associative mechanism, alternative formation of $H_2O_2$ is possible when the O-O bond is left unbroken.[20]

Nevertheless, though studied extensively, the ORR mechanism on Pt may be even more complex than assumed, depending on the Pt particle size as well as environmental parameters.[19,21]

*Table 2.3 Oxygen reduction mechanisms on platinum depending on low or high current densities.*[24,30]

| **Dissociative mechanism (low current densities)** | **Associative mechanism (high current densities)** |
|---|---|
| | $O_2 + Pt \rightarrow Pt\text{-}O_2^*$ |
| | $Pt\text{-}O_2^* + H^+ + e^- \rightarrow Pt\text{-}O_2H^*$ |
| $½\ O_2 + Pt \rightarrow Pt\text{-}O^*$ | $Pt\text{-}HO_2^* + H^+ + e^- \rightarrow H_2O + Pt\text{-}O^*$ |
| $Pt\text{-}O^* + H^+ + e^- \rightarrow Pt\text{-}OH^*$ | $Pt\text{-}O^* + H^+ + e^- \rightarrow Pt\text{-}OH^*$ |
| $Pt\text{-}OH^* + H^+ + e^- \rightarrow H_2O + Pt$ | $Pt\text{-}OH^* + H^+ + e^- \rightarrow H_2O + Pt$ |

* adsorbed molecule on active site of platinum catalyst

A way to reduce the cost while producing a fuel cell, but keeping platinum as a catalyst, is the reduction of the Pt loading and the improvement of its long term stability. Three different classes of Pt-based electrocatalysts can be distinguished, pure Pt, shell-core Pt and Pt alloys.[19] Research focuses on changing the shape or reducing the particle size of pure Pt catalysts making them more electrocatalytically active,[32,33] while shell-core structures can reduce the amount of Pt used by coating a thin layer of Pt on a cheaper metal core (Pd, Ru or Re).[34,35] Alloying platinum with other noble metals like Ru, Pd, Au or transition metals, such as Cu, Ni or Fe is also a promising approach to reduce the amount of Pt necessary and reduce the cost.[36–38] Another approach is the use of more stable carbon supports such as carbon nanotubes or graphene to reduce carbon corrosion and subsequently avoid detachment/agglomeration of the Pt catalyst.[39–41]

Another method to overcome the shortcomings of Pt is the fall back on other noble metals, such as Pd, Au or Ag, though Pt has the highest mass activity out of all,[21] which is why the replacement with other precious materials is questionable due to similar shortcomings in terms of availability and price as platinum.

### *2.1.3.2 Non-noble metal catalysts*

As an approach to replace platinum-based electrocatalysts, non-noble metals like Fe, Cu, Co and Ni were found as convenient alternatives. Many of these non-noble metal catalysts are inspired by biomolecules such as the heme group in haemoglobin cytochrome c oxidase, an iron protoporphyrin, responsible for oxygen binding/transport in the human body. The potential of using these metal/nitrogen macrocyclic compounds as ORR catalysts in alkaline electrolyte was first reported by Jasinski in 1964.[42] A variety of electrocatalysts have emerged from this, usually based on a carbon support, though the electrocatalytic activity of these materials depends on the metal itself, as well as on the

metal and nitrogen precursors used, the synthesis procedure and the metal content. Research in the 1990's has shown that Fe-based catalysts showed the most favourable electrocatalytic activity towards the ORR compared to other transition metals like Co, Mn, Cr, Ni, Zn and Cu.[43–45] Interestingly, the catalytic activity increases with rising metal content up to a certain limit (depending on the metal precursor) at which the activity plateaus,[44,46,47] which is explained by the increasing concentration of catalytic sites until all the nitrogen of the phenanthroline type is coordinated with metal and inactive metal clusters are formed. In a more recent study by Liu et al,[48] a similar trend was found, showing that traces of Fe, with an optimum as low as 0.05 wt%, can boost the catalytic activity, followed by a second (lower) activity peak around 8 wt%.

Though extensive research has been carried out on these non-noble metal catalysts with many reporting promising catalytic activity and stability, the ORR mechanism and active sites are still debated due to contradictory reports. The most common concept is based on $MeN_x$ active sites incorporated into the carbon framework, similar to the metal phthalocyanines first reported by Jasinski.[42] Proposed structures of these active sites of non-noble metal catalysts containing iron can be found in Figure 2.7. Most research assumes the iron ion to be surrounded by four nitrogen atoms in two different planar configurations, one named $FeN_{2+2}/C$ containing phenanthroline pyridinic N and the other being $FeN_4/C$ containing pyrrolic N.[49] Owing to its nature, the latter is more difficult to incorporate into a graphitic framework, especially in combination with high temperature pyrolysis. Other studies also suggested a square-pyramidal coordination of the iron ion with five nitrogen atoms as shown by Sun et al.[50] via DFT calculations. They suggested that a five coordinated Fe centre is more likely due to the high adsorption energy of Fe for a fifth ligand, although it weakens the bonding of $O_2$. Further, they also found that the Fe centre occurs in the ferrous ($Fe^{2+}$) or ferric state ($Fe^{3+}$) depending on its coordination with four or five ligands, respectively.

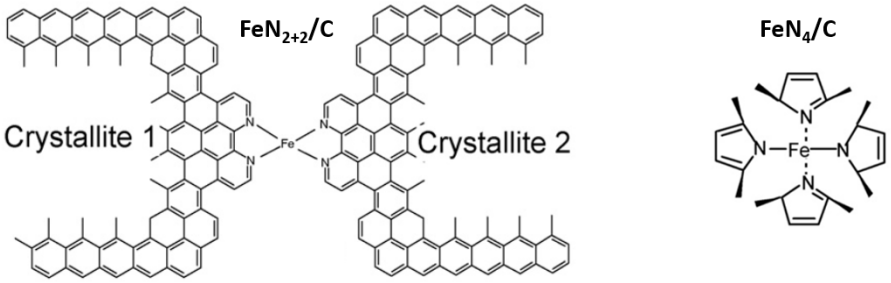


*Figure 2.7 Proposed active sites of metal phthalocyanines catalysts for the oxygen reduction reaction with iron as example. Reproduced from Charreteur et al.,[49] Copyright 2008 Elsevier Ltd.*

Apart from theoretical studies, a number of experimental investigations, mostly employing x-ray absorption fine structure (XANES and EXAFS) and Mössbauer spectroscopy, have shown the involvement of $FeN_x/C$ sites in the oxygen reduction reaction.[51–54] Besides $FeN_x/C$, few research suggests that the active sites are metallic or carbide nanoparticles formed during high temperature pyrolysis surrounded by a protective graphitic layer.[55,56] More commonly though, findings report a favoured ORR activity for catalysts containing a combination of both, $FeN_x/C$ and Fe nanoparticles.[57,58] Other research also showed enhanced ORR activity in the presence of iron oxide, often as particles, suggesting the latter could also be a probable active site.[59–61]

Studies using ex and in situ XAFS have given insights into the binding mechanism of $O_2$ in Fe-containing catalysts, [62–65] a schematic for the proposed mechanism can be found in Figure 2.8 both under acidic and alkaline conditions. Here, two different active sites were suggested, one being $FeN_x/C$, active in both electrolytes, and the other being Fe nanoparticles ($Fe_{NPs}/C$) additionally active at a low pH. Ex situ XAFS found that the Fe-$N_x/C$ sites are present as $Fe^{3+}N_x/C$ under aerobic conditions and at high potentials, poisoned with adsorbed oxygen, which switches to the catalytically active $Fe^{2+}N_x/C$ at potentials close to the $Fe^{2+}/Fe^{3+}$ redox potential, enabling the adsorption of oxygen and initiating the ORR. While the $Fe^{2+}N_x/C$ active site enables the first reduction to peroxide intermediates in both electrolytes, they are also responsible for the further reduction of $HO^{2-}$ to $OH^-$ under alkaline conditions. Whereas in acidic electrolyte, the second active site $Fe_{NPs}/C$ is needed in close proximity to complete the $4e^-$ reduction pathway.

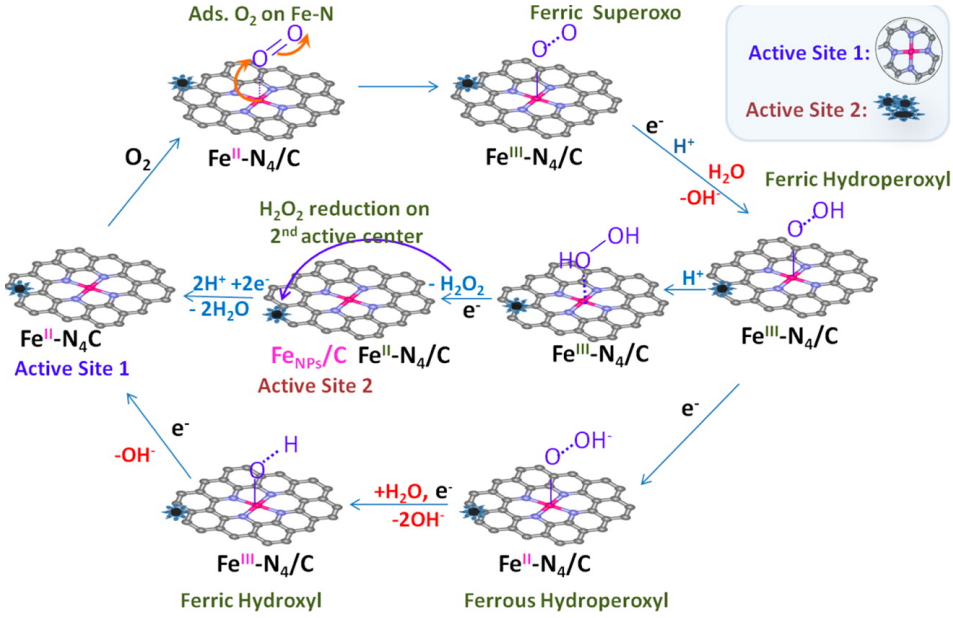


*Figure 2.8 Proposed oxygen reduction reaction pathways determined via in situ XAFS under acidic (blue font) and alkaline (red font) conditions. The schematic includes two types of active sites, $FeN_x/C$ and Fe nanoparticles ($Fe_{NPs}/C$). Reproduced from Tylus et al.,[64] Copyright 2014 American Chemical Society.*

Though most researchers agree that ferrous iron is the active species to bind $O_2$ for the ORR, there are contradictory reports relating ferric iron to the adsorption of $O_2$. Wang et al.[66] used halogen poisoning with NaF to show that the active sites in their catalyst are mainly consisting of $Fe^{3+}$.

A contentious idea reported in literature is that the metal precursor only helps to create defects in the heteroatom doped carbon framework, promoting "metal-free" C/N active sites, without the metal taking part in the ORR. While few reports present reasonable proof for the actual absence of active metal sites by poisoning experiments or adequate characterisation,[67,68] most other research claims metal-free activity after acid washing/etching via XPS, XRD, TEM or EDX.[69–71] As discussed earlier, already trace amounts of metal can drastically boost the catalytic activity of a material, leaving doubt about actual metal-free catalysts when any metal precursor was used during the synthesis. Pumera and his research group showed that amounts as low as 18 ppm of Mn influenced the ORR activity of their catalyst, they further proved that detecting these trace metal amounts is unreliable with characterisation techniques such as XPS, TGA or SEM/TEM coupled with EDX, but rather needs analysis via ICP, magnetic susceptibility, neutron activation analysis, electron paramagnetic resonance or x-ray fluorescence.[72–75]

A very recent study carried out by Varnell et al.[76] demonstrated the definitive involvement of Fe in both alkaline and acidic electrolyte in the ORR by selective removal of Fe and remaining content analysis via ICP. They found that a control sample containing 70 % less Fe still exhibited comparable ORR performance in both electrolytes to their standard catalyst, suggesting that only a certain amount (0.2 – 0.5 wt%) of Fe close to the catalyst surface is acting as active sites.

Considering the conflicting claims about the active sites in heteroatom doped carbon catalysts containing Fe, the heterogeneity of such materials still prevents a definite assignment. Apart from general discussions about active sites, recent findings have indicated the possibility of different active sites depending on the electrolyte due to the common observation that $FeN_x/C$ catalysts show increased activity in alkaline compared to acidic electrolyte, which is often explained by leaching of active sites under acidic conditions, suggesting additional nitrogen functionalities or quinone groups contributing to the catalysts activity.[77,78] Malko et al.[79] found that poisoning a $FeN_x/C$ catalyst with nitrite or nitric oxide resulted in a drastic activity decrease under acidic conditions, but made little to no difference when tested in alkaline media, which indicated the presence of metal-free active sites under alkaline conditions. Ramaswamy and Mukerjee[80] proposed a difference in inner- and outer-sphere mechanism during the ORR depending

on the electrolyte pH, where the mechanism relies on inner-sphere electron transfer in acidic and a combination of inner- and outer-sphere electron transfer in alkaline media, which was later supported by another research group.[81] The proposed mechanism can be seen in Figure 2.9, where the double layer of the inner and outer Helmholtz plane are shown schematically in alkaline media.

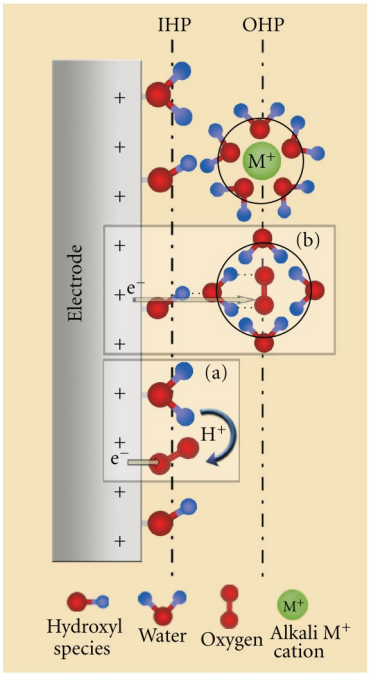


*Figure 2.9 Schematic depicting the inner Helmholtz plane (IHP) and outer Helmholtz plane (OHP) in alkaline media showing the inner sphere (a) and outer sphere (b) electron transfer mechanism during the oxygen reduction reaction. Reproduced from Ramaswamy et al.,[80] Copyright 2012 Hindawi.*

At alkaline conditions, hydroxyl, water and chemisorbed oxygen are present at the inner Helmholtz plane.[80] The inner sphere mechanism (Figure 2.9a) relies on the chemisorption of oxygen, followed by the complete reduction of adsorbed intermediates until the final product is desorbed, leading to the 4-electron pathway. Whereas the outer sphere mechanism (Figure 2.9b) involves solvated molecular oxygen, which can interact with adsorbed surface hydroxyl groups via hydrogen bonds, resulting in the release of peroxide species. Interestingly, the proposed outer sphere mechanism implies a certain unspecificity towards the nature of the catalyst, e.g. no direct involvement of the metal is assumed. Ramaswamy and Mukerjee further found that for $FeN_x$ catalysts, the inner sphere mechanism was favoured as compared to the outer sphere mechanism, though the formation of stable iron peroxide compounds in alkaline media caused efficient reduction of any intermediate peroxide species, while the reduction of peroxide in acidic media was unlikely due to weak binding between iron and $H_2O_2$, which explained the improved catalytic activity of $FeN_x$ catalysts in alkaline as compared to acidic media.[80]

### *2.1.3.3 Metal-free catalysts*

Completely metal-free electrocatalysts for the ORR remain as an ideal and highly desired target within fuel cell research, preferably produced from sustainable precursors with an easy to scale up synthesis route. Commonly, carbon nanomaterials are used such as carbon nanotubes or graphene, but also heteroatom doped carbons that contain nitrogen, sulphur, phosphorus, boron and/or oxygen have proved to be promising candidates.

While the ORR mechanism seems to be widely understood on metal surfaces, the actual active sites and reduction of oxygen on metal-free surfaces are still a case of speculation. Most assumptions on the enhanced activity of those heteroatom doped carbons are based on differences in electronegativity and atomic size between the carbon atoms and the heteroatom dopant, values can be found in Table 2.4.

*Table 2.4 Values for electronegativity and covalent radius of carbon and heteroatom dopants nitrogen, sulphur, boron, phosphorus and oxygen, values taken from Mortimer and Müller.*[82]

| | C | N | S | B | P | O |
|---|---|---|---|---|---|---|
| Electronegativity | 2.6 | 3.0 | 2.6 | 2.0 | 2.2 | 3.4 |
| Covalent radius [pm] | 77 | 74 | 103 | 82 | 106 | 66 |

With nitrogen being the most common dopant amongst metal-free carbons, the different species of nitrogen can add beneficial properties to the carbon material. Pyridinic N can offer a lone electron pair, while graphitic N can introduce an extra electron in the delocalized π-system, which both enhance the basicity and electron-donor capacity of the material and thus its ORR activity.[83] A lot of research has been carried out in order to understand which of the nitrogen species are truly involved in the enhanced catalytic activity and while some suggest pyridinic N is the active species,[84] others claim it is graphitic N.[85,86] More recent studies indicate that a synergistic effect between both of these species causes the improved ORR activity, where Kim et al.[87] proposed an interconversion of the two N species during the ORR process, while Lai et al.[88] observed an influence of pyridinic N on the catalysts onset potential and of graphitic N on its limiting current density. Likewise, the effect of nitrogen species on the catalysts selectivity towards the 2- or 4-electron pathway also remains unclear with adverse findings being reported.[84,89,90] Due to a lack of techniques to experimentally identify the actual active sites in metal-free catalysts, most studies rely on theoretical density functional theory (DFT) calculations to get a better insight. Likewise, a proposed ORR mechanism for nitrogen doped graphene can be seen in Figure 2.10. It was found that oxygen was likeliest adsorbed by the edge carbon atom closest to the nitrogen atom.[87] While the cycle starts with the nitrogen atom in graphitic configuration, it is converted to

pyridinic nitrogen after oxygen adsorption (1), the first electron transfer (2) and subsequent release of $OH^-$ (3). Further electron and proton transfer (4) causes closing of the broken C-N bond and the nitrogen atom is reverted back into the graphitic configuration, while water is released after another electron/proton transfer (5).

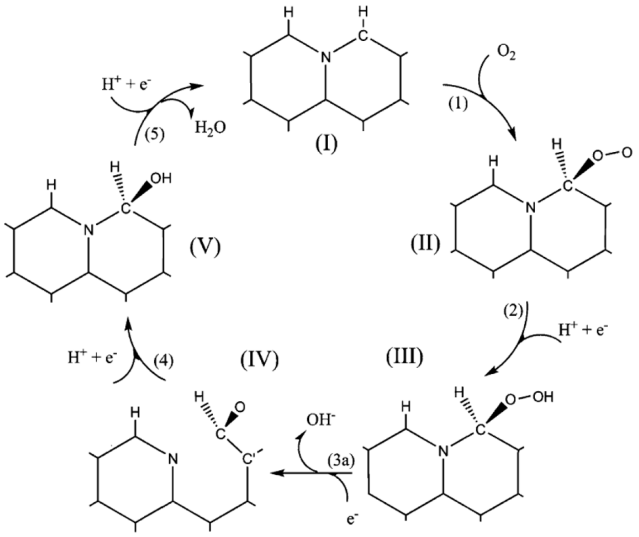


*Figure 2.10 Schematic showing a proposed ORR mechanism on nitrogen doped graphene. Reproduced from Kim et al.,[87] Copyright 2011 Royal Society of Chemistry.*

Based on the above presented ORR mechanism on N doped graphene, the authors suggested that the pyridinic N configuration (IV) could exist in high oxygen amount graphene or if the carbon is prepared in the presence of oxygen, thus creating another possible active site apart from graphitic N.[87]

Similarly to nitrogen, doping boron or phosphorus can cause a disruption in the charge uniformity and induce high spin densities on the carbon framework due to their difference in electronegativity compared to the carbon atoms.[83,91] While nitrogen has a higher electronegativity than carbon, creating a positive charge on the neighbouring carbon atom, boron and phosphorus have a lower electronegativity, creating a positive charge on the dopant itself, causing acidic defects which present possible adsorption sites for $O_2$ species.[91] When co doping nitrogen with boron or phosphorus this charge density profile can change the chemisorption of oxygen by acting as a bridge to transfer electrons directly from the positively charged atom to $O_2$ thus weakening O-O bonds and increasing the ORR activity.[83]

Due to its large atomic size compared to carbon or nitrogen, doping sulphur can cause structural defects and increase polarisability additional to enhancing the spin density of neighbouring carbon atoms, which can facilitate easier interaction between molecules in the electrolyte.[83,92] Once more, co doping nitrogen with sulphur has been reported to

enhance the catalytic activity even further compared to single doped materials, which is usually explained by a synergistic effect between both dopants due to a higher spin and charge density.[93]

The influence of oxygen doping on the ORR activity is also under discussion, with adverse findings being reported. Disagreement is caused by the difficulty to produce carbons completely absent of oxygen, which results in most carbon materials containing at least small amounts of oxygen functionalities. Thus, assigning any true influence of oxygen on the ORR activity proves difficult, especially as most other heteroatom dopants occur in combination with oxygen. Nevertheless, similar to other dopants, the change in charge density is thought to be responsible for the altered ORR activity. Quinone groups have been shown to be active towards the ORR.[94–97] While some research showed little to detrimental influence of oxygen doping in carbons on the electron transfer,[98,99] others have reported a general favour towards the 2-electron pathway,[100,101] where additional functionalisation with nitrogen, resulting in co doping, yielded a catalyst proceeding via the 4-electron pathway.[101,102]

DFT calculations on nitrogen doped graphene suggested that catalytically active sites are more likely to either have a high positive charge or spin density,[23,103] where a similar trend can be assumed for other heteroatom doped carbons. In Figure 2.11 and 2.12 typical configurations for single and co doped heteroatoms nitrogen, sulphur, boron, phosphorus and oxygen in a carbon matrix are shown.

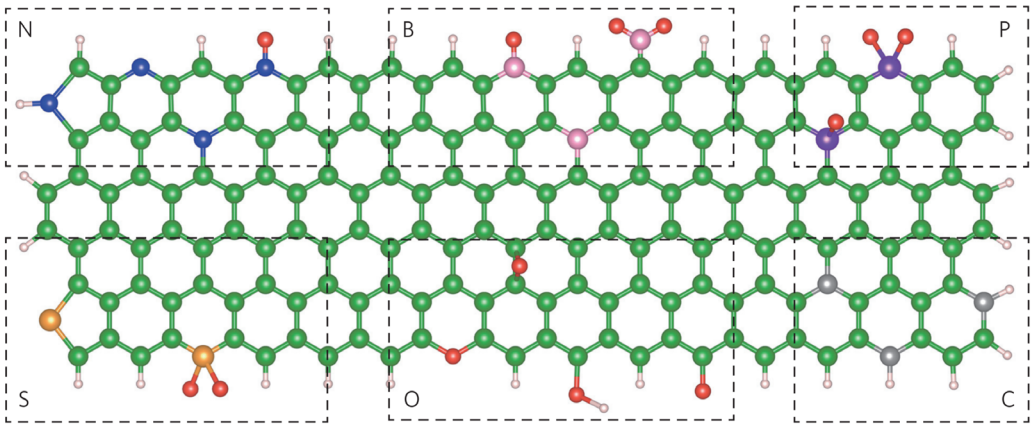


*Figure 2.11 Different heteroatom dopants incorporated into a carbon matrix. C- green/grey, N – blue, B- pink, P – purple, S – orange, O – red, H - rose (small). Reproduced from Jiao et al.,*[104] *Copyright 2016 Springer Nature Ltd.*

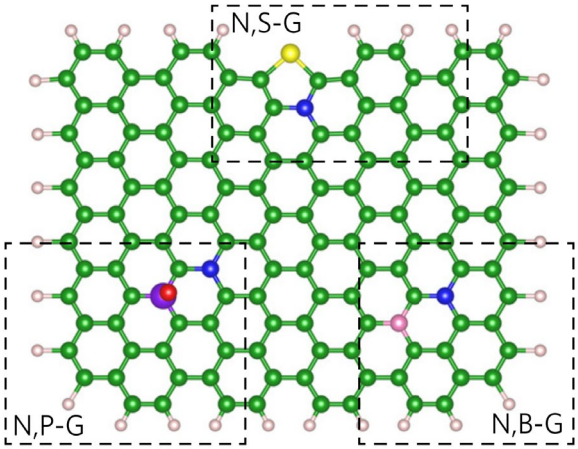


*Figure 2.12 Different heteroatom co dopants incorporated into a carbon matrix. C- green/grey, N – blue, B- pink, P – purple, S – yellow, O – red, H - rose (small). Reproduced from Jiao et al.,*[104] *Copyright 2016 Springer Nature Ltd.*

Jiao et al.[105] investigated possible active sites in differently heteroatom doped graphene via theoretical DFT calculations based on experimentally derived results. They compared the overall reaction barriers for different configurations of each heteroatom, which were determined via XPS for the actual doped graphene catalysts. For the pure graphene the edge atoms were observed to be most active, while carbon atoms in the middle of the basal plane seemed unlikely to bind oxygen due to the evenly distributed $sp^2$ bonds causing unsurmountable reaction barriers.[105] The most likely active sites in the sulphur doped graphene were found to be neighbouring carbon atoms, with the direct neighbouring carbon atom in the C-S-C configuration and the second neighbouring carbon in a thiophene type configuration. In oxygen doped graphene, the lowest reaction barrier was calculated for the carbon atom next to oxygen in a pyran type configuration, followed by the carbon next to oxygen in a C-OH setup. Phosphorus doping was found to lead to active sites being most likely the out of plane upward facing P-O in a P-$C_3$-O configuration. Boron doped graphene was found to exhibit the boron atom in a graphitic boron ($BC_3$) type setup as most likely active sites, while in a B-$C_2$-O configuration the second neighbouring carbon atom at the edge had the lowest reaction barrier. For the most commonly reported heteroatom dopant nitrogen, they investigated graphitic N, pyridinic N and pyrrolic N, where they found that graphitic N exhibited the lowest overall reaction barrier. Within the graphitic and pyrrolic N setup, the most likely active sites was found to be a neighbouring carbon atom, while in pyridinic N the nitrogen atom itself was observed to act as active site due to the lone electron pair offered by pyridinic nitrogen.[105] The volcano plot derived from experimental and theoretical results comparing the most active configuration of each heteroatom dopant is shown in Figure 2.13.

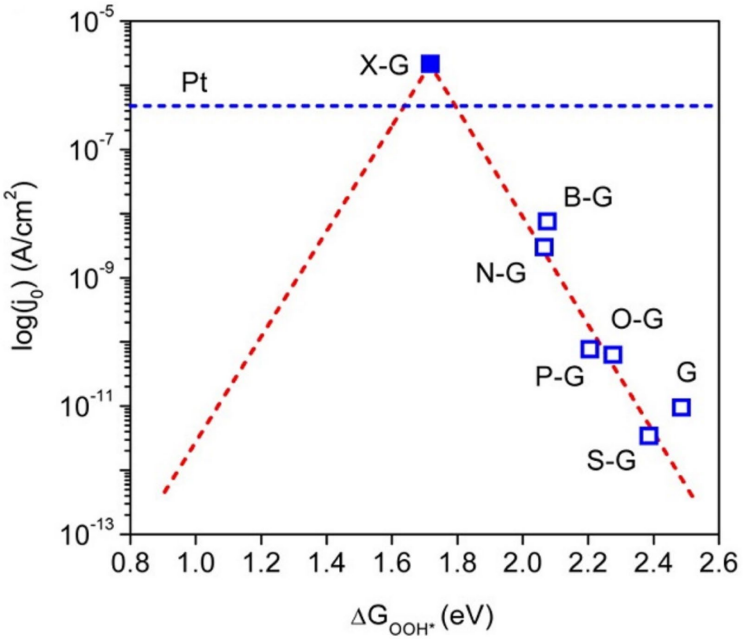


*Figure 2.13 Volcano plot showing experimentally derived $j_0$ vs theoretically derived $\Delta G_{OOH}$ for different heteroatom doped graphene (hollow blue squares) compared to the experimentally derived $j_0$ for platinum (dashed blue line) and an ideal, theoretical x doped graphene (full blue square). Reproduced from Jiao et al.,*[105] *Copyright 2014 American Chemical Society.*

Generally, the incorporation of different heteroatom dopants can influence the electrical carrier properties of the carbon material and enhance its electrical conductivity, which in turn can positively affect the catalytic activity of the material. This, usually, increase in electrical conductivity is due to a change in electronic band structure upon the incorporation of the dopants as they alter the energy gap between valence and conduction band. Here, different types of doping can be distinguished, achieved via different dopants, resulting either in n-type doping, for heteroatoms such as nitrogen, which can add extra valence electrons, or p-type doping, for heteroatoms such as boron, which have less valence electrons as compared to carbon.[106]

While the above mentioned assumptions on the enhanced catalytic activity of heteroatom doped carbons are mostly based on a change in the electronic properties/environment due to electronegativity and atomic size, some research also suggests that structural defects are the actual ORR enhancing sites.[107] Research has shown the edge of carbon materials exhibits a higher electrocatalytic activity compared to carbon in the basal plane, due to a delocalised charge distribution.[108] Intrinsic defects in the carbon framework, induced by heteroatom dopants or at the edge itself, can change the electric density and thus offer a higher binding affinity with ORR intermediates.[107,109] Among different defects, a combination of a pentagon and heptagon ring at the edge of a pure carbon catalyst displayed favourable performance, the authors suggested that such topological defects

with the addition of nitrogen could ever further enhance the ORR activity.[109] Other studies suggested that a combination of two pentagons and one octagon, as well as two pentagons and two heptagons on the edge of a graphene plane (Figure 2.14) can lower the activation barrier and enable easier reduction of the oxygen.[110,111]

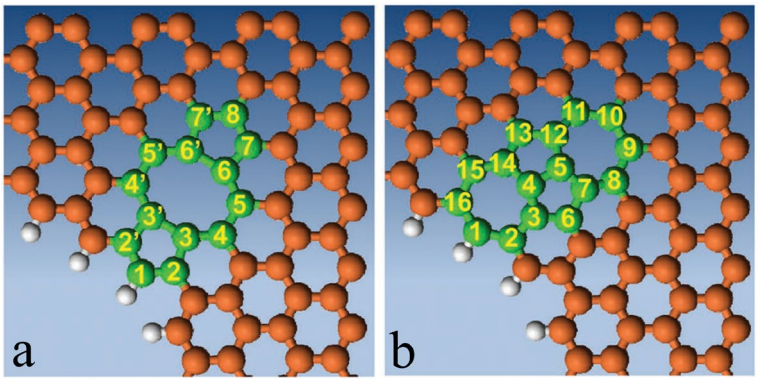


*Figure 2.14 Exemplary defects in graphene. a) 585 defect and b) 7557 defect. Reproduced from Jia et al.,[110] Copyright 2016 Wiley VCH.*

Similar to non-noble metal catalysts, different ORR mechanisms on nitrogen doped carbons are proposed depending on the pH of the electrolyte including inner sphere electron transfer in acidic and a combination of inner and outer sphere electron transfer in alkaline media.[112] Generally, carbon catalysts, especially metal-free, exhibit a pH dependant difference in performance, with superior activity and stability in alkaline media, due to the protonation of surface groups obstructing charge delocalisation under acidic conditions.[92,112]

## 2.2 Hydrothermal carbonisation

Hydrothermal carbonisation (HTC) nowadays represents a commonly used sustainable process to convert biomass, as well as their precursors, into valuable carbon materials with various applications including energy storage, electrocatalysis and gas storage. The very first idea of this process arose in 1913, when Friedrich Bergius reported the production of synthetic coal from cellulose at high temperatures and pressures.[113]

The process of hydrothermal carbonisation is based on the concept of coal formation which occurred over millions of years on earth, converting biomass with water as a solvent in a lab autoclave into carbon materials under self generated pressure and mild temperatures (180-200 °C) in a matter of hours. Surface area, pore properties, morphology and chemical composition of the resulting carbon material is highly dependent on the type of starting material as well as the reaction conditions. While soft plant tissue and biomass precursors like glucose, without a crystalline cellulose scaffold

usually form small carbon spheres with interstitial porosity, hard plant biomass containing structural crystalline cellulose results in a replica similar to its original structure.[114]

The HTC of pure glucose is shown in Figure 2.15, which proceeds via different steps starting with an isomerisation to fructose (not shown in Figure 2.15), which is then dehydrated to 5-hydroxymethylfurfural (HMF). HMF can further hydrolyse to levulinic acid and formic acid but can also undergo other complex reactions such as self-condensation, Diels-Alder reactions and cross condensation with aldehydes or ketones. These formed compounds can then polymerise or nucleate and subsequently carbonise via additional intermolecular dehydration, typically yielding carbon spheres.[115] These carbon spheres grow in size with increased process time. With a change of starting material, the addition of other chemicals, or a change in reaction conditions the resulting product changes due to even more complex reactions occurring.

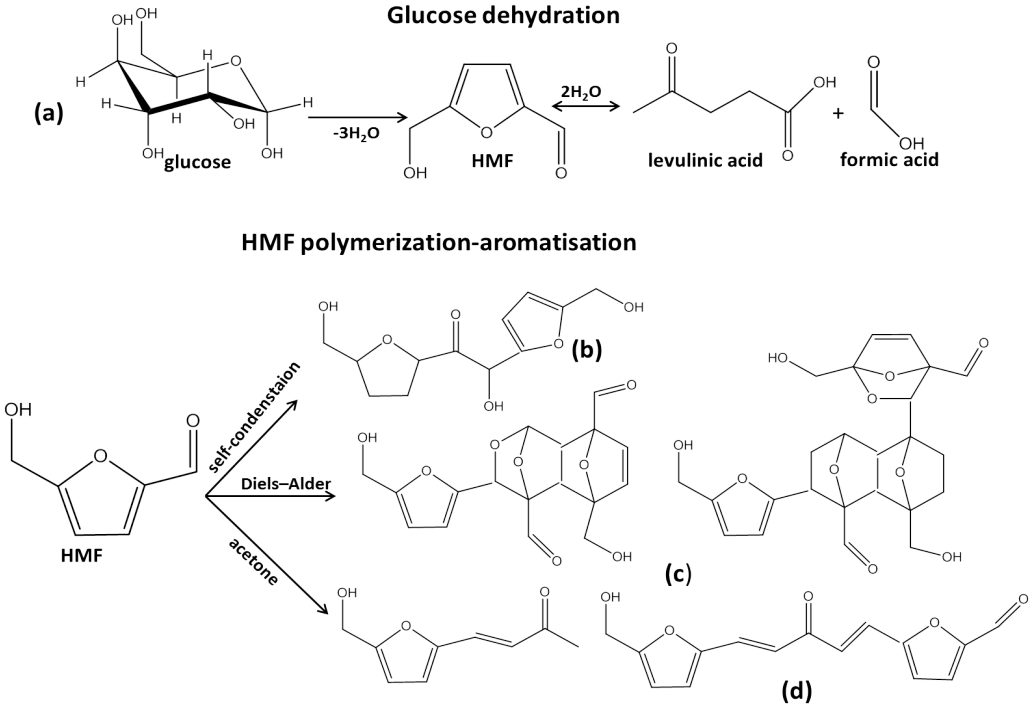


*Figure 2.15 Chemical reactions involved during the hydrothermal carbonization of glucose: a) Dehydration of glucose to HMF and potentially to levulinic and formic acid; b) Self-condensation of HMF; c) Diels Alder HMF condensations; d) Reaction of acetone with HMF. Reproduced from Dai et al.,*[116] *Copyright 2018 John Wiley & Sons, Ltd.*

A typical example for this is the presence of nitrogen containing precursors, which causes additional reactions between a reducing sugar and amines, a cascade of reactions classified as Maillard reactions, changing the typical HTC formation by creating nitrogen doped carbons.[117] Maillard reactions are extremely complex and many different compounds can be formed based on the starting materials. The initial step of the Maillard chemistry starts with the sugar-amine condensation by a nucleophilic attack on the sugars'

aldehyde forming glycosylamines.[118] Via the loss of water, a Schiff base is formed which then converts into aminoketoses via Amadori rearrangement.[5] These compounds can then, among other reactions, undergo dehydration to form HMF. Exemplary chemical reactions for the aforementioned Maillard chemistry can be found in Figure 2.16.

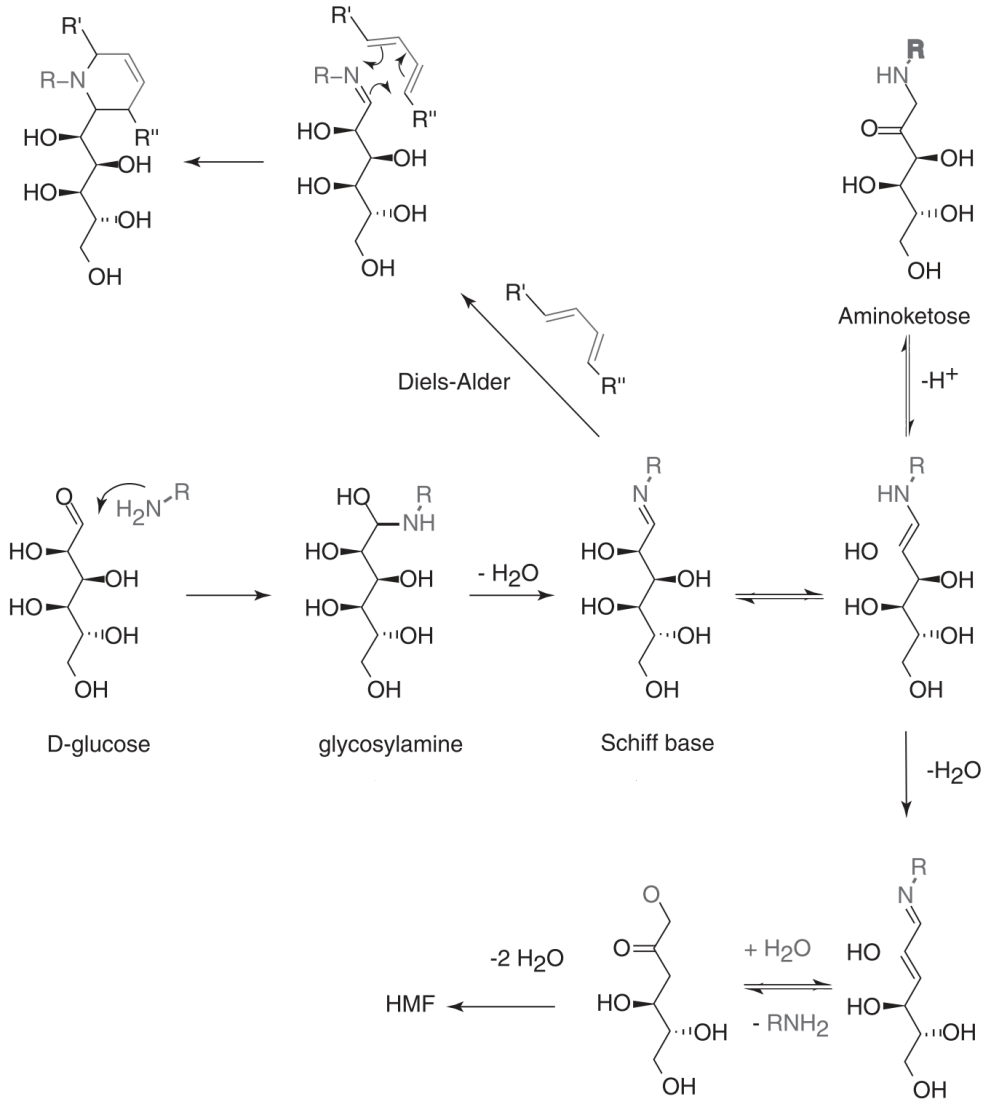


*Figure 2.16 Examples for the Maillard reaction of glucose and an amine. Reproduced from Titirici et al.,[5] Copyright 2013 John Wiley & Sons, Ltd.*

HMF can further react with ammonia, formed during the oxidation of, for example, amino acids, or other amines to form pyrrole and pyridine-like compounds via various steps (Figure 2.17).[118] At the same time, HMF can also form other nitrogen free compounds via polymerisation and aromatisation, as described above (Figure 2.15). These different compounds can then polymerise and nucleate to form nitrogen doped carbon structures.

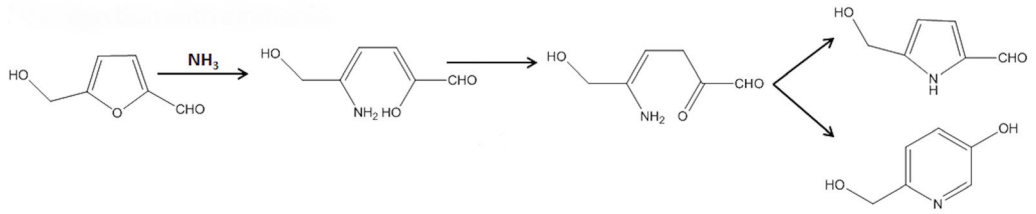


*Figure 2.17 Example chemical reactions involved in the Maillard reaction of HMF and ammonia. Reproduced from Dai et al.,*[116] *Copyright 2018 John Wiley & Sons, Ltd.*

During the HTC process, precursors containing other dopants, such as sulphur, boron or iron can be added, which can change the cascade of reactions and alter the final product. Considering the change in reaction chemistry by the addition of different precursors, unsurprisingly, parameters such as morphology, surface area and pore properties are hard to control during the HTC process. Thus, templating methods are used to impose certain desired criteria, with the distinction between soft and hard templating. The former usually relies on the self assembly of block-copolymers with the HTC precursor materials using sol-gel chemistry (Figure 2.18a).[5] The latter relies on structural replication of a porous template (often silica), by infiltration with carbon precursors and subsequent removal after the carbonisation process (Figure 2.18b). Both methods have their disadvantages, while soft templating often cannot control the surface area and pore volume if additional precursors are added, due to altered HTC chemistry, hard templating depends on the removal of the template, often with harsh chemicals.

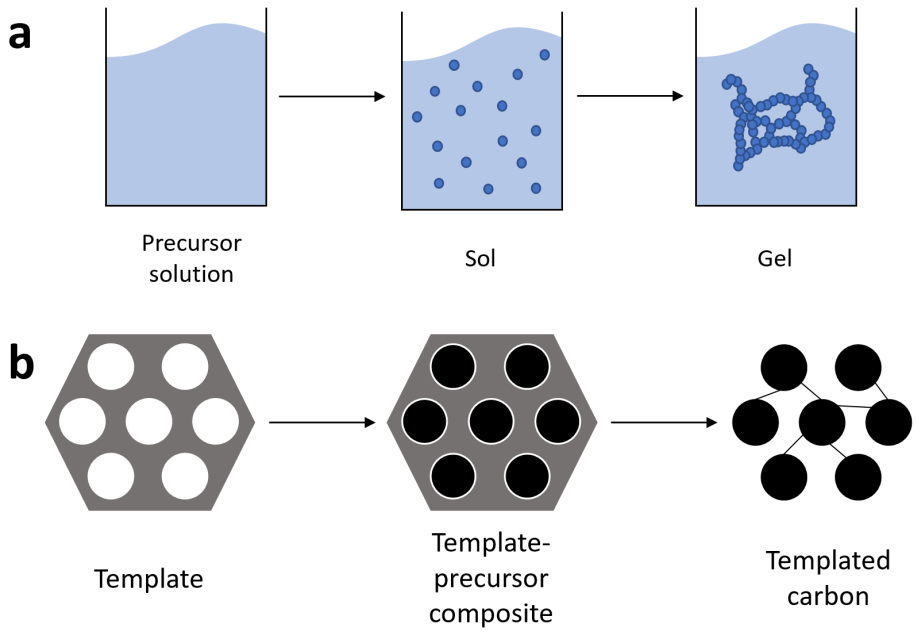


*Figure 2.18 Exemplary schematics for a) soft templating and b) hard templating methods.*

### 2.2.1 Carbogels

Carbogels are porous carbon materials usually derived from aeorgels, cryogels or xerogels via hydrothermal carbonisation and/or pyrolysis treatment. The precursor gels are usually formed via sol-gel chemistry and exists as a porous monolith. The nomenclature is based on the drying technique used to remove the solvent, with aerogels usually being prepared via supercritical $CO_2$ drying, cryogels via freeze drying and xerogels via drying at ambient conditions. Highest porosities (90 - 98 vol%) can be achieved for aerogels, due to elimination of surface tensions during the drying process, avoiding shrinkage of the material.[119] Freeze drying yields the second largest pore volume, though at the cost of obvious shrinkage and occurrence of channels due to ice crystals forming during the necessary pre-freezing of the material.[120] Drying under ambient conditions can result in structural change and drastic loss of porosity (50 vol%),[119] making the former two techniques more favourable.

Different types of carbogels derived via hydrothermal carbonisation have been reported in literature synthesised from various starting materials. Most synthesis methods involve a sugar, glucose or fructose, as carbon precursor and an additive directing the particle size and structure formation of the carbogel during the HTC process. One example for this are phloroglucinol-derived carbogels with monosaccharides as carbon precursor, where the phenolic compound acts as a crosslinker via intermolecular condensation with dehydrated sugars (HMF or furfural) creating carbogels as well as increasing the overall yield.[121,122] Another approach involved carbogels made from glucose and borax, where the borax was found to have a catalytic effect, controlling the particle size, and aid crosslinking of polyfurane chains formed during the HTC via boron didiol complexes, directing the porous network structure.[123,124] Boron complexes have been found to catalyse the dehydration of fructose/glucose to HMF by forming strong complexes with diols and sugars, facilitating acid catalysed dehydration.[125,126] Nitrogen doped carbogels have been synthesised via HTC from glucose and ovalbumin, a protein in chicken egg white, which acts as surface stabilising/structure directing agent and nitrogen source at the same time.[117,127] As mentioned earlier, the presence of amines during the HTC of glucose can drastically change the typical HTC cascade, not only changing the resulting materials chemistry, but also its structure. For the glucose/ovalbumin derived carbogels it was proposed that the protein causes the carbon precursor to demix from the aqueous phase in a spinodal fashion after the sugars dehydrated, inhibiting further polymerisation/nucleation of formed carbon particles and directing their crosslinking into the carbogel network structure.[5,119] Additional sulphur doping of the glucose/ovalbumin derived carbogels was later reported, where the resulting carbogel was determined by the

type of sulphur precursor.[92] While the addition of cysteine resulted in spherical particles, similar to the HTC of glucose without ovalbumin present, 2-thiophenecarboxaldehyde yielded the expected carbogel structure, as the sulphur was incorporated via electrophilic aromatic substitution or cycloaddition, not interfering with the crosslinking process.[92] TEM images in Figure 2.19 show the interconnected network structure of the different carbogels discussed in this subchapter.

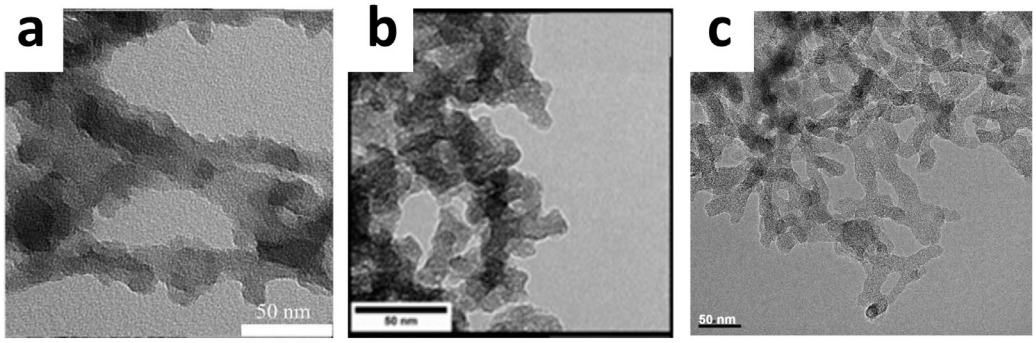


*Figure 2.19 TEM images for a) phloroglucinol-derived carbogel, reproduced from Brun et al.*[122]*, Copyright 2013 Royal Society of Chemistry. b) borax-mediated carbogel, reproduced from Fellinger et al.,*[123] *Copyright 2012 Wiley VCH. c) glucose/ovalbumin derived carbogel, reproduced from White et al.,*[117] *Copyright 2011 Royal Society of Chemistry. All scale bars depict 50 nm.*

# Chapter 3 | Metal-free carbogels as electrocatalyst

## 3.1 Introduction

Metal-free electrocatalysts for the oxygen reduction reaction have experienced increasing interest due to limitations and shortcomings of noble metal catalysts such as platinum. It has to be emphasised though that the term "metal-free" should be used with care as it has been shown that even the smallest traces of metals like Fe, Ni or Mn can drastically boost the activity of a supposedly metal-free catalyst, as mentioned in chapter 2.1.3.2. These traces can either originate from metal salts used during the synthesis or from metal impurities present in the precursor used for carbonisation.

The concept of replacing platinum with metal-free catalysts does not only originate from the idea of cost reduction, but also to make fuel cells more sustainable. To achieve this, biomass and biomass precursors can be a promising starting material. Synthesis of ORR materials from biomass or biomass precursors usually follows two heat treatments, where first the starting material is converted into heteroatom doped carbons via hydrothermal carbonisation which is then followed by a high temperature pyrolysis under inert atmosphere, sometimes in the presence of activation agents, to increase the materials conductivity/graphitisation, surface area and stability.[83] The origin of this biomass can usually be classified in food based, plant/food waste and synthetic biomass precursors. As always with food based biomass, a conflict over the use of food can be caused when utilising food resources for new energy applications like biofuels or catalysts. While promising metal-free catalysts have been reported in literature,[100,128–130] feasibility in terms of upscaling any of these synthesis approaches should be considered with care due to the arising contradiction with food shortage and rising food prices. A more viable alternative for the synthesis of metal-free catalysts could be plant and food waste, which unarguably cannot interfere with food supply and would even offer a useful solution to deal with waste. Though researchers have managed to synthesise promising ORR catalysts from plant parts,[131–133] plant waste[134] and actual food waste,[135] the issue of compositional variability based on the species, location, harvest and storage of the biomass should not be neglected. Studies have shown that there can be significant differences in the elemental composition of the same plant species/food waste between various habitats as well as between different parts of the same plant or food waste.[136,137]

Based on these concerns, many researchers have fallen back on using biomass precursors, which for example can be won from real biomass, such as glucose, cellulose, chitosan and many more to ensure better repeatability of the synthesis process. One of the first hydrothermal carbon ORR catalysts from sustainable biomass precursors was reported by

Wohlgemuth et al.[92] in 2012 who synthesised nitrogen and sulphur co doped carbogels from glucose and ovalbumin, a protein from chicken egg white. Their synthesis was based on earlier reports by the same research group.[117,127] The authors investigated co doping nitrogen and sulphur on the materials properties and catalytic performance by simple addition of a sulphur precursor (2-thiophenecarboxaldehyde) to the reaction mixture before the HTC, followed by supercritical $CO_2$ drying and pyrolysis at 900 °C under inter atmosphere. Their control sample without the addition of any sulphur resulted in a surface area of 267 $m^2/g$ and 3.6 at% of nitrogen, while the addition of sulphur slightly decreased the surface area to 224 $m^2/g$ and nitrogen content to 3.3 at% with a sulphur doping of 0.5 at%. Electrochemical testing in alkaline and acidic media clearly revealed superior performance for the N/S co doped version over the purely nitrogen doped sample, though less favourable than a platinum standard. Surprisingly, stability testing showed a better stability over platinum of the N/S doped sample in acidic, but not alkaline media. The authors explained this trend due to sulphur sites being oxidized or decomposed in alkaline media, while they are being protonated and thus chemically more stable under acidic conditions.

Shortly after, the same research group reported nitrogen doped carbon aerogels prepared under the same conditions but based on the hydrothermal carbonisation of glucose catalysed by borax.[124] For this, they either mixed glucose with borax to obtain a nitrogen free carbogel or they added an additional nitrogen source (2-pyrrol-carboxaldehyde) to obtain N doped materials. With this, the authors presented an approach to easily tune their materials surface area and nitrogen content by simply varying the concentration of borax to the nitrogen source. They found that with increasing borax concentration, the particle size decreased and thus the surface area increased, while the nitrogen content remained similar (3.0 – 3.5 wt%). An increase in the concentration of nitrogen source resulted in increasing nitrogen content (4.6 – 6.3 wt%) with a slight decrease in surface area. The sample without additional N doping resulted in the highest surface area of 373 $m^2/g$ after pyrolysis. Electrochemical testing revealed a clear influence of surface area and nitrogen doping on the catalytic activity, where a trend could be found between high surface area, high nitrogen content and favourable catalytic performance. They found their most catalytically active material in alkaline media to be made with the highest borax and nitrogen source concentration, resulting in a surface area of 265 $m^2/g$ and a nitrogen content of 6.3 wt%. Their sample had a less positive onset potential but a more negative limiting current when compared to a platinum standard with an electron transfer number of 3.3 and outstanding stability and methanol tolerance. It should be mentioned that the

authors found 35 ppm of iron via ICP analysis in their sample, which they did not correlate to their good performance but nevertheless should be considered with care.

In the same year, Brun et al.[121,122] synthesised nitrogen doped carbogels based on a phenolic-saccharide reaction by combining carbohydrate derivatives with phenolic compounds via hydrothermal carbonisation followed by supercritical $CO_2$ drying and pyrolysis under $N_2$ atmosphere at 950 °C. Their sample with the best onset potential and limiting current was made from glucose and N-acetylglucosamine with a surface area of 450 $m^2/g$ and a nitrogen content of 3.3 at% (22 % pyridinic, 18 % pyrrolic, 35 % graphitic). Though the highest electron transfer number (around 3.7) was found for the sample made with only N-acetylglucosamine with a lower surface area of 224 $m^2/g$ and a nitrogen content of 4.5 at% (13 % pyridinic, 26 % pyrrolic 36 % graphitic), which the authors attributed to the more favourable combination of pyridinic to pyrrolic N. A comparison with pure hydrothermal carbon microspheres, a nitrogen free and a nitrogen containing carbogel revealed a positive influence of the carbogels' porous network structure and surface area on the catalytic activity regardless of nitrogen doping.

Another type of nitrogen doped carbogels was reported by Alatalo et al.[138] who combined glucose or cellulose with soy bean flour via hydrothermal carbonisation followed by freeze drying and high temperature pyrolysis under inert $N_2$ atmosphere at 1000 °C. The mix of cellulose and soy flour resulted in a higher surface area of 697 $m^2/g$ compared to 449 $m^2/g$ for the glucose/soy flour mix whereas the nitrogen content was reverse with 1.9 wt% and 0.5 wt%, respectively. The sample made from glucose and soy flour exhibited a more favourable onset potential and limiting current with an electron transfer number of 3.3 - 3.7 and a $H_2O_2$ yield below 30 %, which the authors attributed to the higher nitrogen content.

The following chapter is based on metal-free carbogels as electrocatalysts for the oxygen reduction reaction. The synthesis of the presented carbogels is based on earlier work by Baccile et al.,[127] White et al.[117] and Wohlgemuth et al.[92] Though the same starting precursors, glucose and ovalbumin, were used, drastic differences arose by the use of freeze drying instead of supercritical $CO_2$ drying as well as oxygen activation during the high temperature pyrolysis.

The influence of oxygen activation and different heteroatom dopants on the morphology, surface area and electrocatalytic activity were systematically investigated and are presented in the following. A schematic of the synthesis process can be seen in Figure 3.1.

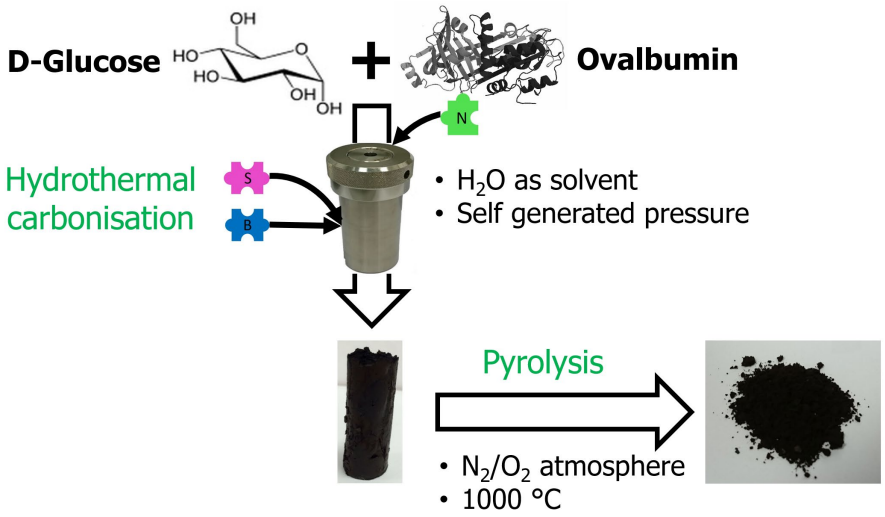


*Figure 3.1 Schematic of the synthesis process for metal-free heteroatom doped carbogels.*

## 3.2 Influence of oxygen activation during the pyrolysis

Various methods can be used for improving the surface area, pore properties and surface groups of carbon materials. Many are done by activation during the pyrolysis process, which can either be achieved via physical ($CO_2$ or steam) or chemical activation. The latter usually employs harsh chemicals (i.e. KOH, $H_3PO_4$), requiring a purification step to remove those from the sample afterwards. Physical activation presents a gentler way of creating surface area, though in the case of $O_2$ gas at the cost of yield loss and incorporated oxygen surface groups.

The influence of oxygen activation on the surface area, pore properties and catalytic performance of a nitrogen doped carbogel (CN), by pyrolysis under different $N_2/O_2$ ratios at 1000 °C, was investigated. For this, samples were either pyrolysed under pure nitrogen atmosphere or under a mixture of nitrogen and compressed air with ratios of 1, 2 or 4 % of oxygen.

Scanning electron micrographs (Figure 3.2) showed similar morphologies for all samples, suggesting that the different activation ratios only affected the sample's microstructure.

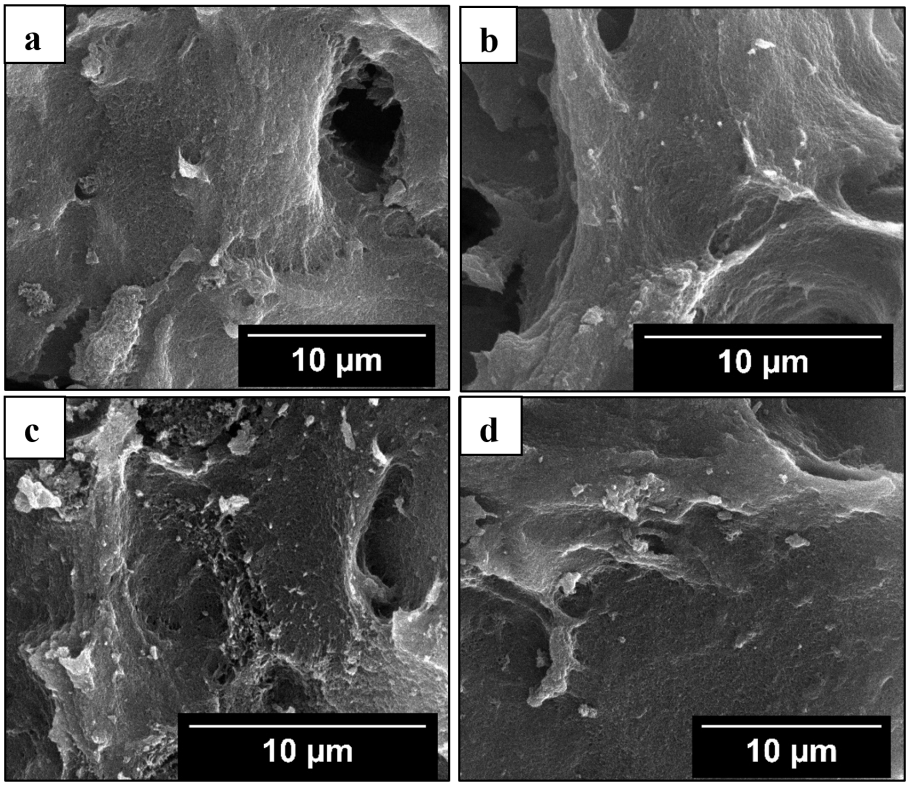


*Figure 3.2 SEM images of carbogels pyrolysed at 1000 °C under inert nitrogen atmosphere (a) or under a mix of nitrogen and air, corresponding to an oxygen content of 1% (b), 2% (c) or 4% (d).*

By contrast, drastic changes were observed in BET surface areas, pore volumes and yields, as can be seen in Table 3.1 and the corresponding nitrogen sorption isotherms and pore size distributions in Figure 3.3. It should be mentioned that micropore regions in the pore size distributions shown in the following are given for guidance but may not be taken as definite due to the use of density functional theory as well as low resolution isotherms.

*Table 3.1 BET surface area, total pore volume, micro- and mesopore volume and yield of nitrogen doped cryogel (HTC) and carbogels pyrolysed at 1000 °C under either pure nitrogen atmosphere or a mixture of nitrogen and compressed air corresponding to 1, 2 or 4 % of $O_2$.*

| **Sample** | **$S_{BET}$ [$m^2\ g^{-1}$]** | **$V_{tot}$ [$cm^3\ g^{-1}$]** | **$V_{meso}$ [$cm^3\ g^{-1}$]** | **$V_{micro}$ [$cm^3\ g^{-1}$]** | **Yield [%]** |
|---|---|---|---|---|---|
| CN-HTC | 101 | 0.640 | 0.640 | 0 | - |
| CN-$N_2$ | 110 | 0.300 | 0.283 | 0.017 | 42.3 |
| CN-1% $O_2$ | 634 | 0.552 | 0.353 | 0.199 | 39.1 |
| CN-2% $O_2$ | 874 | 0.594 | 0.303 | 0.291 | 33.1 |
| CN-4% $O_2$ | 1150 | 0.824 | 0.445 | 0.379 | 29.8 |

As expected, the surface area only increased marginally after the pyrolysis under inert $N_2$ atmosphere from 101 $m^2\ g^{-1}$ to 110 $m^2\ g^{-1}$, though shifting from larger mesopores to micro- and small mesopores, thus reducing the total pore volume. With increasing oxygen

content during the pyrolysis, surface area increased, while the percentage yield decreased due to an increase in the amount of sample burning off in the presence of oxygen.

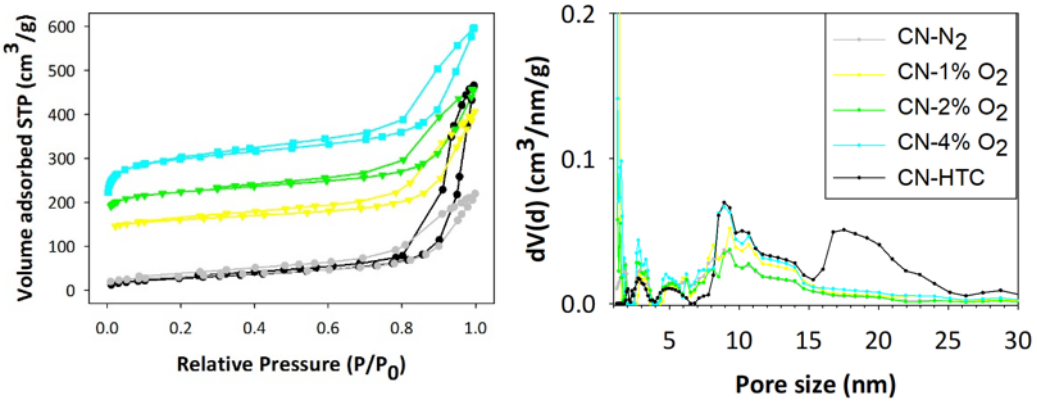


*Figure 3.3 Nitrogen sorption isotherms obtained at 77 K and pore size distribution for nitrogen doped cryogel (HTC) and carbogels pyrolysed at 1000 °C under either pure nitrogen atmosphere or a mixture of nitrogen and compressed air corresponding to 1, 2 or 4 % of $O_2$.*

This phenomenon can be described as hole burning due to the oxidation of the carbon surface.[139] Studies in the 1980's and 90's,[140–142] observed that $O_2$ gas can act as an etching agent to remove carbon atoms from the basal plane leaving voids and creating carbon monoxide and carbon dioxide.[143] Chu and Schmidt[142,144] showed that temperature conditions and gas pressure can influence this hole burning process. While at lower temperatures, etching initiates exclusively on already existing point defects, at higher temperatures additional new defect sites are created in the basal carbon plane.[144] Originating from these point defects, monolayer pit formation creates holes/pores (corresponding to micro- and small mesopores), while line defects can create multilayer pit growth (corresponding to meso- and macropores).[142] Based on these findings, it can be concluded that an increase in oxygen content also leads to an increase in surface area as well as micro- and mesopore volume. Similar to our materials surface area, the total pore volume also increased with increasing oxygen content, with the exception of CN-2% $O_2$ showing a slightly lower mesopore volume than CN-1% $O_2$, due to its higher micropore content. CN-HTC only consisted of mesopores between 7 and 30 nm, while all pyrolysed samples also exhibited micropores, where the micropore volume increased with increasing oxygen content.

A similar trend was seen in the elemental composition determined via XPS (Table 3.2), where the carbon content decreased, due to hole burning with increasing oxygen percentage during the pyrolysis, while the incorporated oxygen content itself was increased. Elemental composition of the bulk material determined via elemental analysis for CN-HTC and CN-1% $O_2$ was in good agreement with values obtained via XPS and

indicated a homogeneous distribution of nitrogen throughout the materials bulk and surface.

*Table 3.2 Elemental composition determined by XPS in at% and EA in (wt%) of a nitrogen doped cryogel (CN-HTC) and carbogels pyrolysed at 1000 °C under either pure nitrogen atmosphere or a mixture of nitrogen and compressed air.*

| Sample | C | O | N |
|---|---|---|---|
| CN-HTC | 79.8<br>*(63.5 wt%)* | 16.2<br>- | 4.0<br>*(5.0 wt%)* |
| CN-$N_2$ | 92.3 | 4.4 | 3.3 |
| CN-1% $O_2$ | 91.8<br>*(88.6 wt%)* | 5.3<br>- | 2.9<br>*(2.9 wt%)* |
| CN-2% $O_2$ | 91.2 | 7.0 | 1.8 |
| CN-4% $O_2$ | 90.1 | 7.9 | 2.0 |

Deconvolution of C1s spectra were found to have similar peak positions and species fractions around 284.4 eV, 285.2 eV, 285.9 eV and 286.7 eV attributed to $sp^2$ C-C, C-OH or C-O-C, C-N and C-O, respectively.[145] CN-HTC exhibited a considerably higher oxygen content, as well as a different distribution of oxygen species with only C=O and OH present. The pyrolysed samples were observed to have a similar distribution of oxygen bonds around 530.5 eV, 532.2 eV and 533.3 eV attributed to C=O (also possible quinone groups), C-O and O=C-O, respectively.[146,147] A comparative view of the amounts of different carbon and oxygen species can be seen in Figure 3.4.

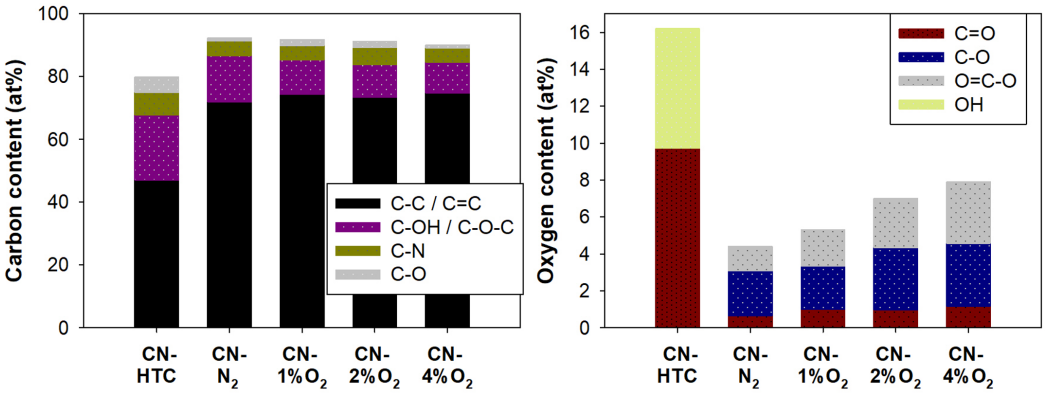


*Figure 3.4 Distribution of carbon and oxygen bonding for nitrogen doped carbogels, after the hydrothermal carbonisation (CN-HTC) or pyrolysed at 1000°C under either pure nitrogen atmosphere (CN-$N_2$) or a mixture of nitrogen and oxygen (1, 2 and 4% $O_2$).*

The highest amount of nitrogen was found in CN-$N_2$ with 3.3 at%, which reduced to 2.9 at% and 1.8 at% in CN-1% $O_2$ and CN-2% $O_2$, respectively (Figure 3.5). This can be expected as nitrogen was incorporated within the carbon framework, parts of it will be lost through hole burning, in a similar way to carbon atoms, creating NO and $NO_2$. A

marginal increase in nitrogen content was found for CN-4% $O_2$ with 2.0 at%, possibly due to the one point XPS measurement which can yield slight variations based on the nature of the material's surface. Generally, due to XPS being a surface analysis technique, results should be treated with caution, especially with the heterogeneous nature of hydrothermal carbon materials in mind. Peak positions and fractions of each species were found to be similar for the pyrolysed samples, apart from the cryogel (CN-HTC) which exhibited a high percentage of pyrrolic nitrogen. The pyrolysed carbogels all consisted of pyridinic N (~ 398.2 eV), graphitic N (~ 400.7 eV) and N oxides (~ 403 eV).[148] CN-4% $O_2$ exhibited the highest amount of N-oxides due to the higher oxygen content in the pyrolysing atmosphere, which caused a reduction of graphitic N as compared to CN-2% $O_2$.

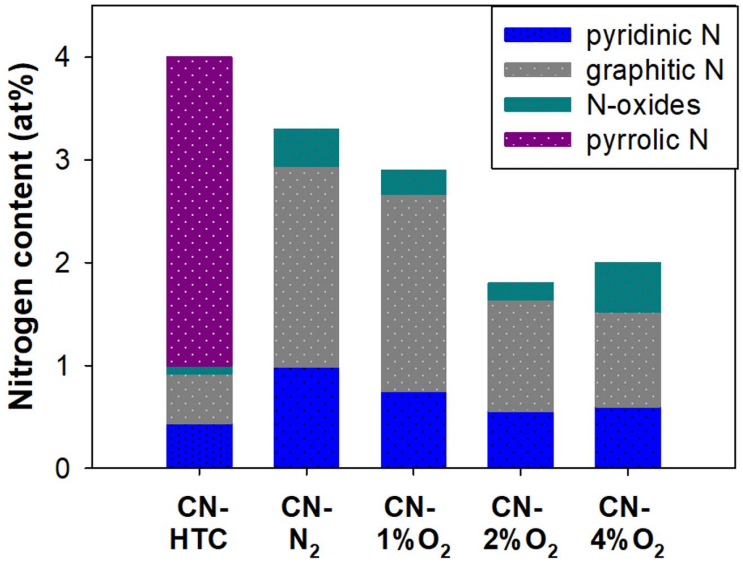


*Figure 3.5 Distribution of nitrogen species for nitrogen doped carbogels, after the hydrothermal carbonisation (CN-HTC) or pyrolysed at 1000°C under either pure nitrogen atmosphere (CN-$N_2$) or a mixture of nitrogen and oxygen (1, 2 and 4% $O_2$).*

Electrochemical testing was carried out under alkaline conditions with a rotating ring disk electrode (RRDE) setup for all four pyrolysed samples and compared to a commercially available platinum standard. The resulting voltammograms are shown in Figure 3.6. CN-2% $O_2$ and CN-4% $O_2$ showed the most positive onset potential, while CN-2% $O_2$ had the lowest limiting current density of all four samples. The better performance of CN-2% $O_2$ compared to CN-$N_2$ and CN-1% $O_2$ might be attributed to the higher surface area, while the slight advantage over CN-4% $O_2$ which has a higher surface area, might be assigned to the difference in nitrogen species, with a similar amount of pyridinc N, but a higher content of graphitic N. Lai et al.[88] reported that pyridinic N might contribute to the onset potential, while graphitic N might determine the limiting current. A study by Kim et al.[87]

suggested that the outermost graphitic N represent the most active catalytic sites, but are converted into pyridinic N after one catalytic cycle, thus making both N species active. At the same time CN-4% $O_2$ had a higher surface area of 1150 $m^2$ $g^{-1}$ compared to 874 $m^2$ $g^{-1}$ for CN-2% $O_2$, which made their overall catalytic performance similar (LSV, electron transfer number and $H_2O_2$ yield). Average electron transfer numbers and $H_2O_2$ yields were similar for all four samples with values of 2.9 (49.6 %), 3.2 (38.5 %), 3.1 (42.4 %) and 3.1 (43.2 %) for CN-$N_2$, CN-1% $O_2$, CN-2% $O_2$ and CN-4% $O_2$, respectively.

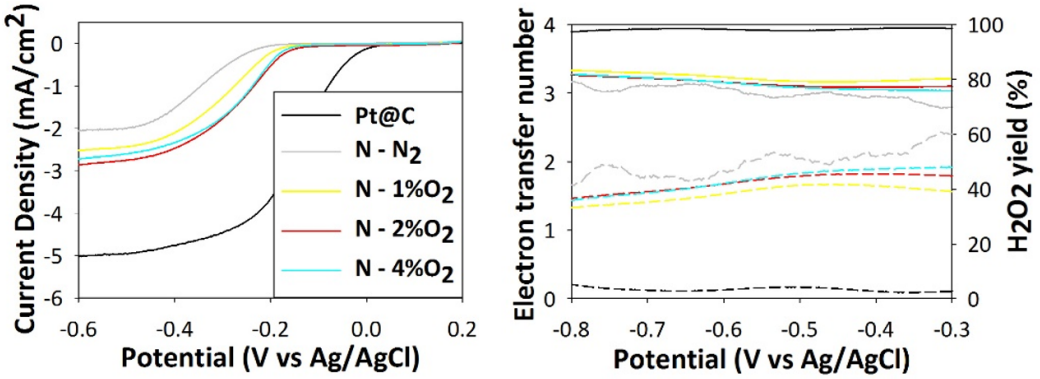


*Figure 3.6 Linear sweep voltammogram recorded in 0.1 M KOH with an RRDE setup at 1600 rpm and electron transfer number and hydrogen peroxide yield of a commercially available platinum catalyst (60 wt% Pt@C) and carbogels pyrolysed at 1000 °C under either pure nitrogen atmosphere or a mixture of nitrogen and compressed air.*

Compared to the nitrogen doped carbogels, synthesised in a similar way by White et al.[117] and Wohlgemuth et al.,[92] clear differences were founded in the morphology and surface area. These changes can mostly be explained due to the use of freeze drying instead of supercritical $CO_2$ drying as well as the additional oxygen activation and higher temperature during the pyrolysis step. Due to the use of freeze drying, the network structure of the carbogel somewhat collapsed, causing a denser morphology as well as a lower surface area after the HTC (276 and 239 $m^2$ $g^{-1}$ for White et al. and Wohlgemuth et al., respectively). In contrast, the higher temperature and presence of air during the pyrolysis resulted in surface areas more than double of those reported by White et al. and Wohlgemuth et al. (308 and 267 $m^2$ $g^{-1}$, respectively).

To get a better insight on how the different parameters and properties such as surface area, dopant content and species can influence the catalytic activity, two combination graphs are shown in Figure 3.7. Figure 3.7a clearly shows the trend observed for the oxygen activation, with an increased surface area and oxygen content at increasing $O_2$ content in the pyrolysing atmosphere at the cost of nitrogen content. Interestingly, the average electron transfer number was not greatly influenced by the, in part, drastic

changes, suggesting that the overall ORR mechanism remained unchanged for the pyrolysed samples.

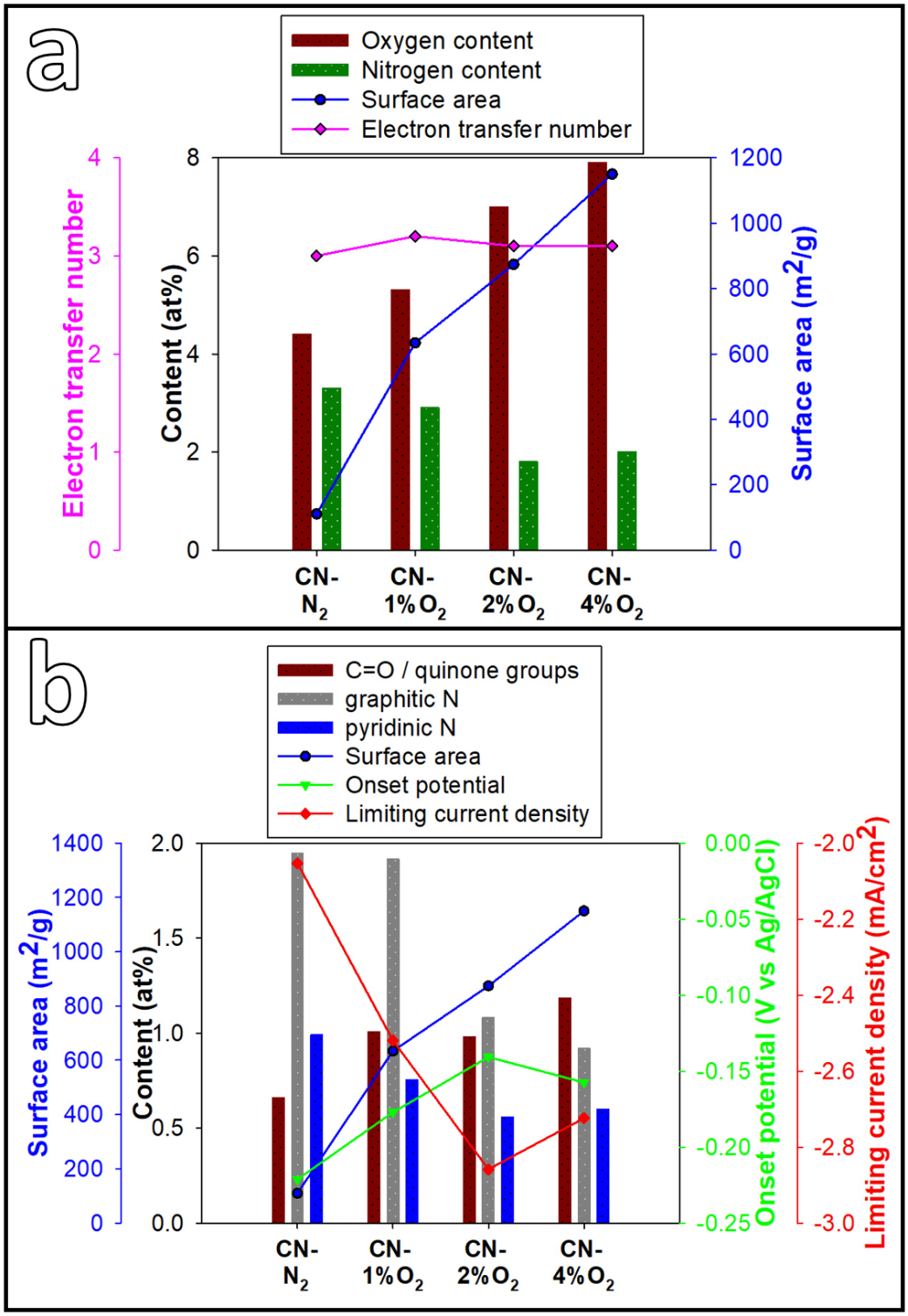


*Figure 3.7 Combination graphs correlating the material's surface area and elemental content with the electrocatalytic activity for nitrogen doped carbogels pyrolysed at 1000°C under either pure nitrogen atmosphere (CN-$N_2$) or a mixture of nitrogen and oxygen (1, 2 and 4% $O_2$). The onset potential was determined at -0.1 mA/cm$^2$ and the limiting current density at -0.6 V (vs Ag/AgCl).*

Figure 3.7b depicts the influence of surface area and oxygen as well as nitrogen species on the onset potential and limiting current density. The most positive onset potential as well as lowest limiting current density were observed for the carbogel pyrolysed under a mixed atmosphere of $N_2$/air (2% $O_2$), though it exhibited a lower surface area as compared to CN-4% $O_2$, and lower content of both nitrogen species as compared to CN-$N_2$ and CN-1% $O_2$. This trend is likely to be due to the more active sites (graphitic and pyridinic N) as compared to CN-4% $O_2$ and a better accessibility of active sites due to the higher surface area as compared to CN-$N_2$ and CN-1% $O_2$. This suggests that surface area and active sites have an interdependency, where one relies on the other such as the density of active sites and the surface area offering accessibility to said active sites.

## 3.3 Influence of heteroatom dopants sulphur and boron

Co as well as triple doping of different heteroatom dopants has received increasing attention, due to enhanced catalytic activity being reported for these electrocatalysts. Most researchers relate this increase in performance to a synergistic effect between the dopants, as has been discussed in chapter 2.1.3.3.

In this subchapter, the influence of the heteroatom dopants sulphur and boron are investigated on the physical, chemical and electrocatalytic properties of the nitrogen doped carbogel. For this, three different versions of the carbogel were synthesised, with nitrogen and sulphur ($CN_S$), nitrogen and boron ($CN_B$), and a triple doped version with nitrogen, sulphur and boron ($CN_{SB}$).

Based on the findings of the $O_2$ activation study (chapter 3.2), all high temperature pyrolysis steps were carried out under a nitrogen atmosphere mixed with compressed air corresponding to 2 % of oxygen. This ratio was chosen due to its beneficial effect on the surface area, pore properties and ORR performance without substantial yield loss (< 30 %).

SEM and TEM images of the pure nitrogen doped carbogel and the three additional doped carbogels can be seen in Figure 3.8. While the incorporation of sulphur did not seem to affect the structure formation of the carbogel, the incorporation of boron changed the overall morphology of the carbogel by creating a particle like structure for both boron doped samples, $CN_B$ and $CN_{SB}$, compared to a more wire/coral like structure, as in the case of CN and $CN_S$. The changes in morphology suggested that the incorporation of boron interfered with the formation of the cryogel structure. As mentioned in chapter 2.2.1, boron compounds have been found to catalyse hexoses, such as glucose or fructose to HMF during the HTC.[123,125] This can be explained by a change in reactivity and physical properties of the sugar solution due to negatively charged borate diol/didiol

complexes.[5,149,150] Fellinger et al.[123,124] reported the synthesis of carbogels made purely from hydrothermally treated glucose and borax with a similar morphology to $CN_B$ and $CN_{SB}$ (Figure 3.8 e/f and g/h). Considering these findings, a catalytic effect of boric acid determining the structure instead of the presence of ovalbumin, creating an altered cryogel architecture, was assumed.

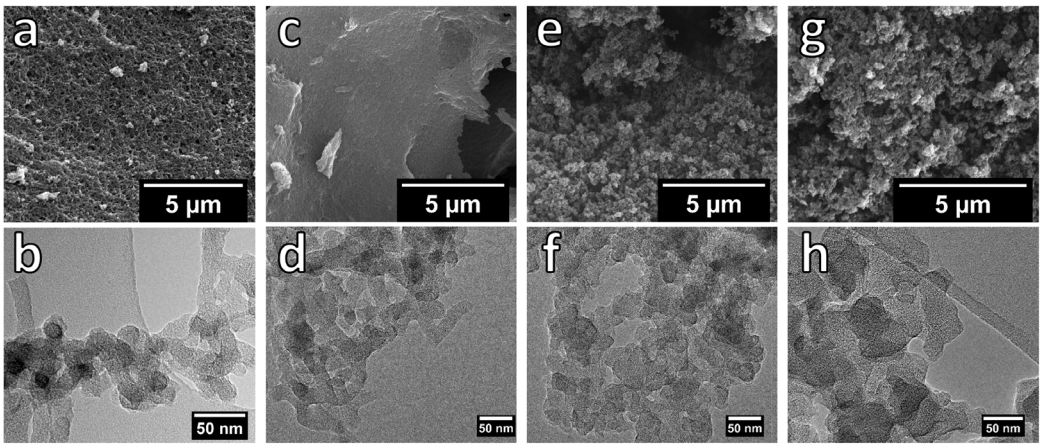


*Figure 3.8 SEM and TEM images of nitrogen carbogels CN (a/b) pyrolysed at 1000 °C doped with sulphur $CN_S$ (c/d), boron $CN_B$ (e/f) and sulphur and boron $CN_{SB}$ (g/h).*

Surface areas for the pure nitrogen doped carbogel (CN) and the three additional doped versions as well as total pore volume, micro- and mesopore volume can be found in Table 3.3, nitrogen sorption isotherms and pore size distributions are shown in Figure 3.9. Additional doping of the nitrogen carbogel resulted in a decrease in surface area for all three samples. The incorporation of sulphur did not greatly interfere with the formation of the carbogel structure, only slightly limiting the surface area to 692 ± 6 $m^2 g^{-1}$, as compared to 889 ± 25 $m^2 g^{-1}$ for the pure carbogel CN.

*Table 3.3 Surface area, total pore, meso- and micropore volume of nitrogen doped, CN, carbogels pyrolysed at 1000 °C with sulphur $CN_S$, boron $CN_B$ and sulphur and boron $CN_{SB}$ ( as average values for three independent carbonisations).*

| Sample | Surface area [$m^2 g^{-1}$] | $V_{tot}$ [$cm^3 g^{-1}$] | $V_{meso}$ [$cm^3 g^{-1}$] | $V_{micro}$ [$cm^3 g^{-1}$] |
|---|---|---|---|---|
| CN | 889 ± 25 | 0.770 ± 0.046 | 0.489 ± 0.056 | 0.281± 0.010 |
| $CN_S$ | 692 ± 6 | 0.503 ± 0.013 | 0.279 ± 0.012 | 0.224 ± 0.003 |
| $CN_B$ | 669 ± 29 | 0.488 ± 0.053 | 0.266 ± 0.047 | 0.222 ± 0.010 |
| $CN_{SB}$ | 605 ± 18 | 0.412 ± 0.031 | 0.209 ± 0.035 | 0.203 ± 0.007 |

A similar trend was observed by Wohlgemuth et. al.,[92] where they concluded that the incorporation of sulphur, from 2-thiophenecarboxaldehyde as a precursor, only occurs via electrophilic aromatic substitution or cycloadditon, suggesting that the crosslinking process during the structure formation remains unaffected. Considering that the gel

formation occurs via a different route in the presence of boric acid, a similar trend was also found here, where the surface area decreased from 669 ± 29 $m^2 g^{-1}$ to 605 ± 18 $m^2 g^{-1}$ for $CN_B$ and $CN_{SB}$, respectively, in the presence of the sulphur precursor. The assumed change in carbogel structure was also supported by the difference in pore properties. All carbogels exhibited similar features in the micro- and small mesoporous region, whereas CN and $CN_S$ also displayed larger mesopores in the region of 5-20 nm.

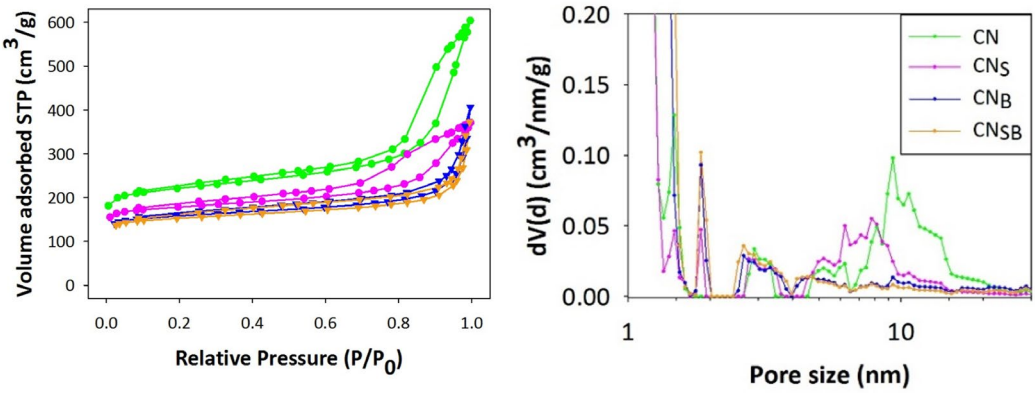


*Figure 3.9 Nitrogen sorption isotherms obtained at 77 K and pore size distribution for nitrogen carbogels, CN, pyrolysed at 1000 °C doped with sulphur $CN_S$, boron $CN_B$, and sulphur and boron $CN_{SB}$.*

The elemental composition for all carbogels was determined via XPS and can be found in Table 3.4. The incorporation of sulphur decreased the nitrogen content from 4 at% in the pure version CN to 2.9 at%, suggesting that, though the structure formation of the cryogel was not influenced, the reaction cascade during the HTC was likely to be affected. As already observed with the morphology and surface area/pore properties, the presence of boric acid promoted the incorporation of a higher nitrogen content (4 at% for CN and 5.1/5.5 at% for $CN_B$/$CN_{SB}$). Due to the changes in the cryogel structure caused by boric acid, it was assumed that ovalbumin was solely utilised as a nitrogen source, not also acting as structure directing/surface stabilising agent. In contrast to the borax mediated carbogels,[123,124] the presence of boric acid lead to the incorporation of small amounts of boron (0.8 at% for $CN_B$ and 0.5 at% for $CN_{SB}$) into the carbon framework.

*Table 3.4 Elemental composition determined by XPS in at% for nitrogen doped carbogels, CN, pyrolysed at 1000 °C doped with sulphur $CN_S$, boron $CN_B$, and sulphur and boron $CN_{SB}$.*

| Sample | C | O | N | S | B |
|---|---|---|---|---|---|
| CN | 78.1 | 17.9 | 4.0 | - | - |
| $CN_S$ | 83.4 | 12.9 | 2.9 | 0.8 | - |
| $CN_B$ | 80.1 | 14.0 | 5.1 | - | 0.8 |
| $CN_{SB}$ | 80.1 | 12.9 | 5.5 | 1.0 | 0.5 |

Deconvolution of C1s and O1s spectra showed similar peak positions and fractions of species (Figure 3.10) for all carbogels, suggesting that the incorporation of additional sulphur and/or boron did not change the binding states of carbon and oxygen. The highest amount of carbon species was found to be $sp^2$ C-C around 284.4 eV, followed by C-OH/C-O-C around 285.1 eV and functional groups C-N/C-S around 286 eV.[145] Distribution of oxygen binding was also similar in all carbogels with peaks around 530.5 eV, 532.2 eV and 533.4 eV attributed to C=O (also possible quinone groups), C-O and O=C-O, respectively.[146,147]

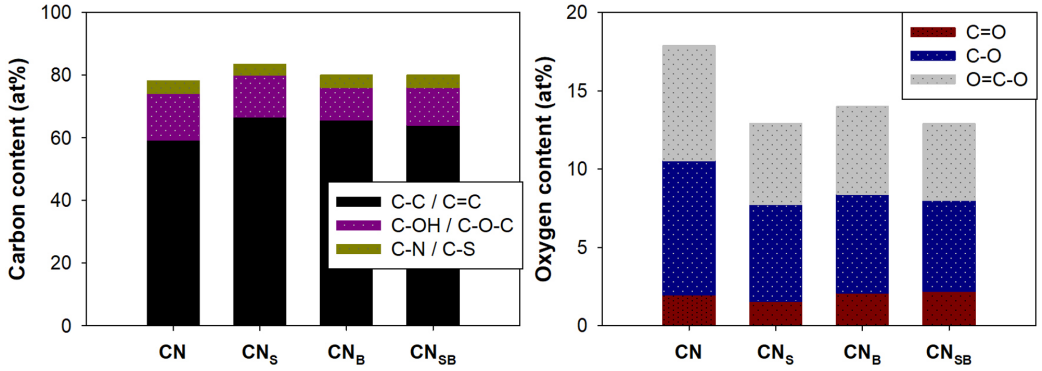


*Figure 3.10 Carbon and oxygen bonding in carbogels pyrolysed at 1000°C doped with nitrogen (CN) and additional heteroatom dopants sulphur ($CN_S$), boron ($CN_B$) or sulphur and boron ($CN_{SB}$).*

N1s spectra revealed the presence of pyridinic N, graphitic N and N-oxides in all carbogels around 398.1 eV, 400.7 eV and 403 eV, respectively ,with a similar distribution of each species (Figure 3.11).[148] All carbogels contained graphitic N as the highest nitrogen species present, followed by pyridinic N and N-oxides.

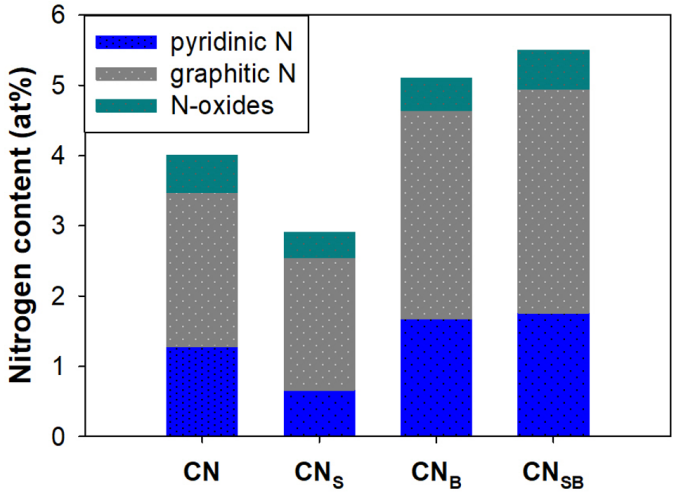


*Figure 3.11 Nitrogen species in carbogels treated at 1000°C doped with nitrogen (CN) and additional heteroatom dopants sulphur ($CN_S$), boron ($CN_B$) or sulphur and boron ($CN_{SB}$).*

Due to very low amounts of boron doping no B-C (282.4 – 283.2 eV) or B-N (397.8 eV) peaks[151,152] could be detected in C1s or N1s spectra for $CN_B$ and $CN_{SB}$. Furthermore, deconvolution of B1s and S2p photoelectron spectra was not possible due to the low amounts of dopant, though peak positions corresponded to B-C (~ 191.3 eV) and C-S-C (~ 163.5 eV), respectively.[146]

To investigate the defects created in the carbon framework by heteroatom doping, Raman spectroscopy was carried out for the pure carbogel version, CN, and the three additional doped versions (Figure 3.12). All samples showed the characteristic D- and G-band values around 1320 $cm^{-1}$ and 1588 $cm^{-1}$, respectively, where the G-band indicates the typical $sp^2$ bond stretching in carbon materials and the D-band relates to the $sp^2$ breathing modes, appearing only in case of defects/disorder in the hexagonal $sp^2$ structure.[153] The ratio of D to G band based on their peak intensity or area can be used to investigate the level of disorder or $sp^2/sp^3$ ratio in carbon. Higher $I_D/I_G$ values can be attributed to the presence of more numerous, but smaller $sp^2$ graphitic domains as well as the existence of defects.[154] $I_D/I_G$ ratios were found to be 2.0, 2.1, 2.0 and 2.1 for CN, $CN_S$, $CN_B$ and $CN_{SB}$, respectively, indicating that all samples exhibited a similar degree of graphitisation and defects, though samples containing sulphur showed a slight increase due to the large atomic size of sulphur causing more defects/disorder.

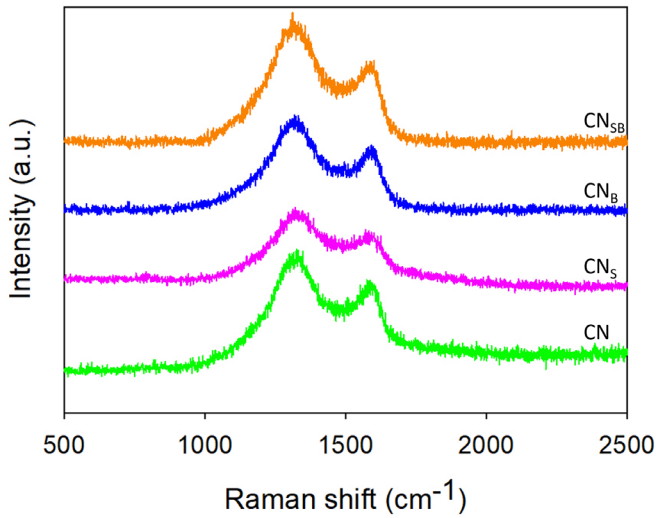


*Figure 3.12 Raman spectra for nitrogen doped carbogels, CN, pyrolysed at 1000°C doped with sulphur $CN_S$, boron $CN_B$, and sulphur and boron $CN_{SB}$.*

Electrochemical testing was carried out for all four carbogels, cyclic voltammograms (CV) recorded in $N_2$ and $O_2$ saturated 0.1M KOH can be seen in Figure 3.13. While in the absence of oxygen ($N_2$ saturated) a featureless CV was recorded, in the presence of oxygen, a clear peak appeared corresponding to the oxygen reduction reaction between -0.2 to -0.3 V (vs Ag/AgCl) for all samples, confirming the activity towards the

ORR. The peak was significantly more pronounced in samples containing additional boron ($CN_B$ and $CN_{SB}$), while sample without boron exhibited a more rectangular shaped CV curve, indicating capacitive behaviour, possibly due to the higher surface area.

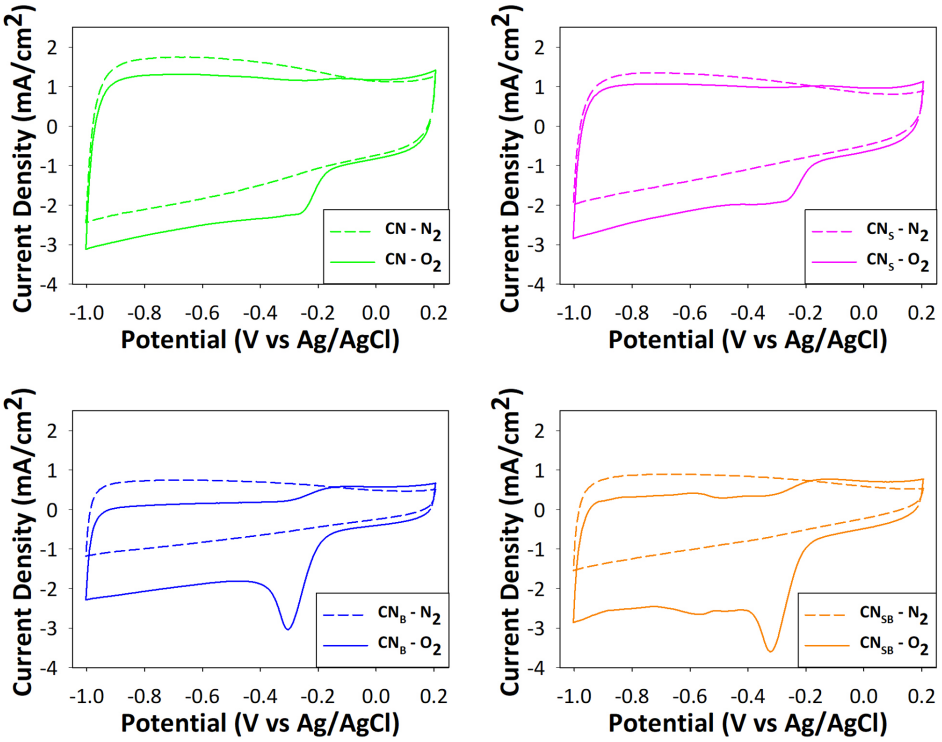


*Figure 3.13 Cyclic voltammograms recorded in $N_2$ and $O_2$ saturated 0.1 M KOH with an RRDE setup for nitrogen carbogels, CN, pyrolysed at 1000 °C doped with sulphur, $CN_S$, boron, $CN_B$, or sulphur and boron, $CN_{SB}$.*

To further investigate the catalytic activity, linear sweep voltammetry was carried out in $O_2$ saturated 0.1 M KOH at 1600 rpm and compared to a commercially available platinum standard (Figure 3.14). All carbogels were clearly outperformed by platinum on carbon in terms of catalytic activity. The onset potential increased in the order CN > $CN_B$ > $CN_{SB}$/$CN_S$, while the limiting current density was lowest for $CN_{SB}$ and $CN_B$, followed by CN and $CN_S$. The halfwave potential was found to be more positive for samples containing boron, as also apparent from the curve shape, which is steeper in the mixed kinetic and diffusion controlled area for $CN_{SB}$ and $CN_B$. In contrast to Wohlgemuth et al.,[92] who observed improved catalytic activity when co doping nitrogen and sulphur, $CN_S$ exhibited the least favourable performance amongst the present samples, indicating that additional sulphur doping does not to have a beneficial influence on the overall morphology or catalytic activity of the studied carbogels. Although the NS co doped carbogel of Wohlgemuth et al.[92] had similar levels of N and S doping and exhibited comparable onset potential and limiting current density to $CN_S$ presented in this thesis, it exhibited a lower surface area and pore volume (224 $m^2$ $g^{-1}$ and 0.27 $cm^3$ $g^{-1}$). The

incorporation of boron seemed to play a crucial role, with $CN_B$ and $CN_{SB}$ showing improved catalytic activity and the best electron transfer numbers as well as hydrogen peroxide yields, where $CN_B$ had the highest and lowest value with 3.5 and 22.6 %, respectively, showing a significant improvement compared to the pure CN carbogel with values of 3.1 and 44.7 %. All carbogels appeared to proceed via a mixture of the 2- and 4-electron pathway with electron transfer numbers between 3.0 and 3.5, and $H_2O_2$ yields between 22.6 - 48.4 %.

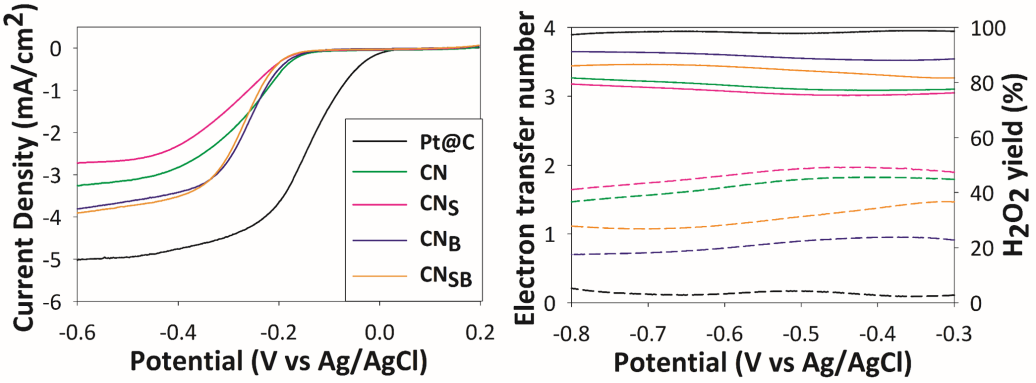


*Figure 3.14 Linear sweep voltammogram recorded in 0.1 M KOH with an RRDE setup at 1600 rpm for a commercially available platinum catalyst (60 wt% Pt@C) and nitrogen carbogels, CN, pyrolysed at 1000 °C doped with sulphur, $CN_S$, boron, $CN_B$, or sulphur and boron, $CN_{SB}$. Electron transfer number and hydrogen peroxide yield calculated from the LSV disk and ring current.*

Based on these observations, a synergistic effect of nitrogen and boron was assumed to contribute towards the slightly superior performance of $CN_B$ and $CN_{SB}$. Similar findings were reported by other researchers, which observed catalytically improved performance of N/B co doped samples compared to their single doped counterparts.[155–158] Zheng et al.[155] investigated the synergistic effect of N and B co doping via DFT calculations, concluding that a B atom meta to a pyridinic N atom, forming a B-C-N heteroring, is more active than an ortho B atom directly bonded to a pyridinic or graphitic N, forming a NB functionality. They suggested that the in between carbon atom can be polarised by the nitrogen atom, to then donate extra electrons to the boron atom, which would improve its oxygen adsorption properties and make it an active site. Contrary to Wohlgemuth et al.,[124] who studied the influence of surface area on borax mediated nitrogen doped carbogels, a clear correlation between surface area/pore properties and the catalytic performance of our studied carbogels was not identified. However, heteroatom doping, especially N and B co doping, as well as the nitrogen content itself, had a much stronger impact. Our samples showed similar, though slightly lower, performance compared to their best performing sample, which had a similar nitrogen (4.5 wt%), but lower oxygen (3.1 wt%) content to our boron doped samples, with a lower surface area of 265 $m^2\ g^{-1}$. It

should be mentioned, that they detected 35 ppm of iron originating from borax residues in their sample, which might have contributed to their sample's superior performance, especially in terms of limiting current density.

Chronoamperometry was carried out for all four carbogels and a commercially available platinum standard, as can be seen in Figure 3.15. The studied samples exhibited a better long-time stability with 85 % of current remaining for CN and $CN_B$, 82 % for $CN_{SB}$, 80 % for $CN_S$ and only 75 % for platinum on carbon after 10000 s.

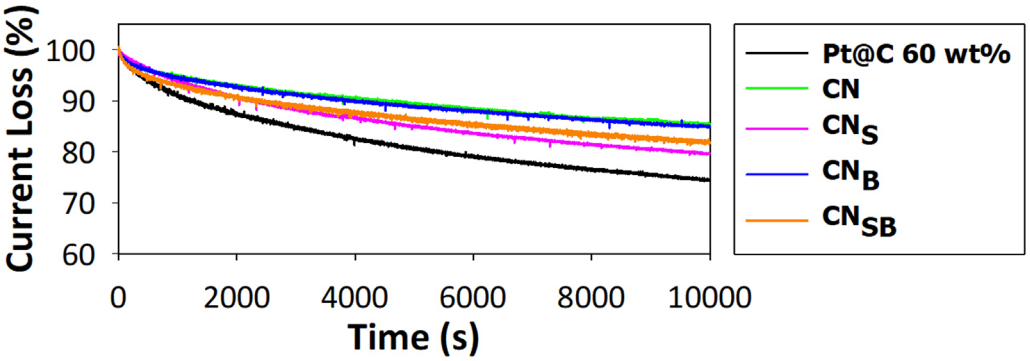


*Figure 3.15 Chronoamperometric response at a constant potential (halfwave potential of each catalyst) in $O_2$ saturated 0.1M KOH at 800 rpm for a commercially available platinum catalyst (60 wt% Pt@C) and nitrogen carbogels, CN, pyrolysed at 1000 °C doped with sulphur, $CN_S$, boron, $CN_B$, or sulphur and boron, $CN_{SB}$.*

Due to possible cross-over in direct methanol fuel cells, the methanol tolerance of ORR electrocatalyst is of importance. In Figure 3.16 the recorded methanol tolerance for all four carbogels and the commercial platinum standard is shown. 5 mL of methanol was added to the electrolyte after 140 s of running a chronoamperometric response. Samples without the addition of boron (CN and $CN_S$) showed only a slight response to the addition of methanol, while $CN_B$ and $CN_{SB}$ suffered a more obvious loss of current, though considerably less than the commercial platinum on carbon.

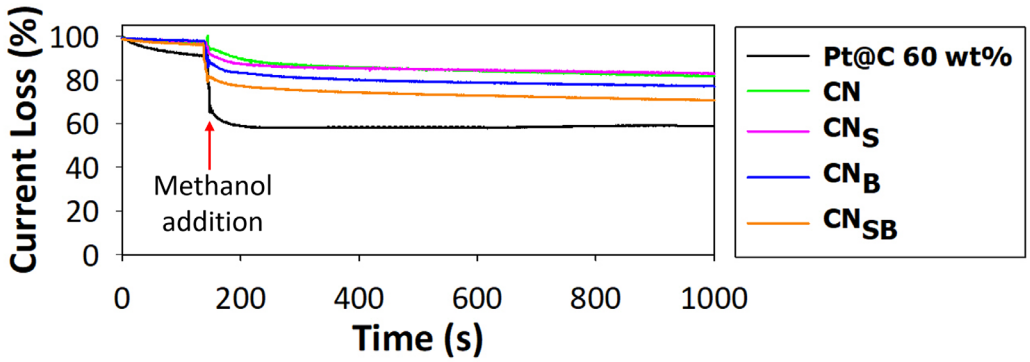


*Figure 3.16 Methanol tolerance recorded at a constant potential (halfwave potential of each catalyst) in $O_2$ saturated 0.1M KOH at 800 rpm for a commercially available platinum catalyst*

*(60 wt% Pt@C) and nitrogen carbogels, CN, pyrolysed at 1000 °C doped with sulphur, $CN_S$, boron, $CN_B$, or sulphur and boron, $CN_{SB}$.*

Table 3.5 summarises the electrochemical values for onset potential, limiting current density, electron transfer number and hydrogen peroxide yield derived from linear sweep voltammograms for the heteroatom doped carbogels and the platinum standard.

*Table 3.5 Electrochemical values derived from linear sweep voltammetry using an RRDE setup in 0.1 M KOH. The onset potential was determined at -0.1 mA/cm² and the limiting current density at -0.6 V (vs Ag/AgCl). Electron transfer number and $H_2O_2$ yield are averaged values between -0.3 V and -0.6 V (vs Ag/AgCl).*

| **Sample** | **Onset potential [V vs Ag/AgCl]** | **Limiting current density [mA/cm²]** | **Electron transfer number** | **$H_2O_2$ yield [%]** |
|---|---|---|---|---|
| Pt@C | 0.006 | -5.0 | 3.9 | 3.3 |
| CN | -0.143 ± 0.010 | -3.25 ± 0.05 | 3.05 ± 0.05 | 46.6 ± 1.9 |
| $CN_S$ | -0.153 | -2.7 | 3.0 | 48.4 |
| $CN_B$ | -0.143 | -3.8 | 3.5 | 22.6 |
| $CN_{SB}$ | -0.158 | -3.9 | 3.3 | 32.8 |

To get a better understanding how the above presented physicochemical parameters influence the catalytic activity towards the ORR, a representative overview including different key results is shown in Figure 3.17. Figure 3.17a correlates the different heteroatom dopant amounts and surface area with the onset potential and limiting current density in alkaline media. Here, it appears that the overall nitrogen content was the critical parameter determining the limiting current density, while the overall oxygen content possibly had an influence on the onset potential, though all samples exhibited a rather similar onset potential. A direct influence of the other heteroatom dopants sulphur and boron could not be observed, neither did the difference in surface area or pore volume seem to affect the onset potential or limiting current density. The region of the mixed kinetic and diffusion controlled area was found to be steeper for samples containing boron, which suggested more favourable reaction kinetics (possibly better $O_2$ adsorption). This observation was also reflected in the electron transfer number, where $CN_B$ and $CN_{SB}$ exhibited slightly higher values as compared to samples without boron, as can be seen in Figure 3.17b. A possible influence on the enhanced ORR mechanism in the presence of boron could be the higher content of C=O/quinone groups, which were reported to act as active sites in alkaline media.[78] Though $CN_B$ and $CN_{SB}$ exhibited roughly the same content of C=O/quinone groups, the slightly higher surface area of $CN_B$ enabled a better accessibility of the active sites, thus resulting in a higher electron transfer number as compared to for $CN_{SB}$. Similarly, a higher nitrogen content was incorporated in the

presence of boron, which lead to an increase in graphitic and pyridinic N, which were reported to act as active sites during the ORR,[87] explaining the better performance as compared to CN and $CN_S$.

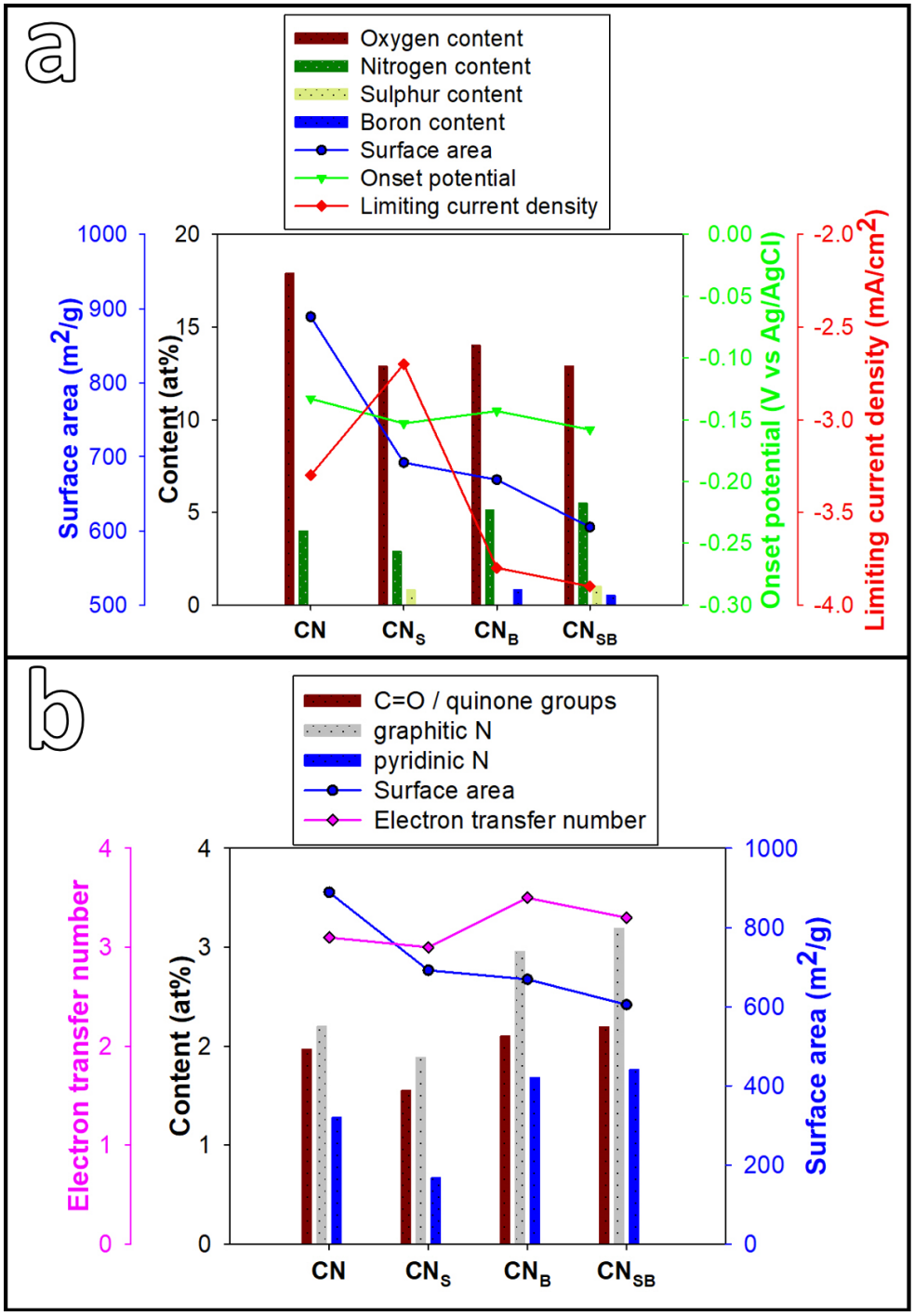


*Figure 3.17 Combination graphs correlating the material's surface area and elemental content with the electrocatalytic activity for nitrogen doped carbogels, CN, pyrolysed at 1000°C under a mixed atmosphere of N2/air (2 % $O_2$) doped with additional heteroatom dopants sulphur, $CN_S$, boron, $CN_B$, or sulphur and boron, $CN_{SB}$. The onset potential was determined at -0.1 mA/cm² and the limiting current density at -0.6 V (vs Ag/AgCl).*

Apart from the actual active sites, differences in mass transport can also influence the catalytic activity of a material. Mass transport limitations can be determined by the morphology, surface area and pore properties leading to superior or inferior contact between the active sites and reactants/products in the electrolyte.[83] While some researchers suggest that mesopores are more beneficial to reduce mass transport limitations,[159,160] others have shown the favourable influence of high surface area microporous carbons.[161,162] Gavrilov et al.[163] suggested that $O_2$ cannot be reduced in micropores, but only on the actual surface of mesoporous carbon materials. Due to enhanced mass transport because of the rotating electrode during LSV experiments, peroxide species which are formed are quickly removed and electron transfer numbers/hydrogen peroxide yields will indicate a 2-electron pathway. Whereas in materials consisting of mesopores, the formed peroxide intermediates remain in the mesopores for longer, allowing further disproportionation of the peroxide, resulting in a higher overall electron transfer number and lower $H_2O_2$ yield due to the quasi-4-electron pathway. Similarly, a thicker catalyst layer on the electrode surface, due to a high catalyst loading or the nature of the carbon material itself, has been shown to enhance the quasi-4-electron pathway, due to trapping of intermediates in gaps/voids.[25,26,163]

Considering these findings with regards to the studied carbogels, the slightly lower micropore volume and overall different morphology (resulting in a different catalyst layer) in the boron containing samples might be another explanation for the higher electron transfer numbers and lower $H_2O_2$ yields.

## 3.4 Summary

Nitrogen doped metal-free carbogels were synthesised via an easy one-pot hydrothermal carbonisation, starting from biomass precursors glucose and ovalbumin, and used as oxygen reduction electrocatalysts. An easy and environmental friendly activation approach was investigated, as well as the influence of heteroatom dopants sulphur and boron on the carbogel properties.

Oxygen activation during the high temperature pyrolysis at 1000 °C increased the carbogel surface area and micropore volume up to 1150 $m^2 g^{-1}$, while incorporating higher amounts of oxygen at the cost of yield loss due to $O_2$ etching of carbon and nitrogen atoms. A mixed atmosphere of nitrogen and 2 % of oxygen was found to deliver the most favourable combination in terms of surface area (874 $m^2 g^{-1}$), elemental composition (beneficial ratio of graphitic and pyridinic N), acceptable yield loss and catalytic activity towards the oxygen reduction reaction.

Additional heteroatom doping of the pure nitrogen doped carbogel with sulphur did not result in an increased catalytic performance due to a decrease in surface area and nitrogen content. The addition of boric acid yielded differently structured cryogels, with lower surface area after the high temperature pyrolysis than the pure carbogel. A structure directing role of boric acid during the formation of the cryogel was proposed, rather than ovalbumin, allowing for the protein to act as more efficient nitrogen source resulting in an overall higher nitrogen content. For the studied carbogels, the nitrogen content seemed to influence the limiting current density, while the oxygen content seemed to affect the onset potential. Further catalytic testing revealed superior ORR activity for samples containing boron, which was assumed to be due to a higher content of C=O groups as well as graphitic and pyridinic N, acting as active sites, as compared to samples without boron. An additional effect due to the different morphology of the boron containing carbogels was suggested to lead to more favourable mass transport, further enhancing the ORR activity. The highest electron transfer number and lowest $H_2O_2$ yield were found for the carbogel containing nitrogen and boron with 3.5 and 22.6 %, respectively. A clear influence/direct involvement in the ORR of the surface area or heteroatom dopants sulphur and boron was not observed.

Findings indicated that key properties such as carbogel structure, surface area, pore properties and dopant level can be controlled by easy addition of heteroatom precursors to the hydrothermal carbonisation reaction mixture, which enabled an improvement of the overall catalytic performance. Though none of the metal-free carbogels studied exhibited a comparable performance to a commercial platinum standard in terms of onset potential, limiting current density, electron transfer number or hydrogen peroxide yield, superior stability and methanol tolerance was observed in alkaline media. Considering that the presented carbogels can be easily synthesised from cheap and abundant precursors, their inferiority in performance could still be traded in return for a cheaper and more sustainable oxygen reduction reaction catalyst than platinum.

# Chapter 4 | Iron containing heteroatom doped carbogels as electrocatalysts

## 4.1 Introduction

Non-noble metal electrocatalysts, especially the combination of iron and nitrogen, have been extensively reported in literature due to their promising performance. These catalysts can be synthesised in various ways, with starting materials ranging from real biomass and their precursors to synthetic chemicals. Different examples for biomass-derived nitrogen and iron doped carbons have been reported in literature.

Li et al.[164] synthesised N/Fe doped nanotubes grown on hollow carbon fibres from catkin, iron(III)chloride and melamine. Their material resulted in a surface area of 461 $m^2$ $g^{-1}$, with 4.15 at% of N and 1.27 at% of Fe. They showed promising catalytic activity both in alkaline and acidic electrolyte with electron transfer numbers close to 4 and good stability and methanol tolerance. Another approach starting from biomass resources was made by Liang et al.[165] who converted bacterial cellulose from a microbial fermentation process into a N doped nanofiber carbogel by direct high temperature pyrolysis. Their material had a high surface area of 916 $m^2$ $g^{-1}$ exhibiting a nanofibrous network structure and a nitrogen content of 5.8 at%. Testing in alkaline media revealed comparable performance to the platinum standard, with hydrogen peroxide yields below 10 % and electron transfer numbers close to 4. Though the authors did not attribute any metal contribution to the good ORR performance, ICP atomic emission spectrometry revealed the presence of 0.01 wt% of metals (such as Fe and Co), which most likely had an influence on the good catalytic activity. Wang et al.[166] used boiled egg white and iron salt to synthesise a N/Fe doped carbon via direct pyrolysis. Their material contained 4.4 wt% of nitrogen and a high iron content of 16.8 wt% and showed good catalytic ORR activity in alkaline media. As mentioned earlier (chapter 3.1), real biomass poses challenges in terms of repeatability as well as possible conflicts, especially if food based. Thus, non-noble metal catalyst made from synthetic chemicals or biomass precursors are more commonly reported.

Song et al.[167] synthesised iron and nitrogen doped nanofiber carbogels from glucosamine hydrochloride and ferrous gluconate with ultrathin tellurium nanowires as template via hydrothermal carbonisation with subsequent pyrolysis under inert atmosphere. Their carbogel nanofibers exhibited a diameter of around 150 nm, with a total surface area of 584 $m^2$ $g^{-1}$. XPS spectra showed 1.76 at% of nitrogen, but did not detect any iron, which was found to be 0.44 wt% via ICP atomic emission spectrometry. A metal-free control sample doped only with nitrogen had a surface area of only 350 $m^2$ $g^{-1}$. The metal

containing sample showed a clear improvement in catalytic performance compared to the control sample, with limiting current density similar to the platinum standard in alkaline electrolyte and an electron transfer number close to 4, under both alkaline and acidic conditions. Their sample exhibited outstanding stability and methanol tolerance in alkaline and acidic electrolyte, which the authors attributed to an additional acid washing step, which removed inorganic nanoparticles and left behind only active and stable $FeN_x$ active sites.

Fan et al[168] reported iron, copper and nitrogen triple doped carbon nanotubes with a bamboo like structure via polymerisation of thiophene with added melamine and metal salts, resulting in a tube diameter of around 80 nm and a surface area of 588 $m^2 g^{-1}$. XPS revealed a high nitrogen content of around 6 at%, as well as traces of sulphur (0.19 at%), iron (0.93 at%) and copper (0.29 at%). Their sample outperformed the platinum standard in alkaline media as well as the metal-free control sample and samples containing only one species of metal. The authors concluded that Cu itself exhibits rather poor ORR activity, but it can contribute towards the formation of active $FeN_x$ sites as well as a favourable structure, resulting in enhanced performance of the dual metal carbon.

Yin et al.[169] reported a hybrid carbogel containing iron nitride and nitrogen doped graphene made by hydrothermal carbonisation of graphene oxide and iron(II)phthalocyanine followed by a high temperature pyrolysis. High resolution TEM confirmed the presence of FeN structures in the final product, with 8.2 at% of nitrogen and 2.3 at% of iron. A control sample made without graphene oxide, made of only the FeN nanoparticles, showed good activity, but the hybrid material exhibited similar catalytic activity and better stability than a commercial platinum standard in alkaline media. The authors attributed this to the synergistic effect of the FeN active sites distributed on the 3D microporous structure of the graphene oxide, resulting in a surface area of 117 $m^2 g^{-1}$.

Apart from nitrogen and iron, additional dopants such as sulphur and/or boron are also used, in the hope of further enhancement of the catalytic activity. Chen et al.[170] synthesised nitrogen, sulphur and iron triple doped porous carbon from melamine formaldehyde resin, KSCN and iron salt using calcium carbonate as a template. They found that the surface area increased with increasing pyrolysis temperature, up to 848 $m^2 g^{-1}$ at 1000 °C, while the dopant contents decreased, as low as 0.5 at % for N, 0.15 at% for S and 0.06 at% for Fe at 1000 °C. Though the sample pyrolysed at 900 °C exhibited the most positive onset potential in acidic media, $H_2O_2$ yields and electron transfer

numbers were nearly identical, regardless of pyrolysis temperature or surface area and dopant levels, below 6 % and around 3.9, respectively.

Guo et al.[171] used porous carbon foams doped with sulphur and trace amounts of nitrogen and iron as ORR catalyst. They found that an increased pyrolysis temperature increases the surface area and graphitisation of the materials, though at the cost of dopant amounts. Their best performing sample in alkaline media was pyrolysed at 800 °C, exhibited a surface area of 370 $m^2 g^{-1}$, 2.6 at% of S, 0.2 at% of N and 0.1 at% of Fe. The superior ORR activity was ascribed to the favourable combination of surface area and dopant amounts as compared to other pyrolysis temperatures.

Kone et al.[172] synthesised iron, nitrogen and sulphur doped hierarchical porous carbon, using a silica template to create the porous structure. They observed the presence of iron oxide particles after pyrolysis, which they removed via acid leaching to create mesopores and a higher surface area of 1148 $m^2 g^{-1}$ as compared to 672 $m^2 g^{-1}$ before acid leaching. Elemental composition determined via XPS revealed 7.21 at% of N, 1.67 at% of S and trace amounts of Fe with 0.64 at% after acid leaching. Though no peak corresponding to FeN binding sites was found in the high resolution XPS spectra, EDX showed a homogeneous distribution of Fe and N on the materials surface, from which the authors inferred that some $FeN_x$ active sites are present. Electrochemical testing showed that both samples, before and after acid leaching exhibited the same onset potential, though the limiting current density was significantly improved after the removal of iron oxide particles due to the higher surface area. They also investigated the role of the two heteroatom dopants and the iron and found that co doping iron and sulphur resulted in a poor catalytic activity, even worse than the metal-free version containing only nitrogen and sulphur. A sample containing nitrogen and iron showed similar catalytic activity as compared to a commercial platinum standard, while triple doping of nitrogen, sulphur and iron further increased the ORR activity and shifted towards a more positive onset potential and lower limiting current density. The author concluded that the enhanced activity of the triple doped version is due to the presence of graphitic and pyridinic N, thiophene S, $FeN_x$ and elemental iron nanoparticles.

A comparison between different non-noble metal dopants (Fe, Co and Ni) in combination with nitrogen and sulphur heteroatom doped carbon was carried out by Wu et al.[173] They found that the triple doped material with iron exhibited a sponge like structure with the most favourable dopant amounts (3.9 at% N, 0.76 at% S and 3.8 at% Fe) and highest surface area of 1200 $m^2 g^{-1}$. It was suggested that the presence of iron not only leads to a beneficial ratio of pyridinic to graphitic nitrogen, but also hinders the formation of

inactive sulphate species, which in combination with the high surface area resulted in the best catalytic performance both in alkaline and acidic electrolyte when compared to the materials containing Co or Ni.

Cao et al.[59] reported on boron, nitrogen and iron ternary doped graphene oxide hybrids, where they found that the addition of graphene oxide not only increased the electrochemical active surface area, but also led to a more favourable evolution and distribution of active sites, such as $FeN_x$-C, B-N and $Fe_3O_4/Fe_3C$ nanoparticles. The presence of boric acid was suggested to stabilise the network, preventing nitrogen loss during the high temperature pyrolysis besides boron reacting with gaseous N during the pyrolysis to form B-N sites. Due to the beneficial surface area and species, the sample outperformed a N/Fe carbon and a N/B/Fe carbon without graphene oxide during electrochemical ORR testing.

An iron doped carbon without any nitrogen, but with additional boron was reported by Zhang et al.[174] synthesised from carbon dioxide, sodium borohydride and iron salt in a high temperature pyrolysis. The material consisted of iron nanoparticles encased in onion like graphitic carbon shells, which was attributed to the reaction between $NaBH_4$ and $CO_2$ leading to a deposition of carbon on the metal nanoparticles. Though the catalyst showed activity towards the ORR, it was far from competing with the platinum standard or other reported $FeN_x$ catalysts, suggesting that the presence of nitrogen, to possibly form $FeN_x$ active sites, is crucial.

Li et al.[175] synthesised nitrogen, sulphur and boron doped carbon nanotubes with encapsulated iron. Though their material exhibited low surface areas (only 82 $m^2\ g^{-1}$), it had high heteroatom dopant levels with 9.88 at% for S, 9.36 at% for N, 3.41 at% for B and traces of Fe (0.7 at%). Electrochemical testing showed a comparable performance with a platinum standard and good stability, though achieved with very high mass loadings (> 500 $\mu g/cm^2$), resulting in electron transfer numbers above 4. Their fourfold doped version was better compared to a triple (N/S/Fe) and dual (N/Fe) doped version, which most likely is due to lower dopant levels in the triple and dual doped versions as well as a more beneficial morphology for the fourfold doped version.

Guo et al.[176] derived an ORR catalyst from *Shewanell oneidensis* bacteria by direct pyrolysis in argon atmosphere. Due to the nature of the bacterium, the pyrolysed samples contained mainly carbon and oxygen with additional nitrogen (2.26 at%), sulphur (0.1 at%), phosphorus (0.46 at%) and iron (0.18 at%) doping and exhibited a surface area of 142 $m^2\ g^{-1}$. Their sample showed a better onset potential as compared to platinum, though a lower limiting current density and exhibited an electron transfer number of 3.9 with

outstanding stability as well as methanol and CO tolerance. The authors attributed the good performance to the presence of different heteroatom dopants as well as exisiting $FeN_x$ sites.

Another approach using a biomass derived electrocatalyst was reported by Tran et al.[177], who used human urine as starting material and combined it with iron salt to yield nitrogen, sulphur, phosphorus and iron doped carbon. Depending on the pyrolysis temperature, surface areas were between 980 and 1080 $m^2$ $g^{-1}$. Their best performing sample was pyrolysed at 800 ºC under a $NH_3$ atmosphere and contained 6.52 at% for N, 0.75 at% of S, 0.57 at% of P and 0.41 at% of Fe and exhibited an electron transfer number around 3.9.

While no doubt exists about the crucial role of nitrogen in non-noble metal ORR catalysts, especially in combination with iron, the presence of boron is often mentioned to have a beneficial effect not only by offering possible metal-free active sites for the ORR, but it is also often suspected to have a favourable influence on the incorporation of nitrogen and structure formation/morphology of the material. In contrast, the role of sulphur is under debate, additional doping with sulphur has sometimes been reported to lead to less active catalysts due to the possible formation of metallic iron, as well as hindering the development of active $FeN_x$ sites and/or poisoning the latter.[178,179] Kramm et al.[180] found that in the presence of sulphur, first elemental iron is formed at temperatures above 350 ºC, as well as iron sulphide above 650 °C, which can in turn prevent the formation of iron carbide. In their study, the formation of iron carbide prevented the homogeneous evolution and distribution of active $FeN_x$ centres, causing loss of ORR activity. An additional etching step after the pyrolysis lead to a more active catalyst as compared to the material prepared without sulphur, which the authors attributed to the removal of FeS and other inactive species, lower degree of graphitisation and a larger amount of active sites, due to the absence of $Fe_3C$.[181]

Apart from the commonly reported heteroatom doped iron catalysts, the use of iron oxide nanoparticles in ORR catalysts has also been reported. Wu et al.[61] synthesised a nitrogen doped graphene aerogel with $Fe_3O_4$ nanoparticles with a surface area of 110 $m^2$ $g^{-1}$. Interestingly, they found that most of the nitrogen was incorporated close to the iron oxide nanoparticles, suggesting the presence of some $FeN_x$ sites, leaving the involvement of the iron oxide particles in the ORR uncertain. More recently, He et al.[60] reported mesoporous carbon containing $Fe_2O_3$ nanocrystals, templated with SBA-15. A comparison with a metal-free carbon also templated with SBA-15 as well as pure $Fe_2O_3$ showed the clear superiority of the hybrid material, which the authors explained due to the iron oxide particles acting as active sites, while the carbon enables better mass transport properties

due to is mesoporous structure. In this study no nitrogen was incorporated, excluding the presence of any formed $FeN_x$ sites, suggesting that $Fe_2O_3$ particles can act as active sites as well.

In order to further improve the metal-free carbogels reported in chapter 3, the influence of iron incorporation was investigated. For this, nitrogen and iron dual doping was examined with two different iron salts as precursors, one containing ferrous and the other ferric iron, as well as different precursor concentrations to get a better understanding how iron can change the physical and chemical properties as well as the electrochemical performance. Further, triple and fourfold doped versions with combinations of nitrogen, sulphur, boron and iron were synthesised to study possible synergistic effects between dopants both during the structure formation of the cryogel and on the elemental composition and electrochemical activity. A schematic of the synthesis process can be seen in Figure 4.1.

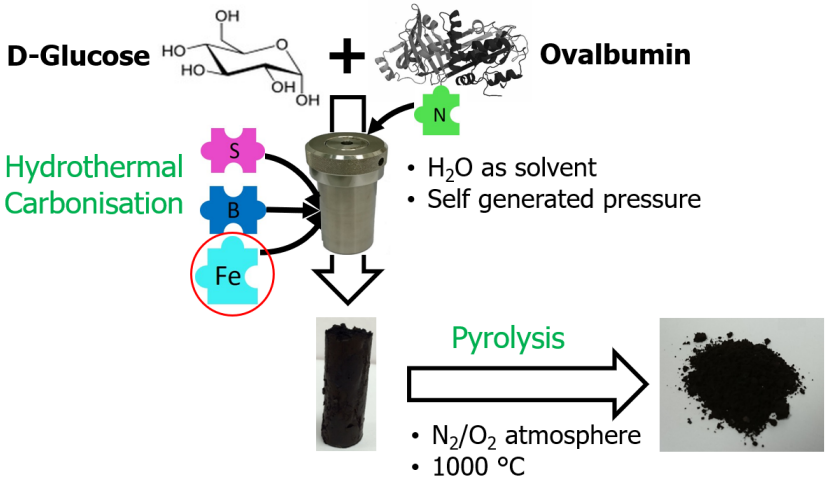


*Figure 4.1 Schematic of the synthesis process for iron containing heteroatom doped carbogels.*

## 4.2 Influence of iron precursor on the cryogel and carbogel formation

The influence of iron incorporation from two different iron salts and in alternating concentration was investigated on the cryogel and carbogel properties in terms of morphology, surface area, pore properties, elemental composition and catalytic activity towards the ORR. For this, four samples were synthesised, as can be seen in Table 4.1, a pure nitrogen doped version CN and three iron doped variations, which were pyrolysed after the hydrothermal carbonisation under a mixed atmosphere of $N_2$/air (corresponding to 2 % of $O_2$) at 1000 °C.

*Table 4.1 Overview of different samples doped with iron from different precursors or in different concentration.*

| Sample name after HTC | Sample name after pyrolysis | Iron precursor | Amount of iron |
|---|---|---|---|
| HTC-CN | CN | - | - |
| HTC-$CN_{Fe3+\_1}$ | $CN_{Fe3+\_1}$ | $FeCl_3$ x $6H_2O$ | 1 mmol |
| HTC-$CN_{Fe3+\_2}$ | $CN_{Fe3+\_2}$ | $FeCl_3$ x $6H_2O$ | 2 mmol |
| HTC-$CN_{Fe2+}$ | $CN_{Fe2+}$ | $FeCl_2$ x $4H_2O$ | 1 mmol |

Figure 4.2 shows SEM images for all four cryogel versions after the hydrothermal carbonisation, where the morphology was changed by the different iron precursors, suggesting that the presence of both types of iron induced an alteration of the HTC mechanism during the cryogel formation. While the nanowire/coral like structure still existed after the addition of ferric iron, but in a more expanded fashion, a particle like cryogel had formed in the presence of ferrous iron. Though different iron precursors were used, Cui et al.[182] reported, similar to our findings, that the nature of the iron ion can cause an altered carbon structure during the hydrothermal carbonisation.

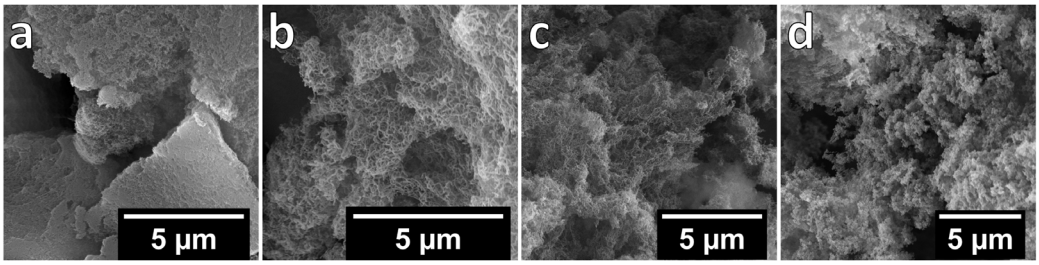


*Figure 4.2 SEM micrographs of nitrogen cryogels after the hydrothermal carbonisation in pure form HTC-CN (a) and doped with 1 mmol of iron from $FeCl_3$ x $6H_2O$, HTC-$CN_{Fe3+\_1}$ (b), 2 mmol of iron from $FeCl_3$ x $6H_2O$, HTC-$CN_{Fe3+\_2}$ (c) and 1 mmol of iron from $FeCl_2$ x $4H_2O$, HTC-$CN_{Fe2+}$ (d).*

Besides the morphology, differences in the mechanic stability of the cryogels were observed after the hydrothermal carbonisation, where HTC-$CN_{Fe3+\_1}$ had the firmest appearance, even better than the pure HTC-CN version, followed by HTC-$CN_{Fe2+}$ and HTC-$CN_{Fe3+\_2}$. This finding was also supported by the dry mass yield after the hydrothermal carbonisation, where HTC- $CN_{Fe3+\_1}$ resulted in 36 %, HTC-CN in 32 %, HTC-$CN_{Fe3+\_2}$ in 17 % and HTC-$CN_{Fe2+}$ in 36%. Figure 4.3 shows the different cryogels after the hydrothermal carbonisation, while HTC-CN and HTC-$CN_{Fe3+\_1}$ resulted in similar sized monoliths, HTC-$CN_{Fe3+\_2}$ did not yield a monolith at all with mostly liquid instead of a solid phase remaining after the HTC process, HTC-$CN_{Fe2+}$ resulted in a very densely packed smaller monolith.

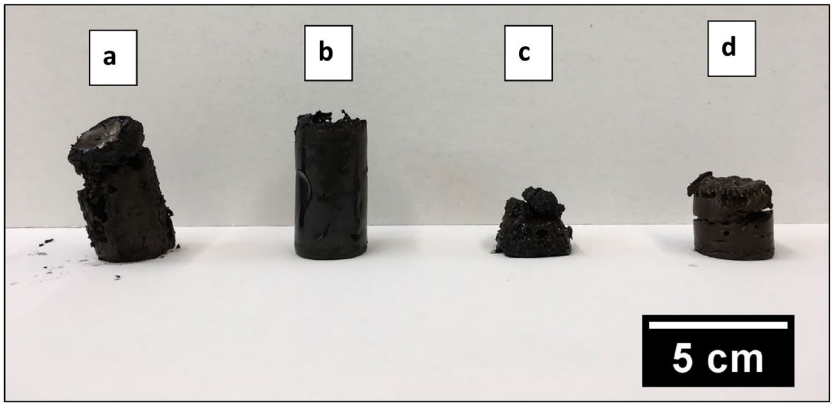


*Figure 4.3 Monoliths after the hydrothermal carbonisation for a) HTC-CN (monolith broke while being removed from the glass inlet but is similar in appearance/size to b), b) HTC-$CN_{Fe3+\_1}$, c) HTC-$CN_{Fe3+\_2}$ and d) HTC-$CN_{Fe2+}$.*

Figure 4.4 shows SEM images of all four carbogels after the pyrolysis at 1000 °C and TEM micrographs for CN and $CN_{Fe3+\_1}$. As already observed after the HTC, the incorporation of iron from the ferric precursor changed the morphology of both $CN_{Fe3+\_1}$ and $CN_{Fe3+\_2}$ compared to the pure sample CN. While the pure carbogel CN was made up of mostly broken and agglomerated carbon nanowires, with a diameter of around 14.6 ± 1.6 nm, the presence of ferric iron appeared to aid the full formation/growth and unfolding of considerably thicker nanowires with a diameter of around 33.5 ± 1.7 nm, creating a coral like structure. The addition of ferrous iron caused a total change of morphology, resulting in a rather drop/particle like arrangement.

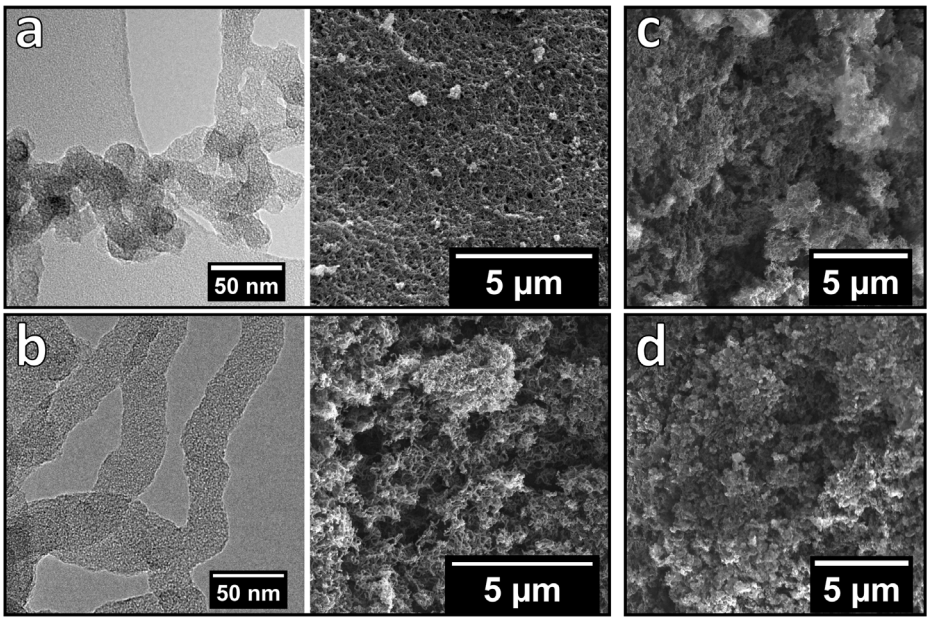


*Figure 4.4 TEM and SEM micrographs of nitrogen carbogels pyrolysed at 1000 °C in pure form CN (a) and doped with 1 mmol of iron from $FeCl_3$ x $6H_2O$, $CN_{Fe3+\_1}$ (b), and SEM micrographs of nitrogen carbogels treated at 1000 °C doped with 2 mmol of iron from $FeCl_3$ x $6H_2O$, $CN_{Fe3+\_2}$ (c) and 1 mmol of iron from $FeCl_2$ x $4H_2O$, $CN_{Fe2+}$ (d).*

Surface area, total pore volume as well as meso- and micropore volume for all four cryogels and carbogels are presented in Table 4.2, nitrogen sorption isotherms can be seen in Figure 4.5. While the surface area was highest for the pure nitrogen doped cryogel, HTC-CN, after the hydrothermal carbonisation, it was lowest after the high temperature pyrolysis under a mixed atmosphere or $N_2$/air. An obvious increase in surface area was observed from 854 $m^2$ $g^{-1}$ for CN to 1271 $m^2$ $g^{-1}$ for $CN_{Fe3+\_1}$. An increase in the concentration of ferric iron ($CN_{Fe3+\_2}$) still showed a positive effect compared to the pure version, CN, though slightly limiting the surface area to 1015 $m^2$ $g^{-1}$. The addition of ferrous iron however seemed to negatively affect the carbogels surface area, possibly due to the altered structure formation, limiting $CN_{Fe2+}$ to 617 $m^2$ $g^{-1}$.

*Table 4.2 BET surface area and pore volumes for the pure sample CN and three iron doped versions before (HTC) and after the high temperature pyrolysis at 1000 ºC.*

| Sample | Surface area [$m^2$ $g^{-1}$] | $V_{tot}$ [$cm^3$ $g^{-1}$] | $V_{meso}$ [$cm^3$ $g^{-1}$] | $V_{micro}$ [$cm^3$ $g^{-1}$] |
|---|---|---|---|---|
| HTC-CN | 101 | 0.640 | 0.640 | - |
| HTC-$CN_{Fe3+\_1}$ | 59 | 0.119 | 0.112 | 0.007 |
| HTC-$CN_{Fe3+\_2}$ | 45 | 0.138 | 0.134 | 0.004 |
| HTC-$CN_{Fe2+}$ | 22 | 0.077 | 0.076 | 0.001 |
| CN | 854 | 0.722 | 0.431 | 0.291 |
| $CN_{Fe3+\_1}$ | 1271 | 0.761 | 0.334 | 0.427 |
| $CN_{Fe3+\_2}$ | 1015 | 0.675 | 0.334 | 0.341 |
| $CN_{Fe2+}$ | 617 | 0.294 | 0.083 | 0.211 |

After the hydrothermal carbonisation, the highest total pore volume was found for HTC-CN with 0.640 $cm^3$ $g^{-1}$, made up solely of mesopores. Once the high temperature pyrolysis took place, all samples increased their total pore volume with a drastic rise in micropore volume. $CN_{Fe2+}$ only showed a marginal increase in mesopore volume after the pyrolysis, resulting in the lowest total pore volume with only 0.294 $cm^3$ $g^{-1}$, which could be attributed to the denser structure of the cryogel after the hydrothermal carbonisation, enabling less possibility to create mesopores during the pyrolysis. The presence of ferric iron had a clear benefit on the micropore volume for both carbogels $CN_{Fe3+\_1}$ and $CN_{Fe3+\_2}$.

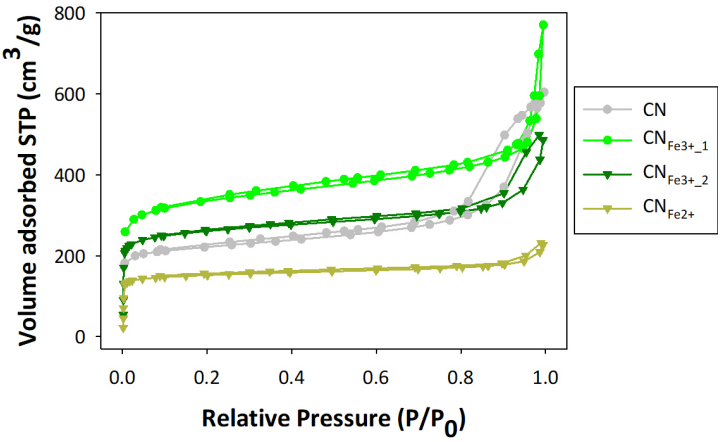


*Figure 4.5 Nitrogen sorption isotherms obtained at 77 K of nitrogen doped carbogels pyrolysed at 1000°C in pure form (CN) and doped with different concentrations of Iron(III)chloride ($CN_{Fe3+\_1}$, $CN_{Fe3+\_2}$) or Iron(II)chloride ($CN_{Fe2+}$).*

The elemental composition was determined via XPS and can be seen in Table 4.3. The highest nitrogen content was found for the pure version CN with 4.1 at%, followed by 1.10 at% for $CN_{Fe3+\_1}$, 1.03 at% for $CN_{Fe2+}$ and 0.66 at% for $CN_{Fe3+\_2}$. $CN_{Fe3+\_1}$ and $CN_{Fe2+}$ showed only traces of iron with 0.05 at% and 0.03 at%, respectively, while no iron could be detected in $CN_{Fe3+\_2}$ (below detection limit of 0.01 at%). Contrary to the low iron concentrations determined via XPS, ICP analysis revealed the presence of 2.7 wt% of Fe in the bulk of $CN_{Fe3+\_1}$. It was assumed that the higher concentration of the iron salt interfered with the formation of the cryogel, thus resulting in a considerably lower yield of dry mass and lower nitrogen content with most of the iron left in the liquid phase instead of incorporated into the carbon framework. A significant difference was also found in the amount of oxygen, with 16.71 at% and 8.43 at% for CN and $CN_{Fe3+\_1}$, respectively, while the other two samples had a lower content of 2.75 at% ($CN_{Fe3+\_2}$) and 3.38 at% ($CN_{Fe2+}$). This drastic difference in oxygen content could be due to the altered HTC mechanism, already resulting in a different structure/morphology of the materials, yielding either a modified cryogel made up of particles ($CN_{Fe2+}$) or no gel at all ($CN_{Fe3+\_2}$).

*Table 4.3 Elemental composition determined by XPS for carbogels pyrolysed at 1000 °C under a mixed atmosphere of $N_2$/air.*

| Sample | C | O | N | Fe |
|---|---|---|---|---|
| CN | 79.19 | 16.71 | 4.10 | - |
| $CN_{Fe3+\_1}$ | 90.41 | 8.43 | 1.10 | 0.05 |
| $CN_{Fe3+\_2}$ | 96.59 | 2.75 | 0.66 | < 0.01 |
| $CN_{Fe2+}$ | 95.56 | 3.38 | 1.03 | 0.03 |

Deconvoluted high resolution C1s and O1s spectra indicated the different carbon and oxygen bonding present in the four carbogels pyrolysed at 1000 °C, as can be seen in Figure 4.6. The lowest carbon content was found in the pure nitrogen doped carbogel,

though the three occurring bond types were similarly distributed throughout the materials. The greatest amount was found to correspond to $sp^2$ C-C bonds around 284.6 eV, followed by functional groups C-OH around 285.5 eV and C-N around 286.3 eV.[148] The oxygen content varied between the samples, with the pure carbogel, CN, exceeding the iron doped carbogels many times over. Three dominant peaks were found in the O1s spectra around 531 eV, 532.3 eV and 533.4 eV corresponding to oxygen functionalities C=O (possibly also quinone groups), C-O and O=C-O, respectively.[183] The pure carbogel as well as the carbogels doped with ferric iron exhibited a similar distribution of oxygen groups, while ferrous iron induced a slight change in C=O and O=C-O bonds.

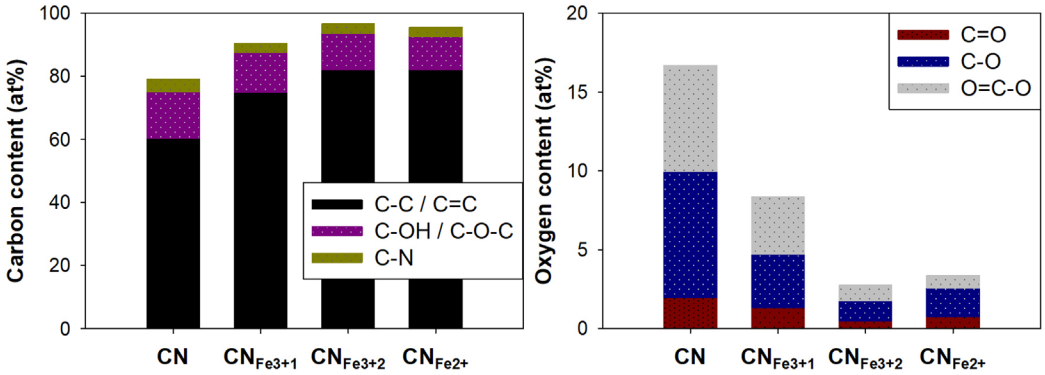


*Figure 4.6 Distribution of carbon and oxygen bonding in carbogels pyrolysed at 1000 °C under a mixed atmosphere of $N_2$/air for a pure nitrogen doped carbogel, CN, and three iron doped versions.*

Deconvolution of the N1s spectra revealed the presence of pyridinic nitrogen, graphitic nitrogen and N-oxide functionalities around 398.1 eV, 400.7 eV and 403 eV, respectively, in all carbogels (Figure 4.7).[148] The highest amount was found to be graphitic nitrogen, followed by pyridinic and N-oxides. With 73 %, $CN_{Fe3+\_1}$ had a significantly higher graphitic nitrogen content as compared to the other samples (around 55 %).

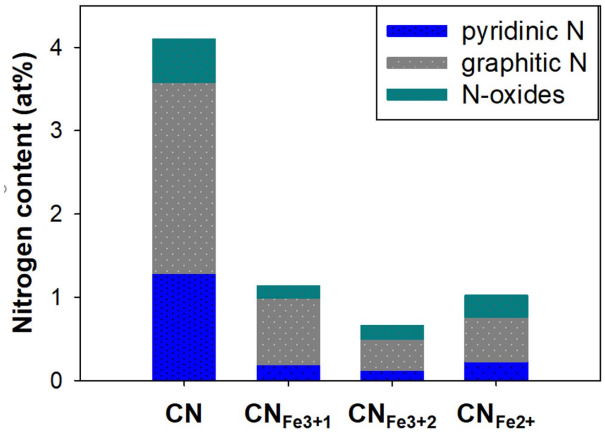


*Figure 4.7 Distribution of nitrogen species, pyridinic N, graphitic N and N-oxides in carbogels pyrolysed at 1000 °C under a mixed atmosphere of $N_2$/air for a pure nitrogen doped carbogel, CN, and three iron doped versions.*

To get a better understanding of the structural defects in the materials, Raman spectra were recorded (Figure 4.8) and the corresponding $I_D/I_G$ ratios calculated. All samples showed the characteristic D- and G-band values around 1320 $cm^{-1}$ and 1590 $cm^{-1}$, respectively, where the G-band indicates the typical $sp^2$ bond stretching in carbon materials and the D-band relates to the $sp^2$ breathing modes, appearing only in case of defects/disorder in the hexagonal $sp^2$ structure.[153] Overall, the broadness of the D- and G-band as well as the absence of a distinct separation between both peaks suggested a mostly amorphous character for all samples. The $CN_{Fe3+\_1}$ exhibited an additional broad peak around 2620 $cm^{-1}$, corresponding to the second order of the D peak (2D), present in layered graphene but also turbostatic graphite,[184] suggesting a slightly less disordered character compared to the other samples. Another widely used method to quantify the degree of disorder in carbon structures is the ratio of D- to G-band based on their peak intensity or area, resulting in the so-called $I_D/I_G$ ratio, where higher numbers indicate a higher degree of disorder/less graphitisation. The $I_D/I_G$ ratios found for the four carbogels were 2.0, 1.6, 2.1 and 2.3 for CN, $CN_{Fe3+\_1}$, $CN_{Fe3+\_2}$, $CN_{Fe2+}$, respectively. This suggested that the addition of low concentrations of ferric iron lowered the degree of disorder, while higher amounts interfered with the HTC mechanism and disturbed the structure formation. A similar observation was made by Dhakate et al.[185] who found that small amounts of iron oxide catalysed the graphitisation of carbon, while a content above 1 % caused localised graphitisation and an increase in interlayer spacing due to a decrease in crystallite size. With the highest $I_D/I_G$ ratio, ferrous iron not only caused a differently structured material, but also a carbon with more defects. Generally, iron compounds are known to catalyse the graphitisation of carbon materials during pyrolysis with different mechanisms proposed depending on the nature of the iron compound as well as the pyrolysis temperature. [172,186–188] At higher temperatures, carbides can be formed which decompose upon further heating and release graphite crystals which act as starting point for the growth of graphite structures.[186] Other reports suggested that the iron can travel or diffuse through the carbon matrix and thus promote graphitisation by changing the lattice structure.[189]

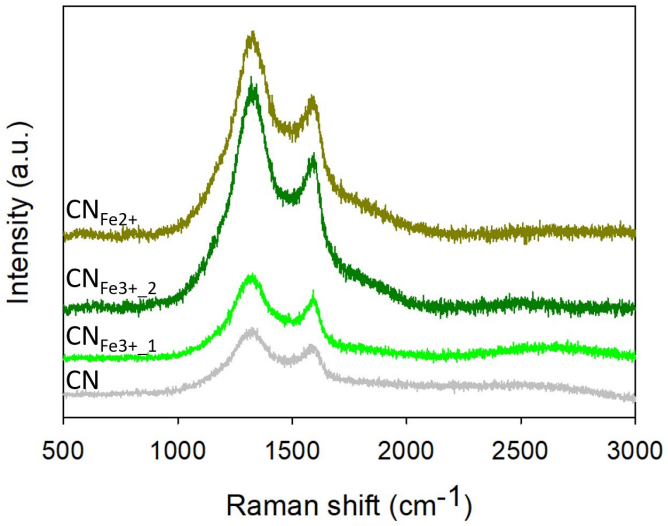


*Figure 4.8 Raman spectra for nitrogen doped carbogels pyrolysed at 1000°C in pure form, CN, and doped with different concentrations of Iron(III)chloride ($CN_{Fe3+\_1}$, $CN_{Fe3+\_2}$) or Iron(II)chloride ($CN_{Fe2+}$).*

Electrochemical testing was carried out in alkaline and acidic media for all four samples with a rotating ring disk setup. Sample $CN_{Fe3+\_1}$ and $CN_{Fe3+\_2}$ exhibited the best onset potential, while $CN_{Fe3+\_1}$ also had the lowest limiting current in both media compared to the other samples, though worse than a commercially available platinum standard (Figure 4.9). The presence of even trace amounts of iron seemed to have a beneficial influence on the onset potential, while surface area possibly played a role in determining the limiting current density, at least for the carbogels with a similar structure (CN, $CN_{Fe3+\_1}$ and $CN_{Fe3+\_2}$), where a higher surface area enabled better accessibility to the active sites as well as offered more favourable contact between the materials surface and reactants. Values for the electron transfer numbers (ETN) and hydrogen peroxide yields ($H_2O_2$%) can be found in Table 4.4 and 4.5. The highest ETN and lowest $H_2O_2$ yield in alkaline media were achieved for $CN_{Fe3+\_1}$ with 3.9 and 7.2 %, respectively. Interestingly, the metal-free sample CN exhibited a similar ETN as compared to $CN_{Fe3+\_2}$ and an even higher ETN than $CN_{Fe2+}$. This trend could possibly be explained by the significantly higher amount of graphitic and pyridinic N in CN, as well as a higher content of C=O/quinone groups, which have all been reported to act as active sites for the ORR.[78,87] Considering our materials elemental composition, especially the considerably lower amount of oxygen in $CN_{Fe3+\_2}$ and $CN_{Fe2+}$, the presence of quinone groups seems highly likely for $CN_{Fe3+\_1}$, which could explain it's better activity in alkaline media. In acidic media all iron doped carbogels performed similarly, though distant from a commercial platinum standard. Compared to the undoped version CN, it became clear that the presence of even trace amounts of iron had a favourable influence on the materials' catalytic activity. Adversely, $CN_{Fe3+\_2}$ and $CN_{Fe2+}$ showed a slightly increased

performance in acidic compared to alkaline media. It should be mentioned that the platinum standard was run/plotted for guidance to allow better comparison with measurements obtained via a different equipment or protocol. Though the platinum standard used here exhibited poorer performance in acidic electrolyte as compared to Pt standards reported in literature, it aids to put the performance of the catalysts synthesised and measured with the available equipment/setup in relation.

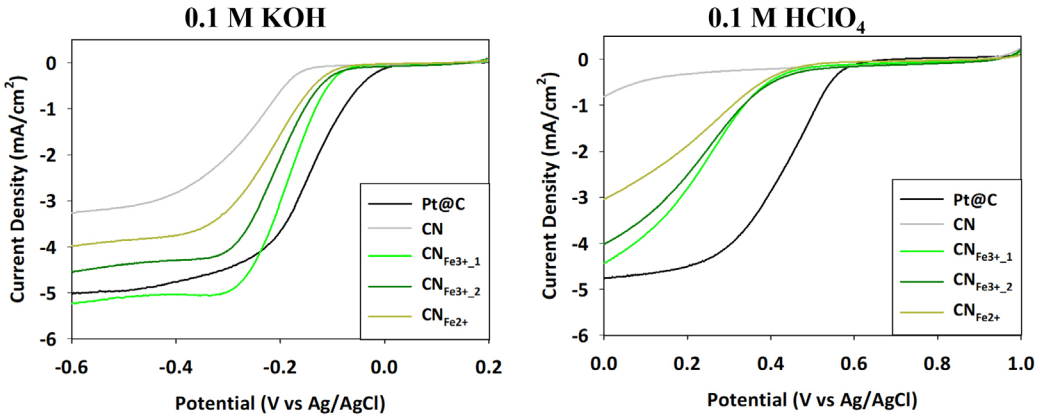


*Figure 4.9 Linear sweep voltammograms recorded with an RRDE setup at a rotational speed of 1600 rpm in 0.1 M KOH (left) and 0.1 M HClO4 (right) for a pure carbogel CN and three iron doped versions compared to a commercially available platinum standard.*

Recent reports[78–81] suggested that the active sites in alkaline and acidic media are fundamentally different for $FeN_x$/C catalysts, relating to inner sphere and outer sphere electron transfers in alkaline media, while only inner-sphere electron transfer is expected to occur in acidic media (chapter 2.1.3.2). Besides the widely believed active $FeN_x$ sites, Sahraie et al.[78] allocated nitrogen species and quinone groups as additional active sites in alkaline media contributing to the enhanced ORR performance as compared to under acidic conditions.

*Table 4.4 Electrochemical values derived from linear sweep voltammograms using an RRDE setup in 0.1 M KOH. The onset potential was determined at -0.1 mA/cm² and the limiting current density at -0.6 V (vs Ag/AgCl). Electron transfer number and $H_2O_2$ yield were averaged between -0.3 V and -0.6 V (vs Ag/AgCl).*

| Sample | Potential [V vs Ag/AgCl] | Limiting current mA/cm²] | ETN | $H_2O_2$ yield [%] |
|---|---|---|---|---|
| Pt@C | 0.006 | -5.0 | 3.9 | 3.3 |
| CN | -0.143 ± 0.010 | -3.25 ± 0.05 | 3.05 ± 0.05 | 46.6 ± 1.9 |
| $CN_{Fe3+\_1}$ | -0.063 | -5.2 | 3.9 | 7.2 |
| $CN_{Fe3+\_2}$ | -0.040 | -4.6 | 3.0 | 47.7 |
| $CN_{Fe2+}$ | -0.092 | -4.0 | 2.6 | 69.6 |

*Table 4.5 Electrochemical values derived from linear sweep voltammograms using an RRDE setup in 0.1 M $HClO_4$. The onset potential was determined at -0.2 mA/cm² and the limiting current density at 0 V (vs Ag/AgCl). Electron transfer number and $H_2O_2$ yield were averaged between 0 V and 0.3 V (vs Ag/AgCl).*

| Sample | Potential [V vs Ag/AgCl] | Limiting current [mA/cm²] | ETN | $H_2O_2$ yield [%] |
|---|---|---|---|---|
| Pt@C | 0.578 | -4.8 | 3.9 | 4.2 |
| CN | N.A. | N.A. | N.A. | N.A. |
| $CN_{Fe3+\_1}$ | 0.478 | -4.4 | 3.5 | 26.0 |
| $CN_{Fe3+\_2}$ | 0.525 | -4.0 | 3.6 | 20.3 |
| $CN_{Fe2+}$ | 0.454 | -3.0 | 3.6 | 17.6 |

An overview correlating the aforementioned parameters can be seen in Figure 4.10. Here it becomes clear, that $CN_{Fe3+\_1}$ showed the most favourable catalytic activity, due to its high surface area enabling good accessibility of the, possible $FeN_x$, active sites and less mass transport limitations. CN and $CN_{Fe3+\_2}$ exhibited the same electron transfer number, suggesting that the absence of iron (CN) can be compensated for by a higher content of metal-free active sites (pyridinic N, graphitic N and quinone groups).

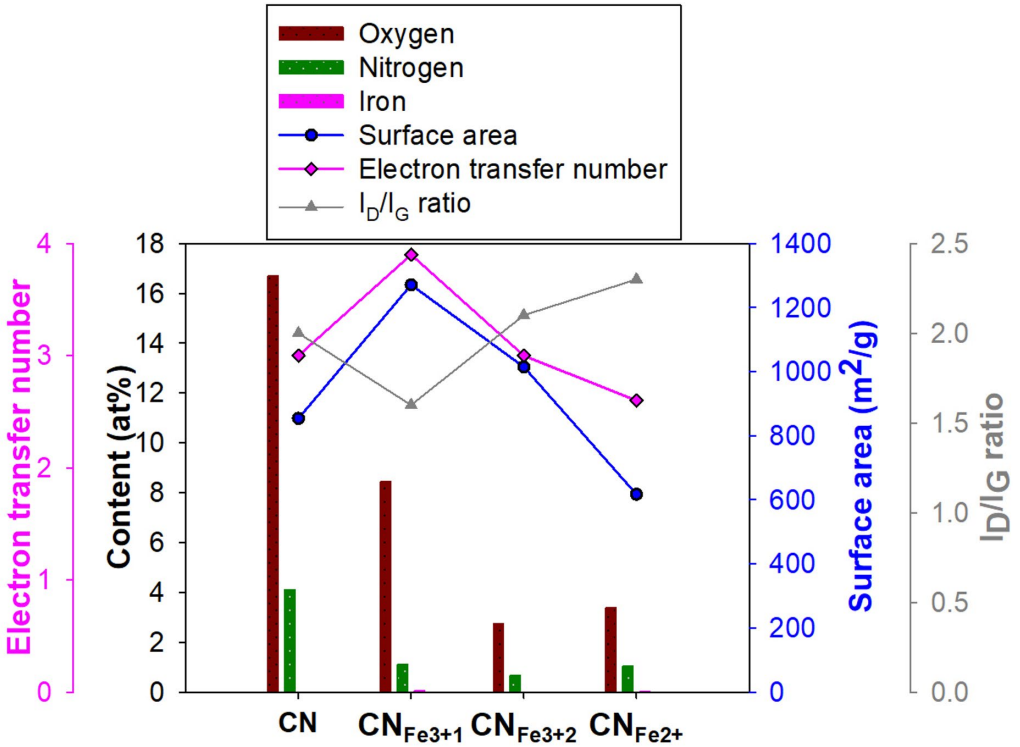


*Figure 4.10 Combination graph correlating the material's surface area and elemental content with the electrocatalytic activity (alkaline media) for nitrogen doped carbogels, CN, pyrolysed at 1000°C under a mixed atmosphere of N2/air (2 % $O_2$) doped with different concentrations of Iron(III)chloride ($CN_{Fe3+\_1}$, $CN_{Fe3+\_2}$) or Iron(II)chloride ($CN_{Fe2+}$). The onset potential was determined at -0.1 mA/cm² and the limiting current density at -0.6 V (vs Ag/AgCl).*

Based on the above presented results, we assume that the addition of a higher iron concentration ($CN_{Fe3+\_2}$) as well as the addition of ferrous iron ($CN_{Fe2+}$) negatively interfered with the formation of the cryogel structure, resulting in either no gel or a different morphology, while the addition of the lower ferric iron concentration seemed to positively affect the resulting cryogel in terms of mechanic stability and appearance. Considering these findings and the increased catalytic activity of $CN_{Fe3+\_1}$, further investigations into the role of iron during the cryogel formation are focused on samples CN and $CN_{Fe3+\_1}$ (abbreviated as $CN_{Fe}$ from hereon).

### 4.2.1 Cryogel structure formation in the presence of ferric iron

Preliminary results showed that the hydrothermal carbonisation of pure ovalbumin resulted in a water-soluble gel/paste, while a mix of ovalbumin and iron(III)chloride did not yield any solid residue (Figure 4.11). On the contrary, HTC of glucose as well as of glucose and iron(III)chloride resulted in a solid phase, with a dry mass yield of 1 % and 16 %, respectively. These findings suggested that ferric iron does not interact with ovalbumin, but presumably catalysed the formation of glucose to solid carbon.

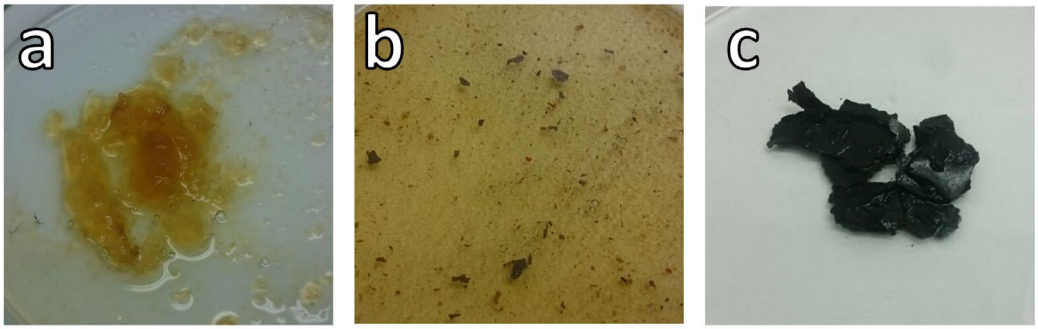


*Figure 4.11 Images of a) pure ovalbumin, b) ovalbumin + iron(III)chloride and c) glucose + iron(III)chloride after hydrothermal carbonisation at 180 °C for 5.5 h.*

As mentioned earlier (chapter 2.2), while heating reducing sugars, like glucose, with proteins Maillard reactions occur. Research on the influence of different parameters on the Maillard reactions have been carried out in the 1980's, including the effect of metals. Kato et. al.[190,191] investigated the influence of ferrous and ferric iron on the storage behaviour of glucose/ovalbumin mixtures. They observed that the presence of iron metals sped up the denaturation process of ovalbumin, thus expediting the Maillard reactions. It should be mentioned that they observed no denaturation of ovalbumin in the control sample where glucose was absent, suggesting no direct interaction between the iron salts and ovalbumin. Furthermore, they noticed that ferric iron was promoting the reaction faster than ferrous iron, which they explained via a possible reduction of the metal as a first step in the cascade of reactions. Based on these findings and above mentioned results, the presence of especially ferric iron was assumed to have catalysed two steps during the

formation of the cryogel. Firstly, it promoted a faster precipitation/nucleation of nanosized carbon particles and secondly it accelerated the denaturation of ovalbumin. The first assumption was supported by the higher dry mass yield as well as SEM images, seen in Figure 4.12, showing the drastic difference in carbon sphere size after the hydrothermal carbonisation of pure glucose or glucose and iron(III)chloride. By the addition of iron(III)chloride to the hydrothermal reaction mixture, the pH of the solution was lowered due to iron ions acting as electron acceptors (Lewis acid), which accelerated the acid catalysed dehydration of glucose as the first step of the HTC mechanism and thus sped up the formation and allowed a faster growth of the carbon microspheres.[192,193]

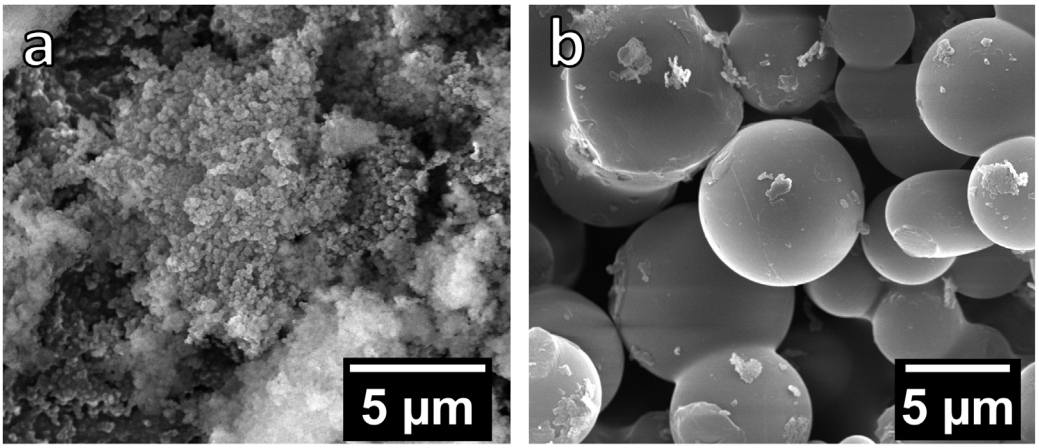


*Figure 4.12 SEM micrographs showing carbon spheres after the hydrothermal carbonisation of pure glucose (a) or glucose and iron(III)chloride (b) at 180 °C for 5.5 h.*

The second assumption would imply that due to the presence of ferric iron the demixing of glucose, after its dehydration, by ovalbumin was accelerated, which prevented further growth of the carbon spheres (as would be the case in the absence of ovalbumin) and directed their crosslinking into the cryogel structure. This would result in larger carbon particles which polymerise/nucleate together to then form a crosslinked networked in the presence of ferric iron, thus forming thicker nanowires, which was well in agreement with the findings. The iron doped version exhibited double the nanowire diameter as compared to the metal-free cryogel, besides creating a tougher/more stable monolith after the hydrothermal carbonisation. This was also in accordance with the cryogels' surface area and pore volumes after HTC, with 101 $m^2 g^{-1}$ (0.640 $cm^3 g^{-1}$) and 59 $m^2 g^{-1}$ (0.119 $cm^3 g^{-1}$) for HTC-CN and HTC-$CN_{Fe}$, respectively. Detailed pore size distributions for both samples after the hydrothermal carbonisation can be seen in Figure 4.13. HTC-$CN_{Fe}$ showed small mesopores and a minimal content of micropores after the hydrothermal carbonisation, while HTC-CN solely consisted of mesopores between 8 and 30 nm, which was also reflected in their total pore volumes. This difference in pore properties was assumed to originate due to the thicker tubes in HTC-$CN_{Fe}$, which had to be fitted in a

similarly sized monolith as CN-HTC, thus creating a more densely packed, stable cryogel with less pore volume/surface area.

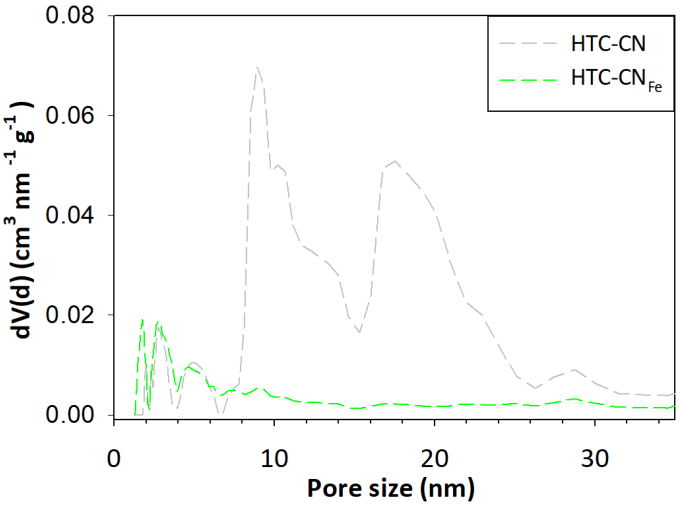


*Figure 4.13 Pore size distribution for a nitrogen doped cryogel and a nitrogen and iron doped cryogel version after the hydrothermal carbonisation (HTC).*

Another notable difference was found in the carbogels' elemental composition after the hydrothermal carbonisation (Table 4.6), where the presence of ferric iron slightly increased the carbon content, while decreasing the oxygen and nitrogen content as well as incorporating 0.54 at% of iron. This alteration in composition again supported the assumption that ferric iron acts as a catalyst, by accelerating the formation of carbon particles (higher C content) and the denaturation of ovalbumin, leaving less time for the Maillard reactions to occur and nitrogen to be incorporated (lower N content).

*Table 4.6 Elemental composition determined via XPS for a nitrogen doped cryogel and an additional nitrogen/iron doped version after the hydrothermal carbonisation.*

| Sample | C | O | N | Fe |
|---|---|---|---|---|
| HTC-CN | 63.50 | 31.54 | 4.96 | - |
| HTC-CN$_{Fe}$ | 69.76 | 25.49 | 4.21 | 0.54 |

FT-IR spectra were recorded for HTC-CN and HTC-CN$_{Fe}$ after the hydrothermal carbonisation, showing typical bonds for hydrothermally treated carbons (Figure 4.14). Both FT-IR spectra, for HTC-CN and HTC-CN$_{Fe}$, exhibited fairly similar peaks, starting with a broad peak around 3280 cm$^{-1}$ corresponding to O-H bonded stretching vibrations.[194] The region between 3000-2800 cm$^{-1}$ indicated N-H and C-H stretching vibration bonds,[5] which were slightly more pronounced in HTC-CN, possibly due to the higher nitrogen content. Peaks in the region of 1700-1400 cm$^{-1}$ were attributed to carbonyl/carboxylic features, with 1658 cm$^{-1}$, 1626 cm$^{-1}$ and 1515 cm$^{-1}$ standing for amide C=O groups, C=O and conjugated/condensed oxygen containing groups, respectively.[117]

The spectral band between 1400-1000 $cm^{-1}$ indicated contributions from different pyridinic, pyridonic and pyrrolic structures, with a C-N bending mode around 1085 $cm^{-1}$.[195] C-H out of plane bending modes were assigned to the region of 900-700 $cm^{-1}$, reflecting a variety of nitrogen containing aromatic groups.[196] Considering the overall similar bonding, the presence of ferric iron was suggested to not drastically alter the cryogels molecular components/structure.

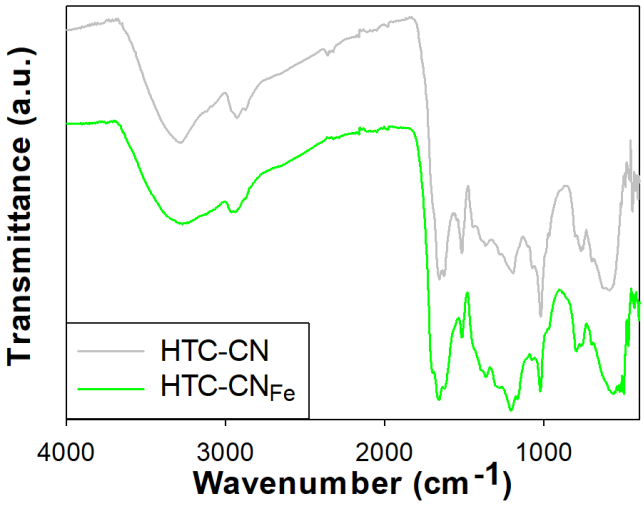


*Figure 4.14 FT-IR spectra for a pure carbogel HTC-CN and an iron doped carbogel HTC-$CN_{Fe}$ after hydrothermal carbonisation.*

### 4.2.2 Changes in carbogel structure due to the presence of ferric iron

The most significant difference between the metal-free version CN and the additional iron containing sample $CN_{Fe}$ remained in their differing surface area after the pyrolysis at 1000 °C under a mixed atmosphere of $N_2$ and compressed air, with 854 $m^2$ $g^{-1}$ and 1271 $m^2$ $g^{-1}$ for CN and $CN_{Fe}$, respectively. As also evident in the pore size distribution in Figure 4.15, $CN_{Fe}$ showed a higher micropore volume with a total pore volume of 0.761 $cm^3$ $g^{-1}$, whereas CN also consisted of larger mesopores with a total pore volume of 0.722 $cm^3$ $g^{-1}$ (Table 4.2).

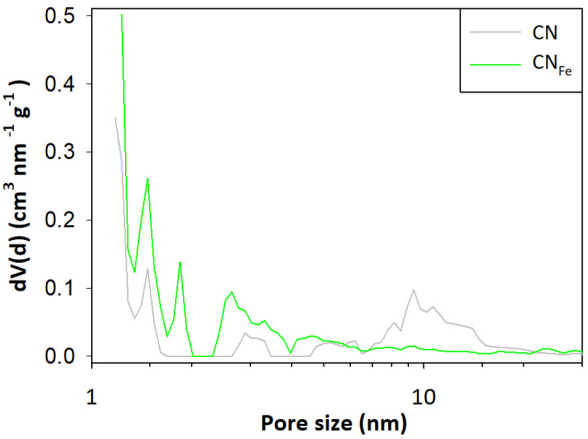


*Figure 4.15 Pore size distribution for a nitrogen doped carbogel and a nitrogen/iron doped version after the pyrolysis at 1000 °C under a mixed atmosphere of $N_2$/air (corresponding to 2% of $O_2$).*

Similar to the elemental composition after the hydrothermal carbonisation, $CN_{Fe}$ consisted of a higher carbon content at the expense of a lower amount of oxygen and nitrogen (Table 4.3). The iron content in $CN_{Fe}$ drastically decreased after the pyrolysis to 0.05 at% from 0.54 at% after the HTC. As the elemental content was determined via XPS, which is a surface analysis technique, bulk composition can greatly vary. Thus, inductively coupled plasma optical emission spectrometry (ICP-OES) was carried out for $CN_{Fe}$ after the pyrolysis to determine the iron concentration in the bulk of the sample, which was found to be considerably higher with 2.7 wt%.

To further investigate the role of iron during the high temperature pyrolysis, HTC-$CN_{Fe}$ was pyrolysed additionally at 400, 600 and 800 °C under a mixed atmosphere of $N_2$/air. TEM micrographs (Figure 4.16) revealed a similar structure for all carbogels as well as the cryogel, made up of nanowires to form a coral like construct. Few crystalline nanoparticles with a size of around 5 nm were found in the pyrolysed carbogels $CN_{Fe}$-400, $CN_{Fe}$-600 and $CN_{Fe}$-800. Particles in $CN_{Fe}$-400 exhibited a larger lattice distance (0.34 nm) as compared to $CN_{Fe}$-600 and $CN_{Fe}$-800 (0.25 nm). In the cryogel (Figure 4.16a) as well as the carbogel pyrolysed at 1000 °C (Figure 4.4b), no nanoparticles could be detected, which would have been clearly visible at high magnifications.

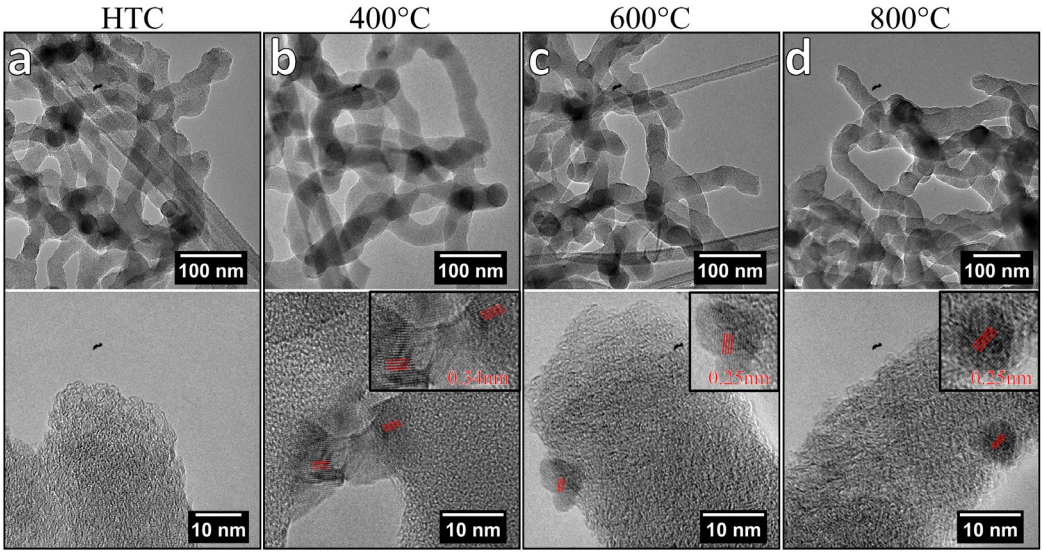


*Figure 4.16 TEM micrographs for nitrogen and iron doped carbogel $CN_{Fe}$, after the hydrothermal carbonisation (a), and after the high temperature pyrolysis under a mixed atmosphere of $N_2$/air at 400 °C (b), 600 °C (c) and 800°C (d).*

Additionally, in situ TEM was carried out for the HTC-$CN_{Fe}$ cryogel under vacuum with a heating rate of 50 °C/min up to a pyrolysis temperature of 1000 °C. Before the start of the in situ experiment, STEM EDX did not detect any distinct iron particles in the cryogel but showed a uniform distribution of Fe throughout the whole network structure. Figure 4.17 displays TEM micrographs taken in situ, where the formation of small iron

nanoparticles was observed above temperatures of 400 °C. With increasing temperature, the number of small nanoparticles increased with particle agglomeration observed at temperatures above 900°C. Due to rapid and continuous movement of the particles, tracking of the formation of a single particle was not possible.

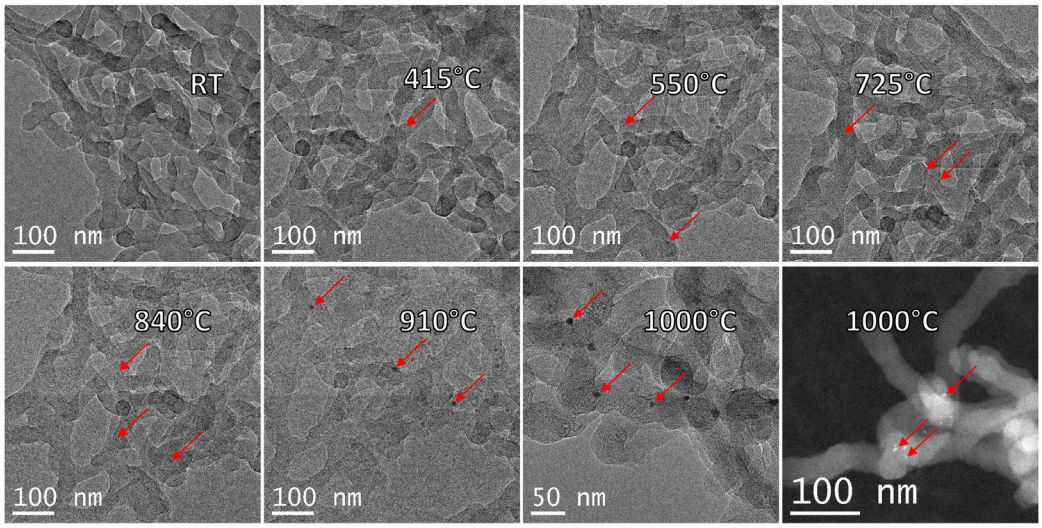


*Figure 4.17 In situ TEM micrographs of a nitrogen and iron doped cryogel (RT) under vacuum with a heating rate of 50 °C/min up to 1000 °C and STEM EDX image after the pyrolysis. Red arrows display exemplary iron particles.*

Marsh et al.[197] also observed movement of iron particles via TEM, which they described to channel or tunnel through the carbon matrix and related this to a simultaneous graphitisation process of the carbon matrix. Similarly, the diffusion or migration of iron (often iron oxide) through the carbon matrix was reported to change the structure and subsequently promote graphitisation.[186,189,197] STEM EDX confirmed that the observed particles consisted of iron. While no formed particles could be detected in the ex situ TEM images for the sample pyrolysed at 1000 °C, the largest and most particles were observed at 1000 °C during the in situ TEM. This discrepancy can be explained by the difference in pyrolysis atmosphere, which was a mix of $N_2$/air for the ex situ and vacuum for the in situ TEM. Additionally, for the sample imaged ex situ, the pyrolysis temperature of 1000 °C was held for 2 hours, while the in situ TEM imaging was stopped as soon as 1000 °C was reached. This observation again confirms the crucial role of oxygen in the pyrolysing atmosphere. Similarly, a control sample pyrolysed under pure nitrogen atmosphere at 1000 °C ($CN_{Fe}$-$N_2$) also contained iron particles as was confirmed via STEM EDX (Figure 4.18).

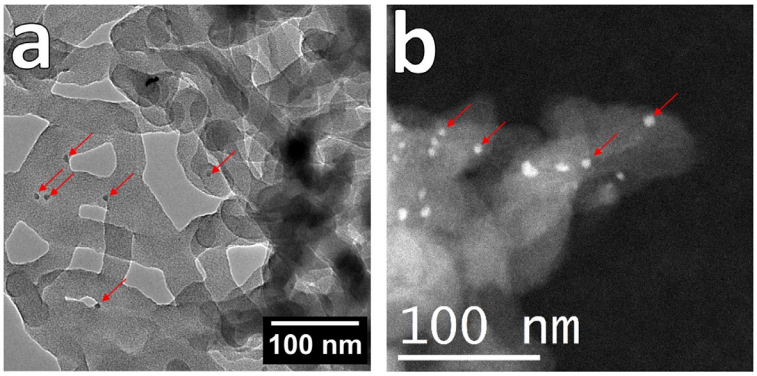


*Figure 4.18 a) TEM micrograph and b) STEM EDX image of a nitrogen and iron doped carbogel $CN_{Fe}$ pyrolysed at 1000 °C under inert $N_2$ atmosphere ($CN_{Fe}$-$N_2$). Red arrows display exemplary iron particles.*

The absence of any distinct iron particles (via TEM) as well as the low surface iron concentration (0.05 at% via XPS) after pyrolysis at 1000 °C under a mixed $N_2$/air atmosphere, suggested that the formed iron oxide particles (presence confirmed in Figure 4.16) leave the sample after formation possibly due to a reaction with the alumina crucible. This assumption was confirmed after the pyrolysis, where a red precipitate was found on the crucible containing the nitrogen and iron doped version (Figure 4.19), which, due to its colour and the elements present, was assumed to be iron oxide.

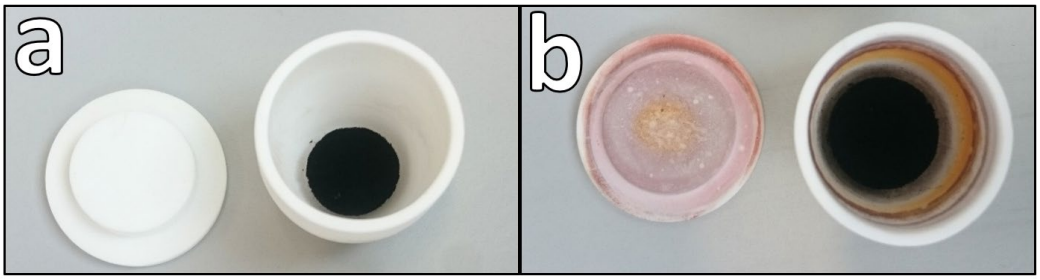


*Figure 4.19 Crucibles after the high temperature pyrolysis of a) a pure carbogel, CN and b) an iron doped version, $CN_{Fe}$ at 1000 °C under a mixed atmosphere of $N_2$ and compressed air (corresponding to 2% of $O_2$).*

Surface area, total pore volume as well as meso- and micropore volume were determined via nitrogen sorption isotherms (Figure 4.20), values are presented in Table 4.7.

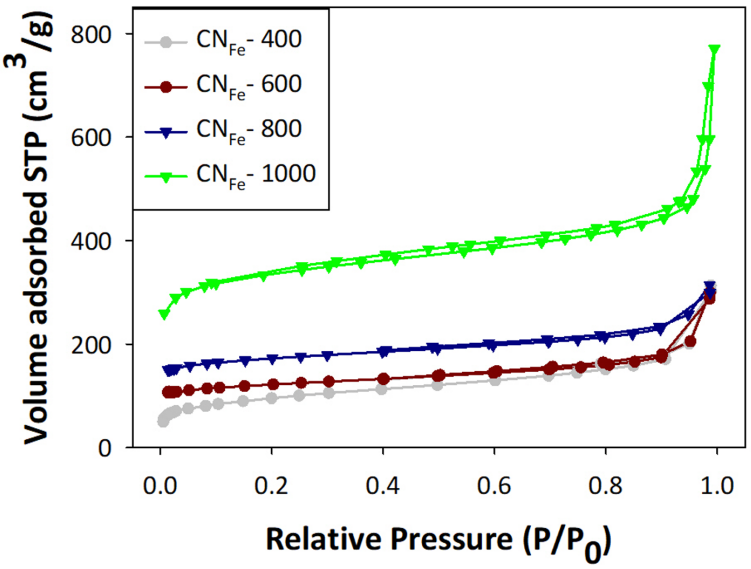


*Figure 4.20 Nitrogen sorption isotherms obtained at 77 K of nitrogen and iron doped carbogels pyrolysed at 400, 600, 800 and 1000 °C under a mixed atmosphere of $N_2$/air.*

Additionally, to further confirm the influence of oxygen in the atmosphere on the surface area , a control sample pyrolysed at 1000 °C under pure nitrogen atmosphere is also listed as $CN_{Fe}$-$N_2$ in Table 4.7. Simultaneously to the increasing pyrolysis temperature, the surface area and pore volumes were also found to increase. Regardless of the materials nature and composition, this trend is typically observed in carbon materials upon increased pyrolysis temperature, due to the release of volatile matter and gases (for example $CO_2$) which can act as activating agents, etching the surface and creating pores, or due to the release of pore blocking substances owing to thermal degradation.[198,199] The sample pyrolysed at 1000 °C, but under inert $N_2$ atmosphere was found to exhibit a similar surface area to $CN_{Fe}$-400, though with a slightly higher pore volume, for both micro- and mesopores, but significantly lower than the sample pyrolysed at 1000 °C under $N_2$/air atmosphere. This observation clearly confirmed that the presence of oxygen played a crucial role during the pyrolysis by creating so called hole burning, as has been described in chapter 3.2. Additionally, possible leftovers of iron(III)chloride could have acted as a chemical activation agent creating an even higher surface area for $CN_{Fe}$.[200,201] Decomposition of the iron salt at high temperatures is suggested to generate iron oxides (as confirmed via TEM, Figure 4.16), especially in the presence of air/$O_2$, which can act as a catalyst to etch neighbouring carbon and/or nitrogen atoms to CO/NO.[202] This process, similarly to hole burning due to the presence of oxygen, created new micropores and enlarged already existing pores, thus increasing the total pore volume.

*Table 4.7 BET surface area and pore volumes for a nitrogen and iron doped cryogel and carbogels pyrolysed at 400, 600, 800 and 1000 °C under a mixed atmosphere of $N_2$/air as well as pyrolysed at 1000 °C under inert $N_2$ atmosphere.*

| Sample | Surface area [$m^2$ $g^{-1}$] | $V_{tot}$ [$cm^3$ $g^{-1}$] | $V_{meso}$ [$cm^3$ $g^{-1}$] | $V_{micro}$ [$cm^3$ $g^{-1}$] |
|---|---|---|---|---|
| $CN_{Fe}$-HTC | 59 | 0.119 | 0.112 | 0.007 |
| $CN_{Fe}$-400 | 335 | 0.223 | 0.133 | 0.090 |
| $CN_{Fe}$-600 | 461 | 0.291 | 0.140 | 0.151 |
| $CN_{Fe}$-800 | 657 | 0.399 | 0.220 | 0.179 |
| $CN_{Fe}$-1000 | 1271 | 0.761 | 0.334 | 0.427 |
| $CN_{Fe}$-$N_2$ | 337 | 0.270 | 0.157 | 0.113 |

The elemental composition of the carbogels pyrolysed at different temperatures was determined via XPS and is presented in Table 4.8, including the nitrogen and iron doped cryogel before pyrolysis ($CN_{Fe}$-HTC) as well as the sample pyrolysed under inert $N_2$ atmosphere at 1000 °C ($CN_{Fe}$-$N_2$). A steady trend was found, where the carbon content increased, while the oxygen, nitrogen and iron amount decreased with rising pyrolysis temperature. A slightly higher oxygen content was determined for the carbogel pyrolysed at 1000 °C with 8.43 at% as compared to the sample pyrolysed at 800 °C (6.24 at%), though no relevance was given to this finding, as the trend was still prevalent in the nitrogen and iron content. As results are based on single point measurements, minor discrepancies can be expected and values should not be taken as definite, but rather as trends. The carbogel pyrolysed under inert $N_2$ atmosphere exhibited the lowest amount of oxygen content and a slightly higher nitrogen content as compared to $CN_{Fe}$-1000, due to less etching of atoms in the absence of oxygen in the atmosphere, while similarly only trace amounts of iron were detected. The increase in carbon and decrease in other elements (oxygen and nitrogen) is further a typical phenomenon at increasing pyrolysis temperatures, due to the carbonisation of the sample where oxygen, hydrogen and nitrogen is lost owing to breakage of weak bonds within the material.[199]

*Table 4.8 Elemental composition in at% determined via XPS for a nitrogen and iron doped cryogel and carbogels pyrolysed at 400, 600, 800 and 1000 °C under a mixed atmosphere of $N_2$/air as well as pyrolysed at 1000 °C under inert $N_2$ atmosphere.*

| Sample | C | O | N | Fe |
|---|---|---|---|---|
| $CN_{Fe}$-HTC | 69.76 | 25.49 | 4.21 | 0.54 |
| $CN_{Fe}$-400 | 79.67 | 16.42 | 3.72 | 0.19 |
| $CN_{Fe}$-600 | 89.04 | 7.33 | 3.49 | 0.15 |
| $CN_{Fe}$-800 | 90.55 | 6.24 | 3.05 | 0.16 |
| $CN_{Fe}$-1000 | 90.41 | 8.43 | 1.10 | 0.05 |
| $CN_{Fe}$-$N_2$ | 93.29 | 4.77 | 1.83 | 0.11 |

Deconvolution of the C1s and O1s spectra (Figure 4.21) revealed clear differences between the cryogel and the carbogels, due to the lack of pyrolysis and thus graphitisation of material after the hydrothermal carbonisation. The greatest amount was found to correspond to $sp^2$ C-C/C=C bonds around 284.6 eV, followed by functional groups C-OH around 285.5 eV and C-N around 286.5 eV.[148] While the carbogels above 600 °C exhibited the typical distribution of carbon species, the cryogel and carbogel pyrolysed at 400 °C included additional carbonate (288.4 eV).[203] Three dominant peaks were found in the O1s spectra around 531 eV, 532 eV and 533.5 eV corresponding to oxygen functionalities C=O (also possible quinone groups), C-O and O=C-O, respectively.[183] The cryogel consisted of C=O and additional OH functionalities (533 eV).[203]

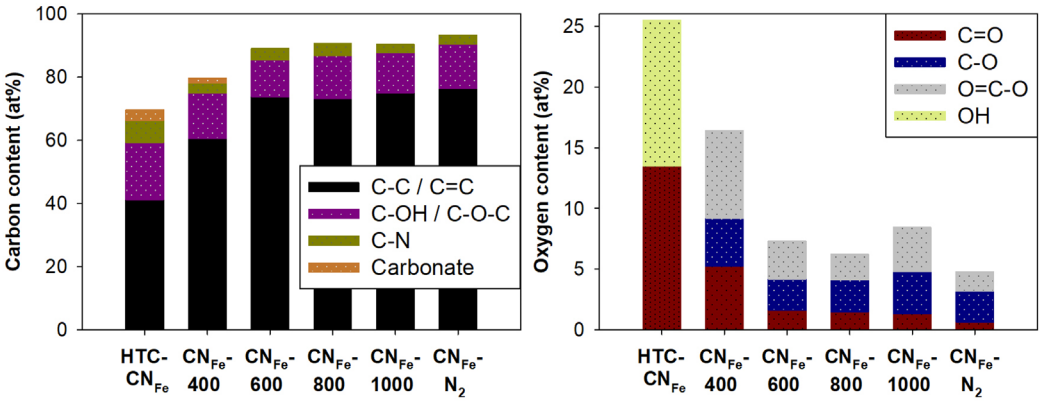


*Figure 4.21 Distribution of carbon and oxygen bonding for a nitrogen and iron doped cryogel and carbogels pyrolysed at 400, 600, 800 and 1000 °C under a mixed atmosphere of $N_2$/air as well as pyrolysed at 1000 °C under inert $N_2$ atmosphere.*

Deconvolution of the N1s spectra revealed the presence of four different nitrogen species, pyridinic nitrogen, pyrrolic nitrogen, graphitic nitrogen and N-oxide functionalities around 398.1 eV, 399.8 eV, 400.7 eV and 403 eV, respectively, as can be seen in Figure 4.22.[148] While up to a temperature of 600 °C the cryo- and carbogels consisted of pyridinic, pyrrolic and graphitic N, the composition changed for the carbogels pyrolysed at 800 and 1000 °C to pyridinic and graphitic N as well as N-oxides. The cryogel exhibited the largest amount of pyrrolic nitrogen, which gradually declined with rising temperatures up to 600 °C, being converted into pyridinic N, while the amount of graphitic N remained similar. At temperatures above 800°C, all pyrrolic nitrogen had been transformed into pyridinic nitrogen, which was subsequently converted into graphitic nitrogen,[204] representing the largest amount of nitrogen species in the higher temperature pyrolysed samples.

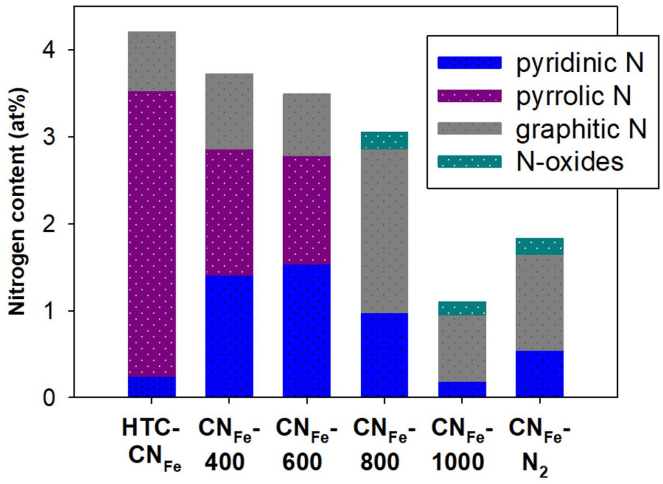


*Figure 4.22 Distribution of nitrogen species, pyridinic N, pyrrolic N, graphitic N and N-oxides for a nitrogen and iron doped cryogel and carbogels pyrolysed at 400, 600, 800 and 1000 °C under a mixed atmosphere of $N_2$/air as well as pyrolysed at 1000 °C under inert $N_2$ atmosphere.*

Deconvolution of the Fe2p$_{3/2}$ spectra (Figure 4.23), revealed the presence of ferric iron in two phases, in all carbogels with peaks around 711 and 714 eV and the typical satellite peak around 718-719 eV (except for $CN_{Fe}$-1000, possibly due to the low Fe content).[205,206] Satellite peaks, occurring at a higher binding energy than the main peak, are usually related to "shake-up" or "shake-off" processes during electron ejection due to energy losses owing to abrupt alterations in effective charge.[207] The two phases at 711 eV and 714 eV were attributed to ferric iron in $Fe_2O_3$,[208,209] the latter had a slight upshift as compared to values reported, which can be ascribed to the functionalisation of the iron atoms within the carbon framework.[210,211] According to other reports, the first two peaks in the Fe2p$_{3/2}$ spectra could also be attributed to ferric iron in different configurations, such as octahedral or tetrahedral sites with possible other binding partners than oxygen, such as nitrogen or carbon.[212] The cryogel, HTC-$CN_{Fe}$ showed a slight downshift in the binding energies with the main peaks at 710 and 713.5 eV and the satellite peak around 717 eV, still suggesting the presence of ferric iron, but in a different configuration/binding partner, values matched with those reported for $FeCl_3$.[213] Though no residue chlorine was detected via XPS, trace amounts could have remained within the sample after washing, or alternatively, iron bound with carbon, oxygen or nitrogen during the hydrothermal carbonisation, but in a similar configuration as iron(III)chloride, thus yielding the same peaks positions in the Fe2p$_{3/2}$ spectra. The carbogel pyrolysed under inert $N_2$ atmosphere only exhibited one distinct peak around 710 eV, which also suggested the presence of ferric iron, though coordinated in a more similar way as in the cryogel, not as iron oxide as in the samples pyrolysed under a mixed atmosphere of $N_2$/air.

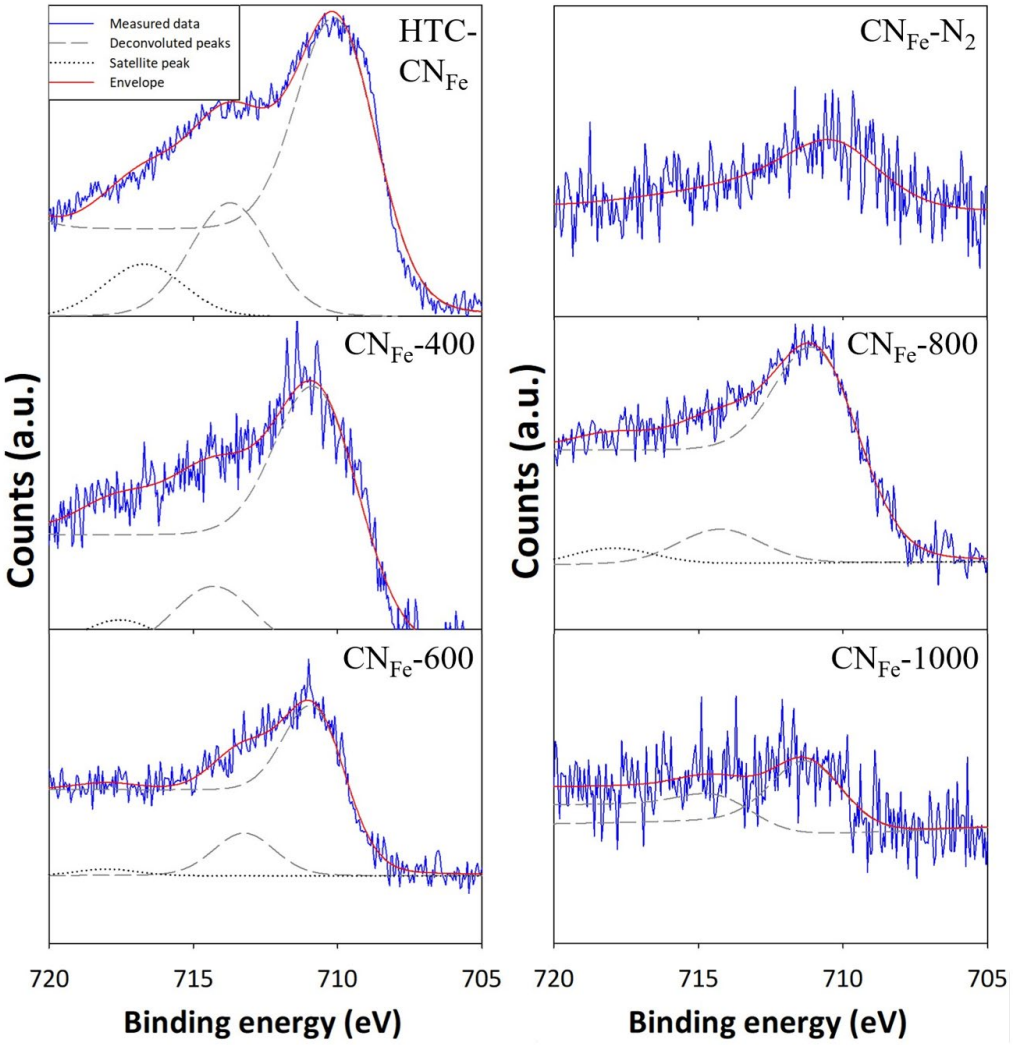


*Figure 4.23 Deconvoluted Fe2p$_{3/2}$ XPS spectra for a nitrogen and iron doped cryogel and carbogels pyrolysed at 400, 600, 800 and 1000 °C under a mixed atmosphere of $N_2$/air as well as pyrolysed at 1000 °C under inert $N_2$ atmosphere.*

To get a better insight into the crystallinity/amorphous character of the carbogels, x-ray diffraction spectra were recorded for the carbogels pyrolysed under a mixed atmosphere of $N_2$/air. All samples exhibited a wide peak around 24° and 43°, as can be seen in Figure 4.24. The peaks were attributed to the typical diffraction of graphite, (002) around 25° and (100) or (101) expected around 42° and 44°, respectively, where an increase in disorder of the graphite structure can cause broadening and shifting of the peaks.[214,215] As the peaks were rather broad and faint, but present in the spectra for all samples, a mix of turbostratic and amorphous carbon was assumed. High intensities observed below 15° were attributed to micropores within the carbon.[172] For the two samples treated above 800 °C, additional peaks were found, around 30.2°, 33.2°, 35.6°, 54°, 57.5° and 62° which were attributed to the reflections of the crystal planes of iron oxide ($Fe_2O_3$).[172,216,217] Though iron particle growth was observed via the in situ TEM (Figure 4.17) starting from

400 °C onwards, only very few particles were found below 700 °C, explaining the absence of any distinct peaks in the XRD spectra of $CN_{Fe}$-400 and $CN_{Fe}$-600.

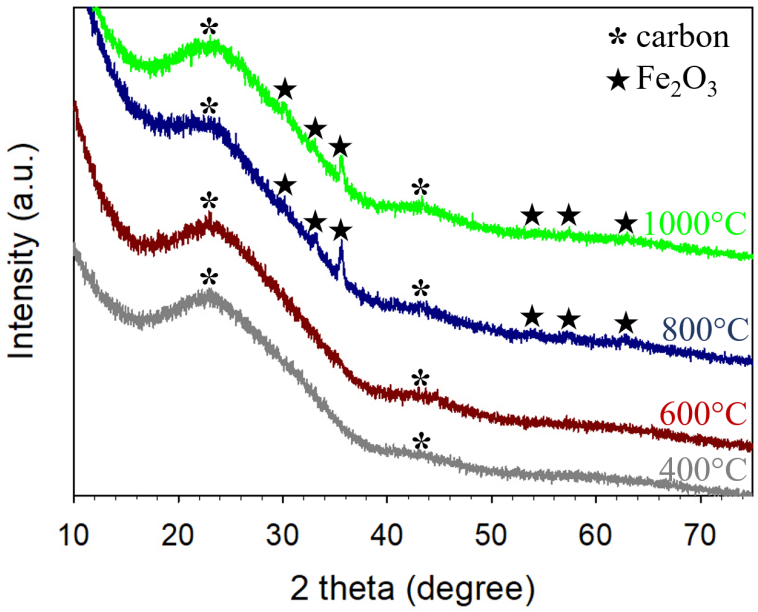


*Figure 4.24 X-ray diffraction spectra for nitrogen and iron doped carbogels pyrolysed at 400, 600, 800 and 1000 °C under a mixed atmosphere of $N_2$ and air.*

To sum up the above presented results, it was found that ferric iron was homogeneously distributed within the carbon material after the hydrothermal carbonisation. During the high temperature pyrolysis under a mixed atmosphere of $N_2$ and air (corresponding to 2 % of $O_2$), decomposition of the iron generated iron oxide ($Fe_2O_3$), which presence was confirmed via TEM (Figure 4.16), XPS (Figure 4.23) and XRD (Figure 4.24). Once formed, the iron oxide moved through the material agglomerating with other iron oxide particles and at the same time acting as a catalyst to etch neighbouring carbon and/or nitrogen atoms creating surface area as well as catalysing graphitisation of the carbon (Raman, Figure 4.8) before leaving the sample due to reaction with/precipitation on the crucible (Figure 4.19).

After the pyrolysis, the iron concentration in the bulk of the material (2.7 wt%) was significantly higher than in the surface (0.05 at%), which was assumed to be due to surface Fe reacting with oxygen present in the pyrolysis atmosphere and eventually reacting with the alumina crucible, while most of the bulk Fe remained homogeneously distributed and coordinated to oxygen, nitrogen or carbon in the sample, which was also confirmed by the absence of any distinct iron particles in the TEM after pyrolysis at 1000 °C. A schematic depicting the proposed process of iron oxide particles forming while moving through the sample is shown in Figure 4.25.

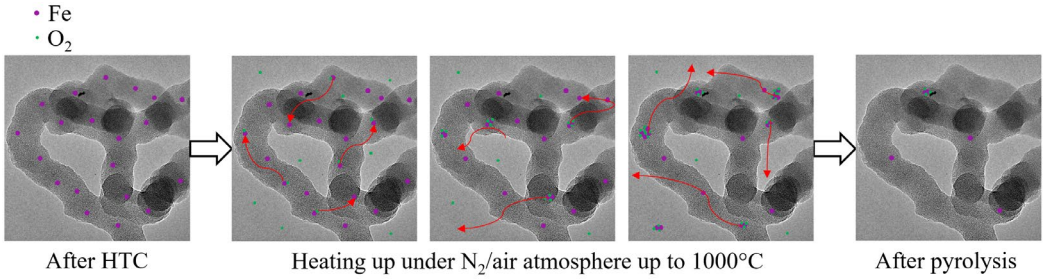


*Figure 4.25 Schematic depicting the proposed process of iron oxide particles forming in the material during high temperature pyrolysis under a mixed atmosphere of $N_2$/air.*

A comparison of the ORR performance in alkaline media between both carbogels pyrolysed at 1000 °C under either a mix of $N_2$/air or under inert $N_2$ atmosphere is shown in Figure 4.26. A drastic difference in the catalytic performance was observed, where $CN_{Fe}$-1000 exhibited a more positive onset potential of more than 100 mV as well as a lower limiting current. The electron transfer number and hydrogen peroxide yield were found to be 3.4 and 26.8 % for $CN_{Fe}$-$N_2$ and 3.9 and 7.2 % for $CN_{Fe}$-1000, respectively.

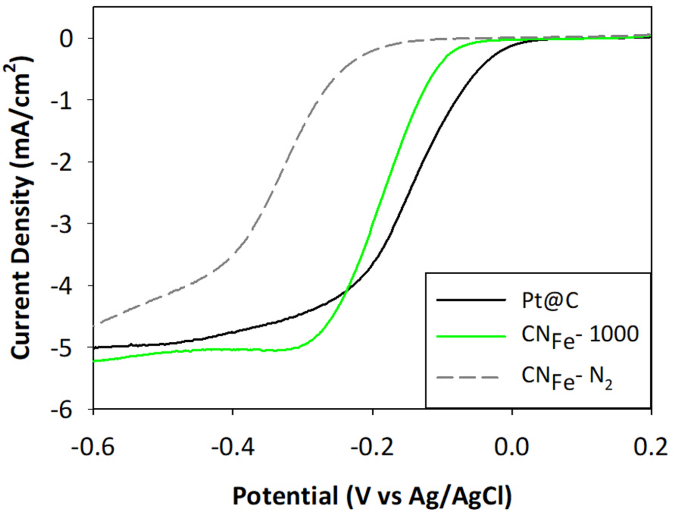


*Figure 4.26 Linear sweep voltammogram recorded in 0.1 M KOH with an RRDE setup at 1600 rpm for a commercially available platinum catalyst (60 wt% Pt@C) and nitrogen/iron doped carbogels pyrolysed at 1000 °C under a mixed atmosphere of $N_2$/air ($CN_{Fe}$-1000) and under inert $N_2$ atmosphere ($CN_{Fe}$-$N_2$).*

This difference suggested that, even though the nitrogen and iron content was higher in the sample pyrolysed under inert $N_2$ atmosphere, the significantly lower surface area and pore volume played a crucial role, offering less accessibility to the active sites. Furthermore, there is also a possibility of an altered combination of active sites present in $CN_{Fe}$-$N_2$, due to the absence of oxygen in the pyrolysis atmosphere inhibiting formation of iron oxide to the extent as was in $CN_{Fe}$-1000. Here, further investigations should be carried out to understand the formation of active sites in the absence of oxygen better. Further electrochemical testing in alkaline media of the carbogels pyrolysed at different

temperatures under a mixed atmosphere of $N_2$/air confirmed the above discussed observations and showed a clear trend, where increased temperature improved the catalytic performance (Figure 4.27). The onset potential increased in the order of pyrolysis temperature, with $CN_{Fe}$-1000 exhibiting the most positive onset potential, close to platinum. $CN_{Fe}$-800 displayed the same limiting current density as $CN_{Fe}$-1000, which could possibly be due to its marginally higher iron, but significantly higher nitrogen content, though with a lower surface area. Similar to the observed linear sweep voltammograms, electron transfer numbers and hydrogen peroxide yields increased and decreased, respectively, in the order of pyrolysis temperature, with the most favourable values exhibited by $CN_{Fe}$-1000, with 3.9 and 7.2 %, respectively.

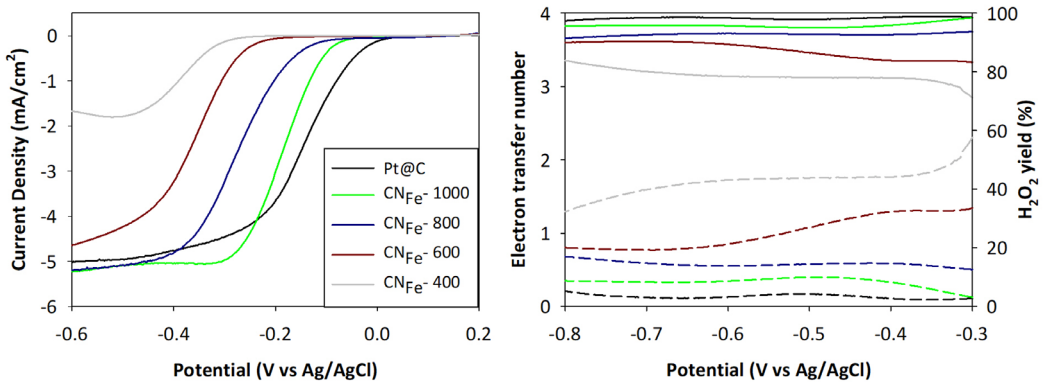


*Figure 4.27 Linear sweep voltammogram recorded in 0.1 M KOH with an RRDE setup at 1600 rpm for a commercially available platinum catalyst (60 wt% Pt@C) and nitrogen/iron doped carbogels pyrolysed at different pyrolysis temperatures, 400, 600, 800 and 1000 °C. Electron transfer number (solid lines) and hydrogen peroxide yield (dashed lines) calculated from the LSV disk and ring current.*

The Tafel plot for the lower current density range (low overpotential) of the carbogels pyrolysed at different temperatures and a commercial platinum standard can be seen in Figure 4.28. The Tafel slope can give an indication of the reaction kinetics and mechanism involved during the ORR, where a smaller slope attributes to a more favourable ORR performance/faster kinetics.[15] A similar slope was found for the platinum standard and $CN_{Fe}$-1000 with 65 and 61 mV $dec^{-1}$, respectively, suggesting both share the same ORR mechanism. Samples pyrolysed at a lower temperature exhibited higher Tafel slopes, possibly due to diminished active site accessibility owing to their lower surface area as well as reduced graphitisation owing to the lower pyrolysis temperature.

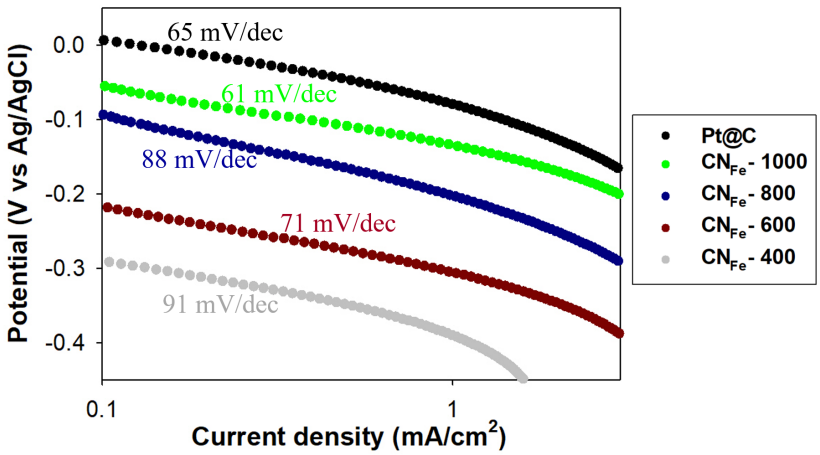


*Figure 4.28 Tafel plot for a commercially available platinum catalyst (60 wt% Pt@C) and nitrogen/iron doped carbogels pyrolysed at different pyrolysis temperatures, 400, 600, 800 and 1000 °C in 0.1 M KOH.*

To get a better overview over the different parameters discussed above, Figure 4.29 displays the correlation between surface area, nitrogen and iron content as well as electron transfer number for the samples pyrolysed at different temperatures and under different pyrolysing atmospheres. The carbogel pyrolysed under inert $N_2$ atmosphere exhibited a similar electrocatalytic activity as compared to the sample pyrolysed under $N_2$/air at 600 °C, which can be explained by the higher content of graphitic nitrogen as well as better graphitisation due to the higher pyrolysing temperature, which compensated for the lower surface area.

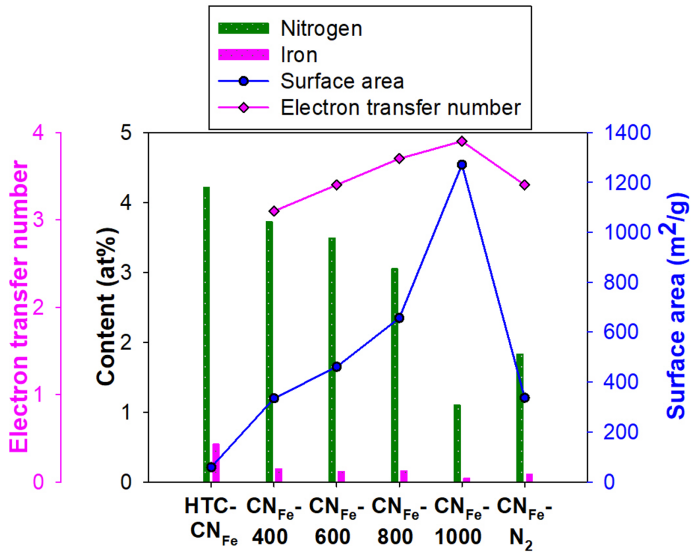


*Figure 4.29 Combination graph correlating the material's surface area and elemental content with the electrocatalytic activity (alkaline media) for a nitrogen and iron doped cryogel and carbogels pyrolysed at 400, 600, 800 and 1000 °C under a mixed atmosphere of $N_2$/air as well as pyrolysed at 1000 °C under inert $N_2$ atmosphere.*

## 4.3 Influence of heteroatom dopants sulphur and boron

After the successful incorporation of iron into the carbogel structure and its subsequent improvement of the ORR activity, the influence of other heteroatom dopants, namely sulphur and boron, on the N/Fe carbogel were investigated. For this, samples consisted of triple ($CN_{SFe}$ or $CN_{BFe}$) as well as fourfold ($CN_{SBFe}$) doping and were compared to the earlier discussed dual doped version, $CN_{Fe}$. All samples discussed in the following chapter were synthesised with ferric iron from iron(III)chloride corresponding to 1 mmol of dopant and were pyrolysed under a mixed atmosphere of $N_2$/air (corresponding to 2 % $O_2$).

SEM and TEM images for the standard version, $CN_{Fe}$, and the additionally doped carbogels $CN_{SFe}$, $CN_{BFe}$ and $CN_{SBFe}$ can be seen in Figure 4.30. A similar coral like morphology made up of nanowires was observed for all four carbogels, besides this, a inhomogeneous morphology was found in both materials containing additional boron with broken nanowires and particles (Figure 4.31).

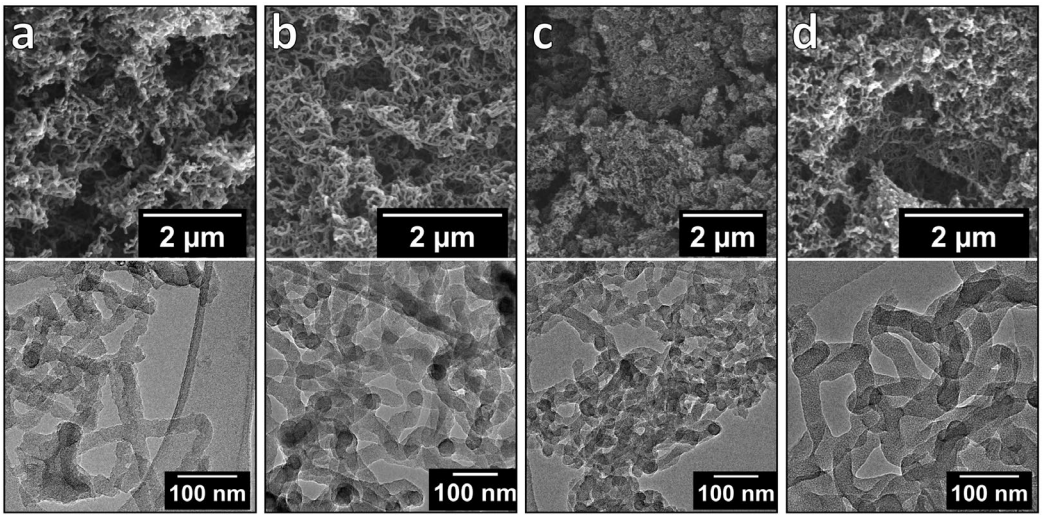


*Figure 4.30 SEM and TEM micrographs of nitrogen and iron containing carbogels, $CN_{Fe}$ (a), pyrolysed at 1000 °C doped with additional sulphur, $CN_{SFe}$ (b), boron, $CN_{BFe}$ (c) or sulphur and boron, $CN_{SBFe}$ (d).*

These heterogeneous structures resembled the particle like morphology discovered in the metal-free versions containing boron, discussed in chapter 3.3, where boric acid was found to catalyse the dehydration of sugars and thus abrogated the structure directing role of ovalbumin. Considering this, a competition between the iron salt or ovalbumin and boric acid catalysing the reaction mechanism and dominating the structure formation during the hydrothermal carbonisation was assumed.

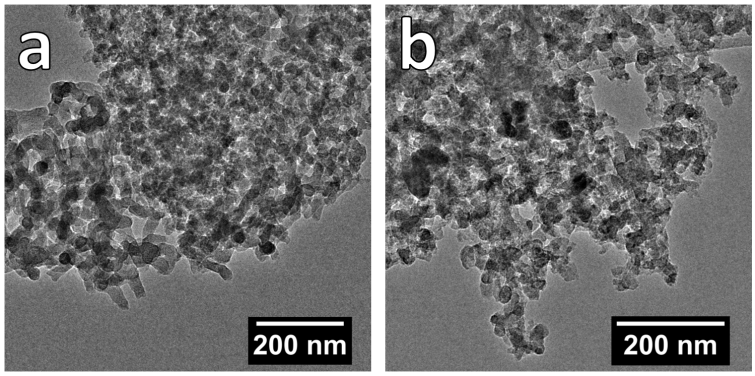


*Figure 4.31 TEM micrographs of nitrogen and iron containing carbogels doped with additional boron, $CN_{BFe}$ (a) and sulphur and boron, $CN_{SBFe}$ (b) depicting the presence of a heterogeneous morphology.*

Averaged surface areas and pore volumes determined via three independent high temperature pyrolyses are shown in Table 4.9 and confirmed the microscopic observations. The addition of sulphur caused only a slight decrease in surface area and pore volume, similar to the metal-free version (chapter 3.3), which again suggested that the sulphur precursor did not drastically interfere with the structure formation of the cryogel during the HTC. Whereas the boron containing samples $CN_{BFe}$ and $CN_{SBFe}$ exhibited a more drastic reduction in surface area concurrent with a significant increase in mesopore volume.

*Table 4.9 Average BET surface areas and pore volumes for iron doped carbogels including different heteroatoms after the high temperature pyrolysis at 1000 °C.*

| Sample | Surface area [$m^2$ $g^{-1}$] | $V_{tot}$ [$cm^3$ $g^{-1}$] | $V_{meso}$ [$cm^3$ $g^{-1}$] | $V_{micro}$ [$cm^3$ $g^{-1}$] |
|---|---|---|---|---|
| $CN_{Fe}$ | 1223 ± 65 | 0.688 ± 0.052 | 0.264 ± 0.057 | 0.424 ± 0.034 |
| $CN_{SFe}$ | 1027 ±69 | 0.570 ± 0.083 | 0.202 ± 0.062 | 0.368 ± 0.033 |
| $CN_{BFe}$ | 769 ± 40 | 0.925 ± 0.081 | 0.681 ± 0.078 | 0.244 ± 0.014 |
| $CN_{SBFe}$ | 672 ± 20 | 1.131 ± 0.091 | 0.927 ± 0.101 | 0.204 ± 0.015 |

Nitrogen sorption isotherms and pore size distributions for the doped carbogels can be seen in Figure 4.32, where the difference in surface area, but especially in mesopore volume became clear. The surface areas for the boron containing samples were only slightly higher as compared to their metal-free counterparts (669 $m^2$ $g^{-1}$ for $CN_B$ and 605 $m^2$ $g^{-1}$ for $CN_{SB}$) due to the additional presence of some coral like nanowires catalysed by the presence of iron salt. It was assumed that the drastic increase in mesopore volume was caused by the inhomogeneous structure of the nitrogen and iron carbogels containing additional boron, creating large mesopores where the different structures are connected.

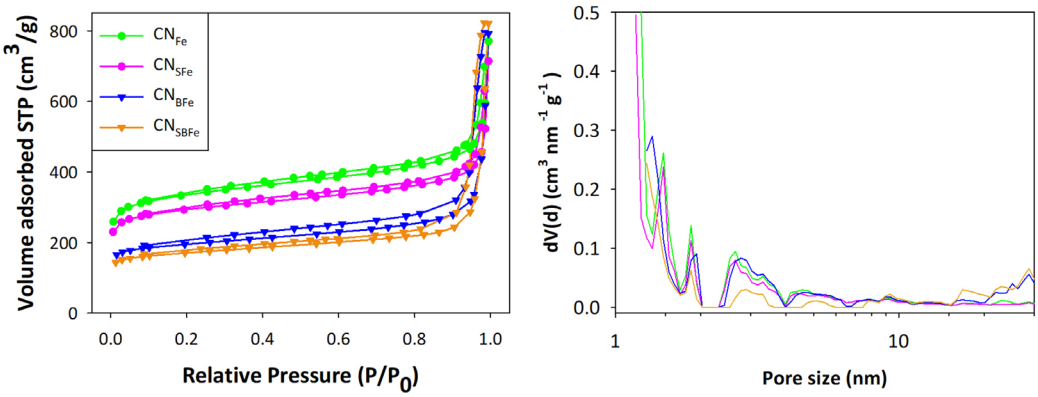


*Figure 4.32 Nitrogen sorption isotherms obtained at 77 K and pore size distribution for nitrogen and iron carbogels, $CN_{Fe}$, pyrolysed at 1000 °C doped with additional sulphur ($CN_{SFe}$), boron ($CN_{BFe}$) or sulphur and boron ($CN_{SBFe}$).*

A difference was also observed in the elemental composition determined via XPS (Table 4.10), where $CN_{Fe}$ and $CN_{SFe}$ exhibited similar levels of carbon, oxygen, nitrogen and iron, whereas samples containing boron showed a lower carbon content and a slightly higher doping of N and Fe, while amounts of oxygen, sulphur and boron remained roughly consistent regardless of dual, triple or fourfold doping. Similar to the metal-free versions discussed in chapter 3.3, the presence of boric acid enabled the incorporation of a higher nitrogen content and, in this case, also of iron, both amounts were roughly doubled as compared to without boric acid. Considering that the morphology was found to be inhomogeneous for the boron containing samples, those parts catalysed/structure directed by boric acid instead of the iron salt or ovalbumin, incorporated a higher content of nitrogen and iron as the precursors could be solely utilised as dopant source. Further, a study also reported that the presence of boric acid could stabilise the network structure and thus avoid loss of nitrogen during high temperature treatments.[59] Taking this into consideration, a possible stabilisation of the elemental framework by boric acid could have also caused the increased nitrogen and iron content and lower surface area, by preventing etching of the atoms during the pyrolysis.

*Table 4.10 Elemental composition determined by XPS in at% for iron doped carbogels pyrolysed at 1000 °C.*

| Sample | C | O | Fe | N | S | B |
|---|---|---|---|---|---|---|
| $CN_{Fe}$ | 86.57 | 11.49 | 0.06 | 1.88 | - | - |
| $CN_{SFe}$ | 85.29 | 11.17 | 0.07 | 1.47 | 2.00 | - |
| $CN_{BFe}$ | 82.99 | 12.65 | 0.11 | 3.36 | - | 0.89 |
| $CN_{SBFe}$ | 82.41 | 11.92 | 0.14 | 2.86 | 1.96 | 0.71 |

Deconvolution of the high resolution C1s spectra revealed a similar distribution of carbon species for all doped carbogels, also in comparison to the corresponding metal-free

versions with the largest fraction being $sp^2$ carbon bonds. O1s spectra showed a slight increase in C=O at the cost of O=C-O bonds for the boron containing samples as compared to the non-boron and all metal-free carbogels. The different amounts of carbon and oxygen species in the heteroatom doped iron carbogels can be seen in Figure 4.33.

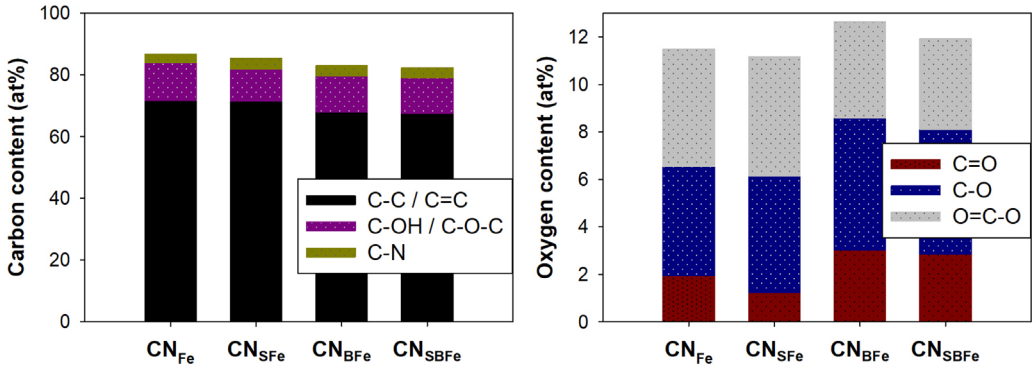


*Figure 4.33 Distribution of carbon and oxygen species in nitrogen/iron carbogels doped with additional sulphur and/or boron pyrolysed at 1000 °C under a mixed atmosphere of $N_2$/air.*

Deconvolution of the N1s spectra revealed the presence of pyridinic, graphitic and N-oxide species in all samples (Figure 4.34), with the largest fraction being graphitic nitrogen in all carbogels, the boron doped materials exhibited the highest amount of pyridinic nitrogen with around 25 %. As compared to the corresponding metal-free versions (chapter 3.3), the amount of graphitic nitrogen increased at the cost of pyridinic nitrogen, which suggested that the presence of iron aided the formation of a more graphitised carbon framework, incorporating graphitic N.

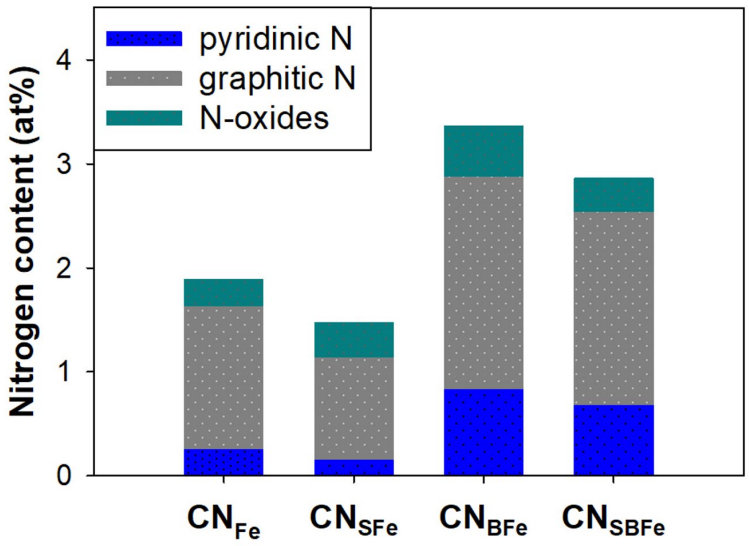


*Figure 4.34 Distribution of nitrogen species, pyridinic N, graphitic N and N-oxides for nitrogen/iron carbogels doped with additional sulphur and/or boron pyrolysed at 1000 °C under a mixed atmosphere of $N_2$/air.*

Raman spectroscopy was carried out to get a better insight into the graphitisation and defects/disorders of the four carbogels, spectra are shown in Figure 4.35. All samples exhibited the characteristic D- and G-band around 1320 and 1590 $cm^{-1}$. An additional peak around 2620 $cm^{-1}$ was found in $CN_{Fe}$ corresponding to the second order/overtone of the D-band, also called 2D peak, typical in graphene or turbostratic samples.[218] The lack of a clear 2D peak in the other carbogels suggested a higher degree of graphitisation in $CN_{Fe}$. Deconvolution of the D- and G-band resulted in three peaks for all four carbogels, with the third small peak between 1830 to 1865 $cm^{-1}$, which was attributed to the D' peak, another feature induced by disorder.[184] Though the D' peak usually occurs around 1620 $cm^{-1}$ in more ordered carbon samples,[219] an upshift was observed due to the amorphous nature of the carbogels and thus the very broad D- and G-bands. As mentioned earlier, the $I_D/I_G$ ratio can indicate the degree of disorder in a carbon structure. While $CN_{Fe}$ exhibited the lowest ratio of 1.6, the inclusion of sulphur caused a slight increase to 1.8, suggesting a slight interference of sulphur during the graphitisation process as well as its larger atomic size creating defects. Ratios for samples containing boron were found to be 1.8 and 2.0 for $CN_{BFe}$ and $CN_{SBFe}$, respectively, again indicating that boric acid interferes/competes with the iron salt and causes a less favourable degree of graphitisation and the additional incorporation of sulphur causes another increase in defects. These findings in combination with results discussed earlier supported again the assumption that boric acid acts as a catalyst competing with the iron salt during the hydrothermal carbonisation, which caused parts of the morphology to match with the non-boron carbogels (nanowired structure) and parts to be similar to the metal-free versions (particle structure). Overall, an improvement of the $I_D/I_G$ ratio was observed for the iron containing carbogels as compared to their metal-free counterparts presented in chapter 3.3, which exhibited values of 2.0 for the non-sulphur samples (CN and $CN_B$) and 2.1 if sulphur was incorporated ($CN_S$ and $CN_{SB}$). This clear trend again suggested that iron aids/catalyses the graphitisation of the carbogel, as was already discussed in chapter 4.2.

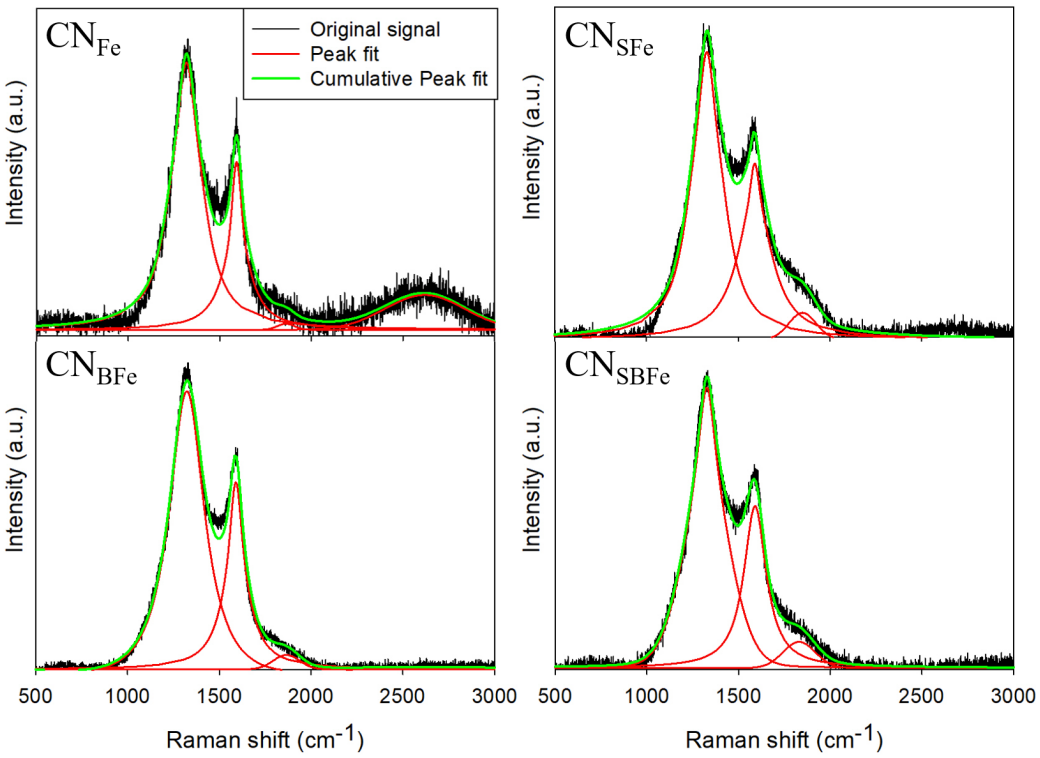


*Figure 4.35 Fitted Raman spectra for nitrogen/iron carbogels pyrolysed at 1000°C in pure form and doped with additional sulphur and/or boron.*

Ex situ Fe K-edge x-ray absorption fine structure (XAFS) was collected for the four iron doped carbogels as well as various iron compound standards. A clear difference was observed between samples containing sulphur and samples containing only nitrogen and/or boron, as can be seen in Figure 4.36, indicating that the presence of sulphur caused a change on how iron is incorporated. Though no significant difference was found regarding the position of the pre-edge, the spectra shape of the sulphur and non-sulphur containing carbogels clearly differed. While the pre-edge of $CN_{Fe}$ and $CN_{BFe}$ was almost identical with a $Fe_2O_3$ standard, suggesting the presence of ferric iron, the pre-edge of $CN_{SFe}$ and $CN_{SBFe}$ appeared to be a mixed valence of ferric and elemental iron (Fe foil). Additionally, the difference in pre-edge shape, edge position and intensity could also indicate different spin states or coordination numbers/geometry between samples with and without sulphur, though the presence of different oxidation states was assumed to determine the different curve shapes in this particular case. [220,221]

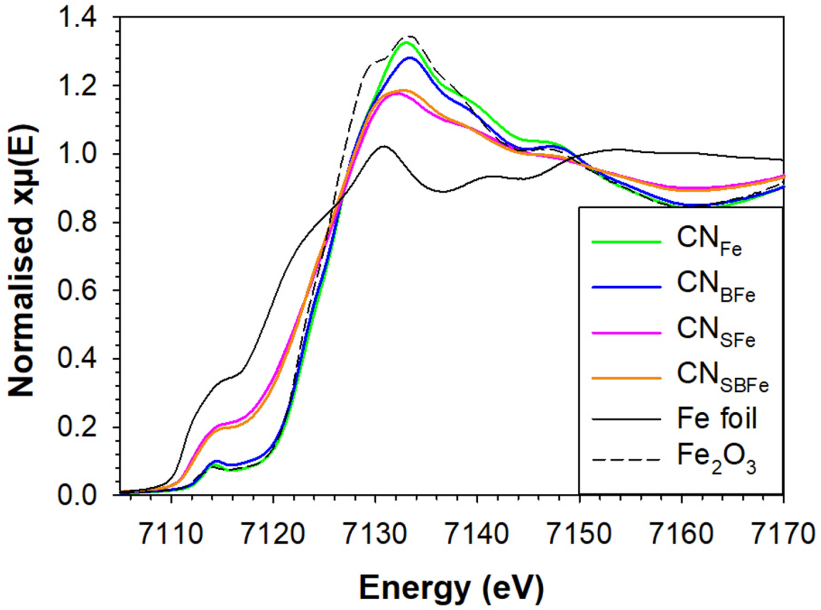


*Figure 4.36 Ex-situ collected normalised Fe K-edge XANES for $CN_{Fe}$, $CN_{BFe}$, $CN_{SFe}$ and $CN_{SBFe}$ with standards (Fe foil and $Fe_2O_3$).*

Figure 4.37 shows the Fourier transform (FT) EXAFS for non-sulphur (a) as well as sulphur containing samples (b) with peak assignments, displayed separately for better clarity. Due to the limitations of x-ray absorption spectroscopy a clear distinction between carbon, nitrogen and oxygen as neighbouring atoms was not possible, thus the suggested peak assignments have been made based on empirical standards (Figure 4.38). The first peak around 1.45-1.55 Å in the FT EXAFS for all samples was assigned to Fe-O/N/C, while the second peak around 2.6 Å for non-sulphur containing samples was suspected to be Fe-(O/N/C)-C or Fe-(O/N/C)-Fe. Due to the elemental composition (amount of carbon to iron) though, a coordination of Fe-(O/N/C)-C seemed more likely. Samples containing sulphur exhibited three significant peaks around 2.25, 3.5 and 4.4 Å, very similar to iron foil, suggesting the presence of Fe-Fe clustering.

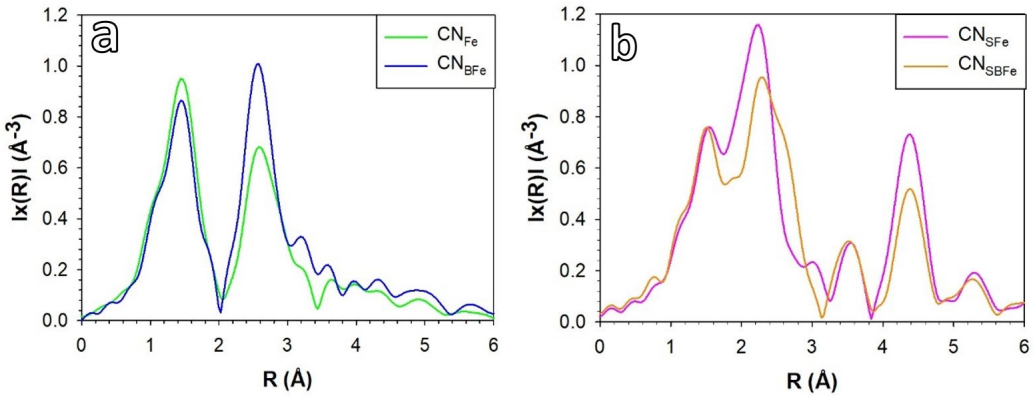


*Figure 4.37 Fourier transform EXAFS for Fe K-edge collected ex-situ for nitrogen iron doped carbogels without the addition of sulphur doping (a) and with sulphur doping (b). No phase shift correction was applied to the Fourier transform spectra.*

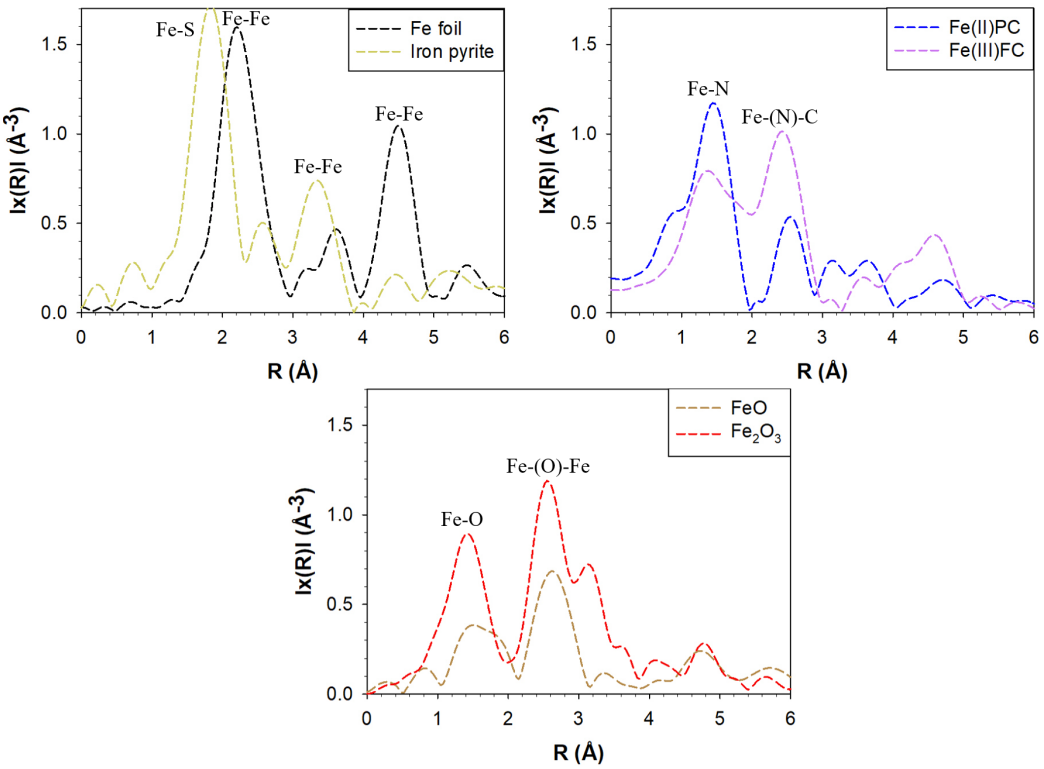


*Figure 4.38 Fourier transform EXAFS for Fe K-edge collected ex-situ for standards iron foil, iron pyrite, iron(II)phthalocyanine, iron(III)ferrocyanide, iron(II)oxide and iron(III)oxide. No phase shift correction was applied to the Fourier transform spectra.*

Considering these findings and results discussed above including TEM, XPS and XRD, iron was assumed to be homogeneously distributed and mainly present as iron coordinated with nitrogen, carbon or oxygen in non-sulphur carbogels, while additional elemental iron was likely to be present in samples containing sulphur. Some iron oxide ($Fe_2O_3$) was also assumed to be present in all samples, though well dispersed within the carbon matrix, as the absence of agglomerated nanoparticles was confirmed via TEM. Though no experimental evidence was found for its presence, presumably due to low concentrations, the formation of $FeN_x$ active sites was assumed nevertheless, in higher amounts for non-sulphur and lower amounts for sulphur containing materials, due to the additional presence of metallic Fe. As discussed above, the presence of boron seemed to have an influence on the morphology and surface area, while XAFS data indicated that the presence of sulphur changed the carbogels atomistic structure and determined how iron was incorporated into the carbon framework and which oxidation state of iron mainly existed. It has been shown that sulphur compounds can act as oxidising agents to reduce iron. Considering that both $H_2S$, during the hydrothermal carbonisation, and $SO_2$, during the high temperature pyrolysis, could be formed, the presence of elemental iron is possible. Similar findings have been reported by other researchers investigating the role of sulphur on FeN catalysts, where elemental iron was found amongst other oxidation

states of iron when sulphur was present during the pyrolysis.[178,180] Both reports did not offer an explanation on this discovery, additionally Kramm et al.[180] reported the formation of FeS at temperatures above 650 °C, whose presence was ruled out in this study based on the FT EXAFS spectra compared to an iron pyrite standard. Singh et al.[179] investigated the effect of $H_2S$ treatment before and after the heat treatment and during ORR testing of a Fe/N/C catalyst. They also observed a change in oxidation state and local bonding environment when sulphur was present and concluded that $H_2S$ hinders the evolution of $FeN_x$ active sites during the heat treatment.

To investigate their catalytic activity towards the oxygen reduction reaction, electrochemical testing was carried out for the four carbogels in alkaline (0.1 M KOH) and acidic (0.1 M $HClO_4$) electrolyte and compared to a commercially available platinum standard (Figure 4.39). $CN_{Fe}$ showed the most favourable catalytic activity in alkaline media, followed by $CN_{BFe}$, $CN_{SFe}$ and $CN_{SBFe}$. Strikingly, non-sulphur ($CN_{Fe}$, $CN_{BFe}$) and sulphur containing samples ($CN_{SFe}$, $CN_{SBFe}$) exhibited a similar relation to each other in terms of shifted onset potential and limiting current density. Non-sulphur carbogels displayed a more positive onset potential compared to the sulphur containing versions, while the presence of boron and thus the decreased surface area influenced halfwave potential and limiting current density. Average electron transfer numbers and hydrogen peroxide yields were found to be best for $CN_{Fe}$ (3.8 and 8.8 %), followed by $CN_{BFe}$ (3.7 and 14.2 %), $CN_{SFe}$ (3.4 and 28.9 %) and $CN_{SBFe}$ (3.4 and 32.7%).

An even clearer difference was observed between samples with and without sulphur in acidic media, where both samples containing sulphur performed very poorly, with a more favourable activity for the non-sulphur samples. Here, the difference between $CN_{Fe}$ and $CN_{BFe}$ was marginal, with $CN_{BFe}$ exhibiting the highest electron transfer number of 3.6 and lowest $H_2O_2$ yield of 21.8 %, closely followed by $CN_{Fe}$ with 3.5 and 26 %, respectively. In acidic media, surface area seemed to have only a slight influence on the catalysts' limiting current densities, with a similar relation as in alkaline media between samples with and without sulphur.

This clear difference between carbogels in acidic media supported the suggestion that active sites are different under alkaline and acidic conditions.[79–81] Findings by Sahraie et al.[78], as already mentioned earlier, showed that nitrogen functionalities and quinone groups were allocated as additional active sites, besides $FeN_x$, in alkaline media, while the $FeN_x$ sites seemed to be largely responsible for the catalytic activity under acidic conditions. Taking this into account as well as findings reported earlier regarding the atomistic structure of our materials, the higher amount of possible $FeN_x$ sites in the non-

sulphur samples explains their superior activity as well as the similarity between $CN_{Fe}$ and $CN_{BFe}$ in acidic media. Our observation that the presence of sulphur during the heat treatment caused declined catalytic activity in alkaline and acidic media was in agreement with other studies reporting similar trends.[178,179] The slightly better performance of $CN_{BFe}$ over $CN_{Fe}$ in acidic media again suggest the assumption that only $FeN_x$ sites are active at a low pH, as $CN_{BFe}$ contained higher amounts of iron and nitrogen, which would suggest a higher probability of $FeN_x$ sites forming and thus a higher site density of the latter. The contrary superior performance of $CN_{Fe}$ over $CN_{BFe}$ in alkaline media can be explained by the considerably higher surface area which also offered better accessibility to other non-metal active sites and thus enhanced the ORR activity.

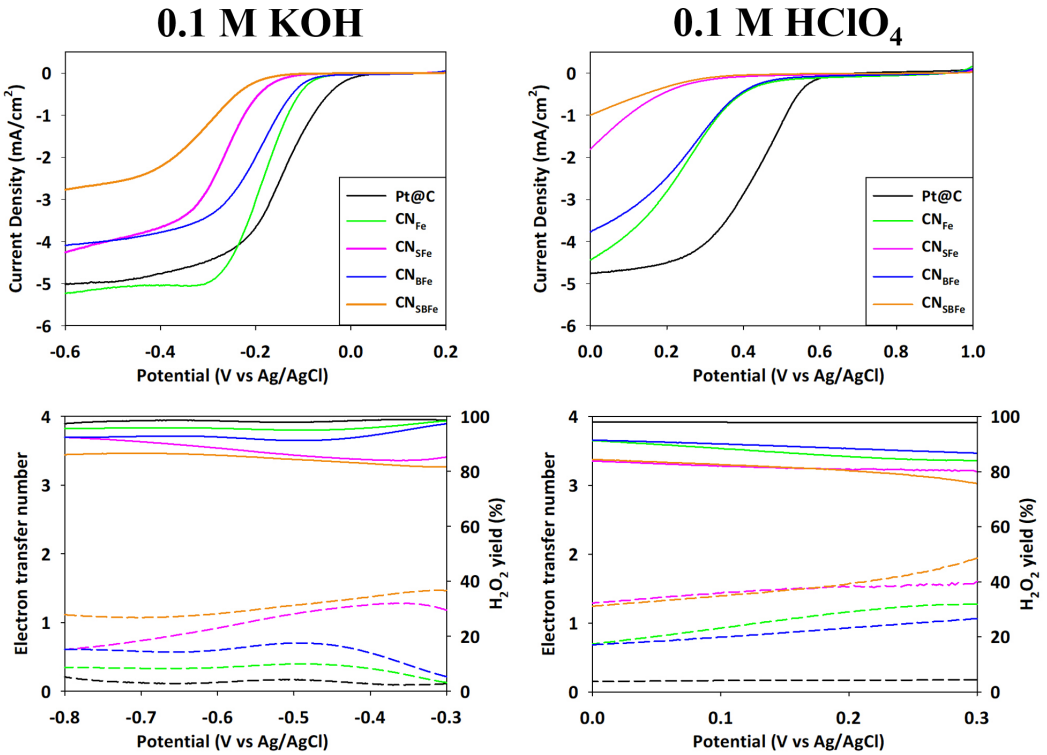


*Figure 4.39 Linear sweep voltammograms recorded in 0.1 M KOH (left) and 0.1 M HClO4 (right) with an RRDE setup at 1600 rpm and electron transfer numbers and hydrogen peroxide yields for a commercially available platinum catalyst (60 wt% Pt@C) and nitrogen/iron carbogels, $CN_{Fe}$, pyrolysed at 1000°C doped with sulphur, $CN_{SFe}$, boron, $CN_{BFe}$, or sulphur and boron, $CN_{SBFe}$.*

Chronoamperometric stability testing and methanol tolerance was carried out additionally in alkaline electrolyte. Figure 4.40 displays the chronoamperometric response and methanol tolerance in alkaline media, with all carbogels exhibiting a better performance as compared to the platinum standard. $CN_{Fe}$ showed the highest stability with 94 % of current remaining after 3 hours, while the platinum standard dropped by 25 %. While there was a response to the initial methanol addition to the electrolyte, all carbogels recovered quickly, unlike the platinum standard.

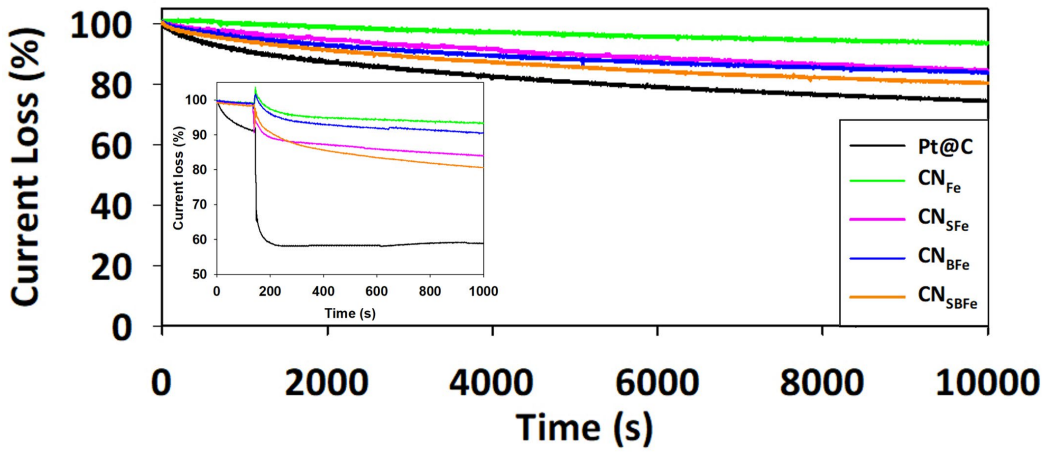


*Figure 4.40 Chronoamperometric response recorded at a constant potential (halfwave potential of each catalyst) in 0.1 M KOH and as inset methanol tolerance in 0.1 M KOH for a commercially available platinum catalyst and nitrogen/iron carbogels pyrolysed at 1000°C doped heteroatoms.*

Figure 4.41 shows linear sweep voltammograms recorded in acidic media before and after chronoamperometry for 3 hours and after methanol addition to the electrolyte. While the carbogels were degrading faster compared to the platinum standard under acidic conditions, they showed less reaction to the presence of methanol. The overall decreased performance and especially stability in acidic media can be explained by etching of the active iron sites, corrosion of the carbon matrix as well as protonation of surface groups which can cause obstruction of charge delocalisation.

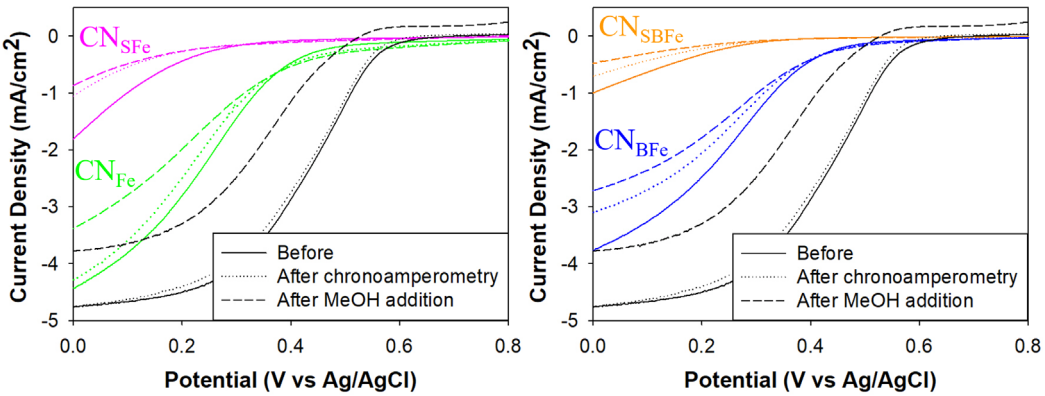


*Figure 4.41 Linear sweep voltammograms recorded at 1600 rpm in 0.1 M HClO4 for nitrogen/iron carbogels, $CN_{Fe}$ (green), doped with sulphur, $CN_{SFe}$ (pink), boron, $CN_{BFe}$ (blue), or sulphur and boron, $CN_{SBFe}$ (orange) compared to a commercially available platinum standard (black). Solid lines were recorded in fresh electrolyte, dashed lines were recorded after chronoamperometry was carried out at a constant potential (halfwave potential of each catalyst) for 10000 seconds, dotted lines were recorded after the addition of 5 mL methanol to the electrolyte.*

To get a better overview of how the alkaline ORR performance (electron transfer number) relates to surface area, elemental species and $I_D/I_G$ ratio in the different carbogels, correlation graphs are shown in Figure 4.42.

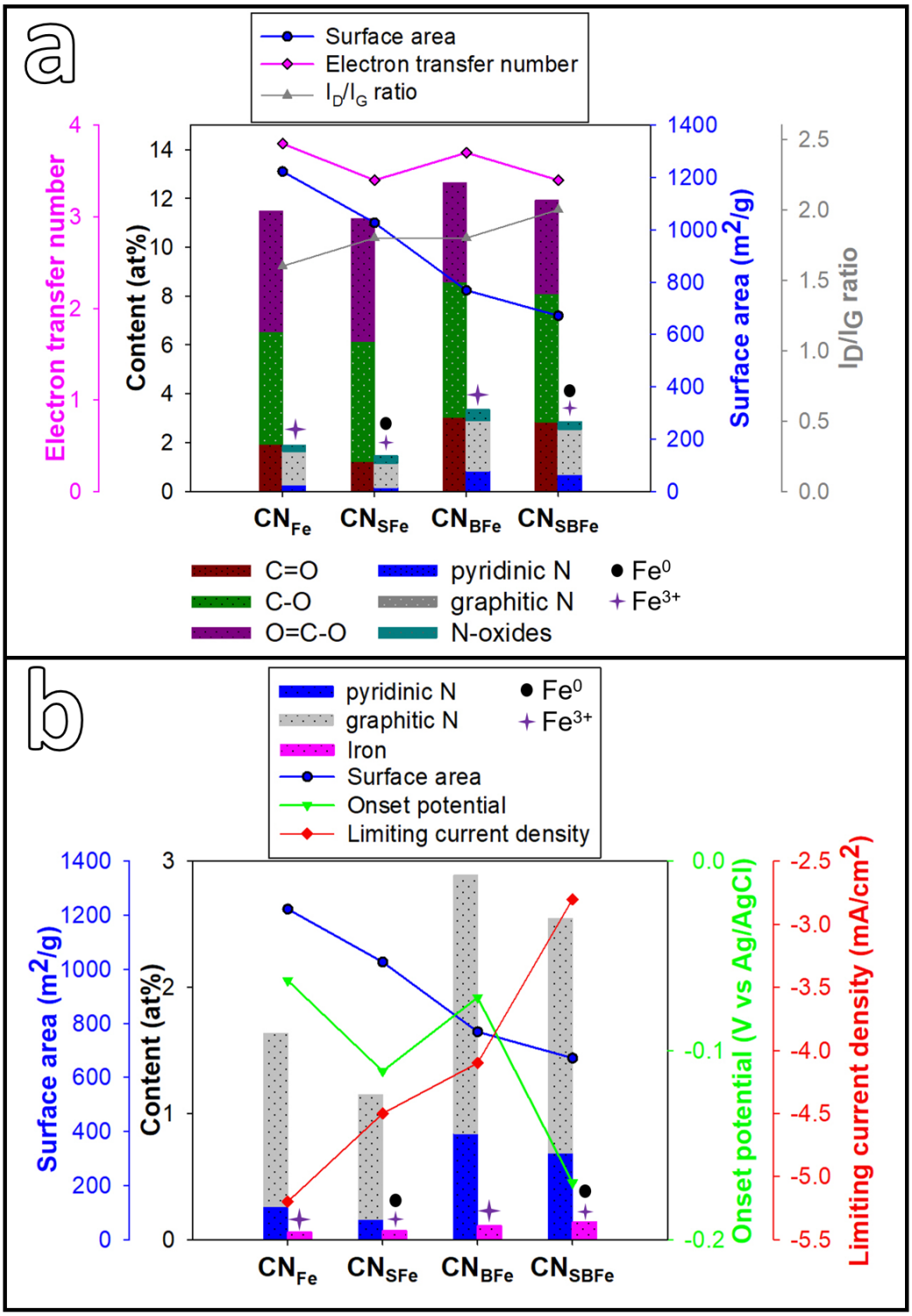


*Figure 4.42 Combination graph correlating the material's surface area and elemental content with the electrocatalytic activity (alkaline media) for nitrogen and iron doped carbogels pyrolysed at 1000 °C under a mixed atmosphere of $N_2$/air doped with additional sulphur, boron or sulphur and boron.*

It becomes clear that samples containing only ferric iron (without sulphur) performed better than samples containing additional elemental iron (sulphur containing). As the ferric iron was assumed to coordinate with nitrogen, oxygen or carbon, the active site density of possible $FeN_x$ sites is higher in non-sulphur carbogels. Other non-metal active sites (graphitic N, pyridinic N and quinone groups (part of C=O)) are also expected to contribute to the ORR performance, which were highest in number for $CN_{BFe}$. Though, due to its higher surface area and homogeneous morphology offering better accessibility to the active sites, $CN_{Fe}$ exhibited the highest electron transfer number amongst all carbogels. The onset potential was found to be more positive for non-sulphur samples, containing only ferric iron, while the limiting current density was lowered in relation to a higher surface area.

Based on the above presented results, activity of possible $FeN_x$ sites, especially in non-sulphur containing samples in acidic electrolyte was assumed, but the presence of any active Fe sites in carbogels containing sulphur ($CN_{SFe}$ and $CN_{SBFe}$) remained unclear. As reports by other researchers claimed the obstruction of $FeN_x$ sites evolving in the presence of sulphur,[179] cyanide poisoning was carried out for $CN_{SFe}$ in 0.1 M KOH to investigate the presence of any active iron sites in the sulphur containing samples (Figure 4.43). Similar to cyanide poisoning in living organisms, where the $CN^-$ ions can block the iron active centre of cytochrome C oxidase, $CN^-$ ions can bind to any $FeN_x$ active sites in the carbogel and thus block the adsorption of oxygen, hindering the ORR. After the addition of KCN, decreased performance was observed in terms of onset potential and limiting current density, confirming the presence of active iron sites in the sulphur containing samples. For comparison, the metal-free counterpart $CN_S$ (chapter 3.3) has also been plotted in Figure 4.43. The onset potential was identical after blocking the active Fe sites, suggesting that this feature may mainly be determined by the latter. The halfwave potential and limiting current density remained more favourable compared to the metal-free version, even after blocking the active Fe sites. Considering the higher surface area of $CN_{SFe}$ ($692 \pm 6$ $m^2$ $g^{-1}$ for $CN_S$ compared to $1027 \pm 69$ $m^2$ $g^{-1}$ for $CN_{SFe}$), but lower amount of nitrogen doping (2.9 at% for $CN_S$ compared to 1.47 at% for $CN_{SFe}$), surface area was assumed to have a clear influence on the halfwave potential and limiting current density in alkaline media due to less mass transport limitations and a better accessibility to additional metal-free active sites.

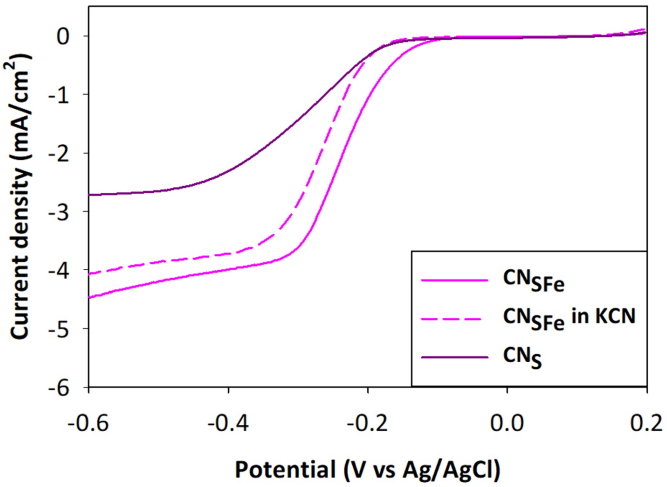


*Figure 4.43 Linear sweep voltammogram for $CN_{SFe}$ in 0.1 M KOH with and without 10mM KCN recorded with an RDE setup at 1600 rpm and, for comparison, the metal-free carbogel, $CN_S$ (chapter 3.3).*

Considering all findings discussed in this chapter, different active sites are proposed in the doped carbogels, which can be seen in Figure 4.44. Non-metal active sites including pyridinic and graphitic nitrogen as well as quinone groups were assumed to be present and contribute to the electrocatalytic performance in alkaline media. Additional metal active sites, namely leftovers of the formed iron oxide remaining in the material after the pyrolysis and presumably iron coordinated with nitrogen ($FeN_x$) were also proposed to enhance the ORR activity at high pH. Due to iron being present in two oxidation states ($Fe^0$ and $Fe^{3+}$) in samples that contained sulphur, their performance was found to be inferior to non-sulphur samples due to a lower amount of possible $FeN_x$ sites owing to the additional presence of non-active elemental iron. Surface area was observed to influence the limiting current density by offering less mass transport limitations and better accessibility to active sites. In acidic media, only active sites containing iron were assumed to promote the ORR activity, while difference in surface area only had a marginal influence.

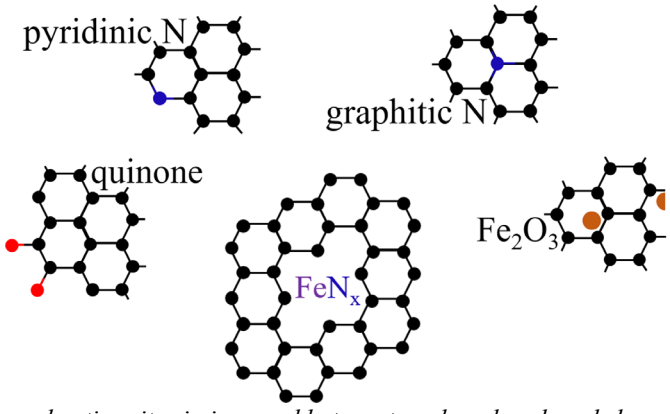


*Figure 4.44 Proposed active sites in iron and heteroatom doped carbogels based on findings from physicochemical and electrochemical characterisation of the materials.*

## 4.4 Summary

The incorporation of iron in nitrogen doped carbogels was investigated, where the presence of ferric iron salt had a beneficial influence during the hydrothermal carbonisation and the high temperature pyrolysis. The presence of ferric iron salt caused an increase in the material's mechanical stability (diameter of nanowires) and mass yield and aided the formation of an expanded coral like structure. These changes were firstly due to the iron salt lowering the pH of the reaction mixture, promoting a faster glucose dehydration as first step in the HTC cascade and thus speeding up the precipitation/nucleation of nanosized carbon particles. Secondly, the iron salt accelerated the denaturation of ovalbumin which caused faster demixing of the glucose (after its dehydration) from the reaction mixture, directing its crosslinking into the network structure. Iron in the cryogel was found to be homogeneously distributed after the hydrothermal carbonisation. During the high temperature pyrolysis under a mixed atmosphere of nitrogen and air, iron oxide nanoparticles were formed in the carbogel starting at temperatures above 400 °C. These particles were subsequently moving through the sample acting as a catalyst aiding the graphitisation of the material and at the same time as an activation agent increasing the surface area before reacting with and precipitating on the crucibles used during pyrolysis. As small amounts (0.05 at%) of iron were still found on the surface of the material but a significantly larger content in the bulk (2.7 wt%) after the pyrolysis, it was assumed that only surface iron accessible to the pyrolysis atmosphere formed iron oxide particles, while the rest remained homogeneously distributed in the carbon framework, coordinated with carbon, oxygen or nitrogen.

The influence of additional heteroatom doping with sulphur and/or boron on the nitrogen and iron cryo- and carbogels was also explored. Here, a clear influence of sulphur and boron doping on the morphology, surface area and atomistic structure was observed. The presence of a boron precursor during the hydrothermal carbonisation caused a competition with the iron salt catalysing the reaction and ovalbumin directing the structure of the carbogel, leading to an inhomogeneous morphology and reduced surface area, while incorporating higher amounts of nitrogen and iron. The presence of a sulphur precursor did not drastically interfere with the formation of the nanowired carbogel structure, but caused a slight reduction in surface area and nitrogen content. A more crucial change was induced by the presence of sulphur on the atomistic structure of the carbogel, causing, besides ferric iron which was found in all carbogels, the additional presence of elemental iron.

The catalytic activity towards the oxygen reduction reaction was found to be more beneficial for samples containing only nitrogen and iron (alkaline media) or nitrogen, boron and iron (acidic media) as compared to samples including sulphur. Active sites were observed to be different under alkaline and acidic conditions, where the presence of iron active sites seemed to be crucial in acidic electrolyte, while other properties such as surface area as well as nitrogen (pyridinic and graphitic N) and oxygen (quinone groups) species also played a role in alkaline electrolyte. The presence of active iron sites was confirmed by cyanide poisoning.

# Chapter 5 | Understanding the influence of heteroatom dopants on the oxygen reduction reaction

## 5.1 Introduction

There are many reports in literature claiming that different heteroatom dopants can enhance the catalytic activity towards the oxygen reduction reaction. First and foremost is nitrogen doping, which has been reported for an array of different carbon materials, ranging from graphene, carbon nanotubes and nanocages to sustainable carbons.[222–225] Here, mostly pyridinic and graphitic nitrogen are assumed to be responsible for the improved activity. But also other heteroatoms like boron, sulphur or phosphorus are said to increase the catalytic performance by disrupting the charge density profile or by inducing defects. More on the theory and mechanisms for the respective dopants can be found in chapter 2.1.3.3.

Commonly, different heteroatoms are compared and reports are trying to claim the superiority of one over the others. Though, as often the case with synthesis methods, the addition of any different precursor chemicals can cause a change in the resulting material's properties in terms of surface area, pore structure, morphology, graphitisation/ conductivity and dopant amount, as has also been the case in the work presented in the previous experimental chapters (chapter 3 and 4). These alterations pose a challenge when trying to compare the resulting catalysts due to the changing parameters affecting the ORR activity beyond just the dopant itself.

Thus, controlled templating synthesis methods are a welcome solution in order to produce materials which are more similar amongst each other and allow an actual comparison between the heteroatom dopants and the influence of surface area and pore structure.

Anibal et al.[226] investigated the influence of different silica templates on the catalytic activity of the resulting carbon. They used silica with varying particle sizes and found that the respective carbon usually exhibited half the pore size as compared to the template diameter. The smaller pore size was assumed to be due to pore collapse after the removal of the template resulting in more stable pore shapes. The best catalyst for the ORR was found to be a carbon containing pores with a diameter of 9 nm, followed by 7 nm, 11 nm and lastly 17 nm.

Meng et al.[102] synthesised a nitrogen, sulphur and oxygen triple doped carbon via templating with colloidal silica. The influence of silica to precursor ratio on the catalytic activity was investigated and the best performing sample was found to contain the highest

silica content. Simultaneously they found that the higher the silica content, the more oxygen was incorporated at the cost of nitrogen and sulphur, and the higher the surface area and pore volume. They concluded that neither sulphur nor nitrogen content, but the higher amount of oxygen and surface area was responsible for the enhanced performance.

Silva et al.[227] synthesised nitrogen and oxygen doped mesoporous carbon from polyaniline, using SBA-15 as a template. They found that the best catalytic performance in terms of onset potential was reached by a sample pyrolysed at 800 °C, while the sample pyrolysed at 900 °C exhibited a higher electron transfer number despite its less positive onset potential. The authors assumed the good catalytic activity to stem from a synergistic effect between nitrogen and oxygen, where the pyridone groups could form a stable adduct (hydroxypyridine) with the oxygen. They also added additional cobalt and/or iron to their catalyst, though no improvement in the catalytic activity was observed, while no metal could be detected via XPS (possibly due to removal during the silica etching) and only trace amounts of nitrogen, which could explain the unexpected poor performance.

Instead of using hard templating methods, there are also reports using model catalysts such as graphene to compare different heteroatom dopants. Quan et al.[228] synthesised and compared a nitrogen and a sulphur doped graphene and their ability to act as ORR catalysts. The materials exhibited very different surface areas and dopant amounts of 1564 $m^2\ g^{-1}$ (22.83 wt%) and 2255 $m^2\ g^{-1}$ (12.25 wt%) for the S and N doped material, respectively. Electrochemical testing revealed that both samples performed better than a pristine graphene due to the higher surface area and degree of graphitisation owing to the additional annealing step after the heteroatom dopant impregnation. Expectedly, the nitrogen doped graphene outperformed the sulphur doped sample in terms of onset potential and limiting current density and exhibited an electron transfer number of 3.4 as compared to 2.6 for the S doped graphene.

Jiao et al.[105] compared heteroatom doped graphene by annealing graphene oxide with different precursors. They investigated the incorporation of nitrogen, oxygen, boron, phosphorus and sulphur. All samples exhibited a similar surface area between 100 to 150 $m^2\ g^{-1}$ as well as $I_D/I_G$ ratios between 1.0 and 1.2, while dopant levels were found to be between 3 to 5 at%. Though not commented on, deconvolution of the XPS spectra suggested the presence of additional oxygen in all samples, making it, as usual, difficult to assign a definitive role to oxygen. Combining experimental data with theoretical predictions, they found the best catalytic performance for the nitrogen doped sample, followed closely by the boron doped graphene. Behind these two, phosphorus and oxygen

were observed to perform similar followed lastly by the sulphur doped sample and the pristine graphene.

Contrary to expectations, a study showed that an increase in nitrogen content does not necessarily cause an increase in catalytic activity. Zhao et al.[111] reported a correlation between enhanced ORR activity and reduction in nitrogen content, due to an increase in defects created by removing/etching nitrogen atoms at higher pyrolysis temperatures. Their observation validates theories claiming that not the heteroatom dopant itself improves the catalytic performance but rather the defects that are caused by incorporating different heteroatom dopants as well as defects created upon heat treatment and their subsequent removal from the carbon matrix leaving behind holes.[107]

Lastly it should be mentioned, that templating methods, especially hard templating with silica, poses challenges in itself. The restriction of volume of precursor solution, to guarantee infiltration without excess coating of the template, can cause issues when changing between different heteroatom precursors due to their concentration as well as appearance (solid, liquid). Additionally, different reactions occurring and gasses evolving during the high temperature pyrolysis depending on the precursors used, can cause changes in the elemental composition and have an influence on surface area and pores. Furthermore, successful etching of the silica template, especially without removing any wanted species, can be challenging.

Keeping the above mentioned challenges in mind, a hard templating method, using two different silica templates, SBA-15 and mesoporous shell silica spheres (MSS), were chosen to synthesise carbons incorporated with different heteroatom dopants. Figure 5.1 displays the schematic how the different templated carbons were produced.

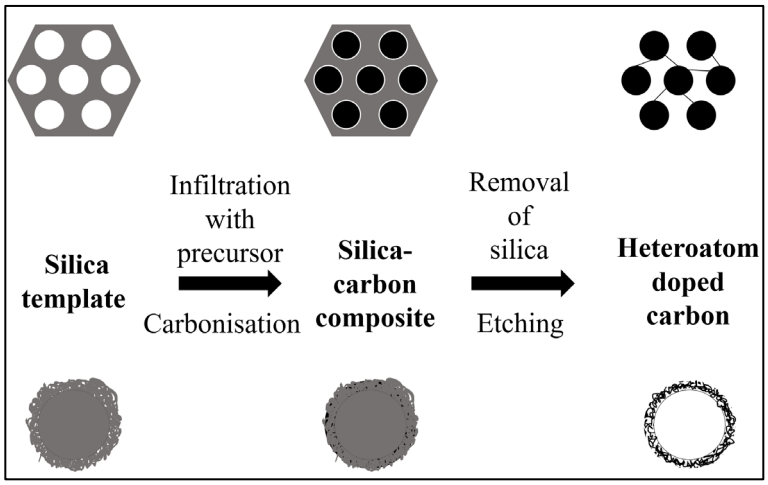


*Figure 5.1 Schematic showing the synthesis process for templated heteroatom doped carbon materials with different silica templates, SBA-15 (top) and mesoporous shell silica spheres (bottom).*

First the silica templates were infiltrated with precursor solution, then high temperature pyrolysis converted the precursor solution into doped carbon which resulted in a silica-carbon composite. Subsequent etching of the silica template yielded the desired heteroatom doped carbons. The resulting materials were compared amongst each other to investigate the ability of different heteroatom precursors to incorporate dopants, get an understanding if any dopant is superior to the other and how surface area can influence the catalytic activity. Combination doping between the metal-free heteroatom dopants as well as with additional iron was examined and its influence on the material's properties and ORR performance.

## 5.2 Experiment validation

Two different silica templates were used to synthesise templated carbon materials with heteroatom dopants. For this SBA-15 and mesoporous shell silica spheres (MSS) were chosen in order to achieve an altered morphology, pore volume, as well as surface area. Figure 5.2 shows the two different silica templates SBA-15 (a) and MSS (d) with the corresponding templated undoped control samples (b and e, respectively) and templated nitrogen doped carbons (c and f, respectively). TEM micrographs confirmed the successful infiltration, conversion into carbon material and subsequent etching of the template, resulting in an inverse replica of both templates.

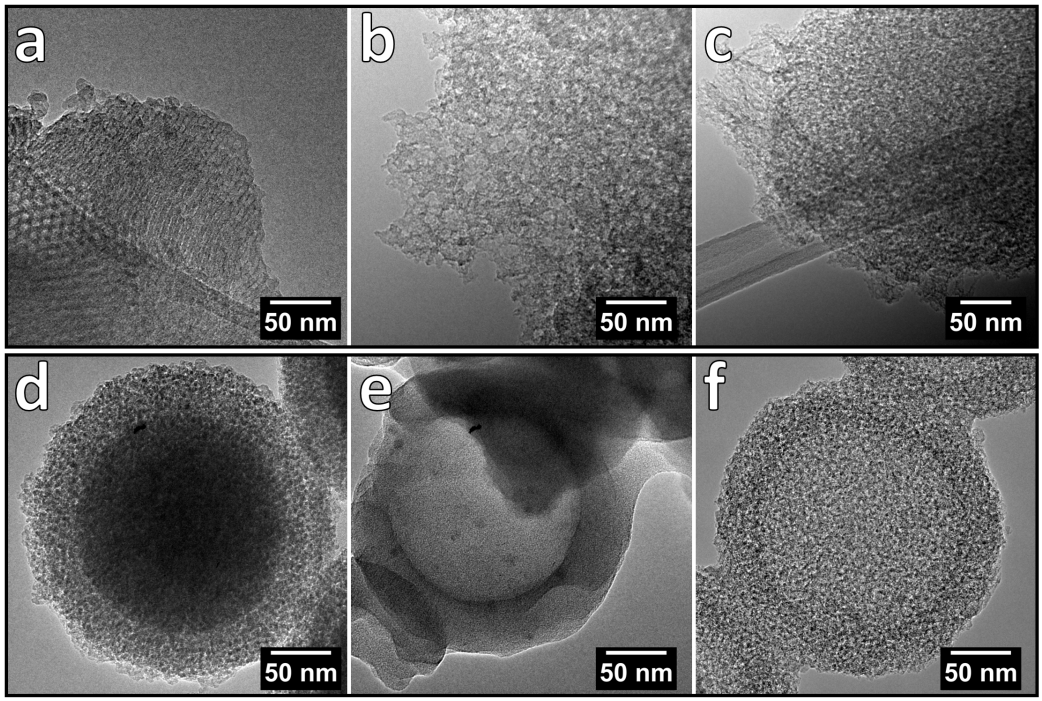


*Figure 5.2 TEM micrographs of silica template SBA-15 (a) and the templated control sample (C-SBA) (b) with additional nitrogen doping (C/N-SBA) (c). Mesoporous silica shell sphere template (d) and the templated control sample (C-MSS) (e) with additional nitrogen doping (C/N-MSS) (f).*

SEM micrographs of the templated undoped control samples for both templates, SBA-15 and MSS, can be seen in Figure 5.3. The SBA-15 templated carbon exhibited the typical rice like structure, while the MSS templated material displayed a hollow spherical shape with occasional broken spheres.

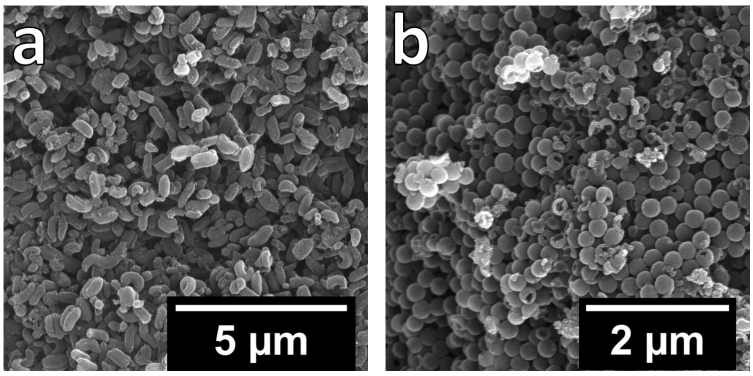


*Figure 5.3 SEM micrographs of the undoped control samples, templated with SBA-15 (C-SBA) (a) or mesoporous shell silica spheres (C-MSS) (b).*

Figure 5.4 shows nitrogen sorption isotherms and pore size distributions for the two silica templates and their corresponding templated control carbons. Due to the lower surface area and pore volume, the inverse replicate (C-MSS) of the MSS template exhibited a higher surface area and pore volume as compared to the SBA control (C-SBA). Pore sizes were similar, but slightly different, with both control samples displaying micropores, 1.2 nm for C-SBA and 1.4 nm for C-MSS, and mesopores around 3.2 and 4.4 nm.

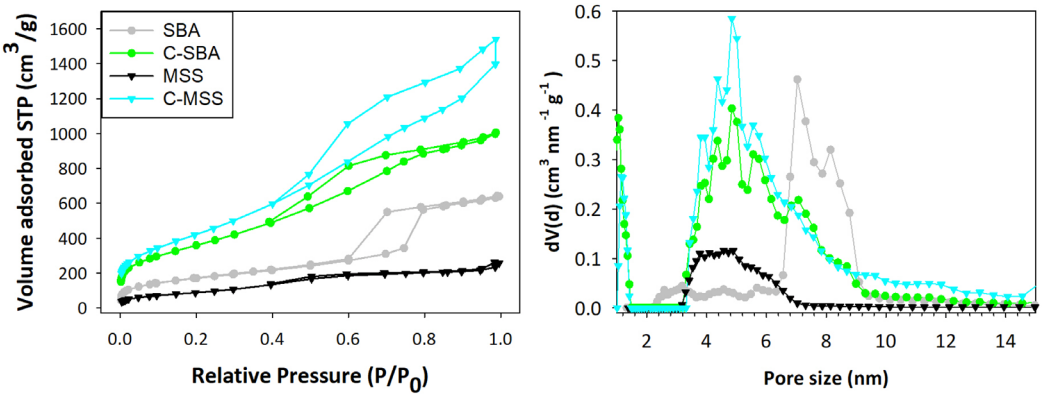


*Figure 5.4 Nitrogen sorption isotherms obtained at 77 K with BET surface areas and pore size distribution for two silica templates (SBA and MSS) and their templated carbon control samples (C-SBA and C-MSS).*

Deconvolution of C1s and O1s XPS spectra revealed a lower carbon and higher oxygen content for C-SBA, though with a similar distribution of carbon and oxygen bonds, as can be found in Figure 5.5. Peaks in the C1s spectra were observed around 284.5 eV, 285.5 eV, 286.2 eV and 286.9 eV which were attributed to $sp^2$ C-C and C=C bonds, as well as

functional groups C-OH, C=O and C-O, respectively.[146] Oxygen bonds were assigned to C=O, C-O, C-OH and chemisorbed oxygen or water with peaks around 531 eV, 532.5 eV, 534 eV and above 535.5 eV.[146] The higher content of chemisorbed water in C-SBA was likely to be due to longer storage before analysis via XPS.

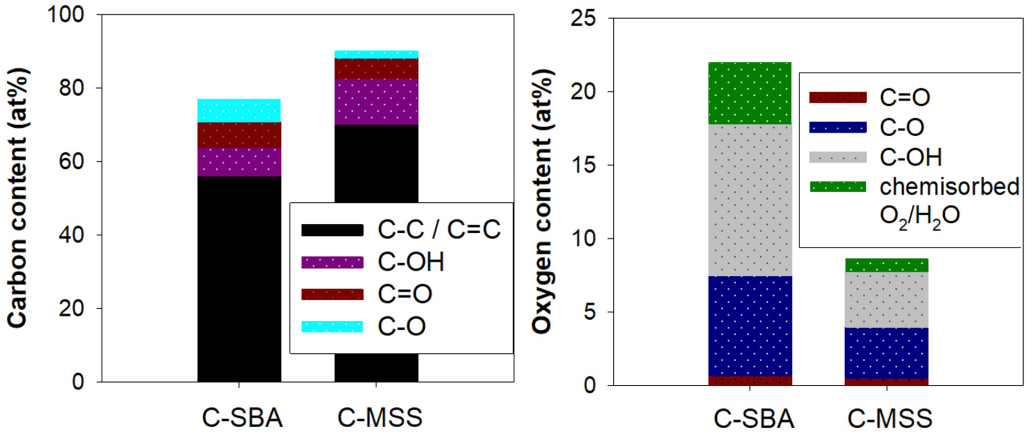


*Figure 5.5 Carbon and oxygen bonds determined via deconvolution of C1s and O1s XPS spectra for C-SBA and C-MSS.*

To confirm the successful etching of the silica templates, thermogravimetric analysis was carried out under air, as can be seen in Figure 5.6. After the analysis a whitish powder remained in the pan, suggesting the incomplete removal of the templates for both control samples and their nitrogen doped counterparts. The leftover mass percentage was found to be 10.6 %, 8.7 %, 13.8 % and 12.7 % for C-SBA and C/N-SBA, as well as C-MSS and C/N-MSS, respectively. Not all the remaining solid was assumed to be leftover silica template, but rather a mixture of silica template, inorganic contaminants and ash. XPS analysis revealed the presence of small amounts (< 1 at%) of Si and F in all samples, left over from the template and etching with $NH_4HF_2$. As all samples showed similar contamination with Si and F, their influence on the catalytic activity was not taken into account.

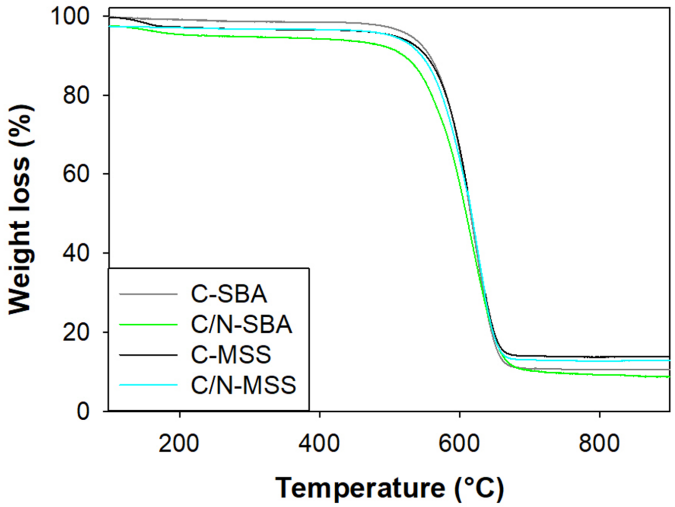


*Figure 5.6 Thermogravimetric analysis of templated carbons C-SBA and C-MSS as control and with nitrogen doping (C/N-SBA and C/N-MSS) with a heating rate of 10 °C/min in air.*

## 5.3 Incorporation from different heteroatom dopant precursors

The ability of doping a templated carbon (C-SBA) with different heteroatom precursors was investigated for nitrogen, boron, sulphur and phosphorus. Precursors were chosen based on their availability, chemical structure and absence of other possible dopants. For nitrogen doping, two aliphatic (urea and arginine) and two aromatic (melamine and adenine) compounds were selected, with one of each being bigger in molecular size/heavier in molar mass than the other. Similarly, the sulphur compounds were picked due to their aromatic (2-thiophenecarboxaldehyde – TCA) and aliphatic (allyl disulphide) structure. For boron and phosphorus doping, boric acid and boron trioxide, as well as phosphoric acid and phytic acid were chosen, respectively. The addition of dopant precursor to the glucose solution was based on 2 mmol of each dopant itself.

SEM micrographs (Figure 5.7) showed a similar morphology for all SBA-15 templated carbons regardless of the different heteroatom precursors, also as compared to the undoped control sample (C-SBA) in Figure 5.3a, which confirmed the successful infiltration of the silica template.

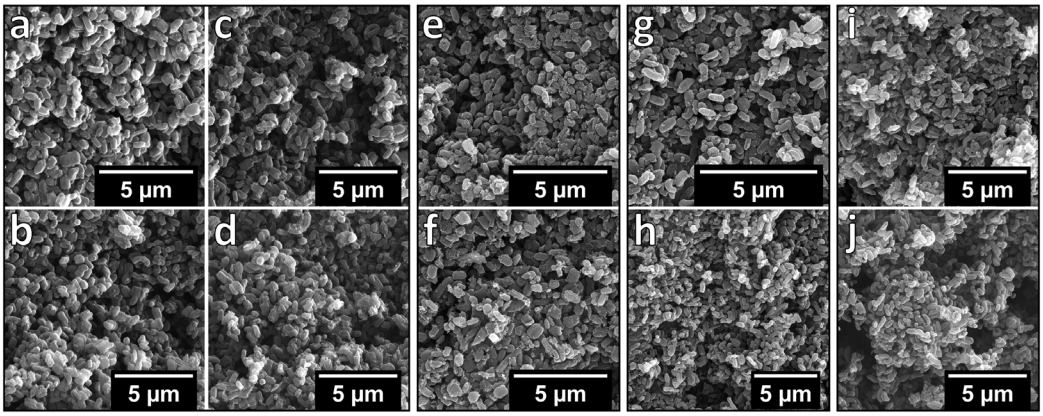


*Figure 5.7 SEM micrographs for SBA-15 templated carbons doped with different heteroatom precursors. a) urea, b) melamine, c) adenine, d) arginine, e) boric acid, f) boron trioxide, g) TCA, h) allyl disulphide, i) phosphoric acid and j) phytic acid.*

Table 5.1 displays the surface areas and pore volumes achieved for the different SBA-15 templated carbons after etching of the silica template and subsequent drying, together with the respective dopant amount determined via XPS. While the surface area and pore volume were found to be highest for the undoped control sample (1264 $m^2 g^{-1}$ and 1.420 $cm^3 g^{-1}$), additional doping with sulphur only had minor influence, whereas the boron and phosphorus precursors reduced the surface area and pore volume more strongly. The incorporation of nitrogen from different precursor compounds resulted in a slightly lower surface area and pore volume for the aliphatic (urea and arginine) as compared to the aromatic structures (melamine and adenine).

*Table 5.1 Surface area, total pore volume, meso- and micropore volume, and respective dopant amount in SBA-15 templated carbons doped with different heteroatom precursors.*

| Sample precursor | Surface area [$m^2 g^{-1}$] | $V_{tot}$ [$cm^3 g^{-1}$] | $V_{meso}$ [$cm^3 g^{-1}$] | $V_{micro}$ [$cm^3 g^{-1}$] | Dopant amount [at%] |
|---|---|---|---|---|---|
| C-SBA | 1264 | 1.420 | 1.221 | 0.199 | - |
| Urea | 1065 | 1.160 | 1.027 | 0.133 | 4.21 |
| Melamine | 1135 | 1.190 | 1.018 | 0.172 | 2.8 |
| Adenine | 1151 | 1.220 | 1.036 | 0.184 | 2.5 |
| Arginine | 1033 | 1.090 | 0.924 | 0.166 | 0.8 |
| Boric acid | 968 | 1.039 | 0.882 | 0.157 | 1.77 |
| Boron trioxide | 995 | 1.184 | 1.038 | 0.146 | 0.67 |
| TCA | 1226 | 1.195 | 0.963 | 0.232 | 0.01 |
| Allyl disulphide | 1183 | 1.203 | 0.993 | 0.210 | 0.02 |
| Phosphoric acid | 1024 | 1.001 | 0.81 | 0.191 | 4.57 - (0.46 N) |
| Phytic acid | 1002 | 0.966 | 0.724 | 0.242 | 2.88 - (0.36 N) |

Generally, the doping of the carbon was assumed to inflate/increase the carbon matrix which would lead to a decrease in pore size and surface area. Another explanation for the

reduction in surface area and change in pore volume as compared to the control sample could be the change of volume of glucose solution used for infiltrating the silica template according to the amount of respective dopant precursor used, to avoid over infiltration of the template, thus less carbon precursor was available.

Though slightly different in total pore volume, nitrogen sorption isotherms (Figure 5.8) confirmed that all samples exhibited similar surface area and pore sizes. Boron trioxide and both phosphorus precursors were found to cause a slightly higher amount of larger mesopores, which could have been caused by a higher incorporation of oxygen. The cost of a higher oxygen content was the reduction in carbon, "etched" by the oxygen atoms thus creating larger pores.

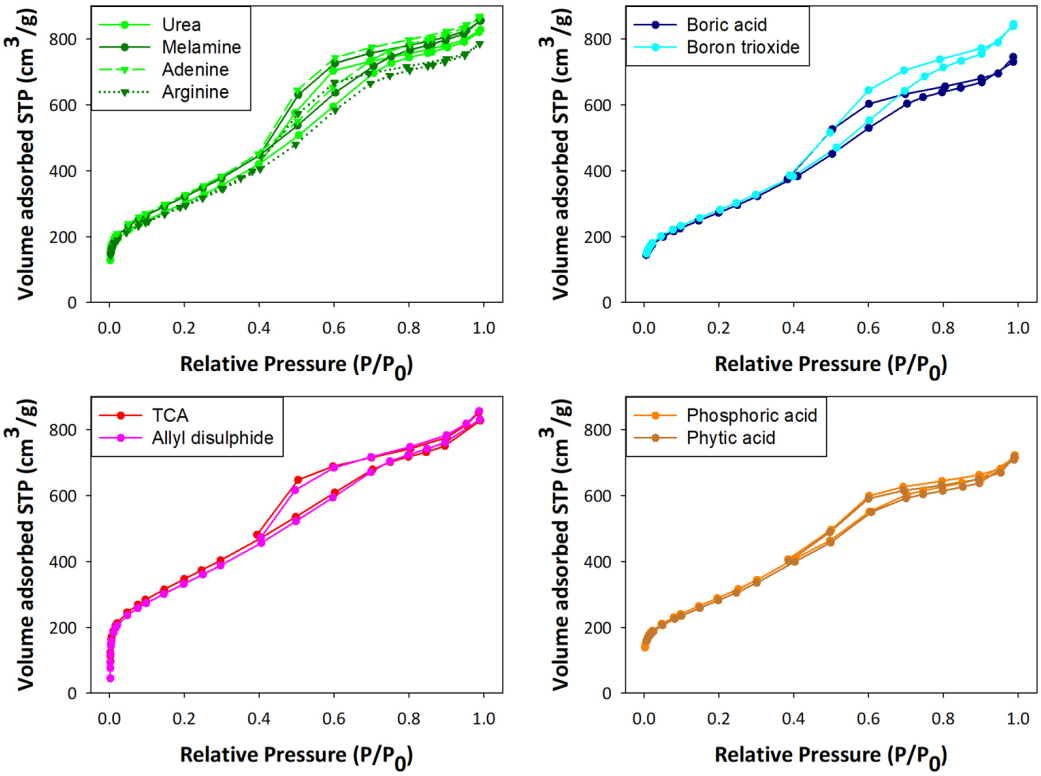


*Figure 5.8 Nitrogen sorption isotherms for SBA-15 templated carbons doped with nitrogen, boron, sulphur or phosphorus from different heteroatom precursors.*

Strikingly, though the same amount of each heteroatom dopant itself was used (2 mmol), final dopant concentrations varied greatly in the templated carbons, with the highest being nitrogen from urea (4.21 at%) and phosphorus from phosphoric acid (4.57 at%), followed by boron from boric acid (1.77 at%) Sulphur doping proved more difficult with considerably lower dopant amounts achieved (0.02 at%), possibly due to the large atomic size of the sulphur atom. All samples doped with phosphorus were found to have low concentrations of nitrogen contamination, with 0.46 at% for phosphoric acid and 0.36 at% for phytic acid. As samples were synthesised together in batches due to resource

limitations and with energy saving in mind, the evolution of ammonia from samples containing nitrogen precursors or contaminants within the furnace tube and their subsequent reaction with phosphorus during the pyrolysis could have caused the low amounts of nitrogen contamination in phosphorus doped carbons. Also, phosphorus doped samples and the boron doped sample from boron trioxide were found to exhibit a significantly higher oxygen content (~ 18 at% for P doped and ~ 9 at% for boron trioxide) as compared to the other doped samples, with an increased peak area for the phosphorus doped samples around 531 eV, likely corresponding to phosphate, overlapping with the peak at 531.1 eV attributed to C=O bonds.[146]

Boron, sulphur and phosphorus species were similarly distributed for the respective doped samples. The B1s spectra exhibited two components with around 70 % of B-C (191.3 eV) and around 30 % of $H_3BO_3$ (193.2 eV).[229,230] Due to the low dopant amount the sulphur spectra could not be deconvoluted, but the peak position corresponded to thiol, -SH around 163.8 eV.[231] Deconvolution of the phosphorus spectra revealed two components around 132.8 eV (~ 90%) and 134 eV (~ 10%) attributed to P-C and P-O bonds, respectively.[232–234] For nitrogen doped carbons, the dopant amount was observed to reduce with increasing molecule size/molar mass of the precursor, suggesting that the larger the compound, the less likely the incorporation. Deconvoluted N1s spectra revealed a similar distribution of nitrogen species (Figure 5.9) for the templated carbon doped with urea, melamine and adenine, while the use of arginine, not only resulted in the lowest dopant amount, but also in a different distribution of species, with mainly pyrrolic nitrogen (81%) present. Similarly, while all other doped samples exhibited a similar distribution of carbon and oxygen species, the carbon doped with nitrogen from arginine, showed an increased content of C-O and C=O groups.

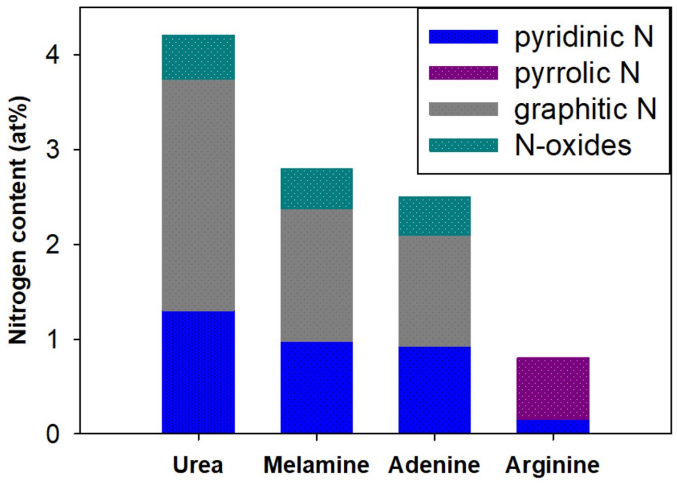


*Figure 5.9 Nitrogen species determined via deconvoluted N1s spectra from XPS for SBA-15 templated carbons doped with nitrogen from different heteroatom precursors.*

Electrochemical testing was carried out and linear sweep voltammograms for all doped carbons compared to their respective dopant sources and the undoped control sample can be seen in Figure 5.10. All nitrogen doped carbons exhibited a slightly more positive onset potential as compared to the control sample, while the other dopants, boron, sulphur and phosphorus caused no improvement or even reduction of the onset potential. Similarly, only some of the nitrogen doped samples showed a slightly more favourable limiting current density in respect to the control.

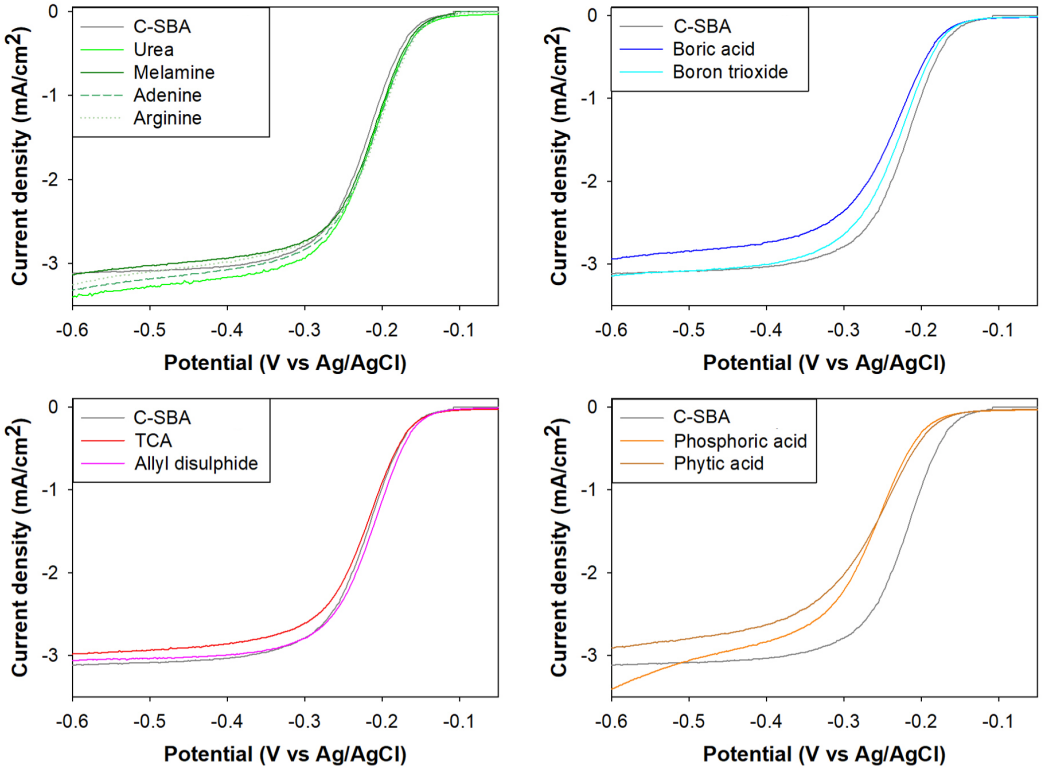


*Figure 5.10 Linear sweep voltammograms recorded with an RRDE setup at 1600 rpm in 0.1 M KOH for SBA-15 templated carbons doped with different heteroatom precursors compared to an undoped control sample (C-SBA).*

Average electron transfer numbers and hydrogen peroxide yields for all samples can be found in Table 5.2. Electron transfer numbers were found to significantly differ if calculated directly from the disk and ring current of the RRDE (rotating ring disk electrode) as compared to calculated from RDE (rotating disk electrode) results via the Koutecký–Levich equation. This difference was likely to come from an overestimation of the quasi-4-electron pathway, where the formed peroxide species are adsorbed on the surface and further reduced to not be detected by the RRDE ring, thus delivering higher electron transfer numbers and too low hydrogen peroxide yields than actually occurring. Another reason for the overestimated RRDE electron transfer numbers could also be due to a rough catalyst surface owing to the high surface area of all samples, which can reduce the collection efficiency of the platinum ring on the RRDE, causing overestimated

electron transfer numbers.[235] Considering the aforementioned limitations, electron transfer numbers were further estimated via Koutecký–Levich equation.

*Table 5.2 Average values (between -0.3 to -0.6 V vs Ag/AgCl) for electron transfer number in 0.1 M KOH determined via RRDE, calculated directly from the measured disk and ring current, as well as via RDE with Koutecký–Levich equation.*

| Sample precursor | Electron transfer number from RRDE | Electron transfer number from RDE |
|---|---|---|
| C-SBA | 2.92 | 2.29 |
| Urea | 2.96 | 2.74 |
| Melamine | 2.84 | 2.58 |
| Adenine | 2.83 | 2.62 |
| Arginine | 2.88 | 2.60 |
| Boric acid | 2.82 | 2.40 |
| Boron trioxide | 2.85 | 2.43 |
| TCA | 3.01 | 2.32 |
| Allyl disulphide | 2.92 | 2.34 |
| Phosphoric acid | 2.91 | 2.50 |
| Phytic acid | 2.92 | 2.47 |

All heteroatom dopants showed an improvement in the electron transfer number as compared to C-SBA (2.29), with the highest numbers achieved for nitrogen doped carbons. Amongst those, the sample doped with urea, exhibiting the highest nitrogen content also had the highest electron transfer number (2.74) and most positive onset potential as well as limiting current density. The other three nitrogen doped carbons displayed similar electron transfer numbers around 2.60, even though the arginine doped sample had a slightly lower surface area and nitrogen content as compared to those doped with melamine or adenine. A higher content of carbon-oxygen bonds were found in the arginine derived samples though, where the presence of possible quinone groups could have balanced out the lower nitrogen content. The second highest electron transfer numbers were achieved by phosphorus doped samples, around 2.50, where both samples performed similar regardless of their difference in phosphorus doping. Considering their poor onset potential and limiting current density though, an influence of the nitrogen by contamination on the catalytic ORR mechanism was assumed, which caused higher electron transfer numbers. These were closely followed by samples doped with boron (around 2.40) and lastly sulphur (around 2.30). Again, no influence of the actual amount of boron was found on the catalytic activity, where the sample containing less than half of the boron content, but with a slightly higher surface area performed slightly better. Sulphur doping resulted in very low dopant amounts, 0.01 at% for TCA, but with a similar surface area as compared to the control sample, resulting in nearly the same electron

transfer number. Based on the above presented results, further investigations concerning the different dopants were carried out with urea, boric acid, allyl disulphide and phosphoric acid for nitrogen (C/N-SBA), boron (C/B-SBA), sulphur (C/S-SBA) and phosphorus (C/P-SBA), respectively, due to their ability of incorporating higher dopant amounts.

## 5.4 Influence of concentration of different heteroatom dopants

To get a better understanding how dopant concentration can influence the catalytic activity as well as material properties, two different dopant concentrations of heteroatom precursors from the same source were investigated.

SEM images (Figure 5.11) revealed a similar morphology for all samples, regardless of their dopant concentration, suggesting that the templating and subsequent etching worked successful.

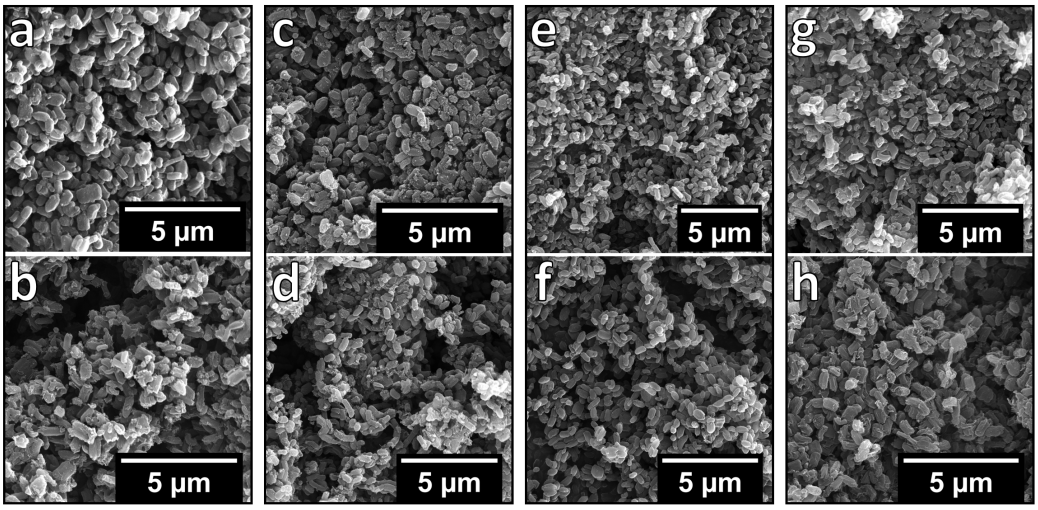


*Figure 5.11 SEM micrographs for SBA-15 templated carbons doped with different heteroatom precursors, urea (C/N-SBA) in low (a) and high concentration (b), boric acid (C/B-SBA) in low (c) and high concentration (d), allyl disulphide (C/S-SBA) in low (e) and high concentration (f) and phosphoric acid (C/P-SBA) in low (g) and high concentration (h).*

Surface areas and pore volume, as well as meso- and micropore volume can be seen in Table 5.3 with respective dopant amounts determined via XPS. The surface area was most influenced by high concentrations of the boron and phosphorus precursors, but also slightly by the nitrogen and sulphur source. Again, most likely this change was caused by the alternating composition of infiltration solution due to varying amounts of the respective precursors. The most drastic reduction was observed for the high concentration phosphorus doped sample, which caused a reduction of surface area from 1024 $m^2 g^{-1}$ to 683 $m^2 g^{-1}$, while the pore volume increased and shifted to mostly larger mesopores.

*Table 5.3 Surface area, total pore volume, meso- and micropore volume, and respective dopant amount in SBA-15 templated carbons doped with different heteroatom precursors.*

| Dopant | Surface area [$m^2\ g^{-1}$] | $V_{tot}$ [$cm^3\ g^{-1}$] | $V_{meso}$ [$cm^3\ g^{-1}$] | $V_{micro}$ [$cm^3\ g^{-1}$] | Dopant amount [at%] |
|---|---|---|---|---|---|
| C-SBA | 1264 | 1.420 | 1.221 | 0.199 | - |
| **C/N**-SBA-low | 1065 | 1.160 | 1.027 | 0.133 | 4.21 |
| **C/N**-SBA-high | 960 | 1.097 | 0.954 | 0.143 | 19.31 |
| **C/B**-SBA-low | 968 | 1.039 | 0.882 | 0.157 | 1.77 |
| **C/B**-SBA-high | 829 | 1.123 | 0.992 | 0.131 | 8.98 |
| **C/S**-SBA-low | 1183 | 1.203 | 0.993 | 0.210 | 0.02 |
| **C/S**-SBA-high | 1114 | 1.210 | 0.999 | 0.211 | 1.76 |
| **C/P**-SBA-low | 1024 | 1.001 | 0.810 | 0.191 | 4.57 (0.46 N) |
| **C/P**-SBA-high | 683 | 1.617 | 1.547 | 0.070 | 15.86 (0.29 N) |

Nitrogen sorption isotherms for all samples can be seen in Figure 5.12, where the incorporation of a higher nitrogen content only caused a slight decrease in pore volume and surface area but did not alter the pore sizes. Sulphur incorporation with different concentrations yielded similar surface area and pore properties, while a higher boron and phosphorus concentration caused an increase in mesopore volume, possibly due to the higher concentrations of mineral acids acting as additional activating agent causing a different pore size distribution or because of the incorporation of higher amounts of oxygen, especially for the phosphorus doped samples.

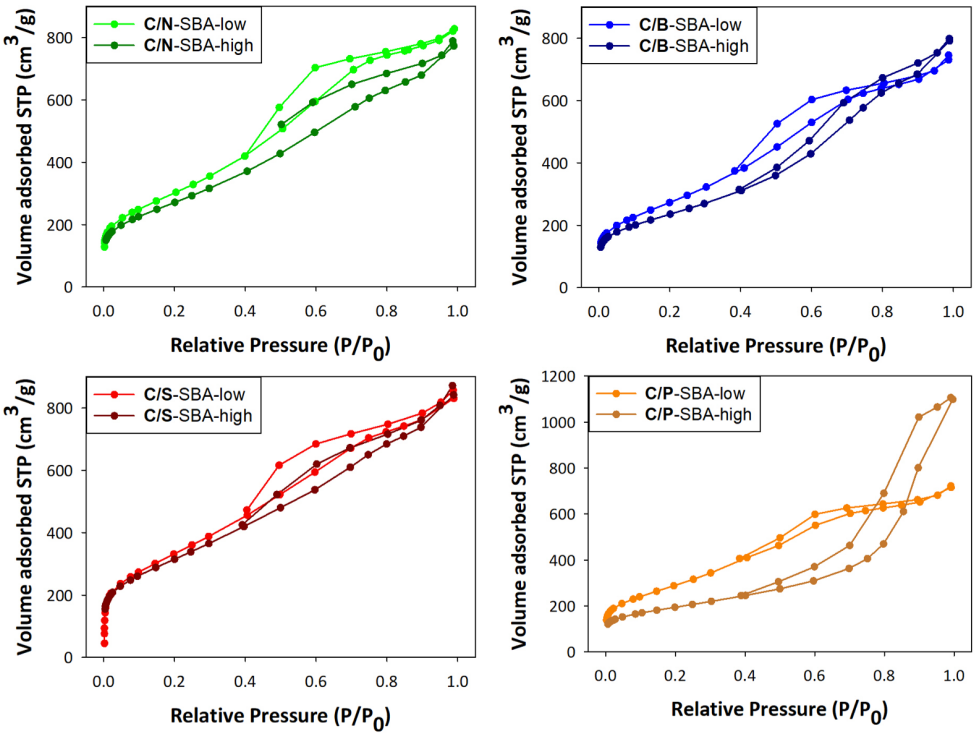


*Figure 5.12 Nitrogen sorption isotherms for SBA-15 templated carbons doped with nitrogen, boron, sulphur or phosphorus in low and high concentration.*

The increased concentration of heteroatom dopant precursor resulted in a successful increase of dopant amount, with at least three-fold higher concentrations, as was determined via XPS (Table 5.3). The higher dopant content caused a reduction in carbon and oxygen percentage, though C and O bonds remained the same with a similar distribution. Similarly, though at a higher amount, the distribution of different boron and phosphorus species stayed alike, while the higher sulphur concentration caused an additional peak at 164.3 eV corresponding to thiophene (~ 40%). The higher nitrogen content resulted in additional pyrrolic nitrogen, as can be seen in Figure 5.13.

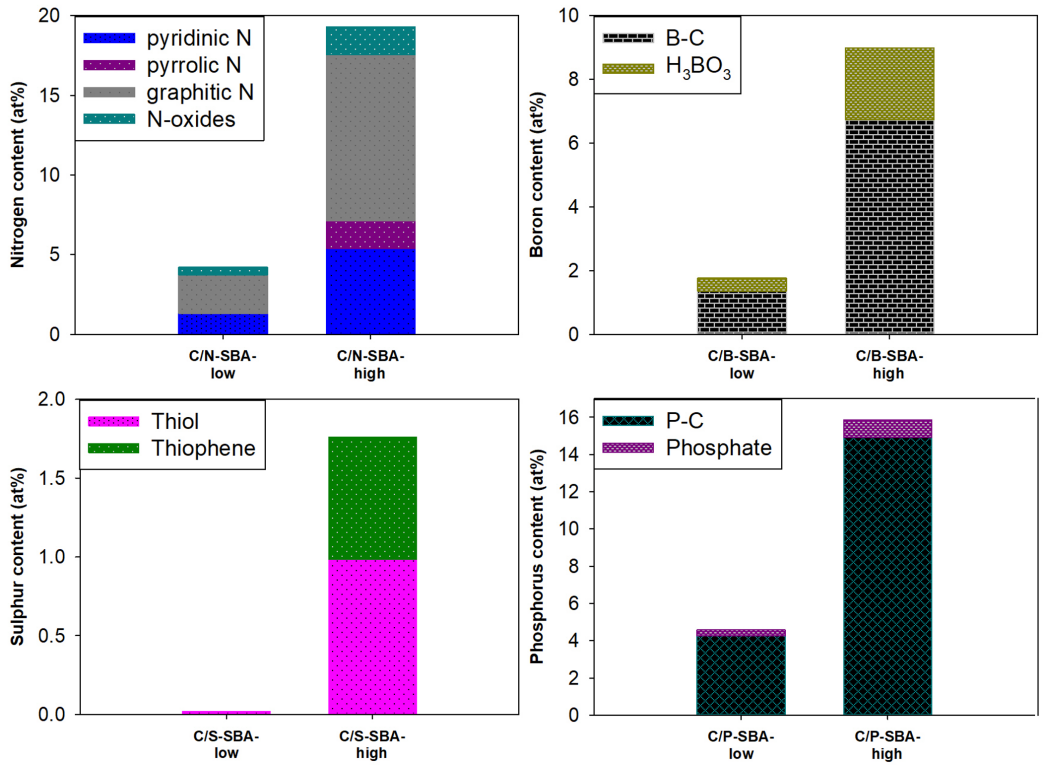


*Figure 5.13 Nitrogen, boron, sulphur and phosphorus species determined via deconvolution of XPS spectra for SBA-15 templated carbons doped with low and high heteroatom dopant amounts.*

Linear sweep voltammograms recorded in 0.1 M KOH for all doped samples and the control sample can be seen in Figure 5.14. A slight improvement was found for all samples containing the higher dopant amount, apart from the phosphorus doped sample, which was shifted towards a more negative onset potential, possibly due to the considerably lower surface area as compared to the low phosphorus doped version.

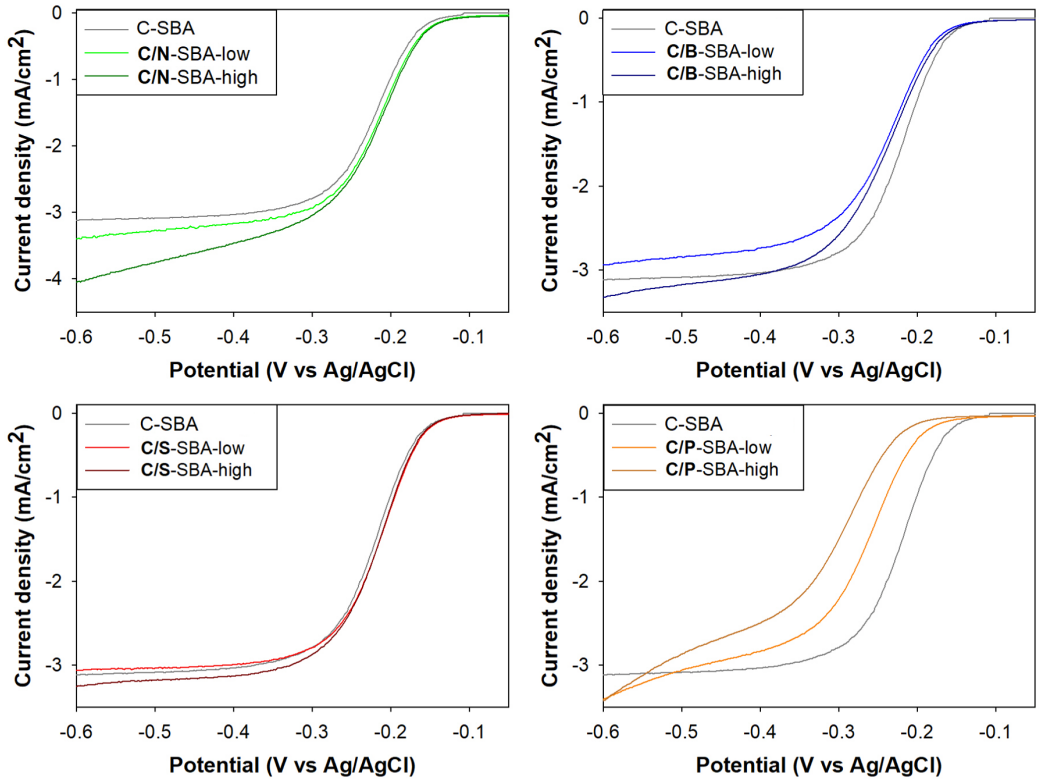


*Figure 5.14 Linear sweep voltammograms recorded with an RRDE setup at 1600 rpm in 0.1 M KOH for SBA-15 templated carbons doped with different heteroatom precursors in low and high concentration compared to an undoped control sample (C-SBA).*

A more detailed insight into the catalytic ORR activity was achieved by comparing the electron transfer numbers between the low and high doped samples, as can be seen in Table 5.4.

*Table 5.4 Average values (between -0.3 to -0.6 V vs Ag/AgCl) for electron transfer number in 0.1 M KOH determined via RDE with Koutecký–Levich equation.*

| Dopant | Electron transfer number |
|---|---|
| C-SBA | 2.29 |
| **C**/**N**-SBA-low | 2.74 |
| **C**/**N**-SBA-high | 3.48 |
| **C**/**B**-SBA-low | 2.40 |
| **C**/**B**-SBA-high | 2.61 |
| **C**/**S**-SBA-low | 2.34 |
| **C**/**S**-SBA-high | 2.49 |
| **C**/**P**-SBA-low | 2.50 |
| **C**/**P**-SBA-high | 2.58 |

An increase in electron transfer number was observed for all samples containing the higher dopant amount, with the most significant improvement obtained for the high concentration nitrogen doped sample from 2.74 to 3.48. The second-best enhancement

was found for the higher boron content, which shifted the electron transfer number from 2.40 to 2.61, followed by sulphur (2.34 to 2.49) and lastly phosphorus (2.50 to 2.58).

To get a better overview of how surface area and dopant species as well as dopant amount influenced the catalytic performance, a combination graph is shown in Figure 5.15. Considering that the ORR activity improved with higher dopant amounts, even at the presence of lower surface areas, the increase in defects due to the heteroatom doping is assumed to be responsible. The only drastic enhancement was seen for the nitrogen doped sample, where there was a considerably higher content of graphitic and pyridinic nitrogen present, which suggested, that only nitrogen can act as actual active sites during the ORR, while for the other dopants, defect sites due to the incorporation into the carbon framework influenced the catalytic performance.

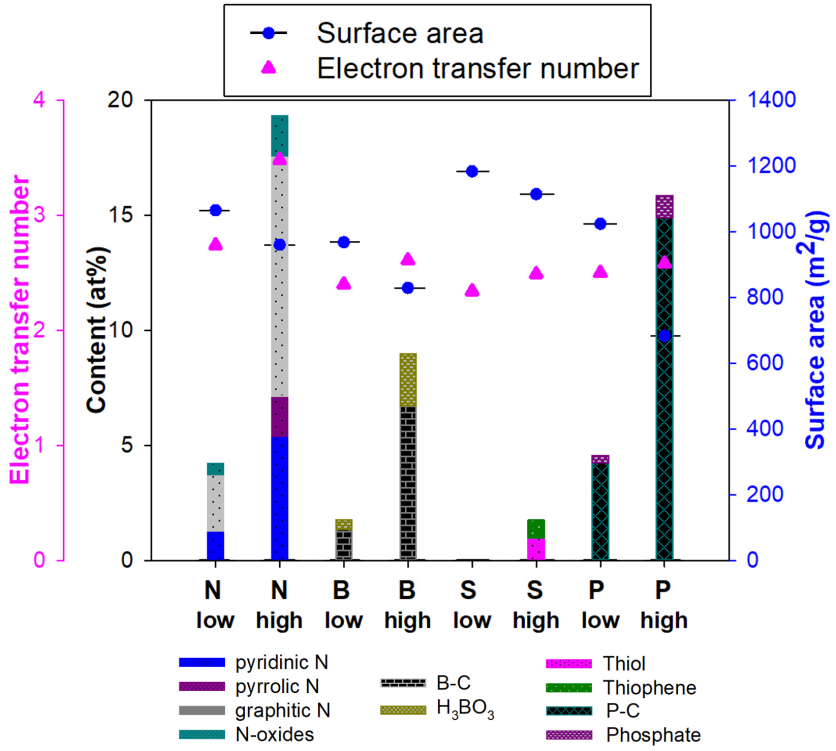


*Figure 5.15 Combination graph correlating the material's surface area and dopant species with the electrocatalytic activity (alkaline media) for SBA-15 templated carbons doped with different heteroatom precursors in low and high concentration.*

## 5.5 Influence of surface area and pore structure

As the influence of surface area remained unclear based on the above presented results, additional SBA-15 templated undoped as well as nitrogen doped carbons with a lower surface area, but similar pore structure and morphology were synthesised.

SEM images of the two undoped and nitrogen doped carbons can be seen in Figure 5.16, where the over infiltrated samples (X-over), Figure 5.16b and d, were found to consist of a mostly agglomerated rice like structure, due to the excess of infiltration solution coating also the outside of the SBA-15 template, instead of just infiltrating its pores.

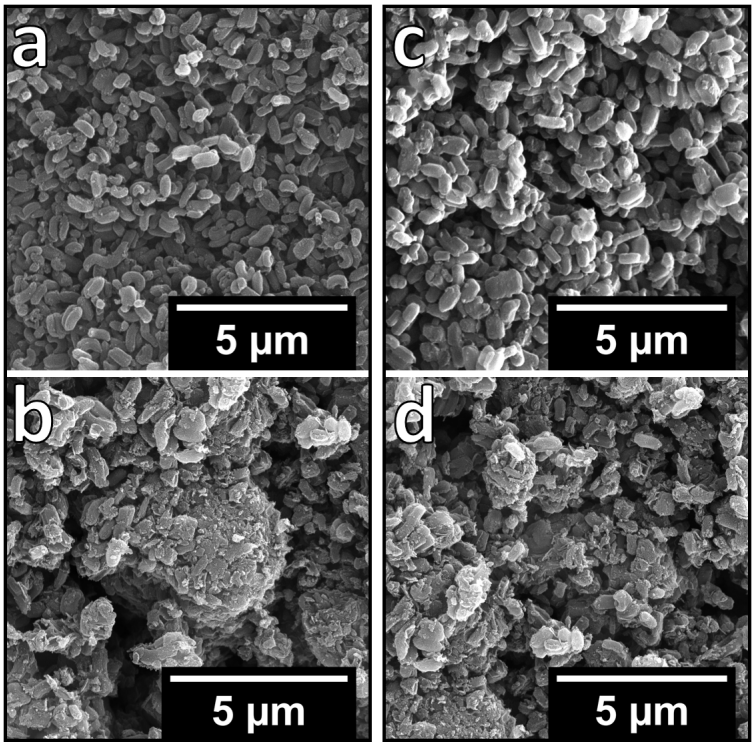


*Figure 5.16 SEM micrographs of SBA-15 templated carbons. a) undoped control (C-SBA), b) undoped control, over infiltrated, causing a lower surface area (C-SBA-over), c) nitrogen doped (C/N-SBA) and d) nitrogen doped, over infiltrated, with a lower surface area (C/N-SBA-over).*

The successful reduction in surface area and pore volume for both over infiltrated samples can be seen in Table 5.5. Though reduction in total pore volume and mesopore volume was only minor, the decrease in micropore volume was observed to be significant, possibly due to the denser and agglomerated structure.

*Table 5.5 Surface area, total pore volume, meso- and micropore volume, and respective dopant amount in SBA-15 templated carbons for an undoped control sample as well as nitrogen doped version and their over infiltrated counter samples with a reduced surface area.*

| Dopant | Surface area [$m^2 g^{-1}$] | $V_{tot}$ [$cm^3 g^{-1}$] | $V_{meso}$ [$cm^3 g^{-1}$] | $V_{micro}$ [$cm^3 g^{-1}$] | Dopant amount [at%] |
|---|---|---|---|---|---|
| C-SBA | 1264 | 1.420 | 1.221 | 0.199 | - |
| C-SBA-over | 705 | 1.199 | 1.129 | 0.070 | - |
| C/N-SBA | 1065 | 1.160 | 1.027 | 0.133 | 4.21 |
| C/N-SBA-over | 691 | 0.882 | 0.795 | 0.087 | 9.26 |

Nitrogen sorption isotherms (Figure 5.17) revealed lower surface areas for the over infiltrated samples, though similarly sized pores for all four carbons, with the addition of some larger mesopores for both over infiltrated samples.

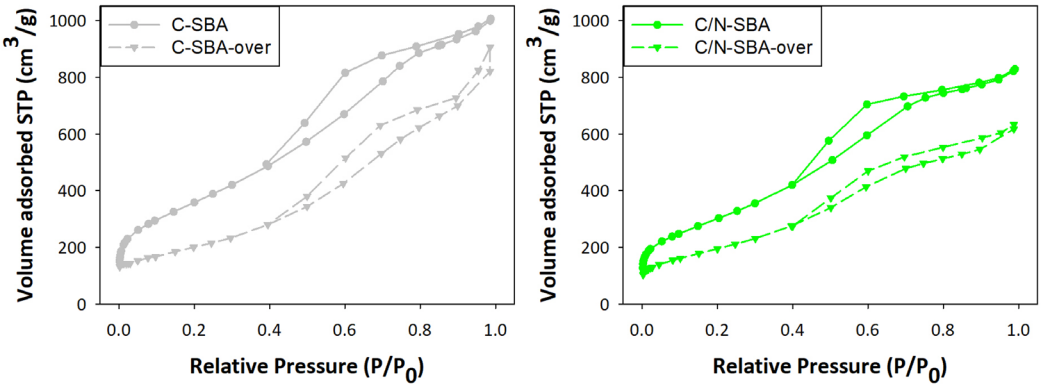


*Figure 5.17 Nitrogen sorption isotherms for SBA-15 templated carbons with high and low surface area for an undoped control sample (C-SBA) and a nitrogen doped version (C/N-SBA).*

Over infiltration of the nitrogen doped carbon caused an unexpected increase of nitrogen content by more than double from 4.21 at% to 9.26 at%, though distribution of nitrogen species remained unaltered, with the highest percentage represented by graphitic N (~ 60%), followed by pyridinic N (~ 30%) and N-oxides (~ 10%). The overall oxygen content remained unchanged after over infiltration of both samples, while the carbon content was slightly reduced after the incorporation of a higher nitrogen content, though the distribution of species stayed identical.

Electrochemical testing revealed the clear superiority of the higher surface area samples, as can be seen in Figure 5.18. Though the onset potential remained nearly the same between the low and high surface area samples, the limiting current density was strongly influenced by the lower surface area. This trend was assumed to be caused by mass transport limitations due to the lower surface and considerably lower amount of micropores, causing less beneficial contact/exchange between the materials surface and reactants.

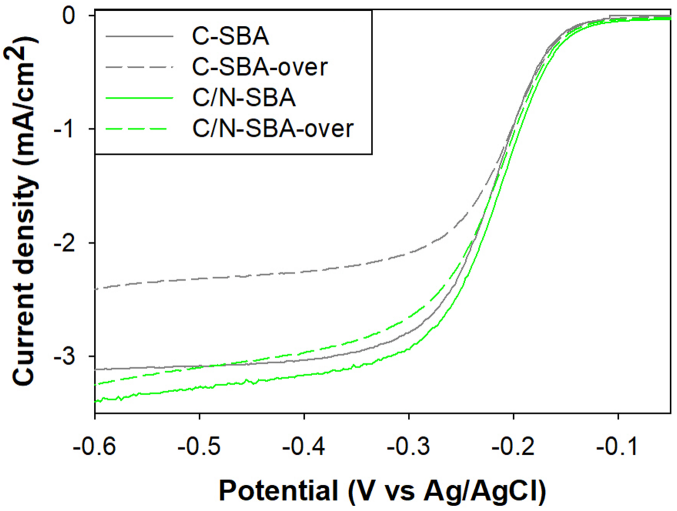


*Figure 5.18 Linear sweep voltammogram recorded with an RRDE setup at 1600 rpm in 0.1 M KOH for SBA-15 templated carbons with low and high surface area for an undoped control sample as well as nitrogen doped version.*

Electron transfer numbers (Table 5.6) revealed a similar trend as observed via linear sweep voltammetry, where the reduction in surface area also caused a decrease in electron transfer number during the ORR, from 2.29 to 2.00 for the undoped version and 2.74 to 2.55 for the nitrogen doped carbon.

*Table 5.6 Average values (between -0.3 to -0.6 V vs Ag/AgCl) for electron transfer number in 0.1 M KOH determined via RDE with Koutecký–Levich equation.*

| Dopant | Electron transfer number |
|---|---|
| C-SBA | 2.29 |
| C-SBA-over | 2.00 |
| C/N-SBA | 2.74 |
| C/N-SBA-over | 2.55 |

Interestingly, the considerably higher nitrogen content of the over infiltrated carbon did not cause an increase in ORR activity, which suggested that density as well as accessibility of the, presumably nitrogen centred, active sites are going hand in hand, where one cannot compensate for the absence or reduction of the other.

Apart from surface area, the influence of morphology and pore structure on the catalytic activity was also investigated. For this, additional templated carbons were synthesised with a different silica template, mesoporous shell silica spheres, MSS (chapter 5.2). The spherical hollow morphology can be seen in Figure 5.19 for a nitrogen (C/N-MSS), boron (C/B-MSS), sulphur (C/S-MSS) or phosphorus (C/P-MSS) doped sample. While some broken spheres were observed for all samples, the version doped with phosphorus yielded a higher amount of broken material, as is noticeable in Figure 5.19d.

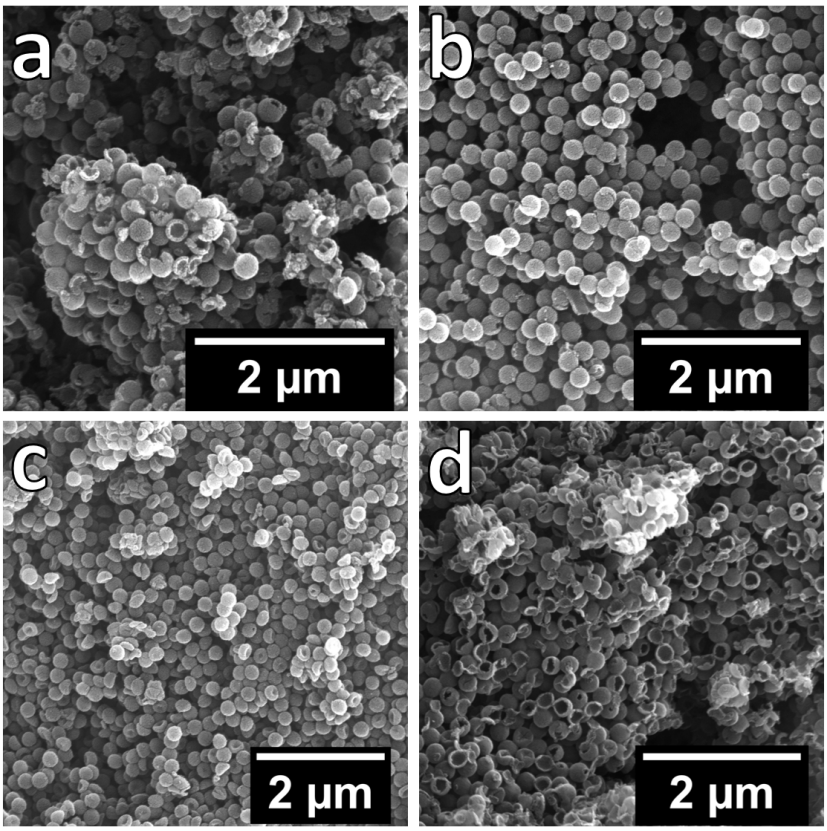


*Figure 5.19 SEM micrographs of doped carbons templated with mesoporous shell silica spheres including nitrogen, C/N-MSS (a), boron, C/B-MSS (b), sulphur, C/S-MSS (c) and phosphorus, C/P-MSS (d).*

Concurrent with the SEM images, the carbon containing phosphorus exhibited the lowest surface area as compared to the other MSS templated samples, possibly due to the high number of damaged spheres. Similar to the SBA templated samples, any heteroatom incorporation resulted in a decreased surface area and pore volume, most likely due to the change in composition of infiltration solution based on the different amounts of heteroatom precursors used, as well as the assumed swelling of the carbon framework due to incorporation of heteroatoms (Table 5.7).

Nitrogen sorption isotherms for the undoped control samples (Figure 5.4) and the different heteroatom doped versions (Figure 5.20), revealed a higher content of mesopores for MSS samples doped with nitrogen, boron and sulphur. Whereas the addition of phosphorus changed the overall pore morphology regardless of the template, resulting in a similar mesopore volume, but a higher micropore volume for the MSS template. MSS doped with phosphorus showed additional larger mesopores possibly due to the high breakage of spheres.

*Table 5.7 Surface area, total pore volume, meso- and micropore volume, and respective dopant amount in MSS and SBA-15 templated carbons for an undoped control sample as well as nitrogen, boron, sulphur and phosphorus doped version.*

| Sample | Surface area [$m^2\ g^{-1}$] | $V_{tot}$ [$cm^3\ g^{-1}$] | $V_{meso}$ [$cm^3\ g^{-1}$] | $V_{micro}$ [$cm^3\ g^{-1}$] | Dopant amount [at%] |
|---|---|---|---|---|---|
| C-MSS | 1496 | 2.160 | 2.024 | 0.136 | - |
| *C-SBA* | *1264* | *1.420* | *1.221* | *0.199* | - |
| C/N-MSS | 1272 | 1.802 | 1.656 | 0.146 | 20.80 |
| *C/N-SBA* | *960* | *1.097* | *0.954* | *0.143* | *19.31* |
| C/B-MSS | 1242 | 1.770 | 1.616 | 0.154 | 6.78 |
| *C/B-SBA* | *829* | *1.123* | *0.992* | *0.131* | *8.98* |
| C/S-MSS | 1397 | 1.843 | 1.686 | 0.157 | 0.05 |
| *C/S-SBA* | *1183* | *1.203* | *0.993* | *0.210* | *0.02* |
| C/P-MSS | 1162 | 1.780 | 1.561 | 0.219 | 13.73 (2.22 N) |
| *C/P-SBA* | *683* | *1.617* | *1.547* | *0.070* | *15.86 (0.29 N)* |

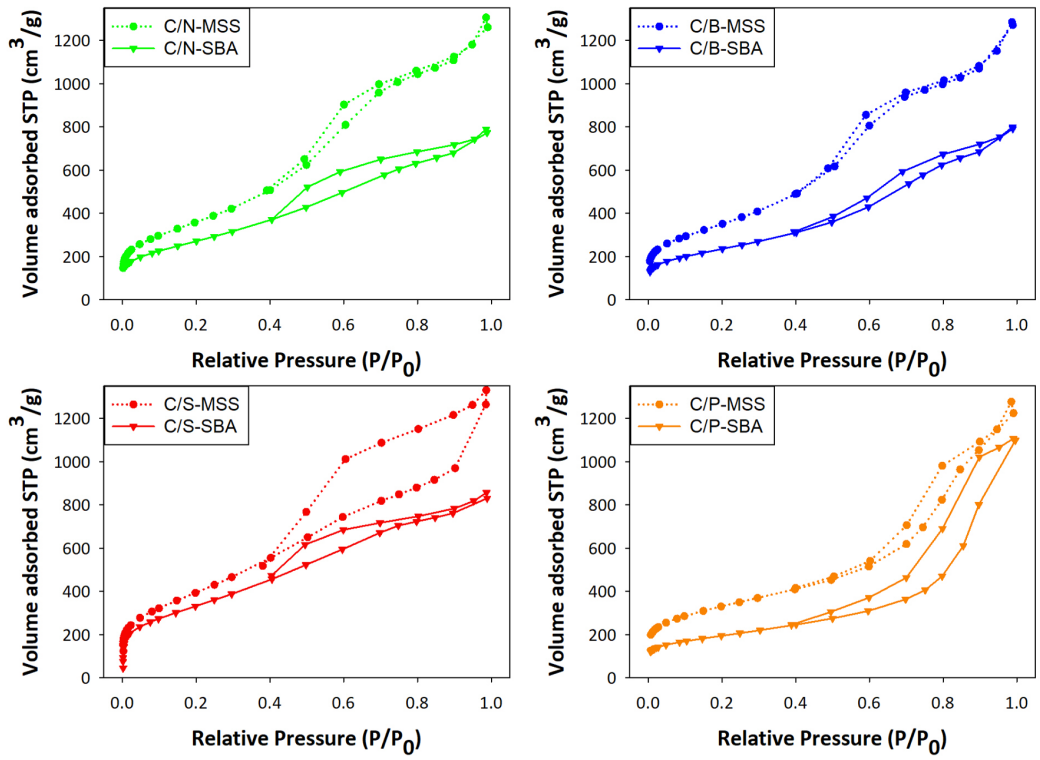


*Figure 5.20 Nitrogen sorption isotherms for MSS and SBA-15 templated carbons for nitrogen, boron, sulphur and phosphorus doped samples.*

A similar elemental composition (carbon, oxygen and respective dopant) was achieved for each pair of heteroatom doped carbons (Table 5.7), as well as the distribution of species, apart from the nitrogen doped samples. Here, in the sample templated with MSS, a higher amount of pyridinic and pyrrolic nitrogen was found, which caused a lower amount of graphitic nitrogen despite the overall higher nitrogen content (Figure 5.21).

The MSS templated phosphorus doped sample, exhibited a considerable amount of nitrogen contamination (2.22 at%) at the expense of a lower phosphorus incorporation as compared to the SBA-15 templated version.

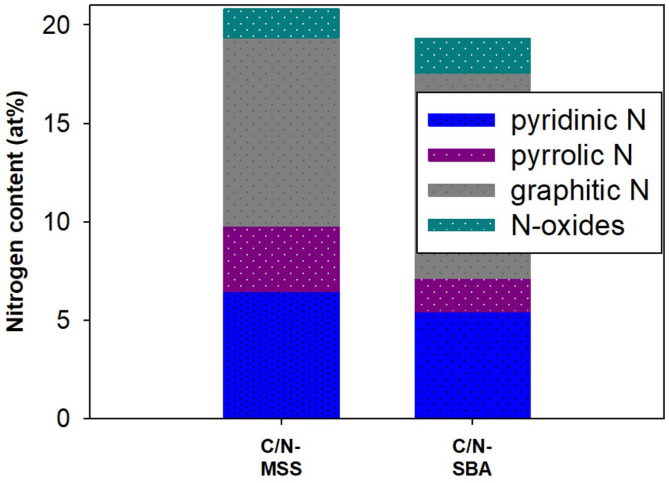


*Figure 5.21 Nitrogen species determined via deconvolution of N1s XPS spectra for MSS and SBA-15 templated carbons doped with nitrogen.*

Linear sweep voltammograms for the undoped control samples and each heteroatom dopant pair for the different templates are plotted in Figure 5.22.

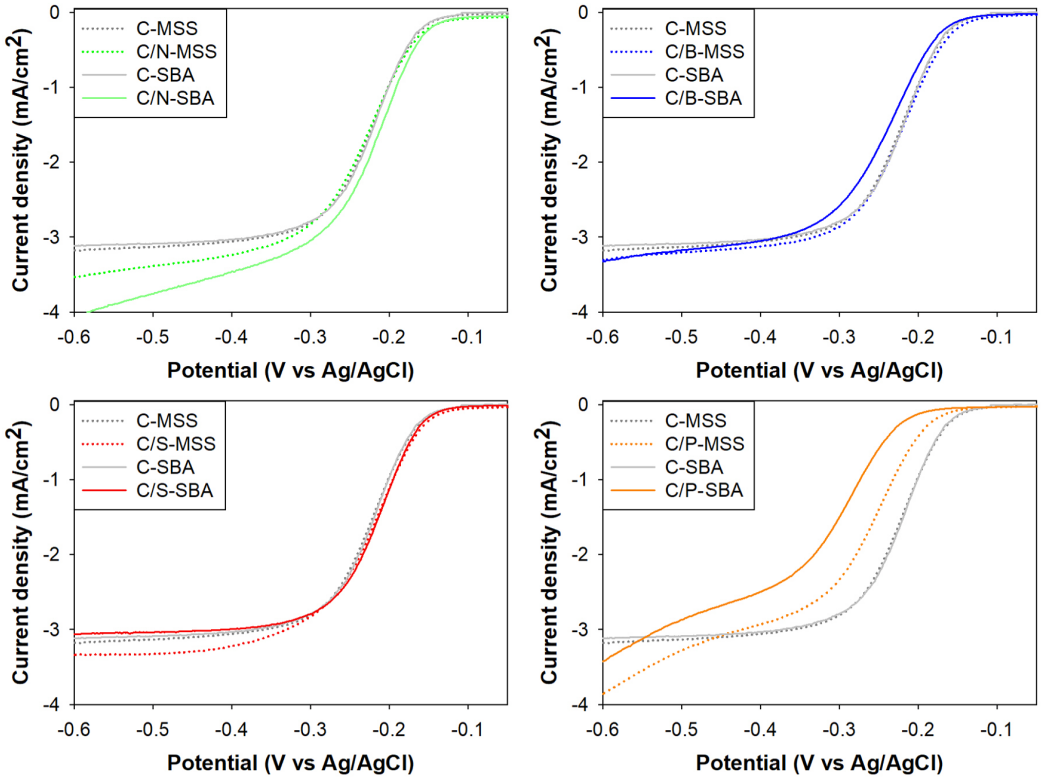


*Figure 5.22 Linear sweep voltammograms recorded with an RRDE setup at 1600 rpm in 0.1 M KOH for MSS and SBA-15 templated carbons for an undoped control sample as well as nitrogen, boron, sulphur and phosphorus doped version.*

Surprisingly, though exhibiting a different surface area and pore volume, both undoped control samples, C-MSS and C-SBA, show nearly identical linear sweep curves. A similar onset potential was found for the nitrogen doped samples, though the SBA-15 templated N doped carbon exhibited a more positive halfwave potential and limiting current density. The sulphur doped sample performed identical with respect to onset potential, while the MSS templated version had a lower limiting current density. For the boron and phosphorus doped samples a similar trend was observed, where the MSS templating caused a shift towards a more favourable onset potential and limiting current density. Electron transfer numbers for the undoped versions and the different heteroatom doped versions templated with MSS and SBA-15 can be seen in Table 5.8. The only improvement was found for the undoped control sample, where the higher surface area and pore volume caused an increase in electron transfer number from 2.29 to 2.51.

*Table 5.8 Average values (between -0.3 to -0.6 V vs Ag/AgCl) for electron transfer numbers in 0.1 M KOH determined via RDE with Koutecký–Levich equation for undoped control samples and heteroatom doped versions templated with different silica templates, MSS and SBA-15.*

| Sample | Electron transfer number for MSS samples | *Electron transfer number for SBA samples* |
|---|---|---|
| C | 2.51 | *2.29* |
| C/N | 3.28 | *3.48* |
| C/B | 2.58 | *2.61* |
| C/S | 2.25 | *2.34* |
| C/P | 2.51 | *2.58* |

Correlation graphs relating the materials surface area and dopant species/amounts to the electrocatalytic performance in terms of electron transfer number can be seen in Figure 5.23. The differently templated carbons doped with boron, sulphur or phosphorus showed only marginal differences in electron transfer number, suggesting that the difference in surface area and pore volume had no influence on the ORR mechanism. A slightly higher electron transfer number was found for the nitrogen doped sample templated with SBA-15 as compared to the MSS templated version with 3.48 and 3.28, respectively, despite its lower surface area. Here, the higher content of graphitic nitrogen in the SBA-15 templated samples was likely to contribute to the better ORR activity.

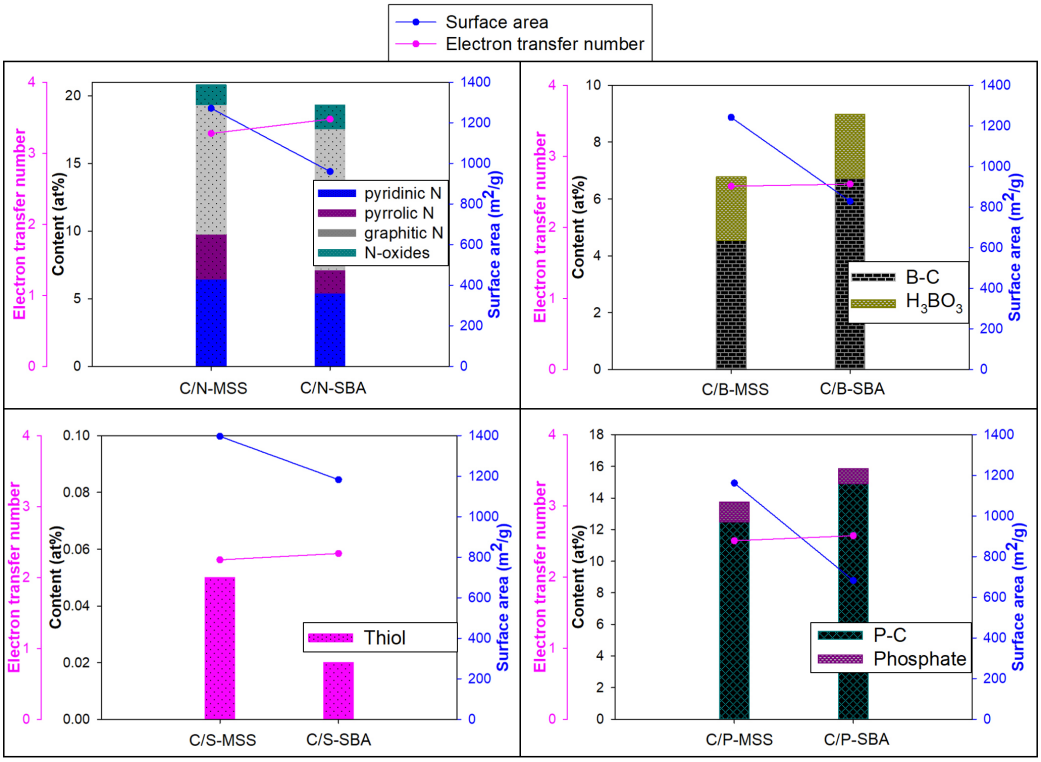


*Figure 5.23 Combination graph correlating the material's surface area and dopant species with the electrocatalytic activity (alkaline media) for SBA-15 and MSS templated carbons doped with different heteroatoms.*

## 5.6 Influence of combination doping

Combination doping of different heteroatom dopants is often reported to enhance the catalytic ability due to a synergistic effect between both dopants. To investigate the synergy between nitrogen and other heteroatom dopants, SBA-15 templated carbons were synthesised containing nitrogen and boron (C/N/B-SBA), nitrogen and sulphur (C/N/S-SBA), or nitrogen and phosphorus (C/N/P-SBA).

SEM images (Figure 5.24) showed a similar rice like morphology for all combination doped samples, although a more densely packed structure was observed for the nitrogen and boron doped version.

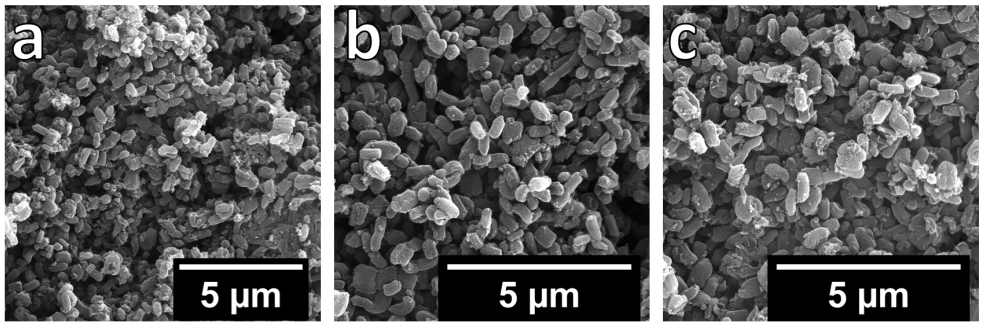


*Figure 5.24 SEM micrographs of SBA-15 templated carbons doped with a) nitrogen and boron, b) nitrogen and sulphur and c) nitrogen and phosphorus.*

In accordance with the SEM images, the nitrogen and boron doped sample also exhibited the lowest surface area and pore volume with only 602 $m^2 g^{-1}$, as compared to 901 $m^2 g^{-1}$ and 909 $m^2 g^{-1}$ for C/N/S-SBA and C/N/P-SBA, respectively, as can be seen in Table 5.9.

*Table 5.9 Surface area, total pore volume, meso- and micropore volume, and respective dopant amount in SBA-15 templated carbons for an undoped control sample as well as nitrogen/boron, nitrogen/sulphur and nitrogen/phosphorus doped versions.*

| Dopants | Surface area [$m^2 g^{-1}$] | $V_{tot}$ [$cm^3 g^{-1}$] | $V_{meso}$ [$cm^3 g^{-1}$] | $V_{micro}$ [$cm^3 g^{-1}$] | Dopant amount [at%] |
|---|---|---|---|---|---|
| C-SBA | 1264 | 1.420 | 1.221 | 0.199 | - |
| C/N/B-SBA | 602 | 0.702 | 0.625 | 0.077 | 11.6 / 6.9 |
| C/N/S-SBA | 901 | 1.062 | 0.917 | 0.145 | 12.2 / - |
| C/N/P-SBA | 909 | 0.955 | 0.800 | 0.155 | 12.6 / 13.4 |

Similarly to the surface area, pore volume of C/N/B-SBA was significantly lower than in the other two samples, though pore sizes remained in the same range, as can be seen in Figure 5.25.

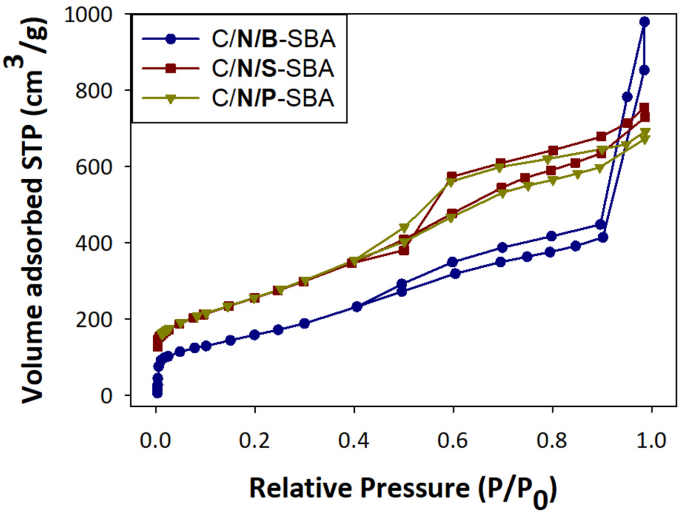


*Figure 5.25 Nitrogen sorption isotherms for SBA-15 templated carbons for nitrogen/boron, nitrogen/sulphur and nitrogen/phosphorus doped versions.*

Elemental composition determined via XPS revealed a similar level of nitrogen doping in all samples between 11.6 to 12.6 at%. Deconvolution of the N1s spectra revealed the presence of pyridinic (~ 25%), pyrrolic (~ 20%) and graphitic (~ 50%) nitrogen, as well as small amounts of N-oxides. Additional boron and phosphorus incorporation were successful with 6.9 and 13.4 at%, respectively, while the sulphur content was below the XPS detection limit. Similar to phosphorus doped samples reported on earlier, C/N/P-SBA contained roughly double the amount of oxygen (13.4 at%) as compared to C/N/B-SBA and C/N/S-SBA, with an increased peak area around 531 eV in the O1s spectra,

indicating the presence of phosphates besides C=O bonding. No B-N binding sites were observed in the N1s or B1s spectra for C/N/B-SBA, which only indicates that the amount present was too low to be detected, and their presence could be possible in the bulk of the sample.

Linear sweep voltammograms for the three combination doped versions and the undoped control sample can be seen in Figure 5.26. The least positive onset potential was found for the sample containing nitrogen and phosphorus, where similar to the other phosphorus doped carbons shown earlier, the shape of the LSV seemed to be determined by the presence of phosphorus, though the addition of nitrogen caused a slight positive shift of the whole curve. Considering the detectable absence of sulphur in C/N/S-SBA, pure nitrogen doping was assumed, where a similar onset potential was found when compared to C/N/B-SBA, but a slightly lower limiting current density, possibly due to the higher surface area and mesopore volume, causing less mass transport limitations. Interestingly, the LSV curve for C/N/B-SBA was found to be identical with the over infiltrated nitrogen doped carbon (C/N-SBA-over in chapter 5.5), which exhibited a similar surface area of 691 $m^2$ $g^{-1}$ and nitrogen doping of 9.26 at%, which also had the identical electron transfer number of 2.55. This observation suggested that the additional boron doping had no influence on the catalytic activity, leaving the nitrogen content and possibly the surface area to determine the ORR performance.

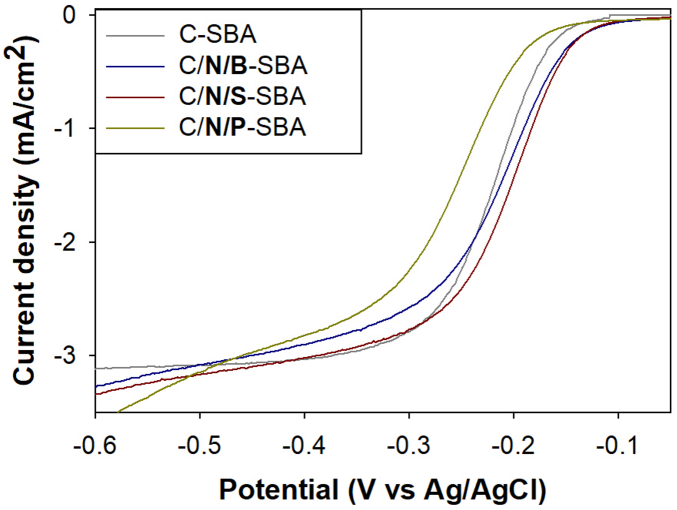


*Figure 5.26 Linear sweep voltammogram recorded with an RRDE setup at 1600 rpm in 0.1 M KOH for SBA-15 templated carbons for an undoped control sample as well as nitrogen/boron, nitrogen/sulphur and nitrogen/phosphorus doped versions.*

Electron transfer numbers determined via RDE can be found in Table 5.10, where all three combination doped carbons were found to exhibit similar values. This result together with the identical performance of C/N/B-SBA and the over infiltrated N carbon (C/N-SBA-over), as mentioned before, indicated that the addition of other heteroatoms

influenced the material's properties in terms of surface area, pore size and LSV curve shape, but had no noticeable influence on the actual ORR activity/mechanism, which seemed to be determined by the presence of nitrogen.

*Table 5.10 Average values (between -0.3 to -0.6 V vs Ag/AgCl) for electron transfer numbers in 0.1 M KOH determined via RDE with Koutecký–Levich equation for an undoped control sample and heteroatom doped versions templated with SBA-15.*

| Dopants | Electron transfer number |
|---|---|
| C-SBA | 2.29 |
| C/N/B-SBA | 2.55 |
| C/N/S-SBA | 2.56 |
| C/N/P-SBA | 2.59 |

A correlation graph (Figure 5.27) relating the materials surface area and dopant species/amounts to the achieved electron transfer numbers highlighted the above made assumption that neither surface nor other dopants, apart from nitrogen, influence the ORR mechanism.

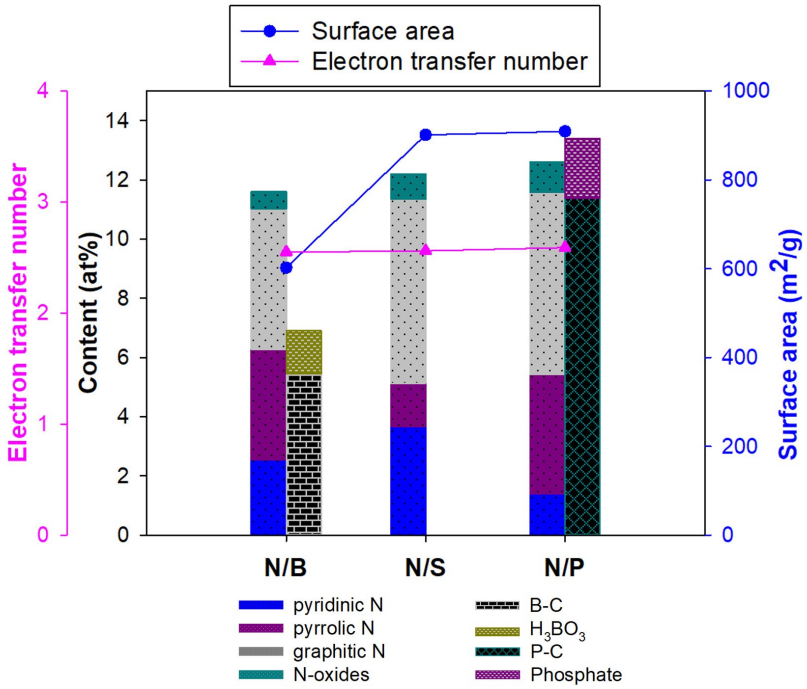


*Figure 5.27 Combination graph correlating the material's surface area and dopant species with the electrocatalytic activity (alkaline media) for SBA-15 templated carbons doped with nitrogen/boron, nitrogen/sulphur and nitrogen/phosphorus.*

## 5.7 Influence of additional iron doping

Lastly, the influence of different heteroatom dopants on the incorporation of iron and the materials ORR performance was investigated. For this, four samples were templated with SBA-15 and doped with iron in combination with nitrogen, boron, sulphur or phosphorus labelled C/N/Fe-SBA, C/B/Fe-SBA, C/S/Fe-SBA and C/P/Fe-SBA, respectively.

SEM images for the four combination doped samples can be seen in Figure 5.28. The typical rice like shape was observed for all carbons, confirming the successful infiltration of the SBA-15 template.

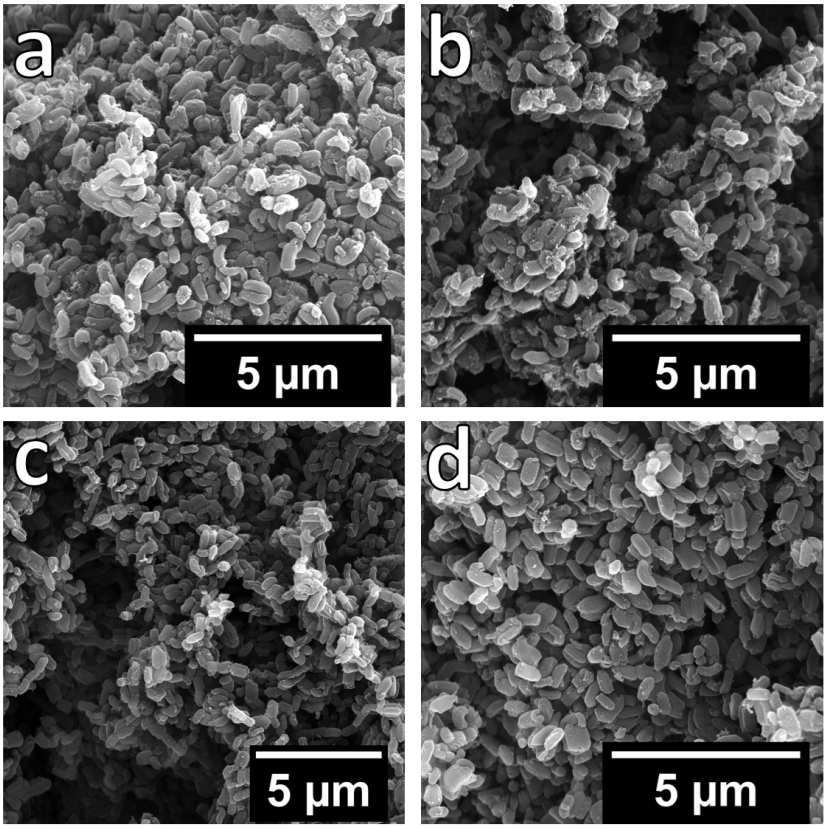


*Figure 5.28 SEM micrographs of SBA-15 templated carbons doped with a) nitrogen and iron, b) boron and iron, c) sulphur and iron, and d) phosphorus and iron.*

Surface area and pore volumes are shown in Table 5.11, where the incorporation of nitrogen/iron as well as sulphur/iron did not interfere greatly, while the addition of boron/iron and phosphorus/iron caused a reduction in surface area and pore volume, as was observed similarly for the corresponding metal-free version.

*Table 5.11 Surface area, total pore volume, meso- and micropore volume, and respective dopant amount in SBA-15 templated carbons for an undoped control sample as well as nitrogen/iron, boron/iron, sulphur/iron and phosphorus/iron doped versions.*

| Dopants | Surface area [$m^2\ g^{-1}$] | $V_{tot}$ [$cm^3\ g^{-1}$] | $V_{meso}$ [$cm^3\ g^{-1}$] | $V_{micro}$ [$cm^3\ g^{-1}$] | Dopant amount [at%] |
|---|---|---|---|---|---|
| C-SBA | 1264 | 1.420 | 1.221 | 0.199 | - |
| C/N/Fe-SBA | 1272 | 1.344 | 1.166 | 0.178 | 11.7 / 0.3 |
| C/B/Fe-SBA | 970 | 1.044 | 0.843 | 0.201 | 4.8 / 0.3 |
| C/S/Fe-SBA | 1112 | 1.590 | 1.440 | 0.150 | 2.8 / - |
| C/P/Fe-SBA | 963 | 0.755 | 0.544 | 0.211 | 17.0 / 1.5 (2.6 N) |

Interestingly, the presence of iron during the pyrolysis enabled the incorporation of higher dopant amounts for all heteroatom dopants at the cost of oxygen incorporation, as compared to without iron. The identically synthesised samples without iron resulted in a nitrogen, boron, sulphur and phosphorus (contamination of N) content of 4.21 at%, 1.77 at%, 0.02 at% and 4.57 at% (0.46 at% N), respectively. Dopant species remained unchanged as compared to their counterparts without iron, and where found to be graphitic N (65%), pyridinic N (24%) and N-oxides (11%) for C/N/Fe-SBA, as well as B-C (74%) and $H_3BO_3$ (26%) for C/B/Fe-SBA, thiol for C/S/Fe-SBA and P-C (84%) as well as P-O (16%) for C/P/Fe-SBA.

Iron doping was found to be very low (0.3 at%) for C/N/Fe-SBA and C/B/Fe-SBA, while the contained iron in C/S/Fe-SBA was below the XPS detection limit. The phosphorus and iron doped sample exhibited a slightly higher amount of iron with 1.5 at%. The overall low presence of iron was likely due to the silica etching step with $NH_4HF_2$, which can also remove/wash out iron species. $Fe2p_{3/2}$ spectra (Figure 5.29) for C/N/Fe-SBA, C/B/Fe-SBA and C/P/Fe-SBA exhibited three distinct peaks between 710-711 eV, around 714 eV and the typical satellite peak between 718-719 eV. Satellite peaks, occurring at a higher binding energy than the main peak, are usually related to “shake-up” or “shake-off” processes during electron ejection due to energy losses owing to abrupt alterations in effective charge.[207] Binding energies, especially of the satellite peaks, were indicative of the presence of ferric iron. While the two first peaks can indicate either different configurations of the ferric iron, e.g. octahedral or tetrahedral, or involvement in different iron oxides, $Fe_2O_3$ and $Fe_3O_4$, respectively.[210–212]

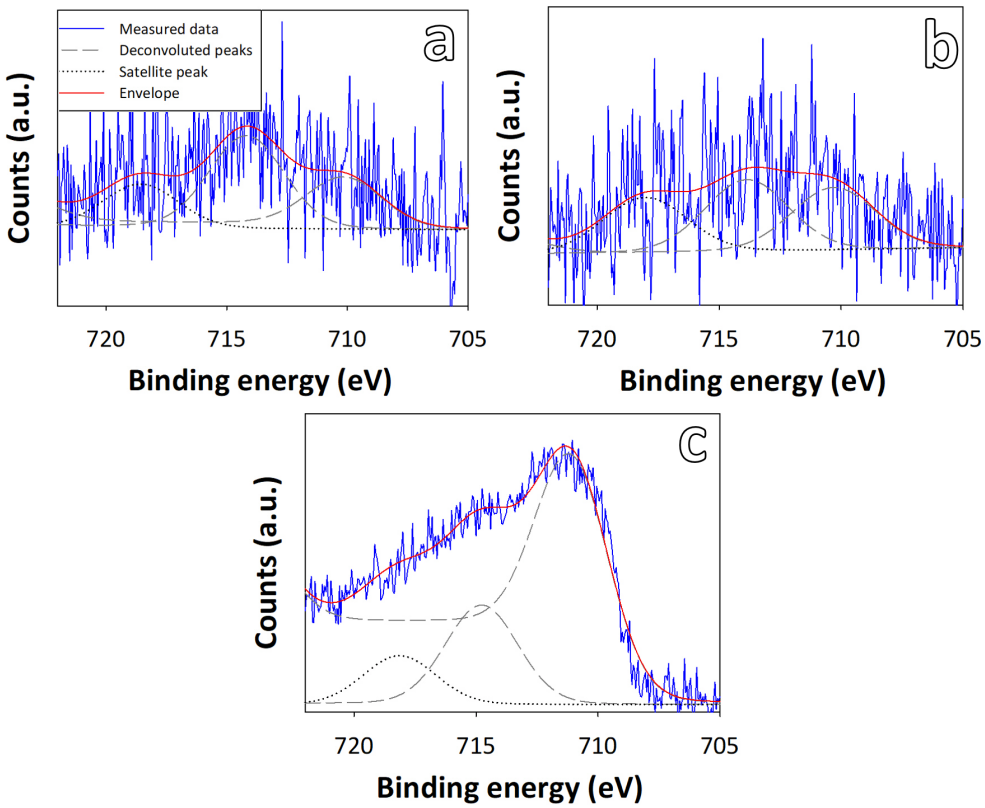


*Figure 5.29 Deconvoluted $Fe2p_{3/2}$ XPS spectra for SBA-15 templated carbons doped with a) iron and nitrogen, b) iron and boron and c) iron and phosphorus.*

Linear sweep voltammetry was carried out in 0.1 M KOH for the four iron doped samples and compared to the undoped control sample (Figure 5.30). The incorporation of nitrogen and iron caused a significant improvement for the onset potential and limiting current density as compared to the other iron combination doped carbons and the undoped control sample, possibly due to the coordination of $FeN_x$-C sites, which are suspected to be catalytically most active (chapter 2.1.3.2).

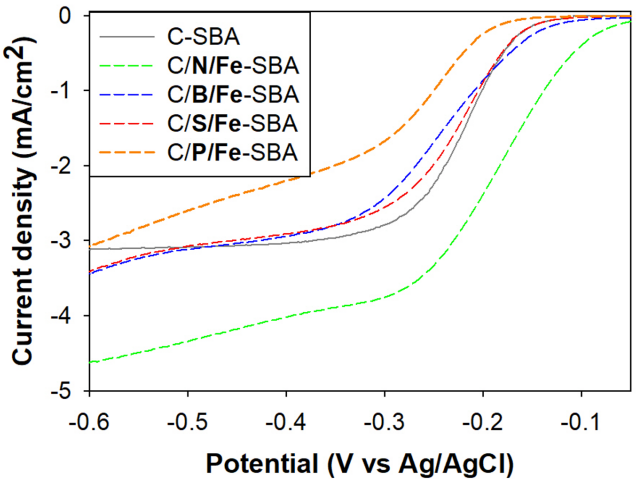


*Figure 5.30 Linear sweep voltammogram recorded with an RRDE setup at 1600 rpm in 0.1 M KOH for SBA-15 templated carbons for an undoped control sample as well as nitrogen/iron, boron/iron, sulphur/iron and phosphorus/iron doped versions.*

Electron transfer numbers determined via both, RRDE and RDE, can be seen in Table 5.12. Interestingly, while the values for all other samples seemed to be overestimated via the RRDE calculations, C/N/Fe-SBA was found to be underestimated as compared to the electron transfer number obtained via Koutecký–Levich equation but was found to be the best performing sample regardless of the collection technique. A general improvement in electron transfer number was also found for the three other iron doped samples as compared to their metal-free counterparts from 2.40 to 2.74 for C/B/Fe-SBA, 2.34 to 2.70 for C/S/Fe-SBA and 2.50 to 2.74 for C/P/Fe-SBA.

*Table 5.12 Average values (between -0.3 to -0.6 V vs Ag/AgCl) for electron transfer numbers in 0.1M KOH determined via RRDE and RDE for SBA-15 templated carbons for an undoped control sample as well as nitrogen/iron, boron/iron, sulphur/iron and phosphorus/iron doped versions.*

| Dopants | Electron transfer number (RRDE) | Electron transfer number (RDE) |
|---|---|---|
| C-SBA | 2.92 | 2.29 |
| C/N/Fe-SBA | 3.53 | 3.95 |
| C/B/Fe-SBA | 3.00 | 2.74 |
| C/S/Fe-SBA | 2.95 | 2.70 |
| C/P/Fe-SBA | 3.32 | 2.74 |

The similarity in electron transfer number for C/B/Fe-SBA, C/S/Fe-SBA and C/P/Fe-SBA, regardless of their difference in surface area and dopant amounts further suggested that neither of these heteroatoms acts as actual active site and that the catalytic activity was most likely determined by the presence of iron species, such as iron oxide, which also became apparent when the parameters were plotted in relation (Figure 5.31).

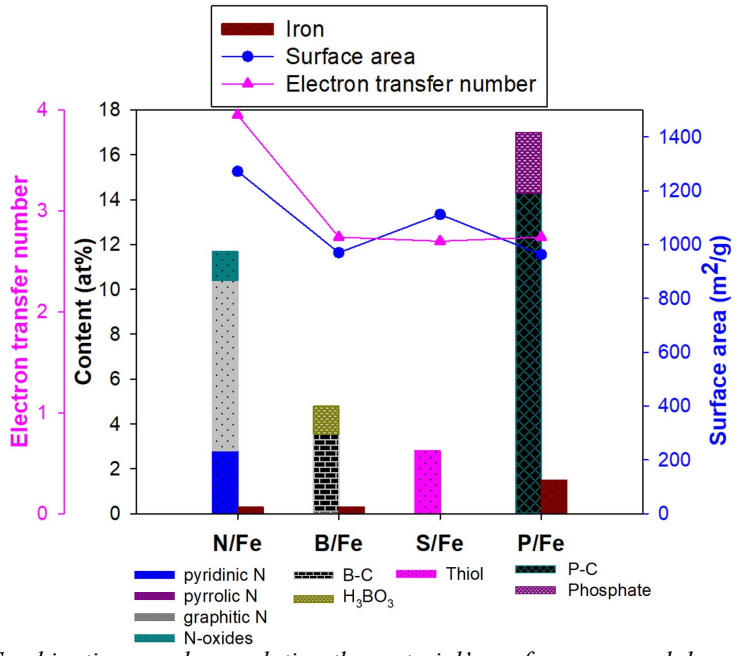


*Figure 5.31 Combination graph correlating the material's surface area and dopant species with the electrocatalytic activity for SBA-15 templated carbons doped with N/Fe, B/Fe, S/Fe and P/Fe.*

## 5.8 Summary

Templated carbons were synthesised to investigate the influence of the metal-free heteroatom dopants nitrogen, boron, sulphur and phosphorus, as well as the influence of surface area and pore volume and their possible formation of active non-noble metal sites via the addition of iron.

Different heteroatom precursors were used to determine their ability of incorporating the respective heteroatom dopant into the carbon matrix. In general, incorporation of nitrogen and phosphorus resulted in higher dopant amounts, as compared to boron and sulphur. Nitrogen incorporation was found to be most successful using urea, which suggested that smaller molecules with a lower molecular mass are more easily built in as compared to larger precursor molecules. Phosphoric acid proved to be the most promising phosphorus dopant source, though all phosphorus doped samples were found to have nitrogen contamination, a higher oxygen content as compared to non-phosphorus carbons and a reduced surface area and slightly changed pore size distribution. The higher oxygen content was attributed to the presence of phosphate, while the nitrogen contamination was assumed to occur due to gases formed during the pyrolysis reacting with phosphorus. The lower surface area but higher pore volume was thought to result from phosphoric acid etching larger mesopores during the pyrolysis as well oxygen atoms replacing carbon. Boric acid offered the highest boron content, though the incorporation of boron caused lower surface areas, sulphur incorporation proved difficult, regardless of the use of an aromatic or aliphatic precursor and was only achieved in trace amounts (0.02 at%), possibly due to the large atomic size of the sulphur atom.

Though a conclusive statement was hard to make due to changes in surface area and dopant amounts amongst the different heteroatom dopants, results suggested that nitrogen was the only heteroatom exerting an actual influence on the catalytic activity, resulting in higher electron transfer numbers as compared to the other dopants. The other dopants exhibited more or less the same performance regardless of the dopant content, though slightly improved when compared to the undoped control. These findings suggested that incorporated nitrogen acts as catalytic sites, be it pyridinic or graphitic nitrogen, while the other dopants only enhanced the catalytic activity by possibly creating defects in the carbon matrix. Interestingly, the presence of phosphorus always caused a change of the shape of the linear sweep voltammogram, resulting in a less positive onset potential and higher limiting current density.

Lowering of surface area at the expense of meso-, but mostly micropores resulted in a similar onset potential, but considerably higher limiting current densities due to increased

mass transport limitations, which also had a negative influence on the electron transfer number. A slightly higher surface area and increased micropore volume, achieved with a different silica template, did not yield any increase in activity, suggesting that active sites present in the micropores are not accessible.

Combination doping of nitrogen/boron, nitrogen/sulphur and nitrogen/phosphorus resulted in a similar performance regardless of the additional dopant, which again suggested that only nitrogen plays a crucial role towards the ORR activity.

The addition of iron and its interaction with the different heteroatom dopants resulted in higher dopant amounts for all heteroatoms as compared to the metal-free counterparts, whereas the oxygen content was reduced. A significant increase in catalytic activity was observed for the nitrogen and iron doped sample with a high electron transfer number of 3.95, while the other dopant combinations caused an increase in electron transfer number when compared to the metal-free versions, but again displayed no significant difference amongst each other, suggesting that the presence of iron determined their ORR performance.

# Chapter 6 | Conclusion and outlook

The aim of this thesis was to synthesise platinum-free electrocatalysts for the oxygen reduction reaction via different synthesis methods to produce doped carbon materials and investigate their catalytic activity and correlate the latter to the materials physicochemical properties.

For this, an environmentally friendly and low-cost approach for producing heteroatom doped materials was used, called hydrothermal carbonisation, where biomass or biomass precursors can be converted into different multifunctional nanoporous carbon materials with a high specific surface area and large pore volume. With this technique cryogels were synthesised from glucose and ovalbumin, a protein from chicken egg white, which adopts a double role as structure directing and surface stabilising agent while also serving as a nitrogen source.

The influence of an easy and environmental friendly activation approach was tested on the nitrogen doped cyrogel, where a mixed atmosphere of nitrogen and compressed air was used for oxygen activation during the high temperature pyrolysis at 1000 °C. The presence of oxygen during the pyrolysis increased the carbogels surface area and micropore volume up to 1150 $m^2$ $g^{-1}$ due to $O_2$ etching of carbon and nitrogen atoms at the cost of yield loss and lower nitrogen amounts. A mixed atmosphere of nitrogen and compressed air, corresponding to 2 % of oxygen, was found to deliver the most favourable material properties with a surface area of 874 $m^2$ $g^{-1}$, 1.8 at% of nitrogen (consisting of a beneficial ratio of graphitic and pyridinic N), while the yield loss stayed in an acceptable range (> 30% yield) and the samples catalytic activity towards the oxygen reduction reaction was more enhanced as compared to other $N_2$/air ratios.

Additional heteroatom doping of the nitrogen doped carbogel with sulphur did not result in an increased catalytic performance due to a decrease in surface area and nitrogen content. The addition of boric acid caused a different cyrogel structure, with lower surface area after the high temperature pyrolysis than the pure nitrogen doped carbogel. A structure directing role of the boron precursor during the formation of the cryogel was proposed, rather than ovalbumin, allowing for the protein to act as more efficient nitrogen source resulting in an overall higher nitrogen content. For the studied metal-free carbogels, the nitrogen content seemed to influence the limiting current density, while the oxygen content seemed to have an effect on the onset potential. Further catalytic testing revealed superior oxygen reduction reaction activity for samples containing boron, which was assumed to be due to a higher content of quinone groups as well as graphitic and

pyridinic N, acting as active sites, as compared to samples without boron. An additional effect due to the different morphology of the boron containing carbogels was suggested to lead to more favourable mass transport, which further enhanced the catalytic activity. The highest electron transfer number and lowest hydrogen peroxide yield were found for the carbogel containing nitrogen and boron.

The influence of iron precursors during the hydrothermal carbonisation of glucose and ovalbumin was further investigated. Here, ferric iron salt was found to increase the material's mechanical stability (diameter of nanowires) and mass yield and aided the formation of a more expanded coral like structure. These changes were assumed to be due to the iron salt lowering the pH of the reaction mixture, which promoted a faster glucose dehydration in the cascade of reactions during the hydrothermal carbonisation and thus speeding up the precipitation/nucleation of nanosized carbon particles. Moreover, the presence of the iron salt caused accelerated denaturation of the ovalbumin which resulted in a faster demixing of the glucose (after its dehydration) from the reaction mixture, directing its crosslinking into the network structure. The iron present in the cryogel was found to be homogeneously distributed after the hydrothermal carbonisation. During the high temperature pyrolysis under a mixed atmosphere of nitrogen and compressed air, iron oxide nanoparticles were formed at temperatures above 400 °C. These particles were found to move through the sample and act as a catalyst to aid the graphitisation of the carbogel, while at the same time act as an activation agent to increase the surface area before reacting and precipitating on the pyrolysis crucible. Only small amounts (0.05 at%) of iron were detected on the surface of the material, while a significantly larger content was found in the bulk (2.7 wt%) of the carbogel. It was assumed that only surface iron accessible to the pyrolysis atmosphere formed iron oxide particles, while the rest remained homogeneously distributed in the carbon framework, coordinated with carbon, oxygen or nitrogen.

The influence of additional heteroatom doping with sulphur and/or boron on the nitrogen and iron cryo- and carbogels was also explored. Here, a clear influence of additional heteroatom dopants on the morphology, surface area and atomistic structure was observed. The presence of a boron precursor during the hydrothermal carbonisation caused a competition with the iron salt catalysing the reaction and ovalbumin directing the structure of the carbogel, leading to an inhomogeneous morphology and reduced surface area, while incorporating higher amounts of nitrogen and iron. The presence of a sulphur precursor did not drastically interfere with the formation of the nanowired carbogel structure but caused a slight reduction in surface area and nitrogen content. A more crucial change was induced by the presence of sulphur on the atomistic structure of

the carbogel, causing, besides ferric iron which was found in all carbogels, the additional presence of elemental iron. The catalytic activity towards the oxygen reduction reaction was observed to be more beneficial for samples containing only nitrogen and iron or nitrogen, boron and iron as compared to samples including sulphur. Active sites were observed to be different under alkaline and acidic conditions, where the presence of iron active sites seemed to be crucial in acidic electrolyte, while other properties such as surface area as well as nitrogen (pyridinic and graphitic N) and oxygen (quinone groups) species also played a role in alkaline electrolyte.

Findings in chapters 3 and 4 indicated that key properties such as carbogel structure, surface area, pore properties and dopant level were easily influenced by the addition of heteroatom and iron precursors to the hydrothermal carbonisation reaction mixture, which significantly influenced the overall catalytic performance. Due to variations occurring for multiple parameters at a time, the role of different heteroatom dopants and their interaction with iron was hard to judge. To overcome this and get a deeper understanding of how each single heteroatom dopant can influence the catalytic activity towards the oxygen reduction reaction templated carbons were synthesised.

Different heteroatom precursors were tested to determine their ability of incorporating the respective heteroatom dopant into the carbon matrix. In general, incorporation of nitrogen and phosphorus resulted in higher dopant amounts, as compared to boron and sulphur. Nitrogen incorporation was found to be most successful using urea, which suggested that smaller molecules with a lower molecular mass are more easily built in as compared to larger precursor molecules. Phosphoric acid proved to be the most promising phosphorus dopant source, though all phosphorus doped samples were found to have nitrogen contamination, a higher oxygen content as compared to non-phosphorus carbons and a reduced surface area and slightly changed pore size distribution. The higher oxygen content was attributed to the presence of phosphate, while the nitrogen contamination was assumed to occur due to gases formed during the pyrolysis reacting with phosphorus. The lower surface area but higher pore volume was thought to result from phosphoric acid etching larger mesopores during the pyrolysis as well oxygen atoms replacing carbon. Boric acid offered the highest boron content, though the incorporation of boron caused lower surface areas, sulphur incorporation proved difficult, regardless of the use of an aromatic or aliphatic precursor and was only achieved in trace amounts, possibly due to the large atomic size of the sulphur atom.

A definitive comparison between different heteroatom dopants proved difficult due to slight variations in surface area owing to the altered composition of infiltration solution

depending on the precursors used. Thus, only trends instead of a conclusive statement are made on the role of the different dopants. Results suggested that nitrogen was the only heteroatom exerting an actual influence on the catalytic activity, resulting in higher electron transfer numbers as compared to the other dopants. The other dopants exhibited more or less the same performance regardless of the dopant content, though slightly improved when compared to the undoped control. These findings suggested that incorporated nitrogen acts as catalytic sites, pyridinic or graphitic nitrogen, while the other dopants only enhanced the catalytic activity by possibly creating defects in the carbon matrix. Interestingly, the presence of phosphorus always caused a change of the shape of the linear sweep voltammogram, resulting in a less positive onset potential and higher limiting current density.

Combination doping of nitrogen/boron, nitrogen/sulphur and nitrogen/phosphorus resulted in a similar performance regardless of the additional dopant, which again suggested that only nitrogen played a crucial role towards the catalytic activity. The addition of iron and its interaction with the different heteroatom dopants resulted in higher dopant amounts for all heteroatoms as compared to the metal-free counterparts, whereas the oxygen content was reduced. A significant increase in catalytic activity was observed for the nitrogen and iron doped sample, where the evolution of active $FeN_x$ sites was assumed, with a high electron transfer number, while the other dopant combinations caused an increase in electron transfer number when compared to the metal-free versions, but again displayed no significant difference amongst each other, suggesting that the presence of iron, for example in the form of iron oxide, determined their oxygen reduction reaction performance.

Lowering of surface area at the expense of meso-, but mostly micropores resulted in a similar onset potential, but considerably higher limiting current densities due to increased mass transport limitations, which also had a negative influence on the electron transfer number. A slightly higher surface area and increased micropore volume, achieved with a different silica template, did not yield any increase in activity, suggesting that active sites present in the micropores were not accessible.

While most of the outcomes and observations on the catalytic activity of the different materials presented in this thesis were in agreement with the general consensus in the field of oxygen reduction reaction electrocatalysis, some findings, especially the detrimental influence of additional sulphur doping, contradicted other research. The actual role of metal-free heteroatom dopants on the catalytic activity and the controversy about possible active sites in these metal-free catalysts still remains unclear, with adverse

findings and mostly speculations being reported. While theoretical works widely agree that nitrogen offers the best catalytic activity out of all heteroatom dopants, experimental validation proves difficult, not the least because of unpredictable influences during materials synthesis as well as oversimplification of the applied theoretical models. Another factor complicating progress in the field is the absence of a standardised testing method for oxygen reduction reaction catalysts, especially in regard to catalyst mass loading, which makes it difficult to compare materials from different research groups.

In order to truly make oxygen reduction reaction catalysts that can compete with platinum, a better understanding of the active sites, especially in metal-free catalysts, must be gained. While many studies have been carried out on non-noble metal catalysts using in situ synchrotron x-ray absorption fine structure spectroscopy, comparable research on metal-free materials is still missing due to the low energy range needed for low atomic number elements and restricted access to the few soft x-ray beamlines at Synchrotron facilities.

Regarding future work building on the research carried out for this thesis, further investigation of the iron containing carbogels is recommended to get a better understanding of the active sites present. The big discrepancy in catalytic performance between the same nitrogen and iron doped sample pyrolysed under either inert nitrogen atmosphere or a mixed atmosphere of nitrogen and compressed air should be clarified. For this, the sample pyrolysed under inert atmosphere should be examined with synchrotron x-ray absorption fine structure spectroscopy to understand how iron is coordinated and draw inferences about its inferior catalytic activity. Further, a range of in situ experiments, amongst them in situ Raman and x-ray diffraction during the high temperature pyrolysis and in situ x-ray absorption fine structure while doing electrochemical testing should be undertaken to track the formation of iron oxide particles and their influence on the degree of graphitisation of the material as well as see how iron is involved in the oxygen adsorption during the oxygen reduction reaction.

Further work on the templated carbons are recommended to strengthen the observed trends. For this, use of different templates, for example solely micro- or mesoporous, would be an interesting approach to better understand if and how the oxygen reduction reaction takes place in micropores. Raman spectroscopy could elucidate on the amount of defects caused by the incorporation of different heteroatom dopants, while in situ soft x-ray absorption fine structure could help understand and reveal the active sites.

# Chapter 7 | Experimental methods

In the following chapter, synthesis methods and characterisation techniques for all samples presented in this thesis can be found.

## 7.1 Synthesis of carbogels as electrocatalysts

Carbogels reported in chapters 3 and 4 are based on a synthesis technique first reported by Baccile et al.,[127] which was further improved by White et al.[117] and Wohlgemuth et al.[92] The composition for the synthesis of carbogels can be found in Table 7.1 and 7.2.

*Table 7.1 Chemical composition for the synthesis of metal-free carbogels in chapter 3.*

| **Chemical** | **CN** | **$CN_S$** | **$CN_B$** | **$CN_{SB}$** |
|---|---|---|---|---|
| D-Glucose (*Sigma Aldrich G8270*) | 1.5 g | 1.5 g | 1.5 g | 1.5 g |
| Lyophilised Albumin (*Sigma Aldrich 5503*) | 0.3 g | 0.3 g | 0.3 g | 0.3 g |
| DI $H_2O$ | 13.5 mL | 13.5 mL | 13.5 mL | 13.5 mL |
| 2-Thiophenecarboxaldehyde (*Sigma Aldrich T23409*) | - | 0.1 g | - | 0.1 g |
| Boric acid (*Sigma Aldrich B0394*) | - | - | 0.06 g | 0.06 g |

*Table 7.2 Chemical composition for the synthesis of non-noble metal carbogels in chapter 4.*

| **Chemical** | **$CN_{Fe}$** | **$CN_{SFe}$** | **$CN_{BFe}$** | **$CN_{SBFe}$** | **$CN_{Fe3+\_2}$** | **$CN_{Fe2+}$** |
|---|---|---|---|---|---|---|
| D-Glucose (*Sigma Aldrich G8270*) | 1.5 g | 1.5 g | 1.5 g | 1.5 g | 1.5 g | 1.5 g |
| Ovalbumin (*Sigma Aldrich 5503*) | 0.3 g | 0.3 g | 0.3 g | 0.3 g | 0.3 g | 0.3 g |
| DI $H_2O$ | 13.5mL | 13.5mL | 13.5mL | 13.5mL | 13.5mL | 13.5mL |
| 2Thiophenecarboxaldehyde (*Sigma Aldrich T23409*) | - | 0.1 g | - | 0.1 g | - | - |
| Boric acid (*Sigma Aldrich B0394*) | - | - | 0.06 g | 0.06 g | - | - |
| Iron(3)chloride hexahydrate (*Sigma Aldrich 31232-M*) | 0.3 g | 0.3 g | 0.3 g | 0.3 g | 0.6 g | - |
| Iron(2)chloride tetrahydrate (*Fluka 44939*) | - | - | - | - | - | 0.22 g |

The components for each sample were weighed into a glass inlet and dissolved in DI water by sonication for 30 minutes. Then, glass inlets were placed in teflon inlets and hydrothermal carbonisation (HTC) was carried out in stainless steel autoclaves (Parr Instruments) at 180 °C for 5.5 h. After the HTC, samples were washed with DI water by stirring for 24 h followed by vacuum filtration and freeze drying (Scanvac Cool Safe 110-4 Pro) for 48 h at -110 °C, after this step materials were called cyrogels. Subsequently, high temperature pyrolysis was carried out in a tubular Carbolite furnace under pure

nitrogen or a mixed atmosphere of nitrogen and compressed air (corresponding to either 1, 2 or 4 % of $O_2$). The pyrolysis was carried out at a heating rate of 7 °C/min up to a temperature of 1000 °C with a dwell time of 2 h, after this, samples were allowed to cool down to room temperature under the respective atmosphere, after this step materials were called carbogels.

Sample names are abbreviated as follows: $CN_{dopants}$, indicating the nitrogen doped carbon, as the pure sample form and added dopants (S/B/Fe) after the pyrolysis treatment. If samples are referred to after the hydrothermal carbonisation without pyrolysis they are labelled as HTC-$CN_{dopants}$.

Ideally, samples should be synthesised and pyrolysed separately to avoid any cross contamination or uncontrollable gas evolution in the furnace. During the pyrolysis, gases can be released (CO, $CO_2$, NO, $SO_2$ etc.) which can create changes in the materials surface area and occasionally composition, especially if multiple different samples are pyrolysed together. Though with sustainability and energy saving in mind, we mostly refrained from pyrolysing each sample separately. Thus, if samples have been pyrolysed together, three independent pyrolysis batches have been carried out and surface areas have been averaged and reported with standard deviation. If surface areas are reported as a single value, samples have either been pyrolysed on its own (repeatability shown in Figure 7.1) or a representative sample has been chosen lying within the mean/standard deviation of three averaged independent pyrolysis processes.

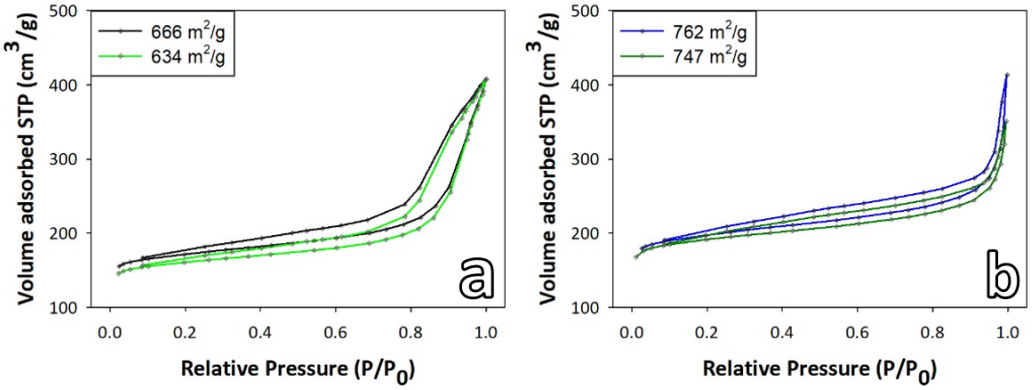


*Figure 7.1 Nitrogen sorption isotherms obtained at 77 K and surface areas calculated via Brunauer-Emmet-Teller theory for two independently single pyrolysed samples for a) CN and b) $CN_{Fe}$ under a mixed atmosphere of $N_2$/compressed air corresponding to 1% of $O_2$.*

## 7.2 Synthesis of electrocatalysts via hard templating with silica

### 7.2.1 Synthesis of SBA-15

The silica template (SBA-15) was synthesised in upscale method based on Zhao et al.[236] For this, 20 g of Pluronic P123 (*Sigma Aldrich 435465*) were dissolved in a mix of 150 mL DI $H_2O$ and 600 mL 2 M HCl while stirring in a water bath at 35 °C. Once completely dissolved, 40 mL of Tetraethyl orthosilicate (*Sigma Aldrich 86578*) was added and the mixture was stirred for 20 h at 35 °C. After this, the mixture was aged for 24 h at 80 °C without stirring. The solid product was then finely ground with a mortar and pestle and transferred to a ceramic crucible. Calcination was carried out in air for 6 h at 550 °C with a heating rate of 1 °C/min.

### 7.2.2 Infiltration of SBA-15

Prior to the infiltration, the SBA-15 template was vacuum dried at 80 °C for 3 h. For the infiltration of the silica template SBA-15, 1 g of silica was thoroughly mixed together with a mortar and pestle with a total of 1.8 mL liquid. The main part of the liquid consisted of a 50 wt% glucose solution (*Sigma Aldrich G8270*) and was mixed as desired with different heteroatom precursors, which can be found in Table 7.3. All nitrogen and boron precursors were available in powder form and the desired mass of dopant was mixed with 1.8 mL of glucose solution prior to infiltrating the silica. As both sulphur and phosphorus precursors were only available in liquid form, the desired volume of dopant was subtracted from the total liquid volume of 1.8 mL and mixed with the remaining glucose solution prior to infiltration. Dopant amounts were calculated to correspond to 2 or 4 mmol of the respective dopant itself, exact dopant amounts can be found in Table 7.4. For additional iron doping, 0.2 g of $FeCl_3$ x $6H_2O$ (*Sigma Aldrich 31232*) was used. After the infiltration of the SBA-15 template, samples were vacuum dried at 80 °C for 3 h and then transferred to alumina crucibles. The samples were pyrolysed under inert nitrogen atmosphere at 900 °C for 2 h with a heating rate of 5 °C/min.

*Table 7.3 Precursors used as heteroatom dopants during the infiltration of silica SBA-15.*

| Nitrogen | Boron | Sulphur | Phosphorus |
|---|---|---|---|
| Urea *(Sigma Aldrich U5128)* | Boric acid *(Sigma Aldrich 202878)* | 2-Thiophene-carboxaldehyde (TCA) *(Sigma Aldrich T23409)* | Phosphoric acid *(Sigma Aldrich 345245)* |
| Melamine *(Sigma Aldrich M2659)* | | | |
| Adenine *(Sigma Aldrich A8626)* | Boron trioxide *(Sigma Aldrich 202851)* | Allyl disulphide *(Sigma Aldrich 317691)* | Phytic acid *(Sigma Aldrich 593648)* |
| L-Arginine *(Sigma Aldrich A5006)* | | | |

*Table 7.4 Exact heteroatom dopant amounts used for the infiltration of the silica template SBA-15 corresponding to 2 and 4 mmol of the respective dopant itself.*

| Dopant precursor | 2 mmol | 4 mmol |
|---|---|---|
| Urea | 0.060 g | 0.120 g |
| Melamine | 0.042 g | - |
| Adenine | 0.054 g | - |
| Arginine | 0.087 g | - |
| Boric acid | 0.124 g | 0.248 g |
| Boron trioxide | 0.070 g | - |
| TCA | 191 µL | - |
| Allyl disulphide | 181 µL | 362 µL |
| Phosphoric acid | 137 µL | 274 µL |
| Phytic acid | 307 µL | - |

### 7.2.3 Synthesis of mesoporous shell silica spheres

Mesoporous shell silica spheres (MSS) with a solid core were synthesised as reported by Büchel et al.[237] For this, a solution was made out of 10 mL DI $H_2O$, 74 mL absolute Ethanol and 3.2 mL 32 wt% Ammonia solution (*VWR 21192.298*) and stirred in a water bath at 30 °C. Once the mix had reached 30 °C, 6 mL of Tetraethyl orthosilicate (*Sigma Aldrich 86578*) was added and the solution was stirred for 1 h at 30 °C. Prior to completion of this hour, a mix of 5 mL of Tetraethyl orthosilicate/TEOS (*Sigma Aldrich 86578*) and 2 mL of Trimethoxy(octadecyl)silane/C18TMS (*Sigma Aldrich 376213*) was prepared and heated to 30 °C. Once the hour was completed, the TEOS/C18TMS mix was slowly added to the solution under stirring. After this, stirring was stopped and the solution was left at room temperature for 1 h. Once the synthesis was finished, the solid product was separated by centrifugation at 10000 rpm for 10 min, washed three times with DI $H_2O$ and transferred into ceramic crucibles. Calcination was carried out under air at 550 °C for 6 h with a heating rate of 1 °C/min.

### 7.2.4 Infiltration of mesoporous shell silica

Prior to the infiltration, the MSS template was vacuum dried at 80 °C for 3 h. For the infiltration of the silica template MSS, 1 g of silica was thoroughly mixed together with a mortar and pestle with a total of 900 µL liquid. The main part of the liquid consisted of a 50 wt% glucose solution (*Sigma Aldrich G8270*) and was mixed as desired with different heteroatom precursors, which can be found in Table 7.3. Nitrogen and boron precursors were available in powder form and the desired mass of dopant was mixed with

900 µL of glucose solution prior to infiltrating the silica. As both sulphur and phosphorus precursors were only available in liquid form, the desired volume of dopant was subtracted from the total liquid volume of 900 µL and mixed with the remaining glucose solution prior to infiltration. Dopant amounts were calculated to correspond to 2 mmol of the respective dopant itself, exact dopant amounts can be found in Table 7.5. After the infiltration of the MSS template, samples were vacuum dried at 80 °C for 3 h and then transferred to alumina crucibles. The samples were pyrolysed under inert nitrogen atmosphere at 900 °C for 2 h with a heating rate of 5 °C/min.

*Table 7.5 Exact heteroatom dopant amounts used for the infiltration of the silica template MSS.*

| Dopant precursor | 2 mmol |
|---|---|
| Urea | 0.060 g |
| Boric acid | 0.124 g |
| Allyl disulphide | 181 µL |
| Phosphoric acid | 137 µL |

### 7.2.5 Etching of silica templates

After the successful infiltration of the silica templates and subsequent pyrolysis, the samples were etched with 4 M ammonium hydrogen difluoride solution (*Sigma Aldrich 224820*) to remove the silica template. For this, each powder sample was mixed with 40 mL of the etching solution in a centrifuge tube (50 mL) and left to shake at 250 rpm on a shaker platform (Grant Bio PSU-10i) for 96 h. After this, the solid samples were collected via vacuum filtration and excessively washed with DI $H_2O$, followed by freeze drying (Scanvac Cool Safe 110-4 Pro) at -110 °C for 48 h.

## 7.3 Material characterisation

Materials synthesised via the above mentioned procedures were characterised with the following methods described below.

### 7.3.1 Electron microscopy

Electron microscopy is a useful tool to determine the morphology and nanostructure of carbon materials. For this, a focused electron beam is used to illuminate/image the sample, which results in electron scattering from the atoms contained in the sample. Due to electrons being readily absorbed by air, electron microscopy is carried out under ultrahigh vacuum.[238] The two types of electron microscopy are TEM (transmission electron microscopy) and SEM (scanning electron microscopy), a schematic of the main working components for both can be seen in Figure 7.2. While the former relies on

electrons passing through a transparent sample, in the latter the electron beam scans an opaque sample.[238]

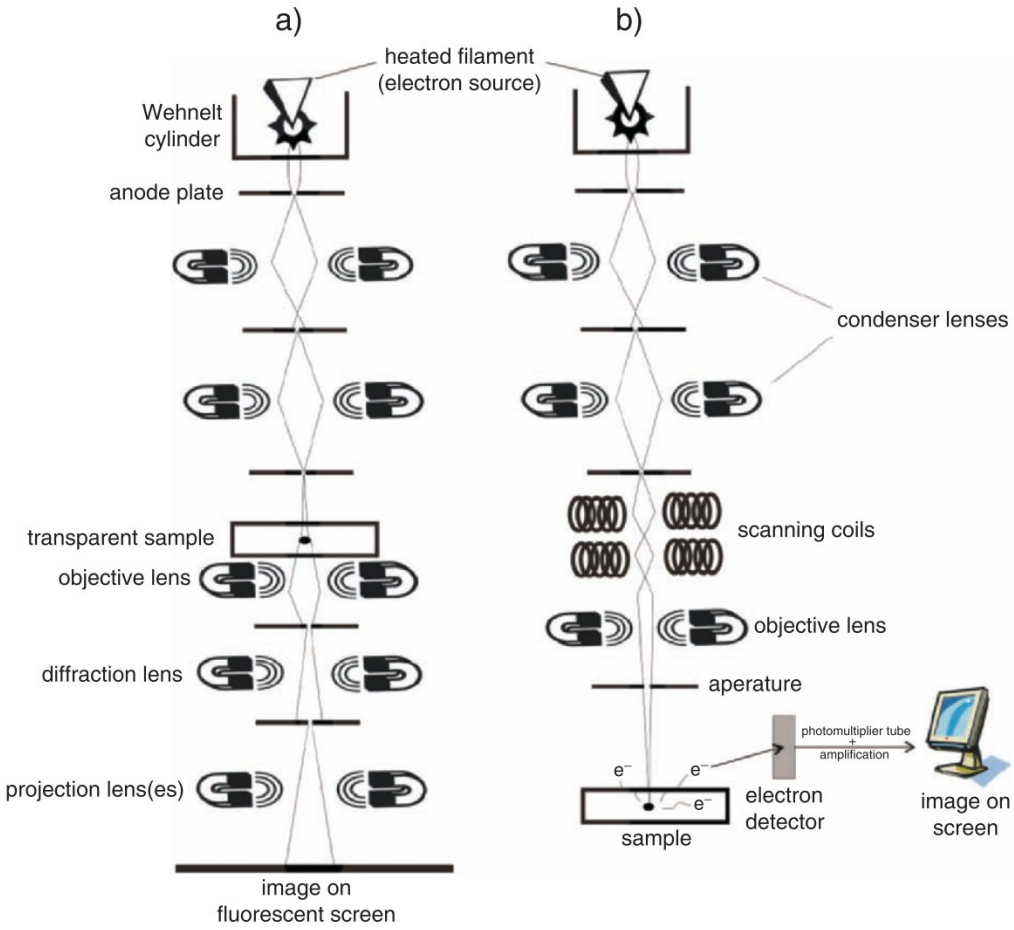


*Figure 7.2 Schematic of the working components of a transmission electron microscope (a) and a scanning electron microscope (b). Reproduced from Fahlman,[238] Copyright 2011 Springer Nature.*

The morphology of the different carbon materials was investigated by scanning electron microscopy with an FEI Quanta 3D electron microscope. Powder samples were supported on sticky carbon tape on top of a steel stub and sputter coated with gold. To study the nanostructure of the carbon materials, transmission electron microscopy was carried out with a JEOL JEM-2010 electron microscope operating at 200 kV. Powder samples were dispersed in ethanol (~ 1 mg/mL) and dropped onto a copper grid with holey carbon mesh (TAAB, Holey Carbon Film 300 Cu) and left at room temperature for the ethanol to evaporate before loading onto the TEM sample holder. In situ TEM was carried out at the King Abdullah University of Science and Technology (KAUST) in Saudi Arabia by Nitin Batra with a Thermo Fisher Scientific Titan G2 CT and ST microscope operating at 300 kV for TEM and STEM imaging. EDX spectra were collected in both STEM and TEM mode with Bruker QUANTAX silicon drift detector. In situ imaging was carried out using a Protochip Aduro TEM holder and chip. Powder samples were suspended in

ethanol and drop casted on $SiN_x$ heating chips from Protochips. The sample was heated at 50°C/min under vacuum atmosphere until 1000 °C was reached.

### 7.3.2 X-ray photoelectron spectroscopy

X-ray photoelectron spectroscopy (XPS) is a surface analysis technique to determine the elemental composition as well as surface groups of a sample. For this, the sample is irradiated with monochromatic X-rays, which cause the release of photoelectrons from the sample at characteristic binding energies corresponding to each atoms' inner shell electrons.[238] The excess kinetic energy ($E_k$) released is determined by the energy of the incident photons ($hv$) and each atom's inner shell electrons binding energy ($E_b$):[239]

$$E_k = hv - E_b.$$

XPS was used to quantitatively determine the composition and surface groups of the different carbon materials. Measurements and deconvolution of the spectra were carried out at the National Institute of Materials Physics in Bucharest, Romania by Dr. Liviu Tănase and Cristina Bucur. The measurements were performed in an AXIS Ultra DLD (Kratos Surface Analysis) setup equipped with an 180° hemispherical analyser, using Al Kα1 (1486.74 eV) radiation produced by a monochromatised X-ray source at an operating power of 300 W (15kV × 20mA). The base pressure in the analysis chamber was at least $1.0\times10^{-8}$ mbar. Charge compensation was reached by using a flood gun operating at 1.52 A filament current, 2.73 V charge balance and 2.02 V filament bias. The survey spectra have been recorded using hybrid lens mode, 160 eV pass energy with a slot aperture. High resolution core level spectra have been recorded using Field of View 2 lens mode at 20 eV pass energy with a 110µm aperture. The binding energy scale was calibrated to the C1s standard value of 284.6 eV and the core level spectra have been deconvoluted using Voigt profiles.

Due to XPS being a surface analysis technique, results should be treated with caution, especially with the heterogeneous nature of hydrothermal carbon materials in mind.

### 7.3.3 X-ray diffraction

X-ray diffraction (XRD) is typically used to determine the degree of crystallinity of a material. For this, a collimated X-ray beam is targeted at a sample which rotates at an angle theta, the detector collects the diffracted X-rays while rotating at an angle of 2 theta.[240] The X-ray beam is diffracted specific to the materials crystalline structure according to Bragg's law, where the wavelength of the radiation ($\lambda$) is related to the lattice spacing ($d$) in the sample and the diffraction angle ($\theta$): [238]

$$n\lambda = 2d(\sin\theta).$$

XRD measurements were carried out at the National Research and Development Institute for Chemistry and Petrochemistry in Bucharest, Romania by Stefan-Ovidiu Dima. Spectra were collected with a Rigaku – SmartLab diffractometer, operating at 45 kV and 200 mA. Measurements were carried out with $Cu_{K\alpha 1}$ radiation (wavelength 1.54059 Å), in parallel beam configuration, using the following system: the incident parallel slit was 5°, the incident slit was 0.2 mm, length limiting slit was 10 mm, the receiving parallel slit analyser was 0.5°, and the receiving parallel slit was 5°. The scanning was performed in theta/2theta mode, in 2θ range from 2° to 90°, with a step of 0.02° and scan speed of 4°/min.

### 7.3.4 Elemental analysis

Elemental analysis (EA) is a quantitative technique to determine the bulk elemental composition (carbon, hydrogen, nitrogen) of a material by flash combustion.

EA was carried using a Vario MICRO Cube elemental analyser system to determine the amount of C, H and N.

### 7.3.5 Inductively coupled plasma spectroscopy

Inductively coupled plasma spectroscopy (ICP) is used to identify and quantify elements present in a sample. For this, inductively coupled plasma is used to cause emission of electromagnetic radiation at a wavelength specific to the element, where the intensity of the emission is correlated with the concentration of the element.[241]

Analysis was carried out at the King Abdullah University of Science and Technology (KAUST) in Saudi Arabia by Amira Aalazmy. Inductively coupled plasma optical emission spectrometry (ICP-OES) was used for determination of iron amount in the samples. For this, 25 mg of the powder sample was dissolved in 7 ml concentrated $HNO_3$ and 1 ml $H_2O_2$ (30%). Subsequently, microwave digestion was carried out in closed vessel for 30 min with a power of 1000 W and at a temperature of 220 °C. The measurements were performed with a Varian Spectra.

### 7.3.6 Surface area and pore size measurements

Nitrogen sorption isotherms are a powerful technique to determine a materials' specific surface area, pore volume and pore size distribution. For this, nitrogen gas is dosed into the sample tube at 77 K and the volume adsorbed by the sample at a specific pressure is calculated. As the gas pressure increases, the adsorbed molecules start to form a monolayer on the surface of the sample, which becomes a multilayer at higher pressures.[242] Based on this, Brunauer, Emmett and Teller (BET) developed a multilayer adsorption theory, with which the specific surface area of the material can be calculated,

using the monolayer capacity ($V_m$), the estimated area of one adsorbate molecule ($A$), the molar volume ($M$) and Avogadro's number ($N$):[243]

$$S_{BET} = \frac{V_m N A}{M}.$$

To also get information about the material's pores, the adsorbate gas condenses in the pores, starting with the smallest pores until saturation is achieved and all pores are filled.[242] Subsequent reduction of the pressure then causes evaporation of the condensed gas and the volume desorbed by the sample is calculated. From the adsorption and desorption branch, pore volume as well as pore sizes can be calculated via non-local density functional theory (NLDFT), which assumes the surface and all pores (cylindrical or slit) to be homogeneous.[242] Based on the fact that pores in amorphous, especially microporous carbons are highly unlikely to be homogeneous, a more appropriate model was developed, which can eliminate artefacts, called quenched solid density functional theory (QSDFT).[244]

Surface area and pore size distribution/pore volumes ($V_{tot}$, $V_{micro}$, $V_{meso}$) were determined via Brunauer-Emmett-Teller (BET) theory and quenched solid density functional theory (QSDFT), respectively, using nitrogen sorption isotherms obtained at 77 K with a Quantachrome Nova 4200e. Samples were degassed under vacuum at 150 °C overnight prior to analysis. NovaWin software provided by Quantrachrome was used to fit the recorded data to the above mentioned theories/models. Due to resource limitations, nitrogen isotherms were mostly recorded in low resolution, which can influence the reliability of the obtained pore size distributions in the micropore area and should thus be treated with caution.

To ensure repeatability of the measurements, the same sample (CN) was prepared for analysis three times, nitrogen sorption isotherms and surface areas are shown in Figure 7.3.

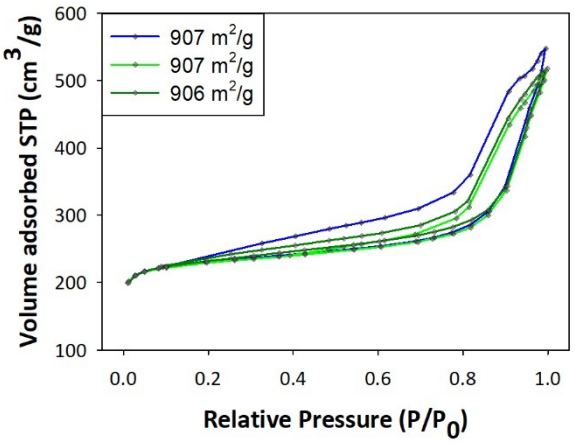


*Figure 7.3 Nitrogen sorption isotherms measured separately three times for the same sample (CN) under the same conditions to ensure repeatability and reliability of the measurement technique.*

### 7.3.7 Raman spectroscopy

Raman spectroscopy is commonly used to determine the degree of graphitisation (crystalline or amorphous) and concurrently the presence of defects or disorder within the carbon material.[153] For this, the sample is excited with a laser at a specific wavelength, which causes vibration, stretching and bending of the molecules within the sample due to inelastic light scattering (emitted energy is lower or higher than incident energy) and the diffused photons are detected/recorded.[239] A Raman spectra is largely determined by how the electrons move, interfere and scatter, thus the peak positions and width of peaks are influenced by changed electronic properties of the carbon materials due to defects or dopants.[219]

Raman spectroscopy was carried out at Diamond Light Source during the use of beamline B18. Spectra of the powder samples were recorded using a Renishaw InVia system with an excitation wavelength of 785 nm. Spectra were fitted using OriginPro PeakAnalyzer software to subtract the background and calculate the $I_D/I_G$ ratio from the integrated peak height/intensity.

### 7.3.8 Fourier transform infrared spectroscopy

Fourier transform infrared spectroscopy (FT-IR) is used to obtain an overview of the functional groups/chemical structures of a material. For this, infrared radiation is sent through the sample causing some of the radiation to be adsorbed while some is transmitted (passes through), which results in rotational and vibrational energy.[245]

FT-IR spectra were recorded with a Bruker Tensor 27 using an ATR (attenuated total reflectance) detector in the range of 400 to 4000 $cm^{-1}$ using the powder samples.

### 7.3.9 Thermogravimetric analysis

Thermogravimetric analysis (TGA) is used to analyse the thermal properties (stability and decomposition) of a sample and determine the amount of doped metals or unwanted residues as well as contaminations. For this, the sample is placed in a platinum pan attached to a microbalance and heated up under a chosen atmosphere (nitrogen or air), during which changes in weight are recorded (mass loss).

TGA was carried out using a TA Instruments Q500. Samples were treated at a heating rate of 10 °C/min from room temperature to 1000 °C under compressed air atmosphere.

### 7.3.10 Electrochemical testing

Electrochemical testing was carried out with a rotating (RDE) and a rotating ring disk electrode (RRDE) on a Metrohm Multi Autolab M101. A three-electrode configuration with a Ag/AgCl as reference and platinum as counter electrode was used, as well as a 3

mm diameter glassy carbon (GC) working electrode for RDE and a 5 mm diameter GC disk with platinum ring for RRDE, respectively. Samples were tested in 0.1 M KOH or 0.1 M $HClO_4$ and compared to a commercially available platinum standard (HiSPEC 60 wt% Pt on Carbon). The mass loading for all samples on the electrode was kept at 106 µg $cm^{-2}$ and 20 $\mu g_{Pt}$ $cm^{-2}$ for the Pt standard, respectively. For the electrochemical testing an ink of each catalyst was prepared by mixing 2 mg of sample with 50 µL Nafion (5 %w/w in water and 1-propanol, Alfa Aesar), 200 µL Isopropanol and 750 µL DI $H_2O$, followed by pulse sonication for 10 minutes with a Sonics VCX500 to ensure homogenisation. The ink was dropped onto the electrode and dried via spin coating at 700 rpm.

Testing was performed in 0.1 M KOH or 0.1 M $HClO_4$, where the electrolyte was first purged with $N_2$ for 15 minutes and cyclic voltammetry (CV) at a scan rate of 100 mV $s^{-1}$ was recorded, followed by purging with $O_2$ for another 20 minutes and subsequently carrying out cyclic voltammetry (CV) and linear sweep voltammetry (LSV) at a scan rate of 10 mV $s^{-1}$ at varying rotational speeds between 400 and 2000 rpm. To calculate the electron transfer number and the $H_2O_2$ yield from RRDE measurements, the measured currents on the disk $I_D$ and the ring $I_R$ and the collection efficiency $N$ of the platinum ring (24.9 %) were used.

$$\%(H_2O_2) = 200 \times \frac{I_R/N}{I_D + I_R/N} \qquad n = 4 \times \frac{I_D}{I_D + I_R/N}$$

Numbers for electron transfer and hydrogen peroxide yield in alkaline media have been cross checked via RDE measurements and calculated with the Koutecky-Levich equation:

$$\frac{\mathbf{1}}{\boldsymbol{j}} = \frac{\mathbf{1}}{\boldsymbol{j_k}} + \frac{\mathbf{1}}{\boldsymbol{j_l}} = \frac{\mathbf{1}}{\boldsymbol{nFAkC}} + \frac{\mathbf{1}}{\mathbf{0.62}\boldsymbol{nFAD^{\frac{2}{3}}\omega^{\frac{1}{2}}\nu^{-\frac{1}{6}}C}} .$$

Where $j$ represents the measured current density, $j_k$ and $j_l$ are the kinetic and the diffusion-limited current densities, respectively. The electron transfer in the oxygen reaction is described by $n$, $F$ is the Faraday constant (96485 C/mol), $A$ is the electrode area, $k$ is the rate constant for the oxygen reduction, $D$ is the diffusion coefficient of oxygen in the electrolyte (1.9 × 10-5 cm2/s), $\omega$ is the angular velocity of the electrode, $\nu$ is the kinematic velocity of the electrolyte (0.01 cm2/s) and $C$ is the concentration of saturated oxygen in the electrolyte (1.2 × 10-3 mol/L). The number of electrons $n$ transferred during the oxygen reduction can then be calculated by the slope, when plotting $\frac{1}{j}$ vs. $\frac{1}{\omega^{\frac{1}{2}}}$, and the hydrogen peroxide yield $p$ can be estimated via $n = 4 - 2p$.

For chapters 3 and 4, values were in good agreement for both methods, RRDE and RDE, example values for the platinum standard and two representative carbogels are shown in Table 7.6 for comparison.

*Table 7.6 Comparison of electron transfer number (ETN) and hydrogen peroxide yield in 0.1 M KOH calculated directly from RRDE measurements and calculated via the Koutecky-Levich equation from RDE measurements for a platinum on carbon, $CN_{Fe}$ and CN (chapter Chapter 3 andChapter 4).*

| | RRDE | | RDE | |
|---|---|---|---|---|
| Sample | ETN | $H_2O_2$ yield [%] | ETN | $H_2O_2$ yield [%] |
| Pt@C | 3.96 | 2.1 | 4.00 | 0 |
| $CN_{Fe}$ | 3.86 | 7.2 | 3.98 | 0.1 |
| CN | 3.11 | 44.6 | 3.05 | 47.5 |

For stability/durability testing a chronoamperometric profile was run for 10000 seconds, where a constant potential was applied and the change in current was recorded. The potential was chosen based on the halfwave potential of each catalyst. Methanol tolerance was tested by adding 5 mL of MeOH to the electrolyte while running the same procedure (chronoamperometric profile) as for the stability testing.

Cyanide poisoning was recorded with the RDE setup under constant $O_2$ purging while rotating at 1600 rpm in 0.1 M KOH with 10 mM KCN. LSV curves were recorded before and after the addition of KCN.

Linear sweep voltammetry was carried out at different rotational speeds for all samples, exemplary graphs can be seen in Figure 7.4 for the platinum standard, a Fe-containing carbogel, a metal-free carbogel and a SBA-templated metal-free carbon. When the RRDE is rotated, convection as well as diffusion can influence the mass transfer of reactants and products. As can be seen, at low overpotentials where kinetics are determined by charge transfer, the onset potential is independent of the rotational rate. However, at higher overpotentials the curves are highly dependent on the rotational rate. While the potential is lowered the increase in current density slows down due to the electrochemical reaction being under mixed control conditions until mass transport limitations contribute and a current density plateau appears. The plateau can exhibit a slight slope, especially for the metal-free carbon samples, which is commonly explained due to the active sites being heterogeneously distributed on the electrode surface.[246,247] To better compare the different catalysts throughout this thesis, LSV curves were plotted together at 1600 rpm.

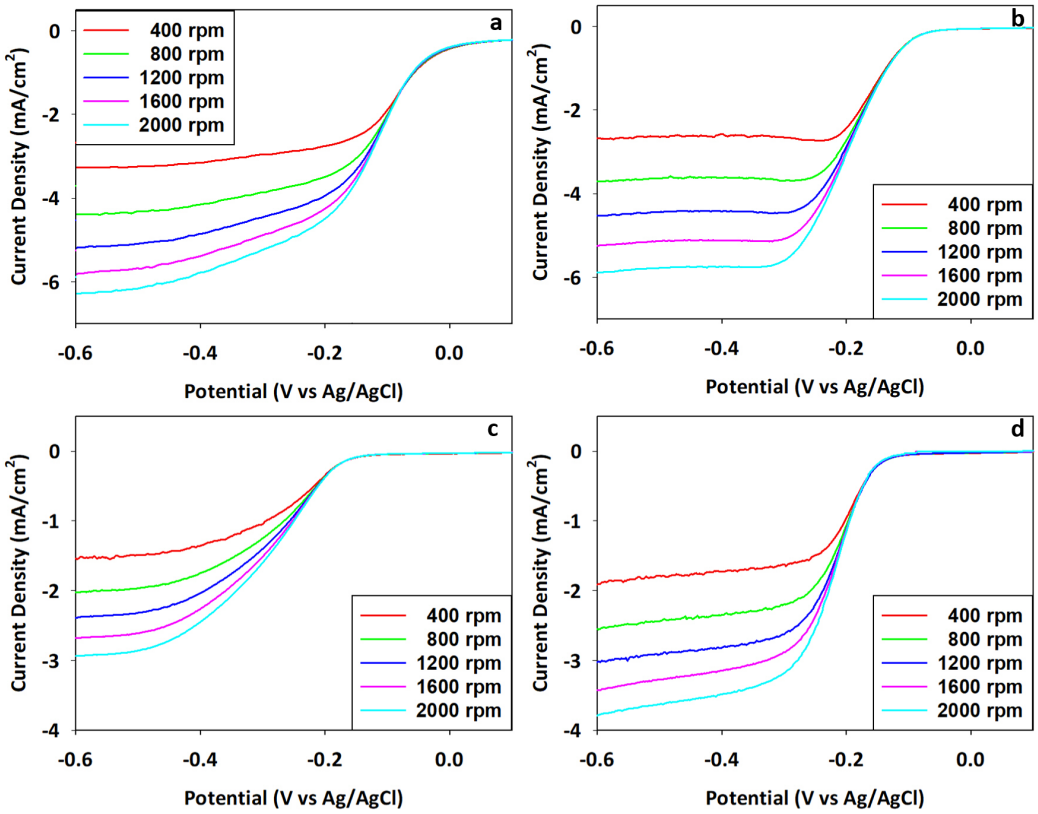


*Figure 7.4 Linear sweep voltammograms at different rotational rates in 0.1 M KOH for a) a commercially available platinum standard, b) a Fe-containing carbogel ($CN_{Fe}$), c) a metal-free carbogel (CN) and d) a SBA 15 templated metal-free carbon (C/N-SBA).*

Deviation of the catalytic performance between different batches of the same sample have been investigated. Therefore, the same sample ($CN_{Fe}$) was tested under the same conditions, synthesised in three separate batches, as can be seen in Figure 7.5. Regardless of variation in surface area throughout the three batches, electrochemical performance was found to be similar. Considering a reasonable degree of manual error during the preparation of the ink (~ 2 mg/mL) as well as variance during the coating of the electrode, the range of deviation shown in Figure 7.5 was considered acceptable. Based on this, electrochemical measurements reported in this thesis have been collected for one representative sample out of the different batches.

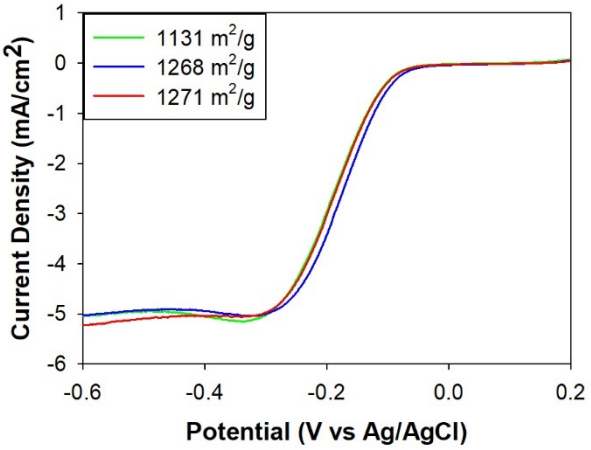


*Figure 7.5 Deviation of electrochemical performance between three batches of the same sample ($CN_{Fe}$) resulting in a variation in surface area, tested under the same conditions (0.1 M KOH purged with $O_2$ at 1600 rpm).*

Repeatability and storage stability of the prepared inks was tested with one sample ($CN_{Fe}$). Two fresh inks were prepared separately and tested, ink 2 was stored for three months and then tested again under the same conditions. As can be seen in Figure 7.6, excellent repeatability and storage stability were achieved for all three measurements.

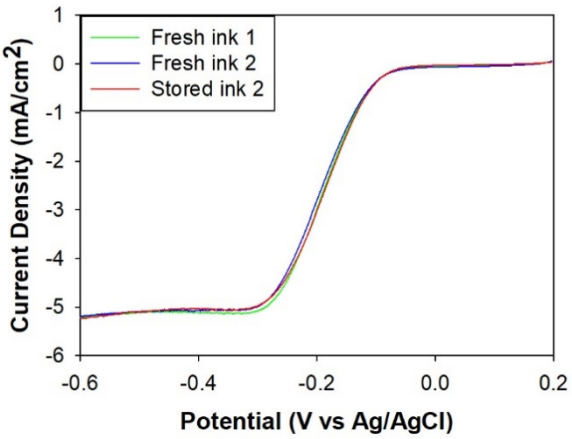


*Figure 7.6 Repeatability and storage stability of a nitrogen/iron doped carbogel shown with two freshly prepared inks and one ink stored for three months.*

Performance of the platinum standard, especially in acidic electrolyte, was found to be highly dependent on the actual platinum loading (Figure 7.7), as has also been reported in literature.[248] Though exhibiting a considerably poorer performance at lower catalyst loading, the loading was adapted to the U.S. Department of Energy (DOE) target of 20 $\mu g_{Pt}\ cm^{-2}$.

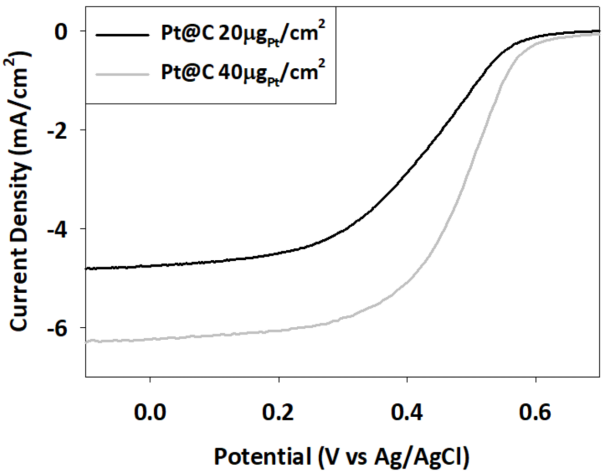


*Figure 7.7 Linear sweep voltammogram recorded in $O_2$-saturated 0.1M $HClO_4$ at 1600rpm for a commercially available platinum standard (HiSPEC 60 wt% Pt on Carbon) at two different catalyst loadings.*

### 7.3.11 Synchrotron x-ray absorption fine spectroscopy

X-ray absorption fine spectroscopy (XAFS) generally refers to a measurement where the absorption of an x-ray beam is recorded as a function of incoming energy.[249] For this, synchrotron radiation can be used to yield photons, which enables the use of specific absorption edges to investigate the chemical environment of a particular element present in the sample.[238] A XAFS spectra can be divided in two parts, x-ray absorption near-edge spectroscopy (XANES), which provides information about the oxidation state and bonding geometry due to an electron in the sample transitioning from a core level to a free state, and extended x-ray absorption fine structure (EXAFS), which offers distances and coordination numbers of the neighbouring atoms due to backscattering of the photoelectrons from the neighbouring atom.[238,249] Different modes can be used to acquire the data, which are transmission and fluorescence, a typical apparatus for a XAFS measurement can be seen in Figure 7.8.

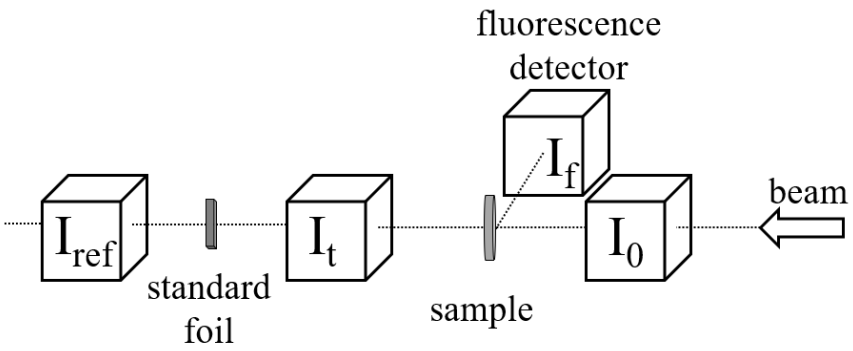


*Figure 7.8 Schematic of an exemplary x-ray absorption fine structure apparatus.*

Transmission is usually used for concentrated samples, where the beam can pass through the sample and the intensity of the beam is recorded before ($I_0$) and after the sample ($I_t$). From this, the absorption coefficient, $\mu(E)$, can be calculated:[250]

$$\mu(E) = \ln(I_0/I).$$

Fluorescence mode is utilised when the sample is thick or low in concentration, which requires the intensity or emission of the fluorescence x-rays to be collected, which allows the absorption coefficient, $\mu(E)$, to be calculated from the intensity of the incident beam ($I_0$) and the emitted signal ($I_f$):[250]

$$\mu(E) = I_f/I_0.$$

The EXAFS fine structure is determined by the oscillation above the absorption edge, which defines the EXAFS function as follows:

$$\chi(E) = \frac{\mu(E)-\mu_0(E)}{\mu_0(E)},$$

where $\mu_0(E)$ is the hypothetical smooth background absorption coefficient.[250] Due to the wave behaviour of the photoelectron generated during the absorption, energy is typically converted into the wavenumber of the photoelectron via the following the equation:

$$k = \sqrt{\frac{2m_e(E-E_0)}{\hbar^2}},$$

where $E$ is the energy of the incident photon, $E_0$ is the energy of the absorption edge, $\hbar$ is the Planck's constant divided by $2\pi$, $k$ is the wavenumber (defined as $2\pi$/wavelength $\lambda$) and $m_e$ is the mass of an electron.[251] $\chi(k)$ then represents the oscillations as a function of the photoelectron wavenumber, which can be influenced by different factors, such as elastic as well as inelastic scattering (from neighbouring atoms), multiple scattering pathways and a phase shift based on the scattering atom, which is expressed as:[251]

$$\chi(k) = \sum_j \frac{N_j f_j(k) e^{-2k^2\sigma_j^2}}{kR_j^2}\, sin\big[2kR_j + \delta_j(k)\big].$$

Here, $N$ is the number of neighbouring atoms, $R$ is the distance to the neighbouring atom, $f(k)$ and $\delta(k)$ represent specific scattering properties of the neighbouring atoms, and $\sigma$ describes the disorder in the neighbour distance.[250] Fourier transform can be applied to $\chi(k)$ yielding $|\chi(R)|$, which shows the distances to the nearest neighbouring atoms in angstrom.

Ex situ XAFS measurements were carried out at room temperature, samples and standards (Iron(II)oxide, Iron(III)oxide, Iron(II)phthalocyanine, Iron(III)ferrocyanide, Iron pyrite)

were mixed with cellulose and pressed into pellets. Measurements were collected at the Diamond Light Source B18 (Si(111) double-crystal monochromator, Pt-coated harmonics rejection mirrors were used for collimating and focusing the beam, Fe foil was used to calibrate the beam energy, with the first spectral inflection point set at 7112 eV) in fluorescence mode using a 4-element Vortex ME-4 silicon drift detector from SII (Hitachi). XAFS data was processed using ATHENA, part of the Demeter package[252] (a total of 10 or 5 spectra were averaged for each sample and standard, respectively).

# Chapter 8 | References


1. Watts, N. *et al.* The Lancet Countdown on health and climate change: from 25 years of inaction to a global transformation for public health. *Lancet* **391,** 581–630 (2018).

2. Basiago, A. D. Methods of defining 'sustainability. *Sustain. Dev.* **3,** 109–119 (1995).

3. Hunt, A. J. *Element Recovery and Sustainability*. (Royal Society of Chemistry, 2013).

4. Brown, T. J. *et al. World mineral production 2007-2011*. *British geological survey* (2013).

5. Titirici, M.-M. *Sustainable Carbon Materials from Hydrothermal Processes*. (John Wiley & Sons, Ltd, 2013).

6. White, R. J. *Porous Carbon Materials from Sustainable Precursors*. (RSC Green Chemistry, 2015).

7. Haseli, Y. Maximum conversion efficiency of hydrogen fuel cells. *Int. J. Hydrogen Energy* **43,** 9015–9021 (2018).

8. Grand View Research. *Fuel Cell Market Size, Share & Trends Analysis Report*. (2018).

9. E4Tech. *The Fuel Cell Industry Review 2017*. (2017).

10. Nikolaidis, P. & Poullikkas, A. A comparative overview of hydrogen production processes. *Renew. Sustain. Energy Rev.* **67,** 597–611 (2017).

11. Dincer, I. & Acar, C. Review and evaluation of hydrogen production methods for better sustainability. *Int. J. Hydrogen Energy* **40,** 11094–11111 (2014).

12. Vielstich, W., Lamm, A. & Gasteiger, H. A. *Handbook of Fuel Cells: Fundamentals, Technology, Applications*. (Wiley, 2003).

13. Haile, S. M. Fuel cell materials and components. *Acta Mater.* **51,** 5981–6000 (2003).

14. Ramani, V. Fuel Cells. *Electrochem. Soc. Interface* **15,** 41–44 (2006).

15. Barbir, F. *PEM Fuel Cells Theory and Practice*. (Elsevier, 2013).

16. Hoogers, G. *Fuel Cell Technology Handbook*. (CRC Press, 2003).

17. Zhang, J. *PEM Fuel Cell Electrocatalysts and Catalyst Layers - Fundamentals and Applications*. (Springer, 2008).

18. Bar-On, I., Kirchain, R. & Roth, R. Technical cost analysis for PEM fuel cells. *J. Power Sources* **109,** 71–75 (2002).

19. Sui, S. *et al.* A comprehensive review of Pt electrocatalysts for the oxygen reduction reaction: Nanostructure, activity, mechanism and carbon support in PEM fuel cells. *J. Mater. Chem. A* **5,** 1808–1825 (2017).

20. Song, C. & Zhang, J. Electrocatalytic Oxygen Reduction Reaction. in *PEM Fuel Cell Electrocatalysts and Catalyst Layers - Fundamentals and Applications* (ed. Zhang, J.) 89–134 (Springer, 2008).

21. Morozan, A., Jousselme, B. & Palacin, S. Low-platinum and platinum-free catalysts for the oxygen reduction reaction at fuel cell cathodes. *Energy Environ. Sci.* **4,** 1238 (2011).

22. Lavacchi, A., Miller, H. & Vizza, F. *Nanotechnology in Electrocatalysis for Energy*. (Springer New York, 2013). doi:10.1007/978-1-4899-8059-5

23. Zhang, L. & Xia, Z. Mechanisms of Oxygen Reduction Reaction on Nitrogen-Doped Graphene for Fuel Cells. *J. Phys. Chem. C* **115,** 11170–11176 (2011).

24. Stacy, J., Regmi, Y. N., Leonard, B. & Fan, M. The recent progress and future of oxygen reduction reaction catalysis: A review. *Renew. Sustain. Energy Rev.* **69,** 401–414 (2017).

25. Muthukrishnan, A. & Nabae, Y. Estimation of the inherent kinetic parameters for oxygen reduction over a Pt-free cathode catalyst by resolving the quasi-four-electron reduction. *J. Phys. Chem. C* **120,** 22515–22525 (2016).

26. Muthukrishnan, A., Nabae, Y. & Ohsaka, T. Role of iron in the reduction of H2O2 intermediate during the oxygen reduction reaction on iron-containing polyimide-based electrocatalysts. *RSC Adv.* **6,** 3774–3777 (2016).

27. Srinivasan, S. ELECTRODE/ELECTROL YTE INTERFACES: STRUCTURE AND KINETICS OF CHARGE TRANSFER. in *Fuel Cells - From Fundamentals to Applications* (Springer, 2006). doi:10.1016/S1369-7021(06)71654-6

28. Helmholtz, H. Ueber einige Gesetze der Vertheilung elektrischer Ströme in körperlichen Leitern mit Anwendung auf die thierisch-elektrischen Versuche. *Ann. der Phys. und Chemie* **165,** 211–233 (1853).

29. Nakamura, M., Sato, N., Hoshi, N. & Sakata, O. Outer Helmholtz Plane of the Electrical Double Layer Formed at the Solid Electrode-Liquid Interface. *ChemPhysChem* **12,** 1430–1434 (2011).

30. Nørskov, J. K. *et al.* Origin of the overpotential for oxygen reduction at a fuel-cell cathode. *J. Phys. Chem. B* **108,** 17886–17892 (2004).

31. Katsounaros, I. *et al.* Hydrogen peroxide electrochemistry on platinum: towards understanding the oxygen reduction reaction mechanism. *Phys. Chem. Chem. Phys.* **14,** 7384 (2012).

32. Chen, J., Lim, B., Lee, E. P. & Xia, Y. Shape-controlled synthesis of platinum nanocrystals for catalytic and electrocatalytic applications. *Nano Today* **4,** 81–95 (2009).

33. Yano, H., Watanabe, M., Iiyama, A. & Uchida, H. Particle-size effect of Pt cathode catalysts on durability in fuel cells. *Nano Energy* **29,** 323–333 (2016).

34. Zhang, G. *et al.* Core–shell Pt modified Pd/C as an active and durable electrocatalyst for the oxygen reduction reaction in PEMFCs. *Appl. Catal. B Environ.* **132–133,** 183–194 (2013).

35. Wang, C. *et al.* Multimetallic Au/FePt 3 Nanoparticles as Highly Durable Electrocatalyst. *Nano Lett.* **11,** 919–926 (2011).

36. Stamenkovic, V. R. *et al.* Improved Oxygen Reduction Activity on Pt3Ni(111) via Increased Surface Site Availability. *Science (80-. ).* **315,** 493–497 (2007).

37. Gupta, G. *et al.* Highly Stable and Active Pt−Cu Oxygen Reduction Electrocatalysts Based on Mesoporous Graphitic Carbon Supports. *Chem. Mater.* **21,** 4515–4526 (2009).

38. Luo, J. *et al.* Design and electrochemical characterization of ternary alloy electrocatalysts for oxygen reduction reaction. *J. Electroanal. Chem.* **688,** 196–206 (2013).

39. Du, S., Lu, Y., Malladi, S. K., Xu, Q. & Steinberger-Wilckens, R. A simple approach for PtNi–MWCNT hybrid nanostructures as high performance electrocatalysts for the oxygen reduction reaction. *J. Mater. Chem. A* **2,** 692–698 (2014).

40. Wang, R. *et al.* Controlled Growth of Platinum Nanowire Arrays on Sulfur Doped Graphene as High Performance Electrocatalyst. *Sci. Rep.* **3,** 2431 (2013).

41. Meier, J. C. *et al.* Design criteria for stable Pt/C fuel cell catalysts. *Beilstein J. Nanotechnol.* **5,** 44–67 (2014).

42. JASINSKI, R. A New Fuel Cell Cathode Catalyst. *Nature* **201,** 1212–1213 (1964).

43. Zagal, J. H. Metallophthalocyanines as catalysts in electrochemical reactions. *Coord. Chem. Rev.* **119,** 89–136 (1992).

44. He, P., Lefevre, M., Faubert, G. & Dodelet, J. Oxygen reduction catalysts for polymer electrolyte fuel cells from the pyrolysis of various transition metal acetates adsorbed on 3, 4, 9, 10-perylenetetracarboxylic dianhydride. *J. new Mater. Electrochem. Syst.* **2,** 243–252 (1999).

45. Masa, J., Zhao, A., Wei, X., Muhler, M. & Schuhmann, W. Metal-free catalysts for oxygen reduction in alkaline electrolytes: Influence of the presence of Co, Fe, Mn and Ni inclusions. *Electrochim. Acta* **128,** 271–278 (2014).

46. Lefèvre, M., Dodelet, J. P. & Bertrand, P. O2 Reduction in PEM Fuel Cells: Activity and Active Site Structural Information for Catalysts Obtained by the Pyrolysis at High Temperature of Fe Precursors. *J. Phys. Chem. B* **104,** 11238–11247 (2000).

47. Wang, H., Côté, R., Faubert, G., Guay, D. & Dodelet, J. P. Effect of the Pre-Treatment of Carbon Black Supports on the Activity of Fe-Based Electrocatalysts for the Reduction of Oxygen. *J. Phys. Chem. B* **103,** 2042–2049 (1999).

48. Liu, J. *et al.* High-Performance Oxygen Reduction Electrocatalysts based on Cheap Carbon Black, Nitrogen, and Trace Iron. *Adv. Mater.* **25,** 6879–6883 (2013).

49. Charreteur, F., Jaouen, F., Ruggeri, S. & Dodelet, J. P. Fe/N/C non-precious catalysts for PEM fuel cells: Influence of the structural parameters of pristine commercial carbon blacks on their activity for oxygen reduction. *Electrochim. Acta* **53,** 2925–2938 (2008).

50. Sun, J., Fang, Y.-H. & Liu, Z.-P. Electrocatalytic oxygen reduction kinetics on Fe-center of nitrogen-doped graphene. *Phys. Chem. Chem. Phys.* **16,** 13733–40 (2014).

51. Zitolo, A. *et al.* Identification of catalytic sites for oxygen reduction in iron- and nitrogen-doped graphene materials. *Nat. Mater.* **14,** 937–42 (2015).

52. Sougrati, M. T., Goellner, V., Schuppert, A. K., Stievano, L. & Jaouen, F. Probing

active sites in iron-based catalysts for oxygen electro-reduction: A temperature-dependent 57Fe Mössbauer spectroscopy study. *Catal. Today* **262,** 110–120 (2016).

53. Sa, Y. J. *et al.* A General Approach to Preferential Formation of Active Fe–N $_x$ Sites in Fe–N/C Electrocatalysts for Efficient Oxygen Reduction Reaction. *J. Am. Chem. Soc.* **138,** 15046–15056 (2016).

54. Kramm, U. I. *et al.* On an Easy Way to Prepare Metal-Nitrogen Doped Carbon with Exclusive Presence of MeN4-type Sites Active for the ORR. *J. Am. Chem. Soc.* **138,** 635–640 (2016).

55. Varnell, J. A. *et al.* Identification of carbon-encapsulated iron nanoparticles as active species in non-precious metal oxygen reduction catalysts. *Nat. Commun.* **7,** 1–9 (2016).

56. Hu, Y. *et al.* Hollow spheres of iron carbide nanoparticles encased in graphite layers as oxygen reduction catalysts. *Angew. Chemie - Int. Ed.* 3675–3679 (2014). doi:10.1002/anie.201400358

57. Jiang, W.-J. *et al.* Understanding the High Activity of Fe-N-C Electrocatalysts in Oxygen Reduction: Fe/Fe3C Nanoparticles Boost the Activity of Fe-Nx. *J. Am. Chem. Soc.* **138,** 3570–8 (2016).

58. Jia, Q. *et al.* Spectroscopic insights into the nature of active sites in iron–nitrogen–carbon electrocatalysts for oxygen reduction in acid. *Nano Energy* **29,** 65–82 (2016).

59. Cao, C., Wei, L., Wang, G. & Shen, J. Superiority of boron, nitrogen and iron ternary doped carbonized graphene oxide-based catalysts for oxygen reduction in microbial fuel cells. *Nanoscale* **9,** 3537–3546 (2017).

60. He, J. *et al.* Four-electron oxygen reduction from mesoporous carbon modified with Fe2O3 nanocrystals. *J. Mater. Sci.* 1–10 (2017). doi:10.1007/s10853-017-1192-5

61. Wu, Z.-S. *et al.* 3D Nitrogen-Doped Graphene Aerogel-Supported Fe 3 O 4 Nanoparticles as Efficient Electrocatalysts for the Oxygen Reduction Reaction. *J. Am. Chem. Soc.* **134,** 9082–9085 (2012).

62. Li, J. *et al.* Structural and mechanistic basis for the high activity of Fe–N–C catalysts toward oxygen reduction. *Energy Environ. Sci.* **9,** 2418–2432 (2016).

63. Jia, Q. *et al.* Experimental Observation of Redox-Induced Fe-N Switching Behavior as a Determinant Role for Oxygen Reduction Activity. *ACS Nano* **9,** 12496–12505 (2015).

64. Tylus, U. *et al.* Elucidating Oxygen Reduction Active Sites in Pyrolyzed Metal–Nitrogen Coordinated Non-Precious-Metal Electrocatalyst Systems. *J. Phys. Chem. C* **118,** 8999–9008 (2014).

65. Strickland, K. *et al.* Highly active oxygen reduction non-platinum group metal electrocatalyst without direct metal–nitrogen coordination. *Nat. Commun.* **6,** 7343 (2015).

66. Wang, Q. *et al.* Phenylenediamine-based FeNx/C catalyst with high activity for oxygen reduction in acid medium and its active-site probing. *J. Am. Chem. Soc.* **136,** 10882–10885 (2014).

67. Deng, D. *et al.* Iron Encapsulated within Pod-like Carbon Nanotubes for Oxygen Reduction Reaction. *Angew. Chemie - Int. Ed.* **52,** 371–375 (2013).

68. Bayati, M. & Scott, K. Synthesis and Activity of A Single Active Site N-doped Electro-catalyst for Oxygen Reduction. *Electrochim. Acta* **213,** 927–932 (2016).

69. Yang, D.-S., Song, M. Y., Singh, K. P. & Yu, J.-S. The role of iron in the preparation and oxygen reduction reaction activity of nitrogen-doped carbon. *Chem. Commun.* **51,** 2450–2453 (2015).

70. Jin, H. *et al.* Nitrogen-doped carbon xerogels as novel cathode electrocatalysts for oxygen reduction reaction in direct borohydride fuel cells. *Electrochim. Acta* **222,** 438–445 (2016).

71. Gong, K., Du, F., Xia, Z., Durstock, M. & Dai, L. Nitrogen-Doped Carbon Nanotube Arrays with High Electrocatalytic Activity for Oxygen Reduction. *Science (80-. ).* **323,** 760–764 (2009).

72. Pumera, M. Carbon nanotubes contain residual metal catalyst nanoparticles even after washing with nitric acid at elevated temperature because these metal nanoparticles are sheathed by several graphene sheets. *Langmuir* **23,** 6453–6458 (2007).

73. Kolodiazhnyi, T. & Pumera, M. Towards an ultrasensitive method for the determination of metal impurities in carbon nanotubes. *Small* **4,** 1476–1484 (2008).

74. Wang, L., Ambrosi, A. & Pumera, M. ‘Metal-free’ catalytic oxygen reduction reaction on heteroatom-doped graphene is caused by trace metal impurities. *Angew. Chemie - Int. Ed.* **52,** 13818–13821 (2013).

75. Wang, L., Wong, C. H. A., Kherzi, B., Webster, R. D. & Pumera, M. So-called ‘metal-free’ oxygen reduction at graphene nanoribbons is in fact metal driven. *ChemCatChem* **7,** 1650–1654 (2015).

76. Varnell, J. A. *et al.* Revealing the Role of the Metal in Non-Precious-Metal Catalysts for Oxygen Reduction via Selective Removal of Fe. *ACS Energy Lett.* **3,** 823–828 (2018).

77. Bukola, S. *et al.* Fe-N-C electrocatalysts for oxygen reduction reaction synthesized by using aniline salt and Fe3+/H2O2catalytic system. *Electrochim. Acta* **146,** 809–818 (2014).

78. Sahraie, N. R. *et al.* Quantifying the density and utilization of active sites in non-precious metal oxygen electroreduction catalysts. *Nat. Commun.* **6,** 1–9 (2015).

79. Malko, D., Kucernak, A. & Lopes, T. Performance of Fe-N/C Oxygen Reduction Electrocatalysts toward NO2-, NO, and NH2OH Electroreduction: From Fundamental Insights into the Active Center to a New Method for Environmental Nitrite Destruction. *J. Am. Chem. Soc.* **138,** 16056–16068 (2016).

80. Ramaswamy, N. & Mukerjee, S. Fundamental mechanistic understanding of electrocatalysis of oxygen reduction on Pt and non-Pt surfaces: Acid versus alkaline media. *Adv. Phys. Chem.* **2012,** (2012).

81. Malko, D. & Kucernak, A. Kinetic isotope effect in the oxygen reduction reaction (ORR) over Fe-N/C catalysts under acidic and alkaline conditions. *Electrochem. commun.* **83,** 67–71 (2017).

82. Mortimer, C. E. & Müller, U. *Chemie*. (Thieme Medical Publishers, 2007).

83. Daems, N., Sheng, X., Vankelecom, I. F. J. & Pescarmona, P. P. Metal-free doped carbon materials as electrocatalysts for the oxygen reduction reaction. *J. Mater. Chem. A* **2,** 4085 (2014).

84. Lee, K. U. K. R., Lee, K. U. K. R., Lee, J. W., Ahn, B. T. & Woo, S. I. Electrochemical oxygen reduction on nitrogen doped graphene sheets in acid media. *Electrochem. commun.* **12,** 1052–1055 (2010).

85. Niwa, H. *et al.* X-ray absorption analysis of nitrogen contribution to oxygen

reduction reaction in carbon alloy cathode catalysts for polymer electrolyte fuel cells. *J. Power Sources* **187,** 93–97 (2009).

86. Luo, Z. *et al.* Pyridinic N doped graphene: synthesis, electronic structure, and electrocatalytic property. *J. Mater. Chem.* **21,** 8038 (2011).

87. Kim, H., Lee, K., Woo, S. I. & Jung, Y. On the mechanism of enhanced oxygen reduction reaction in nitrogen-doped graphene nanoribbons. *Phys. Chem. Chem. Phys.* **13,** 17505 (2011).

88. Lai, L. *et al.* Exploration of the active center structure of nitrogen-doped graphene-based catalysts for oxygen reduction reaction. *Energy Environ. Sci.* **5,** 7936 (2012).

89. Qu, L., Liu, Y., Baek, J.-B. & Dai, L. Nitrogen-Doped Graphene as Efficient Metal-Free Electrocatalyst for Oxygen Reduction in Fuel Cells. *ACS Nano* **4,** 1321–1326 (2010).

90. Niwa, H. *et al.* X-ray photoemission spectroscopy analysis of N-containing carbon-based cathode catalysts for polymer electrolyte fuel cells. *J. Power Sources* **196,** 1006–1011 (2011).

91. Agnoli, S. & Favaro, M. Doping graphene with boron: A review of synthesis methods, physicochemical characterization, and emerging applications. *J. Mater. Chem. A* **4,** 5002–5025 (2016).

92. Wohlgemuth, S.-A., White, R. J., Willinger, M.-G., Titirici, M.-M. & Antonietti, M. A one-pot hydrothermal synthesis of sulfur and nitrogen doped carbon aerogels with enhanced electrocatalytic activity in the oxygen reduction reaction. *Green Chem.* **14,** 1515 (2012).

93. Liang, J., Jiao, Y., Jaroniec, M. & Qiao, S. Z. Sulfur and nitrogen dual-doped mesoporous graphene electrocatalyst for oxygen reduction with synergistically enhanced performance. *Angew. Chemie - Int. Ed.* **51,** 11496–11500 (2012).

94. Hossain, M. S., Tryk, D. & Yeager, E. The electrochemistry of graphite and modified graphite surfaces: the reduction of O2. *Electrochim. Acta* **34,** 1733–1737 (1989).

95. Sarapuu, A., Vaik, K., Schiffrin, D. J. & Tammeveski, K. Electrochemical reduction of oxygen on anthraquinone-modified glassy carbon electrodes in alkaline solution. *J. Electroanal. Chem.* **541,** 23–29 (2003).

96. Vaik, K., Sarapuu, A., Tammeveski, K., Mirkhalaf, F. & Schiffrin, D. J. Oxygen reduction on phenanthrenequinone-modified glassy carbon electrodes in 0.1 M KOH. *J. Electroanal. Chem.* **564,** 159–166 (2004).

97. Nabae, Y., Yamanaka, I. & Otsuka, K. Electro-catalysis of the Cu/carbon cathode for the reduction of O2 during fuel-cell reactions. *Appl. Catal. A Gen.* **280,** 149–155 (2005).

98. Choi, E. Y. & Kim, C. K. Fabrication of nitrogen-doped nano-onions and their electrocatalytic activity toward the oxygen reduction reaction. *Sci. Rep.* **7,** 1–9 (2017).

99. Matsubara, K. & Waki, K. The Effect of O-Functionalities for the Electrochemical Reduction of Oxygen on MWCNTs in Acid Media. *Electrochem. Solid-State Lett.* **13,** F7 (2010).

100. Zhu, C., Zhai, J. & Dong, S. Bifunctional fluorescent carbon nanodots: green synthesis via soy milk and application as metal-free electrocatalysts for oxygen reduction. *Chem. Commun. (Camb).* **48,** 9367–9 (2012).

101. Zhong, R. S. *et al.* Effect of carbon nanofiber surface functional groups on oxygen reduction in alkaline solution. *J. Power Sources* **225,** 192–199 (2013).

102. Meng, Y. *et al.* N-, O-, and S-Tridoped nanoporous carbons as selective catalysts for oxygen reduction and alcohol oxidation reactions. *J. Am. Chem. Soc.* **136,** 13554–13557 (2014).

103. Zhang, L., Niu, J., Dai, L. & Xia, Z. Effect of Microstructure of Nitrogen-Doped Graphene on Oxygen Reduction Activity in Fuel Cells. *Langmuir* **28,** 7542–7550 (2012).

104. Jiao, Y., Zheng, Y., Davey, K. & Qiao, S. Z. Activity origin and catalyst design principles for electrocatalytic hydrogen evolution on heteroatom-doped graphene. *Nat. Energy* **1,** (2016).

105. Jiao, Y., Zheng, Y., Jaroniec, M. & Qiao, S. Z. Origin of the electrocatalytic oxygen reduction activity of graphene-based catalysts: a roadmap to achieve the best performance. *J Am Chem Soc* **136,** 4394–4403 (2014).

106. Liu, H., Liu, Y. & Zhu, D. Chemical doping of graphene. *J. Mater. Chem.* **21,** 3335–3345 (2011).

107. Yan, D. *et al.* Defect Chemistry of Nonprecious-Metal Electrocatalysts for

Oxygen Reactions. *Adv. Mater.* **29,** 1–20 (2017).

108. Shen, A. *et al.* Oxygen reduction reaction in a droplet on graphite: Direct evidence that the edge is more active than the basal plane. *Angew. Chemie - Int. Ed.* **53,** 10804–10808 (2014).

109. Tang, C. *et al.* Topological Defects in Metal-Free Nanocarbon for Oxygen Electrocatalysis. *Adv Mater* **28,** 6845–6851 (2016).

110. Jia, Y. *et al.* Defect Graphene as a Trifunctional Catalyst for Electrochemical Reactions. *Adv. Mater.* **28,** 9532–9538 (2016).

111. Zhao, H. *et al.* Carbon for the oxygen reduction reaction: a defect mechanism. *J. Mater. Chem. A* **3,** 11736–11739 (2015).

112. Wan, K. *et al.* pH Effect on Electrochemistry of Nitrogen-Doped Carbon Catalyst for Oxygen Reduction Reaction. *ACS Catal.* **5,** 4325–4332 (2015).

113. Bergius, F. Production of hydrogen from water and coal from cellulose at high temperatures and pressures. *J. Soc. Chem. Ind.* **32,** 462–467 (1913).

114. Titirici, M. M., Thomas, A., Yu, S. H., Müller, J. O. & Antonietti, M. A direct synthesis of mesoporous carbons with bicontinuous pore morphology from crude plant material by hydrothermal carbonization. *Chem. Mater.* **19,** 4205–4212 (2007).

115. Titirici, M.-M. M. & Antonietti, M. Chemistry and materials options of sustainable carbon materials made by hydrothermal carbonization. *Chem. Soc. Rev.* **39,** 103–116 (2010).

116. Preuss, K., Qiao, M. & Titirici, M.-M. Hydrothermal Carbon Materials for the Oxygen Reduction Reaction. in *Carbon-Based Metal-Free Catalysts: Design and Applications* (ed. Dai, L.) 746 (Wiley, 2018).

117. White, R. J., Yoshizawa, N., Antonietti, M. & Titirici, M.-M. A sustainable synthesis of nitrogen-doped carbon aerogels. *Green Chem.* **13,** 2428 (2011).

118. Nursten, H. *The Maillard Reaction: Chemistry, Biochemistry and Implications*. (2005). doi:10.1039/9781847552570

119. Antonietti, M., Fechler, N. & Fellinger, T. P. Carbon aerogels and monoliths: Control of porosity and nanoarchitecture via Sol-Gel routes. *Chem. Mater.* **26,** 196–210 (2014).

120. Job, N. *et al.* Carbon aerogels, cryogels and xerogels: Influence of the drying method on the textural properties of porous carbon materials. *Carbon N. Y.* **43,** 2481–2494 (2005).

121. Brun, N., Wohlgemuth, S. A., Osiceanu, P. & Titirici, M. M. Original design of nitrogen-doped carbon aerogels from sustainable precursors: application as metal-free oxygen reduction catalysts. *Green Chem.* **15,** 2514 (2013).

122. Brun, N., García-González, C. A., Smirnova, I. & Titirici, M. M. Hydrothermal synthesis of highly porous carbon monoliths from carbohydrates and phloroglucinol. *RSC Adv.* **3,** 17088–17096 (2013).

123. Fellinger, T. P., White, R. J., Titirici, M. M. & Antonietti, M. Borax-mediated formation of carbon aerogels from glucose. *Adv. Funct. Mater.* **22,** 3254–3260 (2012).

124. Wohlgemuth, S.-A., Fellinger, T.-P., Jäker, P. & Antonietti, M. Tunable nitrogen-doped carbon aerogels as sustainable electrocatalysts in the oxygen reduction reaction. *J. Mater. Chem. A* **1,** 4002 (2013).

125. Hansen, T. S., Mielby, J. & Riisager, A. Synergy of boric acid and added salts in the catalytic dehydration of hexoses to 5-hydroxymethylfurfural in water. *Green Chem.* **13,** 109 (2011).

126. Ståhlberg, T., Rodriguez-Rodriguez, S., Fristrup, P. & Riisager, A. Metal-free dehydration of glucose to 5-(Hydroxymethyl)furfural in ionic liquids with boric acid as a promoter. *Chem. - A Eur. J.* **17,** 1456–1464 (2011).

127. Baccile, N., Antonietti, M. & Titirici, M.-M. One-Step Hydrothermal Synthesis of Nitrogen-Doped Nanocarbons: Albumine Directing the Carbonization of Glucose. *ChemSusChem* **3,** 246–253 (2010).

128. Liu, R., Xi, X., Xing, X. & Wu, D. A facile biomass based approach towards hierarchically porous nitrogen-doped carbon aerogels. *RSC Adv.* **6,** 83613–83618 (2016).

129. Yu, Y.-N., Wang, M.-Q. & Bao, S.-J. Biomass-derived synthesis of nitrogen and phosphorus Co-doped mesoporous carbon spheres as catalysts for oxygen reduction reaction. *J. Solid State Electrochem.* **21,** 103–110 (2017).

130. Liu, F. *et al.* High-performance doped carbon catalyst derived from nori biomass with melamine promoter. *Electrochim. Acta* **138,** 353–359 (2014).

131. Chen, P. *et al.* Nitrogen-doped nanoporous carbon nanosheets derived from plant biomass: an efficient catalyst for oxygen reduction reaction. *Energy Environ. Sci.* **7,** 4095–4103 (2014).

132. Zhang, H. *et al.* Hydrothermal transformation of dried grass into graphitic carbon-based high performance electrocatalyst for oxygen reduction reaction. *Small* **10,** 3371–3378 (2014).

133. Zhou, L., Fu, P., Wen, D., Yuan, Y. & Zhou, S. Self-constructed carbon nanoparticles-coated porous biocarbon from plant moss as advanced oxygen reduction catalysts. *Appl. Catal. B Environ.* **181,** 635–643 (2016).

134. Liu, L., Xiong, Q., Li, C., Feng, Y. & Chen, S. Conversion of straw to nitrogen doped carbon for efficient oxygen reduction catalysts in microbial fuel cells. *RSC Adv.* **5,** 89771–89776 (2015).

135. Yuan, W.-J. *et al.* Nitrogen-doped nanoporous carbon derived from waste pomelo peel as metal-free electrocatalyst for the oxygen reduction reaction. *Nanoscale* 8704–8711 (2016). doi:10.1039/C6NR00764C

136. Liu, L., Ye, X. P., Womac, A. R. & Sokhansanj, S. Variability of biomass chemical composition and rapid analysis using FT-NIR techniques. *Carbohydr. Polym.* **81,** 820–829 (2010).

137. Boßelmann, F., Romano, P., Fabritius, H., Raabe, D. & Epple, M. The composition of the exoskeleton of two crustacea: The American lobster Homarus americanus and the edible crab Cancer pagurus. *Thermochim. Acta* **463,** 65–68 (2007).

138. Alatalo, S.-M. *et al.* Soy protein directed hydrothermal synthesis of porous carbon aerogels for electrocatalytic oxygen reduction. *Carbon N. Y.* **96,** 622–630 (2016).

139. Fan, J. *et al.* Control of hole opening in single-wall carbon nanotubes and single-wall carbon nanohorns using oxygen. *J. Phys. Chem. B* **110,** 1587–1591 (2006).

140. Yang, R. T. & Wong, C. Mechanism of Single-Layer Graphite Oxidation: Evaluation by Electron Microscopy. *Science (80-. ).* **214,** 437–438 (1981).

141. Yang, R. T. & Wong, C. Kinetics and mechanism of oxidation of basal plane on graphite. *J. Chem. Phys.* **75,** 4471–4476 (1981).

142. Chu, X. & Schmidt, L. D. Reactions of NO, O2, H2O, and CO2 with the basal plane of graphite. *Surf. Sci.* **268,** 325–332 (1992).

143. Hayhurst, A. N. & Parmar, M. S. Does solid carbon burn in oxygen to give the gaseous intermediate CO or produce CO2 directly? Some experiments in a hot bed of sand fluidized by air. *Chem. Eng. Sci.* **53,** 427–438 (1998).

144. Chu, X. & Schmidt, L. D. Gasification of graphite studied by scanning tunneling microscopy. *Carbon N. Y.* **29,** 1251–1255 (1991).

145. Choi, C. H., Park, S. H. & Woo, S. I. Heteroatom doped carbons prepared by the pyrolysis of bio-derived amino acids as highly active catalysts for oxygen electro-reduction reactions. *Green Chem.* **13,** 406–412 (2011).

146. Beamson, G. & Briggs, D. High Resolution XPS of Organic Polymers: The Scienta ESCA300 Database. *J. Chem. Educ.* **70,** A25 (1993).

147. Oh, Y. J. *et al.* Oxygen functional groups and electrochemical capacitive behavior of incompletely reduced graphene oxides as a thin-film electrode of supercapacitor. *Electrochim. Acta* **116,** 118–128 (2014).

148. Matsoso, B. J. *et al.* Time-dependent evolution of the nitrogen configurations in N-doped graphene films. *RSC Adv.* **6,** 106914–106920 (2016).

149. Levy, M. & Doidy, E. A. The Reaction of Borate and Sugars. *J. Biol. Chem.* **84,** 749–762 (1929).

150. Conner, J. M. & Bulgrin, V. C. Equilibria between borate ion and some polyols in aqueous solution. *J. Inorg. Nucl. Chem.* **29,** 1953–1961 (1967).

151. Chen, X., Wang, Z., Ma, S. & Ji, V. Microstructure, mechanical and tribological properties of Ti-B-C-N films prepared by reactive magnetron sputtering. *Diam. Relat. Mater.* **19,** 1336–1340 (2010).

152. Xu, C., Su, Y., Liu, D. & He, X. Three-dimensional N,B-doped graphene aerogel as a synergistically enhanced metal-free catalyst for the oxygen reduction reaction. *Phys. Chem. Chem. Phys.* **17,** 25440–25448 (2015).

153. Ferrari, A. C. & Robertson, J. Interpretation of Raman spectra of disordered and amorphous carbon. *Phys. Rev. B* **61,** 14095–14107 (2000).

154. Xie, R., Fan, G., Ma, Q., Yang, L. & Li, F. Facile synthesis and enhanced catalytic performance of graphene-supported Ni nanocatalyst from a layered double hydroxide-based composite precursor. *J. Mater. Chem. A* **2,** 7880 (2014).

155. Zheng, Y., Jiao, Y., Ge, L., Jaroniec, M. & Qiao, S. Z. Two-step boron and nitrogen doping in graphene for enhanced synergistic catalysis. *Angew. Chemie -*

*Int. Ed.* **52,** 3110–3116 (2013).

156. Gong, Y. *et al.* Boron- and nitrogen-substituted graphene nanoribbons as efficient catalysts for oxygen reduction reaction. *Chem. Mater.* **27,** 1181–1186 (2015).

157. Han, J. S. *et al.* Nitrogen and boron co-doped hollow carbon catalyst for the oxygen reduction reaction. *Carbon N. Y.* **105,** 1–7 (2016).

158. Tai, J., Hu, J., Chen, Z. & Lu, H. Two-step synthesis of boron and nitrogen co-doped graphene as a synergistically enhanced catalyst for the oxygen reduction reaction. *RSC Adv.* **4,** 61437–61443 (2014).

159. Ferrero, G. A., Preuss, K., Fuertes, A. B., Sevilla, M. & Titirici, M.-M. The influence of pore size distribution on the oxygen reduction reaction performance in nitrogen doped carbon microspheres. *J. Mater. Chem. A* **4,** 2581–2589 (2016).

160. Liu, Y. L., Shi, C. X., Xu, X. Y., Sun, P. C. & Chen, T. H. Nitrogen-doped hierarchically porous carbon spheres as efficient metal-free electrocatalysts for an oxygen reduction reaction. *J. Power Sources* **283,** 389–396 (2015).

161. He, Y. *et al.* Bifunctional Nitrogen-Doped Microporous Carbon Microspheres Derived from Poly(o-methylaniline) for Oxygen Reduction and Supercapacitors. *ACS Appl. Mater. Interfaces* **8,** 3601–3608 (2016).

162. Zhao, X. *et al.* One-step synthesis of nitrogen-doped microporous carbon materials as metal-free electrocatalysts for oxygen reduction reaction. *J. Mater. Chem. A* **2,** 11666–11671 (2014).

163. Gavrilov, N. *et al.* Electrocatalysis of oxygen reduction reaction on polyaniline-derived nitrogen-doped carbon nanoparticle surfaces in alkaline media. *J. Power Sources* **220,** 306–316 (2012).

164. Li, M. *et al.* Iron and nitrogen co-doped carbon nanotube@hollow carbon fibers derived from plant biomass as efficient catalysts for the oxygen reduction reaction. *J. Mater. Chem. A* **3,** 9658–9667 (2015).

165. Liang, H. W., Wu, Z. Y., Chen, L. F., Li, C. & Yu, S. H. Bacterial cellulose derived nitrogen-doped carbon nanofiber aerogel: An efficient metal-free oxygen reduction electrocatalyst for zinc-air battery. *Nano Energy* **11,** 366–376 (2015).

166. Wang, K. *et al.* Biomass-derived activated carbon as high-performance non-precious electrocatalyst for oxygen reduction. *RSC Adv.* **3,** 12039 (2013).

167. Song, L. T. *et al.* Sustainable Hydrothermal Carbonization Synthesis of

Iron/Nitrogen-Doped Carbon Nanofiber Aerogels as Electrocatalysts for Oxygen Reduction. *Small* **12,** 6398–6406 (2016).

168. Fan, Wenjun; Li, Zelong; You, Chenghang; Zong, Xu; Tian, Xinlong; Miao, Shu; Shu, Ting; Li, Can; Liao, S. Binary Fe, Cu-doped Bamboo-like Carbon Nanotubes as Efficient Catalyst for the Oxygen Reduction Reaction. *Nano Energy* **37,** 187–194 (2017).

169. Yin, H., Zhang, C., Liu, F. & Hou, Y. Hybrid of iron nitride and nitrogen-doped graphene aerogel as synergistic catalyst for oxygen reduction reaction. *Adv. Funct. Mater.* **24,** 2930–2937 (2014).

170. Chen, C. *et al.* Fe, N, S-doped porous carbon as oxygen reduction reaction catalyst in acidic medium with high activity and durability synthesized using CaCl 2 as template. *Chinese J. Catal.* **38,** 673–682 (2017).

171. Guo, Z. *et al.* Sulfur, trace nitrogen and iron codoped hierarchically porous carbon foams as synergistic catalysts for oxygen reduction reaction. *ACS Appl. Mater. Interfaces* **6,** 21454–21460 (2014).

172. Kone, I. *et al.* Hierarchical Porous Carbon Doped with Iron/Nitrogen/Sulfur for Efficient Oxygen Reduction Reaction. *ACS Appl. Mater. Interfaces* **9,** 20963–20973 (2017).

173. Wu, M. *et al.* N/S-Me (Fe, Co, Ni) doped hierarchical porous carbons for fuel cell oxygen reduction reaction with high catalytic activity and long-term stability. *Appl. Energy* (2016). doi:10.1016/j.apenergy.2016.03.065

174. Zhang, J., Byeon, A. & Lee, J. W. Boron-doped carbon-iron nanocomposites as efficient oxygen reduction electrocatalysts derived from carbon dioxide. *Chem. Commun.* **50,** 6349–6352 (2014).

175. Li, G. L. *et al.* N/S/B-doped graphitized carbon encased Fe species as a highly active and durable catalyst towards oxygen reduction reaction. *J. Colloid Interface Sci.* **514,** 108–116 (2018).

176. Guo, Z. *et al.* High Performance Heteroatoms Quaternary-doped Carbon Catalysts Derived from Shewanella Bacteria for Oxygen Reduction. *Sci. Rep.* **5,** 1–10 (2015).

177. Tran, T. N. *et al.* Iron Phosphide Incorporated into Iron-Treated Heteroatoms-Doped Porous Bio-Carbon as Efficient Electrocatalyst for the Oxygen Reduction

Reaction. *ChemElectroChem* **5,** 1944–1953 (2018).

178. Domínguez, C., Peña, M. A., Rojas, S. & Pérez-Alonso, F. J. Effect of the pyrolysis atmosphere and nature of iron precursor on the structure and activity of Fe/N based electrocatalysts for the oxygen reduction reaction. *Int. J. Hydrogen Energy* **41,** 22560–22569 (2016).

179. Singh, D., Mamtani, K., Bruening, C. R., Miller, J. T. & Ozkan, U. S. Use of $H_2S$ to Probe the Active Sites in FeNC Catalysts for the Oxygen Reduction Reaction (ORR) in Acidic Media. *ACS Catal.* **4,** 3454–3462 (2014).

180. Kramm, U. I. *et al.* On the Influence of Sulphur on the Pyrolysis Process of FeTMPP-Cl-based Electro-Catalysts with Respect to Oxygen Reduction Reaction (ORR) in Acidic Media. *ECS Trans.* **25,** 659–670 (2009).

181. Herrmann, I., Kramm, U. I., Radnik, J., Fiechter, S. & Bogdanoff, P. Influence of Sulfur on the Pyrolysis of CoTMPP as Electrocatalyst for the Oxygen Reduction Reaction. *J. Electrochem. Soc.* **156,** B1283 (2009).

182. Cui, X., Antonietti, M. & Yu, S. H. Structural effects of iron oxide nanoparticles and iron ions on the hydrothermal carbonization of starch and rice carbohydrates. *Small* **2,** 756–759 (2006).

183. Xing, Z. *et al.* One-pot hydrothermal synthesis of Nitrogen-doped graphene as high-performance anode materials for lithium ion batteries. *Sci. Rep.* **6,** 26146 (2016).

184. Malard, L. M., Pimenta, M. A., Dresselhaus, G. & Dresselhaus, M. S. Raman spectroscopy in graphene. *Phys. Rep.* **473,** 51–87 (2009).

185. Dhakate, S. R., Mathur, R. B. & Bahl, O. P. Catalytic effect of iron oxide on carbon/carbon composites during graphitization. *Carbon N. Y.* **35,** 1753–1756 (1997).

186. Marsh, H. & Warburton, a. P. Catalysis of graphitisation. *J. Appl. Chem.* **20,** 133–142 (1970).

187. Kong, A. *et al.* One-pot synthesized covalent porphyrin polymer-derived core-shell Fe3C@carbon for efficient oxygen electroreduction. *Carbon N. Y.* **116,** 606–614 (2017).

188. Thompson, E., Danks, a. E., Bourgeois, L. & Schnepp, Z. Iron-catalyzed graphitization of biomass. *Green Chem.* **17,** 551–556 (2015).

189. Oya, A. & Marsh, H. Phenomena of catalytic graphitization. *J. Mater. Sci.* **17,** 309–322 (1982).

190. Kato, Y., Watanabe, K. & Sato, Y. Effect of some metals on the Maillard reaction of ovalbumin. *J. Agric. Food Chem.* **29,** 540–543 (1981).

191. KATO, Y., WATANABE, K. & SATO, Y. Effect of the maillard reaction on the attributes of egg white proteins. *Agric. Biol. Chem.* **42,** 2233–2237 (1978).

192. Hamid, S. B. A., Teh, S. J. & Lim, Y. S. Catalytic hydrothermal upgrading of α-cellulose using iron salts as a lewis acid. *BioResources* **10,** 5974–5986 (2015).

193. Reiche, S., Kowalew, N. & Schlögl, R. Influence of Synthesis pH and Oxidative Strength of the Catalyzing Acid on the Morphology and Chemical Structure of Hydrothermal Carbon. *ChemPhysChem* **16,** 579–587 (2015).

194. Ding, H., Wei, J.-S. & Xiong, H.-M. Nitrogen and sulfur co-doped carbon dots with strong blue luminescence. *Nanoscale* **6,** 13817–13823 (2014).

195. Jia, Y. F., Xiao, B. & Thomas, K. M. Adsorption of metal ions on nitrogen surface functional groups in activated carbons. *Langmuir* **18,** 470–478 (2002).

196. Lua, A. C. & Yang, T. Effect of activation temperature on the textural and chemical properties of potassium hydroxide activated carbon prepared from pistachio-nut shell. *J. Colloid Interface Sci.* **274,** 594–601 (2004).

197. Marsh, H., Crawford, D. & Taylor, D. W. Catalytic graphitization by iron of isotropic carbon from polyfurfuryl alcohol, 725-1090 K. A high resolution electron microscope study. *Carbon N. Y.* **21,** 81–87 (1983).

198. Rehrah, D. *et al.* Production and characterization of biochars from agricultural by-products for use in soil quality enhancement. *J. Anal. Appl. Pyrolysis* **108,** 301–309 (2014).

199. Rafiq, M. K. *et al.* Influence of pyrolysis temperature on physico-chemical properties of corn stover (zea mays l.) biochar and feasibility for carbon capture and energy balance. *PLoS One* **11,** 1–17 (2016).

200. Rufford, T. E., Hulicova-Jurcakova, D., Zhu, Z. & Lu, G. Q. A comparative study of chemical treatment by FeCl3, MgCl2, and ZnCl2 on microstructure, surface chemistry, and double-layer capacitance of carbons from waste biomass. *J. Mater. Res.* **25,** 1451–1459 (2011).

201. Sahira, J., Mandira, A., Prasad, P. B. & Ram, P. R. Effects of Activating Agents

on the Activated Carbons Prepared from Lapsi Seed Stone. *Res. J. Chem. Sci.* **3,** 19–24 (2013).

202. Boudou, J. P. *et al.* Effects of $FeCl_3$ (intercalated or not in graphite) on the pyrolysis of coal or coal tar pitch. *Fuel* **77,** 601–606 (1998).

203. Reiche, S. *et al.* Reactivity of mesoporous carbon against water - An in-situ XPS study. *Carbon N. Y.* **77,** 175–183 (2014).

204. Sharifi, T., Hu, G., Jia, X. & Wågberg, T. Formation of active sites for oxygen reduction reactions by transformation of nitrogen functionalities in nitrogen-doped carbon nanotubes. *ACS Nano* **6,** 8904–8912 (2012).

205. Biesinger, M. C. *et al.* Resolving surface chemical states in XPS analysis of first row transition metals, oxides and hydroxides: Cr, Mn, Fe, Co and Ni. *Appl. Surf. Sci.* **257,** 2717–2730 (2011).

206. Hallam, P. M., Gómez-Mingot, M., Kampouris, D. K. & Banks, C. E. Facile synthetic fabrication of iron oxide particles and novel hydrogen superoxide supercapacitors. *RSC Adv.* **2,** 6672–6679 (2012).

207. Allen, G. C. & Tucker, P. M. Satellite Phenomena in X-ray photoelectron spectra of actinide compounds. *Chem. Phys. Lett.* **43,** 254–257 (1976).

208. McIntyre, N. S. & Zetaruk, D. G. X-ray Photoelectron Spectroscopic Studies of Iron Oxides. *Anal. Chem.* **49,** 1521–1529 (1977).

209. Lv, H. *et al.* Efficient degradation of high concentration azo-dye wastewater by heterogeneous Fenton process with iron-based metal-organic framework. *J. Mol. Catal. A Chem.* **400,** 81–89 (2015).

210. Bhattacharya, S., Roychowdhury, A., Das, D. & Nayar, S. Multi-functional biomimetic graphene induced transformation of Fe3O4 to ε-Fe2O3 at room temperature. *RSC Adv.* **5,** 89488–89497 (2015).

211. Grosvenor, A. P., Kobe, B. A., Biesinger, M. C. & McIntyre, N. S. Investigation of multiplet splitting of Fe 2p XPS spectra and bonding in iron compounds. *Surf. Interface Anal.* **36,** 1564–1574 (2004).

212. Zhu, K., Jin, C., Klencsár, Z., Ganeshraja, A. & Wang, J. Cobalt-iron Oxide, Alloy and Nitride: Synthesis, Characterization and Application in Catalytic Peroxymonosulfate Activation for Orange II Degradation. *Catalysts* **7,** 138 (2017).

213. Pecchi, G. *et al.* EFFECT OF CHLORINE PRECURSOR IN SURFACE AND CATALYTIC PROPERTIES OF Fe/TiO2 CATALYSTS. *Boletín la Soc. Chil. Química* **47,** (2002).

214. Saleh, T. A. The Role of Carbon Nanotubes in Enhancement of Photocatalysis. in *Syntheses and Applications of Carbon Nanotubes and Their Composites* (InTech, 2013). doi:10.5772/51050

215. Maldonado-Hódar, F. J., Moreno-Castilla, C., Rivera-Utrilla, J., Hanzawa, Y. & Yamada, Y. Catalytic graphitization of carbon aerogels by transition metals. *Langmuir* **16,** 4367–4373 (2000).

216. Ordomsky, V. V., Legras, B., Cheng, K., Paul, S. & Khodakov, A. Y. The role of carbon atoms of supported iron carbides in Fischer-Tropsch synthesis. *Catal. Sci. Technol.* **5,** 1433–1437 (2015).

217. Wang, Y., Han, H., Pan, D. & Zhang, P. One-Step Electrochemical Synthesis of Cobalt-Doped $Fe_2O_2CO_3$ -Reduced Graphene Oxide Nanocomposites and Their Application for $H_2O_2$ Electro-Catalytic Reduction. *J. Electrochem. Soc.* **164,** H579–H583 (2017).

218. Ferrari, A. C. Raman spectroscopy of graphene and graphite: Disorder, electron-phonon coupling, doping and nonadiabatic effects. *Solid State Commun.* **143,** 47–57 (2007).

219. Ferrari, A. C. & Basko, D. M. Raman spectroscopy as a versatile tool for studying the properties of graphene. *Nat. Nanotechnol.* **8,** 235–246 (2013).

220. Wilson, S. a *et al.* X-ray absorption spectroscopic investigation of the electronic structure differences in solution and crystalline oxyhemoglobin. Supporting Info. *Proc. Natl. Acad. Sci. U. S. A.* **110,** 16333–8 (2013).

221. Wilke, M., Farges, F., Petit, P. E., Brown, G. E. & Martin, F. Oxidation state and coordination of Fe in minerals: An FeK- XANES spectroscopic study. *Am. Mineral.* **86,** 714–730 (2001).

222. Geng, D. *et al.* High oxygen-reduction activity and durability of nitrogen-doped graphene. *Energy Environ. Sci.* **4,** 760 (2011).

223. Nagaiah, T. C., Kundu, S., Bron, M., Muhler, M. & Schuhmann, W. Nitrogen-doped carbon nanotubes as a cathode catalyst for the oxygen reduction reaction in alkaline medium. *Electrochem. commun.* **12,** 338–341 (2010).

224. Chen, S. *et al.* Nitrogen-Doped Carbon Nanocages as Efficient Metal-Free Electrocatalysts for Oxygen Reduction Reaction. *Adv. Mater.* **24,** 5593–5597 (2012).

225. Liu, Q. *et al.* Direct Synthesis of Nitrogen-Doped Carbon Nanosheets with High Surface Area and Excellent Oxygen Reduction Performance. (2014).

226. Anibal, J. *et al.* Effect of silica morphology on the structure of hard-templated, non-precious metal catalysts for oxygen reduction. *Appl. Catal. B Environ.* **198,** 32–37 (2016).

227. Silva, R., Voiry, D., Chhowalla, M. & Asefa, T. Efficient Metal-Free Electrocatalysts for Oxygen Reduction: Polyaniline-Derived N- and O-Doped Mesoporous Carbons. *J. Am. Chem. Soc.* **135,** 7823–7826 (2013).

228. Quan, B. *et al.* Single source precursor-based solvothermal synthesis of heteroatom-doped graphene and its energy storage and conversion applications. *Sci. Rep.* **4,** 23–25 (2014).

229. Sahoo, M., Sreena, K. P., Vinayan, B. P. & Ramaprabhu, S. Green synthesis of boron doped graphene and its application as high performance anode material in Li ion battery. *Mater. Res. Bull.* **61,** 383–390 (2015).

230. Lu, X., Liu, W., Ouyang, J. & Tian, Y. Distinct surface hydration behaviors of boron-rich boride thin film coatings. *Appl. Surf. Sci.* **311,** 749–752 (2014).

231. Watcharinyanon, S. *et al.* Molecular orientation of thiol-derivatized tetraphenylporphyrin on gold studied by XPS and NEXAFS. *Surf. Sci.* **603,** 1026–1033 (2009).

232. Paraknowitsch, J. P., Zhang, Y., Wienert, B. & Thomas, A. Nitrogen- and phosphorus-co-doped carbons with tunable enhanced surface areas promoted by the doping additives. *Chem. Commun.* **49,** 1208 (2013).

233. Huang, Z. *et al.* Molybdenum Phosphide: A Conversion-type Anode for Ultralong-Life Sodium-Ion Batteries. *Chem. Mater.* **29,** 7313–7322 (2017).

234. Yang, J., Xu, M., Wang, J., Jin, S. & Tan, B. A Facile Approach to Prepare Multiple Heteroatom-Doped Carbon Materials from Imine-Linked Porous Organic Polymers. *Sci. Rep.* **8,** 1–11 (2018).

235. Zhou, R., Zheng, Y., Jaroniec, M. & Qiao, S.-Z. Determination of the Electron Transfer Number for the Oxygen Reduction Reaction: From Theory to

Experiment. *ACS Catal.* **6,** 4720–4728 (2016).

236. Zhao, D., Huo, Q., Feng, J., Chmelka, B. F. & Stucky, G. D. Nonionic Triblock and Star Diblock Copolymer and Oligomeric Surfactant Syntheses of Highly Ordered, Hydrothermally Stable, Mesoporous Silica Structures. *J. Am. Chem. Soc.* **120,** 6024–6036 (1998).

237. Büchel, G., Unger, K. K., Matsumoto, A. & Tsutsumi, K. A Novel Pathway for Synthesis of Submicrometer-Size Solid Core/Mesoporous Shell Silica Spheres. *Adv. Mater.* **10,** 1036–1038 (1998).

238. Fahlman, B. D. *Materials Chemistry*. (Springer, 2011).

239. Imelik, B. & Vedrine, J. C. *Catalyst Characterization - Physical Technqiues for Solid Materials*. (Springer, 1994).

240. Guinier, A. *X-Ray Diffraction in Crystals, Imperfect Crystals, and Amorphous Bodies. Journal of the American Chemical Society* (W. H. Freeman and Company, 1963).

241. Xiandeng, H. & Jones, B. T. Inductively Coupled Plasma-Optical Emission Spectroscopy. in *Encyclopedia of Analytical Chemistry* 9468–9485 (John Wiley & Sons, Ltd, 2000). doi:10.1021/ac60349a722

242. Sing, K. The use of nitrogen adsorption for the characterisation of porous materials. *Colloids Surfaces A Physicochem. Eng. Asp.* **187–188,** 3–9 (2001).

243. Beaudoin, J. & Marchand, J. Pore Structure. in *Handbook of Analytical Techniques in Concrete Science and Technology* 528–628 (William Andrew Inc, 2001). doi:10.1016/B978-0-12-223650-1.50008-5

244. Kupgan, G., Liyana-Arachchi, T. P. & Colina, C. M. NLDFT Pore Size Distribution in Amorphous Microporous Materials. *Langmuir* **33,** 11138–11145 (2017).

245. Griffiths, P. R., Haseth, J. A. & Winefordner, J. D. *Fourier Transform Infrared Spectrometry*. (Wiley, 2007).

246. Bull, R. A., Fan, F. R. & Bard, A. J. Polymer Films on Electrodes. *J. Electrochem. Soc.* **131,** 687 (1984).

247. Jiang, R. & Anson, F. C. The origin of inclined plateau currents in steady-state voltammograms for electrode processes involving electrocatalysis. *J. Electroanal. Chem. Interfacial Electrochem.* **305,** 171–184 (1991).

248. Chaiburi, C. & Hacker, V. Catalytic activity of various platinum loading in acid electrolyte at 303 K. *Energy Procedia* **138,** 229–234 (2017).

249. Kanellopoulos, N. *Nanoporous Materials - Advanced Techniques for Characterization, Modeling, and Processing*. (2011).

250. Rehr, J. J., Kas, J. J., Vila, F. D. & Newville, M. Theory and Analysis of XAFS. in *XAFS Techniques for Catalysts, Nanomaterials, and Surfaces* (Springer, 2017). doi:10.1007/978-3-319-43866-5

251. Calvin, S. *XAFS for Everyone*. *Igarss 2014* (2014). doi:10.1007/s13398-014-0173-7.2

252. Ravel, B. & Newville, M. ATHENA , ARTEMIS , HEPHAESTUS : data analysis for X-ray absorption spectroscopy using IFEFFIT. *J. Synchrotron Radiat.* **12,** 537–541 (2005).

# Chapter 9 | Appendix

## 9.1 List of Publications

1. **Preuss, K.**, Qiao, M. and Titirici, M.-M. (2018) Vol. 2 - Chapter 3. Hydrothermal Carbon Materials for the Oxygen Reduction Reaction in *Carbon-Based Metal-Free Catalysts: Design and Applications*. Wiley VCH, pp.369-401.
2. **Preuss, K.**, Tănase, L.C., Teodorescu, C.M., Abrahams, I., and Titirici, M.-M. (2017) Sustainable metal-free carbogels as oxygen reduction electrocatalysts. *J. Mater. Chem. A*, **5** (31), 16336–16343.
3. **Preuss, K.**, Kannuchamy, V.K., Marinovic, A., Isaacs, M., Wilson, K., Abrahams, I., and Titirici, M.-M. (2016) Bio-inspired carbon electro-catalysts for the oxygen reduction reaction. *J. Energy Chem.*, **25** (2), 228–235.
4. Butt, M., **Preuss, K.**, Titirici, M.-M., Rehman, H., Briscoe, J. (2018) Biomass-Derived Nitrogen-Doped Carbon Aerogel Counter Electrodes for Dye Sensitized Solar Cells. Materials, **11**(7), 117.
5. Lu, Y., Wang, L., **Preuss, K.**, Qiao, M., Titirici, M.-M., Varcoe, J., Cai, Q. (2017) Halloysite-derived nitrogen doped carbon electrocatalysts for anion exchange membrane fuel cells. *J. Power Sources*, 372, 82-90.
6. Kumar, K.V., **Preuss, K.**, Titirici, M.M., and Rodríguez-Reinoso, F. (2017) Nanoporous Materials for the Onboard Storage of Natural Gas. *Chem. Rev.*, **117** (3), 1796–1825.
7. Kumar, K.V., Gadipelli, S., **Preuss, K.**, Porwal, H., Zhao, T., Guo, Z.X., and Titirici, M.-M. (2017) Salt Templating with Pore Padding: Hierarchical Pore Tailoring towards Functionalised Porous Carbons. *ChemSusChem*, **10** (1), 199–209.
8. Ferrero, G.A., **Preuss, K.**, Marinovic, A., Jorge, A.B., Mansor, N., Brett, D.J.L., Fuertes, A.B., Sevilla, M., and Titirici, M.-M. (2016) Fe–N-Doped Carbon Capsules with Outstanding Electrochemical Performance and Stability for the Oxygen Reduction Reaction in Both Acid and Alkaline Conditions. *ACS Nano*, **10** (6), 5922–5932.
9. Ferrero, G.A., **Preuss, K.**, Fuertes, A.B., Sevilla, M., and Titirici, M.-M. (2016) The influence of pore size distribution on the oxygen reduction reaction performance in nitrogen doped carbon microspheres. *J. Mater. Chem. A*, **4** (7), 2581–2589.

10. Alatalo, S.-M., Qiu, K., **Preuss, K.**, Marinovic, A., Sevilla, M., Sillanpää, M., Guo, X., and Titirici, M.-M. (2016) Soy protein directed hydrothermal synthesis of porous carbon aerogels for electrocatalytic oxygen reduction. *Carbon N. Y.*, **96**, 622–630.
11. Chouler, J., Padgett, G.A., Cameron, P.J., **Preuss, K.**, Titirici, M.-M., Ieropoulos, I., and Di Lorenzo, M. (2016) Towards effective small scale microbial fuel cells for energy generation from urine. *Electrochim. Acta*, **192**, 89–98.
12. Kumar, K.V., **Preuss, K.**, Guo, Z.X., and Titirici, M.M. (2016) Understanding the Hydrophilicity and Water Adsorption Behavior of Nanoporous Nitrogen-Doped Carbons. *J. Phys. Chem. C*, **120** (32), 18167–18179.
13. Kumar, K.V., **Preuss, K.**, Lu, L., Guo, Z.X., and Titirici, M.M. (2015) Effect of Nitrogen Doping on the $CO_2$ Adsorption Behavior in Nanoporous Carbon Structures: A Molecular Simulation Study. *J. Phys. Chem. C*, **119** (39), 22310–22321.

## 9.2 List of Oral Presentations

- "Pt-free Electro-catalysts for the Oxygen Reduction Reaction in Fuel Cells". Fuel Cell and Hydrogen Technical Conference 2015, Birmingham UK.
- "Sustainable catalysts for the oxygen reduction reaction in PEM fuel cells". New Electrochemical Analytical Methods and Trends in Energy Conversion and Storage – NEAMTECS 2015, Herisau, Switzerland. Invited speaker.
- "Biomass-derived porous carbons for the oxygen reduction reaction in PEM fuel cells". H2FC Supergen Conference 2015, Bath, UK.
- "Biomass-derived catalysts for the oxygen reduction reaction in fuel cells". Sustainable Functional Materials 2016, Scarborough, UK.
- "Sustainable carbon catalysts for the oxygen reduction reaction in fuel cells". H2FC Supergen Conference 2016, Belfast, UK. 3 Minute Thesis competition.
- "Tunable heteroatom doped carbogels as sustainable electro-catalysts". 1st International Symposium on Hydrothermal Carbonisation 2017, London, UK.
- "Sustainable electro-catalysts for the oxygen reduction reaction in fuel cells". International Conference on Advanced Materials: ROCAM 2017, Bucharest, Romania.
- "Sustainable carbon materials for the oxygen reduction reaction in fuel cells". London Energy Materials & Devices Hub - First Symposium between QMUL and UCL 2017, London, UK.

## 9.3 List of Poster Presentations

- H2FC Supergen Conference 2014, Birmingham, UK.
- European Technical School on Hydrogen and Fuel Cells 2015, Crete Greece.
- Carbon 2015, Dresden, Germany.
- RSC Symposium 2015 (Renewable chemicals from waste), London, UK.
- RSC Symposium 2016 (UK-Korea Symposium on Lithium and Sodium Batteries) London, UK.
- Electron microscopy characterisation of organic-inorganic interfaces 2016. London, UK.
- RSC Symposium 2016 (7$^{th}$ UK-Japan Symposium on Fundamental Research Advances in Carbon Nanomaterials), London, UK.
- Carbon 2016, PennState College, USA.
- RSC Faraday Discussion (Bio-resources: feeding a sustainable chemical industry) 2017, London, UK.

## 9.4 Prizes and Awards

- Poster prize at the 7$^{th}$ UK-Japan Symposium on Fundamental Research Advances in Carbon Nanomaterials held by the RSC in June 2016 in London, UK
- Poster prize at the Industrial Liaison Forum held by the School of Engineering and Materials Science, Queen Mary University of London in November 2016 in London, UK
- Winner of the 3 Minute Thesis (3MT) competition at the H2FC Supergen Conference in December 2016 in Belfast, UK.
- Travel grant awarded by the Royal Society of Chemistry for conference travel in July 2016 (£800)
- Travel grant awarded by the Institute of Materials, Minerals and Mining for conference travel in July 2016 (£250)